TECHNISCHE UNIVERSITÄT MÜNCHEN
Lehrstuhl für Experimentalphysik E12

Measurement and Simulation of the Radiation Environment in the Lower Atmosphere for Dose Assessment

Christian Dieter Pioch

Vollständiger Abdruck der von der Fakultät für Physik der Technischen Universität München zur Erlangung des akademischen Grades eines

Doktors der Naturwissenschaften (Dr. rer. nat.)

genehmigten Dissertation.

Vorsitzender: Univ.-Prof. Dr. J. Leo van Hemmen

Prüfer der Dissertation:

1. Hon.-Prof. Dr. Herwig G. Paretzke
2. Univ.-Prof. Walter Henning, Ph. D.

Die Dissertation wurde am 7. März 2012 bei der Technischen Universität München eingereicht und durch die Fakultät für Physik am 26. April 2012 angenommen.

CONTENTS

ABSTRACT

At typical aircraft altitudes crew members are occupationally exposed to radiation levels induced in the atmosphere by galactic cosmic radiation (GCR) that are approximately hundredfold enhanced with respect to sea-level. According to national directives, their exposure has to be monitored in Germany if the annual effective dose is likely to exceed 1 mSv. Additionally to GCR, sudden and randomly occurring bursts of energetic particles emitted from the Sun can lead to further increased radiation levels. These ground level enhancements (GLE) are expected to occur more frequently as the Sun is approaching its maximum activity within the next 2 - 3 years.

In the present work contributions to the radiation environment in the lower atmosphere by both the galactic and the solar component during GLEs are extensively discussed and, based on a detailed literature review, all features relevant for aircrew dosimetry are summarized (Chapter 2).

As neutrons account for more than 50% of the total effective dose at aircraft altitudes, two Bonner sphere spectrometers (BSS) have been continuously operated throughout the present work allowing detection of secondary neutrons in the energy range from 1 meV to 10 GeV. One spectrometer is located at low atmospheric shielding at the Environmental Research Station “Schneefernerhaus” on the Zugspitze mountain in Germany. The second instrument is located at low geomagnetic shielding at the Koldewey-station in Ny-Ålesund, Spitsbergen at a distance of approximately 800 km to the North Pole. Both systems consist of a unique set of 16 detectors, and they are the only ones worldwide being operated continuously to monitor secondary cosmic ray neutrons. It was shown that both spectrometers provide consistent results.

Because neutrons with energies $>$ 20 MeV account for approximately 50% of the total neutron dose, the response functions of the spectrometers were determined by means of GEANT4 simulations with special emphasis on high energies. For this different intra-nuclear cascade (INC) models were applied in the particle transport calculations and it was shown that differences in hadronic interaction models (i.e. the Bertini and Binary INC model) lead to uncertainties of approximately 18% in unfolded high-energy neutron fluence rates (Chapter 3).

In order to validate the calculated response functions at high energies, the spectrometers were for the first time experimentally calibrated at relevant high energies of 244 and 387 MeV. This unique experiment was carried out at the Research Center for Nuclear Physics of the University in Osaka, Japan, where quasi-monoenergetic neutrons are produced using the ^{7}Li(p,n) reaction. It turned out that basically all response functions calculated with GEANT4 agree rather well with the measurements. A closer look, however, revealed that the Binary INC model appears to describe the real BSS response at the lower beam energy somewhat better, whereas at the higher energy the Bertini INC was closer to measurements (Chapter 4).

The field of secondary cosmic radiation down to sea-level was simulated. Using most recent data on the geomagnetic field and on primary proton and helium spectra of galactic cosmic radiation, the radiation environment in the lower atmosphere was fully characterized including all components of secondary cosmic radiation (protons, neutrons, muons, electrons, positrons, photons, pions) produced in the atmosphere up to energies in the TeV range. A comparison of calculated atmospheric protons, neutrons, and muons with measurements performed at various geographic positions, altitudes, and phases in the solar cycle revealed that the Bertini INC model appears to give a somewhat more accurate estimate of secondary particle fluence rates in the atmosphere. In order to finally compare the BSS neutron measurements with simulation results, the influence of local geometrical effects on calculated neutron fluxes such as the soil composition and hydrogen content was studied. Integral neutron fluence rates at sea-level and 0 GV cutoff rigidity calculated with the Bertini INC model were found to agree within approximately 30% with the BSS measurements in Ny-Ålesund, Spitsbergen, and high-energy neutron fluxes even within 16% (Chapter 5).

These computations were also used to calculate doses to aircrews for typical long-haul flights. It turned out that route doses estimated based on secondary particle spectra calculated with the Bertini or the Binary INC model, respectively, agree within a few percent. The calculated doses were also inter-compared with predictions of the European Program Package for the Calculation of Aviation Route Doses (EPCARD) and consistency within less than 10% was found. Good agreement was also found in an inter-comparison of results from the present work with data proposed by the ICRU as reference levels for the exposure of aircrews to galactic cosmic radiation (Chapter 6).

Particular emphasis was placed on calculations of doses during GLEs. As an example, GLE 42 that occurred on September 29, 1989 was considered, and route doses between approximately 90 and 500 μSv for various long-haul flights were estimated, where the main source of uncertainty was found to arise from different primary solar proton spectra. Therefore, an uncertainty of a factor of 3 - 5 must be accepted at present. For the first time, a maximum route dose of approximately 28 mSv for a flight from Buenos Aires to Auckland was estimated in the present work for the most intense GLE ever documented, the Carrington event in September 1859 (Chapter 6).

CHAPTER

1

INTRODUCTION

After the discovery of radioactivity by Henri Becquerel in 1896 it was generally believed that ionization in the Earth's atmosphere is mainly caused by radioactive elements and isotopes contained in the soil. Measurements of ionization rates showing a decrease with increasing altitude due to absorption of the radiation released from ground seemed to confirm this opinion. Surprisingly, in 1912 the Austrian scientist Victor Hess discovered in manned balloon flights reaching altitudes above 5000 m that the electrical conductivity of air is significantly enhanced above approximately 1000 m. Furthermore, no differences were found between day and night and not even during a near-total eclipse blocking the Sun. *Hess* (1912), therefore, ruled out the Sun as source and concluded that his observations can only be explained by assuming a new type of highly-penetrating radiation entering the Earth's atmosphere from interplanetary space.

The phenomenon reported by Hess created extraordinary excitement in the scientific world of the early 20th century and attracted physicists from many different disciplines. In turn, this triggered a rapid development and progress in nuclear and particle physics as well as in space and astrophysics. In a variety of experiments it was finally shown that the newly-discovered extraterrestrial radiation predominantly consists of positively charged particles and the term *cosmic rays* was coined. The increased radiation levels in the lower atmosphere with respect to sea-level result from interactions of this primary cosmic radiation with atmospheric nuclei generating a complex field of secondaries. Two different components of primary cosmic rays are responsible for this, galactic cosmic rays originating from far outside our solar system (Chapter 2.1) and solar energetic particles released in randomly occurring eruptions on the Sun (Chapter 2.2).

Galactic cosmic rays (GCR) are mainly composed of protons, helium nuclei, and minor fractions of heavier ions. On their way to Earth the spectral distribution and intensity of GCR is modulated by the turbulent magnetic fields carried by the solar wind. As a consequence the GCR intensity slowly varies with the eleven year solar cycle being most intense at periods of minimum solar activity and least intense at maximum solar activity (section 2.1.1). Apart from this heliospheric modulation, GCR particles are affected by the magnetic field in the Earth's magnetosphere resulting in a shielding effect. This shielding is most effective near the geomagnetic equator leading to a characteristic intensity distribution of primary and secondary cosmic radiation with maxima at high geographical latitudes and minima at equatorial latitudes (section 2.1.2).

The intensity of secondary cosmic radiation induced by galactic cosmic rays strongly depends on the altitude above sea-level due to absorption processes in the atmosphere. Associated dose rates are, thus, rather low at sea-level. At typical cruising altitudes of commercial aircrafts, on the other hand, radiation levels are approximately hundredfold enhanced. Although so far no evidence for any threat on human health such as an increase in the appearance of cancer has been found in epidemiological studies, the potential biological risk of radiation doses similar to those aircrews are exposed to is still a matter of scientific debate. The exposure of flying personnel to cosmic radiation is, therefore, recommended by the International Commission on Radiological Protection (Publication 60 *ICRP*, 1990) to be regarded occupational. Based on these recommendations international and national regulations and directives have been released, in particular in the European Union. According to European directive *EU* (1996), monitoring of effective dose for aircrews is obligatory in case the yearly accumulated dose is likely to exceed 1 mSv. This for example is comparable to the dose obtained during 10 - 20 typical long-haul flights. Due to the mechanisms affecting the primary GCR intensity outlined above, doses accumulated during single flights depend on the phase of the solar cycle and an airplane's three-dimensional route profile (Chapter 6). The determination of accurate and reliable route doses for flying personnel is one of the main topics of the present work. For this purpose spectral distributions of all components of secondary cosmic radiation were determined for all solar and geomagnetic conditions as well as for all altitudes. This was accomplished by means of Monte Carlo (MC) techniques using the simulation toolkit GEANT4. The computation of secondary cosmic radiation requires a well-tuned assignment of the physics because very high energies in the TeV range have to be modeled. In any MC code hadronic interactions at high energies are handled in a theory-driven approach. Throughout the present work the impact of two state-of-the-art interaction models on calculated secondary particle spectra and associated dose rates is extensively studied. In order to validate the computations of galactic cosmic radiation, results from the present work are compared with a variety of measurements as well as with computation results from other authors (Chapter 5).

In contrast to the galactic cosmic radiation continuously striking the Earth's atmosphere, randomly occurring eruptive events on the Sun can lead to a sudden increase of radiation levels in the lower atmosphere. Such phenomena are called solar energetic particle (SEP) events. The plasma released from the Sun mainly consists of electrons, protons, and minor fractions of heavier elements. The occurrence rate of SEP events ranges from less than one per day during solar minimum to several events per day during solar maximum. In the vast majority of SEP events solar particles reach energies in the order of a few tens of MeV only and are barely faster than the solar wind. These low-energy particles are absorbed in the upper layers of the atmosphere and thus do not contribute to the radiation environment at aircraft altitudes or below. In some cases, however, particles are accelerated to relativistic energies and in turn give rise to enhanced secondary cosmic radiation in the lower atmosphere and even on ground. These so-called ground level enhancements (GLEs) exhibit an average occurrence rate of about one per year. Information on GLEs such as the spectral, temporal, and spatial characteristics outside the magnetosphere are usually derived from Neutron Monitors. A multitude of such ground-based detectors are operated all over the world to continuously monitor the integral intensity of secondary neutrons generated in hadronic interactions of primaries with atmospheric nuclei.

To supplement the information gained from the global Neutron Monitor network during GLEs, two extended Bonner sphere spectrometers (BSS) have been continuously operated by the Helmholtz Zentrum München (Chapter 3). One instrument is located at the Zugspitze mountain in Germany, whereas the other one is located in Ny-Ålesund, Spitsbergen, at a distance of approximately 800 km to the geographic North Pole. Both systems have been maintained and the data have been analyzed throughout the present work. In order to derive information on neutron spectra with a BSS, the detection efficiency of each component of the spectrometer has to be determined by means of MC codes from thermal up to relativistic energies. In the frame of the present work the response of each Bonner sphere to neutrons as well as to protons was calculated with GEANT4. Also for this task, the impact of different hadronic interaction models at high energies was studied. This includes both the impact on calculated responses as well as on unfolded fluence and dose rates (Chapter 4).

In order to validate the calculations at high energies, a unique calibration measurement was carried out in quasi-monoenergetic neutron fields with peak energies of 244 and 389 MeV at the Research Center for Nuclear Physics at the University of Osaka, Japan (Chapter 4). In this experiment the detection efficiencies of Bonner spheres were measured for the first time at such high energies. Considering that BSS systems can also be applied for radiation protection at particle accelerators and hadron therapy facilities, these measurements are of extraordinary value.

Similar to galactic cosmic radiation, also for solar cosmic rays during GLEs dose assessment for aircrews is required. Due to the unpredictable nature of these events in terms of absolute intensity as well as spectral, temporal, and spatial characteristics, doses during GLEs can only be estimated retrospectively. In the frame of the present work secondary particle fluence and dose rates were calculated for a typical but rather intense GLE (Chapter 6). Again this was done by means of the Monte Carlo code GEANT4, and the influence of hadronic interaction models on calculated spectra and dose quantities was studied. The data obtained in these studies have been provided to the European Radiation Dosimetry Group (EURADOS) for an inter-comparison of route doses along selected long-haul flights.

Based on the prescribed GLE analysis a worst case scenario is constructed in the last part of the present work (Chapter 6). In this scenario hypothetical but yet plausible worst case doses for aircrews are estimated by using data on the most intense GLE ever documented, the Carrington event.

CHAPTER

2

BACKGROUND

One major goal of the present work is the computation of the radiation environment in the lower atmosphere induced by cosmic radiation. This comprises both galactic cosmic radiation originating from outside our solar system (Section 2.1) and solar cosmic radiation originating from the Sun during solar energetic particle events (Section 2.2). All background information necessary to describe and understand secondary cosmic radiation generated in the Earth's atmosphere in interactions of primary cosmic ray particles with atmospheric nuclei is provided in this chapter. This includes a detailed discussion and review of the scientific work carried out during the last decades on the modulation of cosmic radiation by solar activity within the heliosphere (Section 2.1.1) as well as the influence of the magnetosphere on primary particle intensities observed on Earth (Section 2.1.2). In particular for solar energetic particle events sound knowledge on available data for such events (Section 2.2.1) and the corresponding techniques to derive spectral, temporal, and spatial characteristics (Section 2.2.2) is essential in order to allow for an accurate estimation of increased radiation levels at aircraft altitudes and on ground. All these issues are addressed in the corresponding sections of this chapter.

2.1 Galactic cosmic rays

The radiation environment in the lower atmosphere and at aircraft altitudes is predominantly caused by galactic cosmic ray (GCR) particles. Originating from far outside our solar system, galactic cosmic rays impinge isotropically on the Earth's atmosphere after traversing the magnetic fields within the heliosphere and the magnetosphere. The major part of the GCR particle flux is composed of atomic nuclei which account for about 98% in particle number. In energetic collisions with the interstellar medium this primary hadronic component produces minor fractions of electrons, positrons (*Boezio et al.*, 2000), and anti-protons (*Beach et al.*, 2001) which contribute about 1-2% to the overall particle flux observed near Earth. In the nucleonic component of the galactic cosmic radiation all stable elements can be found with the most abundant species being hydrogen and helium nuclei which account for about 87% and 12% of the total nuclei number, respectively (see e.g. *Simpson*, 1983). Recently performed high-precision measurements, however, have shown that the fraction of helium and heavier nuclei is only about 6% at energies above 10 GeV/nucleon (*Asakimori et al.*, 1998; *Boezio et al.*, 1999; *Alcaraz et al.*, 2000a,b). The particle composition of galactic cosmic rays with respect to the particles' energies provides useful information about possible sources and acceleration mechanisms. Due to the fact that the energy spectra of GCR particles span a range from several tens of MeV to about 10^{15} MeV, these issues are still a matter of scientific debate. Very high-energetic GCR particles are believed to be accelerated in turbulent magnetic fields of shock-waves created by supernovae remnants (see e.g. *Wiedenbeck et al.*, 2001; *Uchiyama et al.*, 2007), in highly magnetized spinning neutron stars (i.e. pulsars), accreting black holes, or in γ-ray bursts (see e.g. *Waxman*, 1995).

2.1.1 Heliospheric modulation

Galactic cosmic rays entering the heliosphere are subject to deflections in the interplanetary magnetic field and to energy losses in the solar wind. The solar wind intensity and accordingly the magnetic field strength vary with solar activity showing a periodicity of about eleven years. This results in a quasi-periodic modulation of the primary GCR flux and the differential energy spectrum near Earth with the highest intensities occurring during solar minimum and the lowest ones occurring during solar maximum activity. GCR particles with energies above several GeV per nucleon are unaffected by this modulation, and the differential energy spectra for different ion species i follow a simple power law in energy

$$j(E_k)_i = \left(\frac{d^4N}{dt\,dA\,d\Omega\,dE_k}\right)_i \propto E_k^{-\gamma_i}. \tag{2.1}$$

E_k denotes the kinetic energy per nucleon and $j(E_k)$ the differential intensity, i.e. the number of particles dN per time dt, area dA, solid angle $d\Omega$, and kinetic energy (definitions of all physical quantities used throughout this work are given in Appendix A.1). Depending on the ion species, the spectral indices γ_i are in the order of 2.5 - 3.2 and remain constant over many decades of energy. In Figure 2.1 differential particle intensities are shown for several ion species including data from the Balloon-borne Experiment with Superconducting Spectrometer (BESS, *Sanuki et al.*, 2000; *Haino et al.*, 2004), spacecraft data from the Cosmic Ray Isotope Spectrometer (CRIS) on-board the NASA Advanced Composition Explorer[1] (ACE, *Stone et al.*, 1998), and data from the Electron Proton Helium Instrument[2] (EPHIN, *Müller-Mellin et al.*, 1995) on-board the Solar and Heliospheric Observatory (SOHO). Comparison of the absolute particle intensities during solar minimum (top panel in Fig. 2.1) and maximum (bottom panel in Fig. 2.1) conditions demonstrates that the modulation effects need to be taken into account as precisely as possible in order to allow for an

---

[1] http://www.srl.caltech.edu/ACE/ACS/

[2] http://www2.physik.uni-kiel.de/SOHO/phpeph/EPHIN.htm

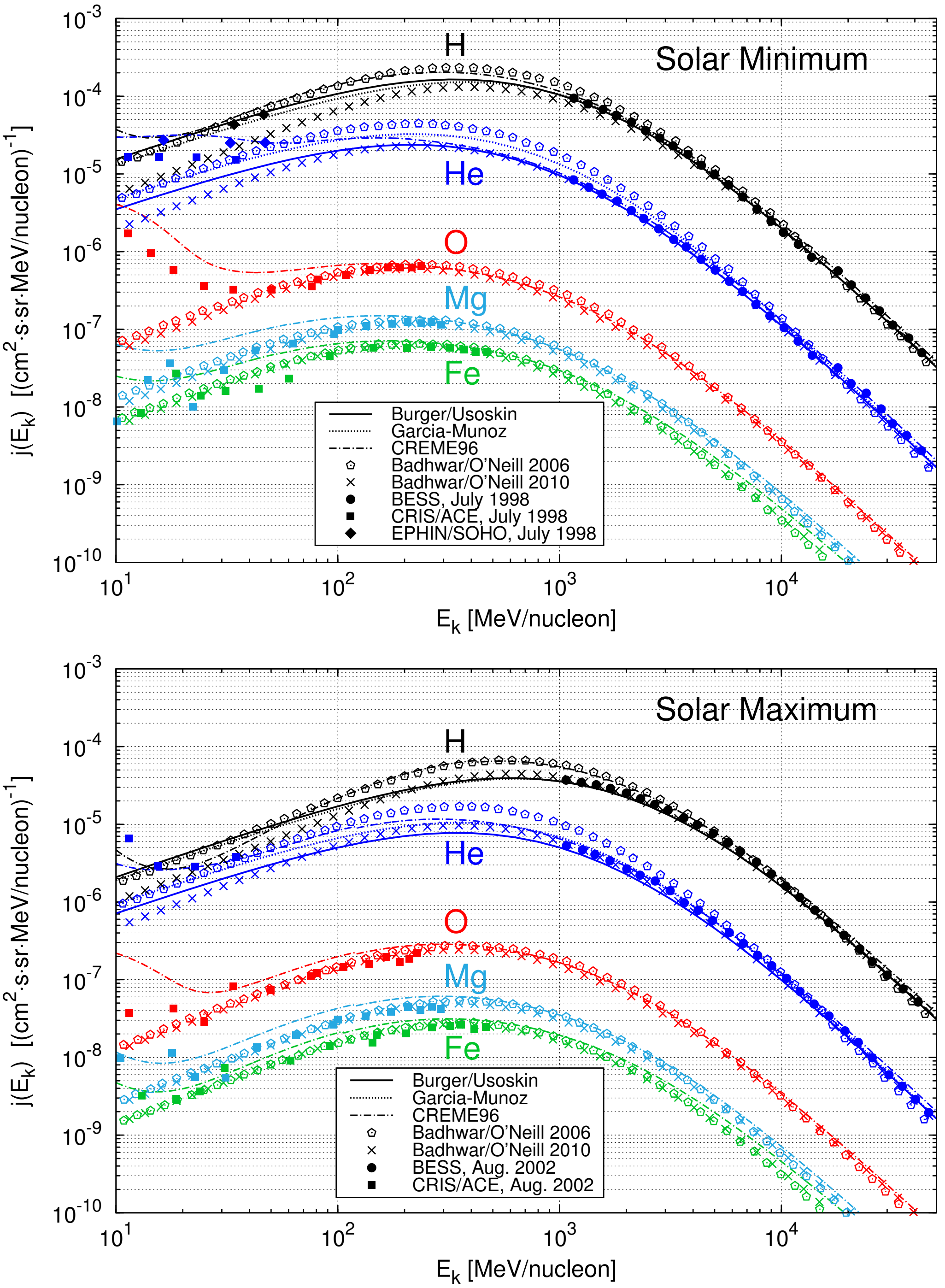

FIGURE 2.1: Differential particle intensities of primary galactic H, He, O, Mg, and Fe ions as a function of kinetic energy per nucleon measured near Earth during the BESS experiments (*Sanuki et al.*, 2000; *Haino et al.*, 2004), with the CRIS detector on-board ACE (*Stone et al.*, 1998; *Haino et al.*, 2004), and with EPHIN on-board SOHO (*Müller-Mellin et al.*, 1995) in July 1998 (top panel), i.e. solar minimum, and August 2002 (bottom panel), i.e. solar maximum conditions. Experimental data are compared with predictions using models of Burger/Usoskin (*Burger et al.*, 2000; *Usoskin et al.*, 2005), Garcia-Munoz (*Garcia-Munoz et al.*, 1975), CREME96 (*Tylka et al.*, 1997), and Badhwar/O'Neill (*O'Neill*, 2006, 2010).

accurate estimation of the radiation environment in the Earth's atmosphere.

The first one providing a full physical description of the intensity modulation within the heliosphere was *Parker* (1965). In this theory the charged particle transport is described by a complex Fokker-Planck equation. Taking diffusion, convection, and adiabatic deceleration processes into account, the intensity and energy of GCR particles entering the heliosphere are lowered due to scattering on irregularities in the interplanetary magnetic field. Under certain assumptions, such as e.g. steady-state conditions and a spherically symmetric heliosphere, the equation derived by *Parker* (1965) can be approximated in the so-called force-field model developed by *Gleeson and Axford* (1968). Comparison of full numerical solutions to the Parker's equation and analytical solutions using the force-field approximation have shown that the force-field model provides a good empirical fit to the modulation of the GCR spectrum observed near Earth for energies above about 100 MeV/n (*Usoskin et al.*, 2002; *Caballero-Lopez and Moraal*, 2004; *McCracken et al.*, 2004).

In the frame of the force-field approximation, the differential intensity j_i of cosmic ray nuclei of species i at a distance of one astronomical unit (1 AU $\approx 1.5\times10^{11}$ m) from the Sun, i.e. near Earth is given as

$$j_i(E_k,\phi) = j_{LIS,i}(E_k+\Phi)\cdot\frac{E_k\cdot(E_k+2\cdot E_0)}{(E_k+\Phi)\cdot(E_k+\Phi+2\cdot E_0)}, \tag{2.2}$$

$$\Phi = \frac{Ze}{A}\cdot\phi, \tag{2.3}$$

where e denotes the elementary charge, E_k the kinetic energy per nucleon, and E_0 the rest energy of nuclei with charge number Z and mass number A. The un-modulated local interstellar (LIS) spectrum outside the heliosphere is denoted by $j_{LIS,i}$. The so-called modulation function Φ is the mean energy loss a cosmic ray nucleus experiences due to adiabatic deceleration in the expanding solar wind while traveling from the termination shock of the heliosphere to one AU. Under the assumptions outlined above, the modulation function is connected to the so-called modulation parameter or modulation potential ϕ via Equation 2.3 which is, apart from the LIS spectrum, the only free parameter in this model. The modulation potential is quoted in MV and can take values between approximately 250 MV during solar minimum and 1500 MV during solar maximum. The force-field model accurately reflects the facts that the strongest modulation occurs during solar maximum and that less deflection in the interplanetary magnetic field occurs the heavier the nuclei are (i.e. the smaller the charge over mass ratio Z/A is) and the higher the kinetic energies are.

For the description of the local interstellar spectra various models have been proposed and many attempts have been made to derive the corresponding modulation potential. For this purpose, a variety of datasets such as e.g. satellite or space shuttle data, sunspot numbers, or data from ground-based Neutron Monitors have been used (see e.g. *O'Brien and de Burke*, 1973; *Castagnoli and Lal*, 1980). It should be noted, however, that the value of the modulation parameter is a function of the local interstellar spectrum and the dataset used. Therefore, it is poorly defined, and modulation potentials derived for different LIS spectra using different datasets are sometimes hardly comparable (*Usoskin et al.*, 2005; *Herbst et al.*, 2010).

In addition to experimental data, Figure 2.1 shows predictions for the differential GCR spectra using several theoretical models. Obviously, large discrepancies between model-predictions are observed. Since in the frame of the present work secondary particle spectra in the Earth's atmosphere were calculated and compared with results of different authors who used different models for the GCR primary spectra, basic features of these models are summarized in the following paragraphs. Furthermore, it should be noted that in contrast to open space conditions heavy nuclei do not contribute significantly to the radiation environment in the lower atmosphere due to their small number and the short mean free paths in the atmosphere (also see discussion in Chapter 5). Therefore, the main focus of the present work is on hydrogen and helium nuclei. Unfortunately, the experimental data shown in Figure 2.1 do not cover the rather important energy region from 100 MeV/n to 1 GeV/n for protons and α-particles. To decide which GCR model agrees best with measurements, high-precision data from the Alpha Magnetic Spectrometer (AMS) collected aboard a space shuttle flight at an altitude of 380 km above sea-level were used (*Alcaraz et al.*, 2000a,b). These data are shown in Figure 2.2 and compared with model predictions.

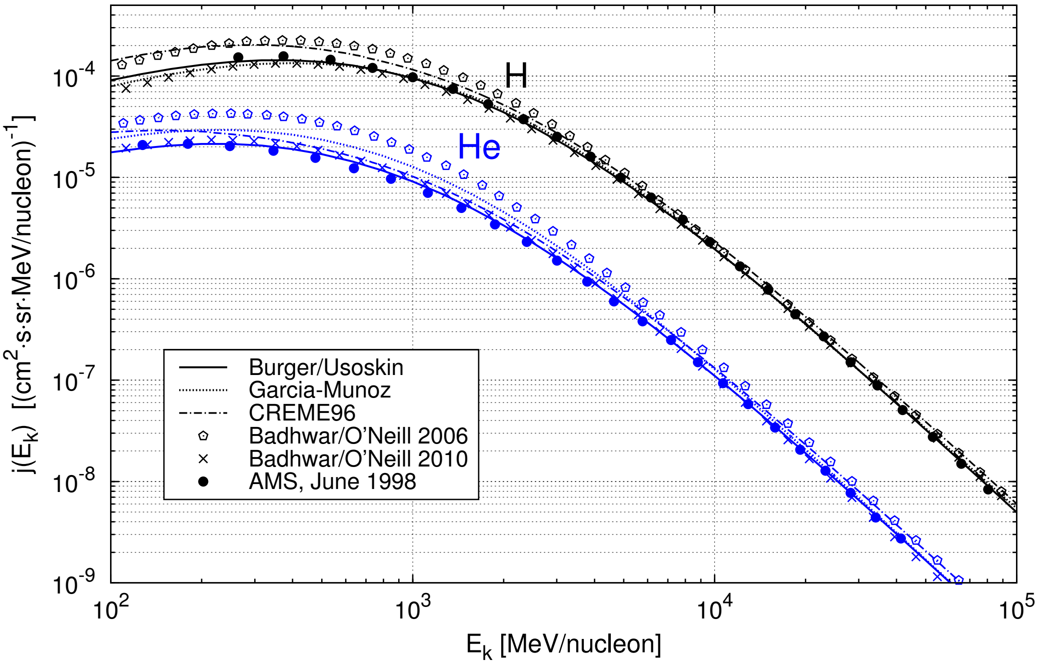

FIGURE 2.2: Differential particle intensities of primary galactic H and He ions as a function of kinetic energy per nucleon measured near Earth with the Alpha Magnetic Spectrometer (AMS, *Alcaraz et al.*, 2000a,b) aboard a space shuttle flight in June 1998, i.e. during solar minimum. Experimental data are compared with model predictions of Burger/Usoskin (*Burger et al.*, 2000; *Usoskin et al.*, 2005), Garcia-Munoz (*Garcia-Munoz et al.*, 1975), CREME96 (*Tylka et al.*, 1997), and Badhwar/O'Neill (*O'Neill*, 2006, 2010).

One widely used model for the LIS spectra is the so-called Badhwar/O'Neill model. Originally, this model is based on Neutron Monitor count rates of the Climax Neutron Monitor in Colorado, U.S.A. (*Badhwar and O'Neill*, 1994, 1996; *Badhwar*, 1997). *O'Neill* (2006) presented an updated version (referred to as Badhwar/O'Neill 2006 model) using data from the Advanced Composition Explorer (ACE) spacecraft and Interplanetary Monitoring Platform

(IMP) satellite measurements. The LIS spectrum with respect to the kinetic energy is given as

$$j_{LIS}^{Badhwar/O'Neill}(E_k) = \frac{j_{0,i}\beta^{\delta_i}}{(E_k + E_0)^{\gamma_i}}, \tag{2.4}$$

where β denotes the ratio of the particle's velocity to the speed of light. The free parameters $j_{0,i}$, δ_i and γ_i were determined by a least square fitting procedure using ACE and IMP measurements. The corresponding numerical values may be found in *O'Neill* (2006). In *O'Neill* (2010) the model was again revised (referred to as Badhwar/O'Neill 2010 model) using all available balloon and satellite data since 1955. The corresponding modulation parameter in the very recent model is derived from the Wolf number (sunspot number) instead of Climax count rates as in the earlier version. The sunspot number is a good measure for solar activity taking a certain time lag of the actual GCR modulation into account. This time lag reflects the fact that the magnetic field responsible for the modulation is carried by the solar wind with a velocity of approximately 400 km/s - 800 km/s. Therefore, direct measurements of solar activity, such as sunspot numbers, precede the GCR modulation by several months, which is the time the solar plasma needs to reach the outer heliosphere where the actual modulation takes place. Comparison of both Badhwar/O'Neill models (see Figs. 2.1, 2.2) shows the great importance of the data set chosen to derive the LIS spectra and the modulation parameter, especially for hydrogen and helium spectra where the 2006 model significantly overestimates the observed particle intensities below several GeV/n. The strength of both Badhwar/O'Neill models, however, is that they provide very accurate estimates for all ion species heavier than He what makes them very useful for space applications.

The same is valid for a model developed by *Nymmik et al.* (1992, 1994, 1996) which is implemented in the "Cosmic Ray Effects on Micro-Electronics" (CREME96) tool developed by *Tylka et al.* (1997). As for the Badhwar/O'Neill 2010 model, in CREME96 the monthly averaged Wolf number is used to estimate the solar activity and the corresponding modulation potential. The differential spectra with respect to the rigidity are given as

$$j_{LIS}^{Nymmik}(R,t) = \frac{D_i\beta^{\alpha_i}}{R^{\gamma_i}}\left(\frac{R}{R + R_0(t)}\right)^{\Delta_i(t)}, \tag{2.5}$$

where the rigidity R is given as the ratio of a particle's momentum to its charge ($R = pc/|q|$). The parameters D_i, α_i, γ_i are fixed for each ion species i, and the parameters $R_0(t)$ and $\Delta(t)$ are adapted according to the current modulation potential (for details refer to *Nymmik et al.*, 1992, 1994, 1996). Data shown in Figures 2.1 and 2.2 were taken from the website of the CREME96 project[3]. As can be seen, predictions of proton intensities show nearly the same features as those of the Badhwar/O'Neill 2006 model, i.e. they overestimate the measurements significantly. The agreement with experimental helium data is somewhat better but still α-particle fluxes are overvalued. For heavier ions the CREME96 data follow the Badhwar/O'Neill models for energies above about 100 MeV/n and match rather well with observations. For the sake of completeness it should be mentioned that in the model of *Nymmik et al.* (1992) the so-called anomalous cosmic ray component is included which is responsible for the characteristic increase around several tens of MeV/n. This results from

---

[3] https://creme.isde.vanderbilt.edu/

reflections of low-energy GCR particles at the termination shock of the heliosphere (see e.g. *Klecker et al.*, 1998).

Another widely used model for the LIS spectra of hydrogen, helium, and carbon nuclei is the one proposed by *Garcia-Munoz et al.* (1975):

$$\begin{aligned} j_{LIS}^{Garcia-Munoz}(E_k) &= A_i \cdot (E_k + \Theta)^{-\gamma_i}, \\ \Theta &= B_i \cdot \exp(-C_i \cdot E_k) \end{aligned} \tag{2.6}$$

The fit parameters A_i, B_i, C_i are given in *Garcia-Munoz et al.* (1975) and were originally derived from IMP-5, IMP-7, and IMP-8 satellite measurements carried out in the early 1970s. Differential particle spectra calculated using the model of Garcia-Munoz accurately agree with experimental proton data. Helium data on the other hand are significantly overestimated, especially at solar minimum conditions (see Figs. 2.1 and 2.2).

One of the most recent models for the LIS spectra was developed by *Burger et al.* (2000). Using ground-based Neutron Monitor data from all available stations since 1951, i.e. spanning six solar cycles, *Usoskin et al.* (2005) provided the corresponding modulation potential (the model using the LIS of *Burger et al.* (2000) and ϕ from *Usoskin et al.* (2005) is referred to as Burger/Usoskin model). The differential intensity of protons outside the heliosphere with respect to the kinetic energy is given as

$$\begin{aligned} j_{LIS}^{Burger/Usoskin}(E_k) &= \frac{1.9 \cdot 10^4 \cdot P(E_k)^{-2.78}}{1 + 0.4866 \cdot P(E_k)^{-2.51}}, \\ P(E_k) &= \sqrt{E_k \cdot (E_k + 2 \cdot E_0)}, \end{aligned} \tag{2.7}$$

where $j(E_k)$ and E_k are expressed in units of $[m^2 \cdot s \cdot sr \cdot GeV/n]^{-1}$ and in $[GeV/n]$, respectively. $P(E_k)/c$ is the momentum of a particle with rest energy E_0. Using the force-field approximation (Eq. 2.2), *Usoskin et al.* (2005) reconstructed the modulation parameter for the years 1951 through 2004 based on Neutron Monitor count rates. In *Usoskin et al.* (2011) ϕ is given for the years 1936 through 2009, where the parameter before 1951 is derived from measurements with ionization chambers and hence subject to large uncertainties. An updated list for later times is available online at the cosmic ray station in Oulu[4]. The differential intensity for helium can be obtained by weighting Equation 2.7 with the proton to helium ratio in particle numbers of 0.05. Of note is that *Usoskin et al.* (2005) inter-calibrated their procedure of deriving the modulation potential with many recently performed precise balloon- and space-born measurements such as e.g. NMSU (*Webber et al.*, 1989), AMS (*Alcaraz et al.*, 2000a,b), BESS (*Sanuki et al.*, 2000; *Haino et al.*, 2004), or CAPRICE (*Boezio et al.*, 1999, 2000). Therefore, the agreement of measurements and calculated particle intensities is remarkable both for hydrogen and helium as well as for all solar conditions. This makes it perfectly suited for calculations of the radiation environment in the Earth's atmosphere. On the other hand, in contrast to Nymmik's and the Badhwar/O'Neill models, the Burger/Usoskin model is not capable of estimating GCR fluxes for ion species heavier than helium. This makes it less applicable for studies of the radiation environment and exposure in open space.

---

[4] http://cosmicrays.oulu.fi/phi/phi.html

The detailed disussion and comparison of models with experimental data was carried out in order to select the most appropriate primary GCR spectra for the calculation of secondary cosmic radiation produced in interactions with atoms and molecules in the Earth's atmosphere. As already argued, primary hydrogen and helium are by far the most important species to consider for this purpose. The models by *Nymmik et al.* (1992) and *Badhwar/O'Neill* (2006) predict much larger hydrogen and helium intensities than observed making them less suitable. The *Badhwar/O'Neill* (2010), the *Garcia-Munoz et al.* (1975), and the *Burger/Usoskin et al.* (2005) models are basically all consistent concerning proton spectra and agree rather well with measurements. Helium intensities given by *Garcia-Munoz et al.* (1975), on the other hand, are somewhat higher than observations near Earth, whereas *Burger/Usoskin et al.* (2005) and *Badhwar/O'Neill* (2010) are in good agreement. Nonetheless, especially referring to the very accurate AMS measurements shown in Figure 2.2, the *Burger/Usoskin et al.* (2005) model appears to agree best. Therefore, this model was chosen for the transport calculations in the Earth's atmosphere, to derive secondary particle intensities, and related dose quantities presented in subsequent chapters.

2.1.2 Influence of the magnetosphere and cutoff rigidity

Beside the influence of the interplanetary magnetic field in the heliosphere discussed in the previous section, GCR particles are highly affected by the magnetic field in the Earth's magnetosphere. The magnetosphere is the region of space surrounding the Earth which is dominated by the influence of the geomagnetic field. At distances of a few Earth radii, this field predominantly results from sources inside the Earth and can well be described by a dipole field. At larger distances interactions of the solar wind plasma with the geomagnetic field induce large currents in various parts of the magnetosphere, especially near the extremal boundary, the so-called magnetopause. This in turn leads to a complex field structure in the outer magnetosphere. The magnetosphere imposes an obstacle to the solar wind and hence is compressed on the side facing the Sun. Measured from the Earth the magnetosphere extends to about ten Earth radii ($\approx$ 64000 km) on the day side, whereas it extends to hundreds of Earth radii in a comet-like tail on the night side (*Axford*, 1982).

Charged galactic cosmic ray particles entering the magnetosphere are subject to deflections due to the Lorentz force. Therefore, particles with a certain momentum are shielded by the magnetic field. This shielding is most effective at low geographical latitudes where the dipole-like field lines of the geomagnetic field are parallel to the top of the Earth's atmosphere. In contrast, charged particles can travel almost freely along the field lines near the poles and are guided towards the Earth.

For the computation of secondary cosmic radiation induced by primary particles in the Earth's atmosphere, a detailed knowledge about the access of primaries to the atmosphere is essential. For this reason, the so-called cutoff rigidities were calculated in the frame of the present work which describe the impact of the magnetosphere on the isotropic galactic cosmic ray flux. Since an understanding of the magnetosphere's influence is necessary for the upcoming discussion of solar particle events, these results are already presented in the following section.

Computation of particle trajectories and cutoff rigidities

The most appropriate physical quantity describing trajectories of charged particles in a given magnetic field is the (magnetic) rigidity R which is connected to the Larmor radius r_L in a field of magnitude $|\vec{B}|$:

$$R = \frac{pc}{|q|} = \frac{pc}{Ze} = r_L|\vec{B}|c, \tag{2.8}$$

where p denotes the momentum, q the charge, and c the speed of light. Particles with identical rigidities follow identical paths in a given magnetic field, whatever their mass and charge is. Moreover, the trajectory of a positively charged particle with given magnetic rigidity is identical, except for the sign of the velocity vector, to that of a negatively charged particle reaching the same location in space but traveling in opposite direction. Therefore, the common method of computing cosmic ray trajectories in the Earth's magnetic field is to follow a negatively charged particle with the mass of a proton starting from a certain geographic position and altitude in reverse direction (*Smart et al.*, 2000). Additionally to the geographic position and the particle's magnetic rigidity, i.e. its mass, velocity, and charge, the direction of incidence on top of the atmosphere defines its trajectory in space. Accordingly, a huge number of trajectories must be calculated for each geographical position of interest in order to take all possible incoming directions into account. For this reason, a commonly used approach is to consider only particles arriving vertically on top of the atmosphere. Especially for studies of the radiation environment in the lower atmosphere due to galactic cosmic rays, this concept has been shown to give an accurate description (*Smart and Shea*, 2003a,b).
Figure 2.3 illustrates backward calculated trajectories of cosmic ray particles of different rigidities starting in vertical direction from a certain geographical position on top of the atmosphere. With decreasing rigidity (labeled by increasing numbers), the curves show increasing bending before escaping into space (labels 1, 2, 3 in Fig. 2.3). Particles with lower rigidities follow a looped trajectory before escaping (labels 4, 5), and those with very low rigidities follow re-entrant trajectories intersecting with the Earth (label 15). Positively charged particles of these rigidities coming from outside the magnetosphere cannot reach the top of the atmosphere at this location. These trajectories and the corresponding rigidities are called forbidden. Negatively charged mirror particles escaping from the magnetosphere indicate access to this location for positively charged particles, and the corresponding trajectories are called allowed.

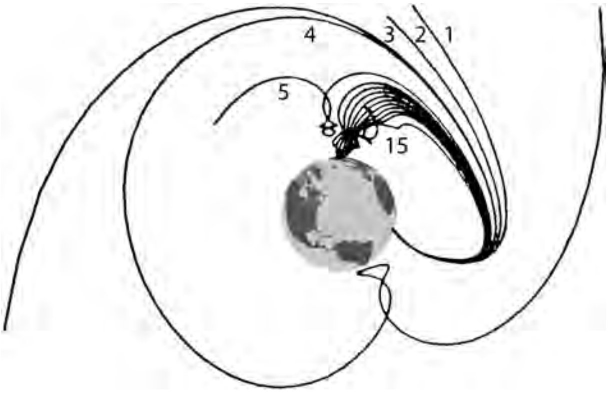

FIGURE 2.3: Illustration of backward calculated charged particle trajectories with different rigidities starting in vertical direction at a certain geographical position on top of the atmosphere (adapted from *Smart et al.*, 2000). Decreasing magnetic rigidities are labeled by increasing numbers.

In calculations of backward trajectories a large range of possible rigidities (about 0.0 GV - 20.0 GV) needs to be covered. This range is scanned with a constant rigidity increment ΔR and for each increment the access of the particle to the geographical position of interest is tested. In Figure 2.4 typical results of such calculations are shown, where black areas depict forbidden and white areas depict allowed rigidities. Obviously, three regions can be distinguished. A region at high rigidities where all particles have access to the point of interest, a region at low rigidities where no particle has access, and an intermediate region, the so-called penumbra, where some rigidities allow access and some do not. The last rigidity allowing access before the first rigidity prohibiting access is called the main cutoff rigidity R_M. The last rigidity for that particles can reach the atmosphere and below which all trajectories are forbidden is called the Störmer cutoff rigidity R_S (*Störmer*, 1930). In Figure 2.4 the main and the Störmer cutoffs are depicted in green.

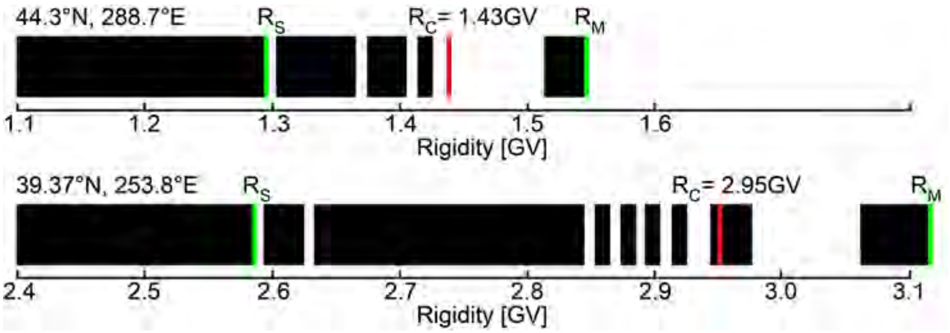

FIGURE 2.4: Illustration of trajectory-derived cutoff rigidities and the penumbral structure for two selected locations and vertical incidence. White regions indicate allowed rigidities, black regions indicate forbidden rigidities. The main and the Störmer cutoff rigidities (R_S, R_M) are depicted in green, and the effective vertical cutoff rigidity R_C is marked in red (adapted from *Smart et al.*, 2000).

To account for the penumbral region, the effective vertical cutoff rigidity is used which is defined as

$$R_C = R_M - \int_{R_S}^{R_M} \kappa(R) dR, \tag{2.9}$$

where $\kappa(R)$ is 1 if the trajectory corresponding to R is allowed and 0 otherwise. A detailed review on the terminology of various cutoff rigidities is given in *Cooke et al.* (1991).

Calculation of cutoff rigidities using MAGNETOCOSMICS

To determine the effective vertical cutoff rigidities in a grid covering the whole globe, the program package MAGNETOCOSMICS, kindly provided by *Desorgher* (2004) from the University of Bern, was used. This program is based on the Monte Carlo simulation toolkit GEANT4 (*Agostinelli et al.*, 2003; *Allison et al.*, 2006) and allows to calculate the propagation of charged cosmic ray particles through different magnetospheric models by numerical integration of the Lorentz equation of motion for a negatively charged mirror-particle. In MAGNETOCOSMICS the effective vertical cutoff rigidity at a user-defined location and altitude is approximated as

$$R_C = R_M - N_{allowed} \cdot \Delta R, \tag{2.10}$$

where $N_{allowed}$ denotes the number of allowed trajectories encountered in the penumbra and $\varDelta R$ denotes the rigidity step size which was set to 0.01 GV.

For the dipole-like geomagnetic field due to sources inside the Earth, the very recently released 11th generation of the International Geomagnetic Reference Field[5] (IGRF-11) model (*Finlay et al.*, 2010b) was applied. The geomagnetic field in this model is defined by the negative gradient of a scalar potential V expressed in spherical harmonics:

$$V(r,\theta,\phi,t) = a\sum_{n=1}^{N}\sum_{m=0}^{n}\left(\frac{a}{r}\right)^{n+1}[g_n^m(t)\cos(m\phi)+h_n^m(t)\sin(m\phi)]P_n^m(\cos\theta), \quad (2.11)$$

where $P_n^m(\cos\theta)$ denote the semi-normalized associated Legendre functions of degree n and order m, $a = 6371.2$ km is the magnetic reference radius, and (r,θ,ϕ) are the geocentric coordinates of the location considered at time t. The numerical Gauss coefficients g_n^m, h_n^m are updated every five years by the International Association of Geomagnetism (IAGA) (details are given in *Finlay et al.*, 2010a,b; *Macmillan and Finlay*, 2011). The newly released coefficients for IGRF-11 were implemented in the MAGNETOCOSMICS code in order to calculate vertical effective cutoffs valid for the years 2010 to 2015.

Apart from the internal geomagnetic dipole field, the complex field structure of the outer magnetosphere has to be taken into account in order to precisely calculate vertical effective cutoff rigidities. For the description of the magnetospheric field due to external sources, various models developed by *Tsyganenko* (1987, 1989, 1995, 2002a,b) are implemented in the MAGNETOCOSMICS code. In the frame of the present work the model described in *Tsyganenko* (1989) was chosen which accurately accounts for the tail current sheet, the ring currents, and the magnetospheric boundary. It provides seven different states of the magnetosphere related to the K_p index quantifying disturbances in the horizontal component of the magnetic field with an integer in the range of 0 - 9 (0 being calm and 5 or more indicating a geomagnetic storm). The calculations of the cutoff rigidities were performed for calm magnetospheric conditions with a K_p index of 0.

The results of the calculations of the vertical effective cutoff rigidities using the MAGNETOCOSMICS program package and the prescribed magnetic field models are shown in Figure 2.5. Depicted are isolines of constant cutoff rigidities from 0 to 17 GV as a function of geographic position. The figure reflects the characteristic influence of the geomagnetic field on the isotropic GCR particle flux resulting in low cutoff rigidities at high geographical latitudes and maximum cutoffs of about 17 GV in equatorial latitudes. The red squares in Figure 2.5 show the positions of the geomagnetic poles in 2010 indicating the tilt of the geomagnetic dipole axis with respect to the axis of rotation. Apart from the tilt, the magnetic axis is shifted regarding the center of the Earth. As a consequence, the cutoff rigidities show a longitudinal asymmetry along the equator with the highest values in south Asian regions.

---

[5] http://www.ngdc.noaa.gov/IAGA/vmod/igrf.html

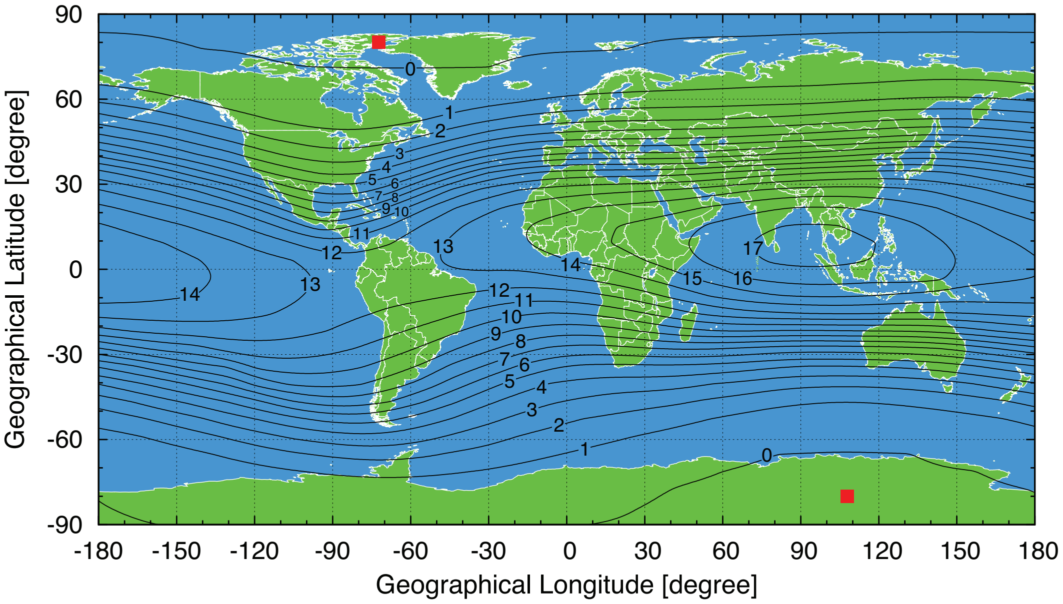

FIGURE 2.5: Vertical effective cutoff rigidities R_C in GV as a function of geographic position for the years 2010 to 2015 calculated with MAGNETOCOSMICS using the IGRF-11 model for the internal geomagnetic field (*Finlay et al.*, 2010a,b; *Macmillan and Finlay*, 2011) and the model by *Tsyganenko* (1989) for the description of the outer magnetosphere. Red squares indicate the positions of the magnetic poles in the year 2010.

2.2 Solar energetic particles and ground level enhancements

Apart from galactic cosmic rays described in section 2.1, energetic particles produced in randomly occurring eruptive events on the surface of the Sun may influence the radiation environment in near-Earth orbits and in the Earth's atmosphere. Such phenomena are called solar energetic particle (SEP) events. In SEP events ejecta with masses ranging from $10^7 - 10^{10}$ tons are emitted containing a maximum mechanical energy in the order of 10^{25} Joules (see e.g. *Hundhausen et al.*, 1994; *Ohyama and Shibata*, 1998). The released plasma mainly consists of electrons, protons, and minor fractions of heavier ions with average energies in the order of several hundreds of keV to several tens of MeV. Solar energetic particles are either generated by so-called solar flares (SF) or by coronal mass ejections (CME).

A solar flare is defined as a rapid and intense brightening on the Sun caused by a sudden release of magnetic energy stored in the solar atmosphere (*Cliver*, 1995). The first solar flare was independently recorded on September 1, 1859 by *Carrington* (1860) and *Hodgson* (1860) who were observing sunspots at that time. As a result of accelerated electrons, solar flares are accompanied by the emission of Bremsstrahlung covering the entire electromagnetic spectrum from radio waves, through optical emission, to X-rays, and gamma rays. According to the peak energy fluence Ψ in the X-ray emission with wavelengths of

TABLE 2.1: Solar flare classification according to the peak energy fluence in 1-8 Å X-ray emission measured by the GOES satellites.

X-ray flare class	Peak Energy Fluence Ψ [W/m^2]
B	$\Psi < 10^{-6}$
C	$10^{-6} \leq \Psi < 10^{-5}$
M	$10^{-5} \leq \Psi < 10^{-4}$
X	$\Psi > 10^{-4}$

1 - 8 Å measured by the Geostationary Operational Environmental Satellites[6] (GOES), solar flares are categorized in four classes as indicated in Table 2.1. Additionally to the logarithmic scale given by these classes, solar flares are sub-categorized on a linear scale within each class, i.e. an energy fluence of $1{\times}10^{-4}$ W/m^2 corresponds to a X1-class flare, a fluence of $2{\times}10^{-4}$ W/m^2 corresponds to a X2-class flare and so on. Solar energetic particles generated by flares are believed to be accelerated in stochastic processes involving resonant wave-particle interactions, where energy is transferred from plasma waves at the flare site to the ambient particle population (*Mandzhavidze and Ramaty*, 1993). Due to the fact that these processes take place deep in the solar atmosphere, the energetic particles produced usually show high ionization states which are expected in the Sun's chromosphere.

The second source of solar energetic particles, coronal mass ejections, are defined as an observable change in the Sun's coronal structure occurring on a time scale of a few minutes to several hours accompanied by the outward motion of coronal plasma clouds (*Hundhausen et al.*, 1984). Huge parts of the Sun's corona can be involved in the generation of these clouds, which in turn can reach enormous extensions of up to 180° in helio coordinates (*Cane and Lario*, 2006). CMEs exhibit an occurrence rate of about 0.5 per day during solar minimum to about 2.5 per day during solar maximum (*Yashiro et al.*, 2004; *Gopalswamy et al.*, 2009). The speeds of the plasma clouds launched from the corona range from several hundreds of km/s to more than 2500 km/s (*Yurchyshyn et al.*, 2005). Most of the CMEs, however, are only slightly faster than the solar wind. It is now widely agreed that in CMEs energetic particles are generated via diffusive shock acceleration. Hereby, particles either from the corona or from the ambient solar wind gain energy in multiple reflections on turbulences at both sides of the CME-driven shock. Since the energy gain in this process depends linear on the particle velocity, this process is called a first order Fermi mechanism. In order to develop a supersonic shock front, the CME must be much faster than the solar wind. Therefore, only the fastest CMEs give rise to SEP events (details may be found e.g. in *Reames*, 2000; *Ng and Reames*, 2008).

The two different sources of solar energetic particles with their specific acceleration mechanisms result in different time profiles of the associated SEP events observed in space. Solar flares release so-called impulsive events with a duration of several hours, whereas CME shocks produce gradual events lasting up to several days. Apart from the temporal characteristics, the two classes of events exhibit different signatures in terms of e.g. different

---

[6] http://www.oso.noaa.gov/goes/

elemental abundances or ionization states of the accelerated particles. Although CMEs and SFs are not caused by each other, they are strongly related processes. Therefore, in most cases one phenomenon accompanies the other, and the associated SEP events exhibit features of both. A detailed discussion of the specific signatures due to mechanisms on the Sun, however, is beyond the scope of this work, but the interested reader may refer to review articles by e.g. *Reames* (1990, 1999) or *Kahler* (1992, 1994).

As already stated at the beginning of this section, in most of the SEP events particles reach kinetic energies in the order of several tens of MeV only. Therefore, the vast majority of these events are irrelevant concerning contributions to the radiation environment in low-Earth orbits or in the Earth's atmosphere. In some cases, however, particles are accelerated to relativistic energies which in turn may lead to highly increased radiation levels near and even on Earth. *Mason et al.* (1984) and *Reames* (1998) have shown that such increases are mainly caused by SEP events containing major fractions of high-energetic protons (so-called solar proton events (SPE)). Of note is furthermore, that *Kahler et al.* (1978, 1984, 2001) found a correlation of 96% between large solar proton events and CMEs. For this reason, it is nowadays commonly accepted that very intense SPEs are caused or at least accompanied by fast CMEs. High-energetic protons in these events can penetrate deep into the Earth's atmosphere and generate secondary particles that may be even detected on ground. Such intense events are accordingly called ground level enhancements (GLE). The threshold kinetic energy for an increase in radiation at sea-level is about 450 MeV for a primary proton striking the Earth's atmosphere. This corresponds to a magnetic rigidity of about 1 GV, the so-called atmospheric cutoff. Solar protons of this energy move with relativistic velocities of nearly 75% of the speed of light and hence reach the Earth within approximately eleven minutes.

The first GLE in history was recorded on February 28th, 1942 by *Lange and Forbush* (1942) and *Edward et al.* (1942) who detected sharp increases in ionization rates. This ground level enhancement is the first in the chronological list containing 70 events with the most recent one recorded on December 13th, 2006. For the sake of completeness it should be mentioned that the rapid increase detected during the first GLE coincided with an intense geomagnetic storm occurring a few hours later. This resulted in a several days lasting decrease of the measured ionization rates with respect to calm conditions, a so-called Forbush decrease. Soon after the first GLE, however, another two were detected and *Forbush* (1946) suggested charged particles emitted by the Sun being associated with these sudden increases.

Shea and Smart (1990) investigated a total number of 218 relativistic solar proton events ($E_k > 450$ MeV) during solar cycle 19, 20, and 21 from 1955 through 1986 and found a frequency of up to 20 SEP events per year near solar maximum. Only 35 of them resulted in GLEs on Earth. Hence, the average occurrence rate of GLEs is about one per year with a higher frequency during solar maximum and a lower frequency during solar minimum. The temporal distribution of GLEs over the period considered by *Shea and Smart* (1990) is depicted in Figure 2.6 on the left, where the accumulation near solar maxima, i.e. during periods of high sunspot numbers, is obvious.

Apart from the outlined requirements concerning the minimum kinetic energies, SEP events have to take place on the right location on the Sun in order to give rise to a GLE. This is a result of the magnetic connection between Sun and Earth. Due to the Sun's intrinsic rotation, the field lines of the interplanetary magnetic field (IMF) exhibit a spiral pattern, the so-called

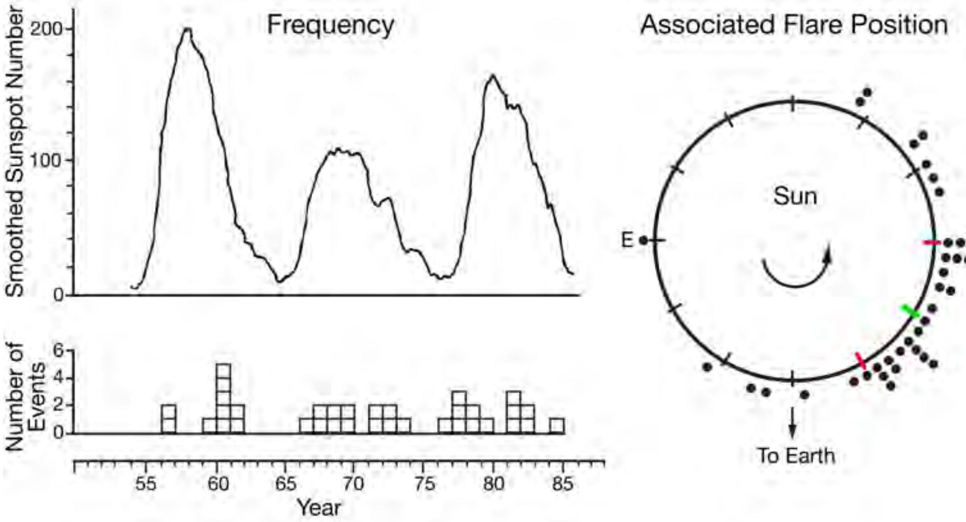

FIGURE 2.6: Observed relativistic solar proton events during solar cycles 19, 20, and 21 (adapted from *Shea and Smart*, 1990). The smoothed sunspot number (top panel on the left) is compared with the occurrence rate of ground level enhancements (bottom panel on the left). The heliolongitudes of the associated X-ray flare sites are depicted in the right panel. Red marks indicate the range of coordinates magnetically best connected to Earth ($\approx$ 30°W - 90°W) and the green mark indicates the foot-point location of the Sun-Earth interplanetary magnetic field line around 60°W.

Parker spirals (*Parker*, 1958). The field line connecting the Earth with the Sun has its foot-point on the western hemisphere at approximately 60°W heliolongitude (*Zimbardo et al.*, 2006). Charged particles emitted by the Sun propagate most easily along this interplanetary magnetic field line to Earth. Therefore, SEP events are most likely to result in GLEs if the eruption on the Sun occurs near the foot-point, i.e. at about 30°W - 90°W. *Shea and Smart* (1990) also studied the position of the X-ray flares associated with the GLEs observed during solar cycles 19, 20, and 21. The results are shown in the right panel of Figure 2.6. Obviously, the flare sites exhibit a pronounced accumulation around heliolongitudes near the foot-point of the Sun-Earth field line (indicated as green and red marks in Fig. 2.6) which is in good agreement with studies by *Mullan and Schatten* (1979). Nevertheless, the spatial distribution is widely spread. This indicates that in many GLEs examined by *Shea and Smart* (1990) the actual source of relativistic particles were not the flares but rather fast CMEs involving huge parts of the Sun's surface.

To give an example for an SEP event, Figure 2.7 shows images captured with instruments on-board SOHO on 15th April, 2001. In the top panel pictures of the active region before the event are displayed, which were taken with the Extreme Ultraviolet Imaging Telescope (EIT, *Delaboudinière et al.*, 1995) at wavelengths of 304 Å, 171 Å, and 195 Å (at 07:19 UT, 13:00 UT, 13:48 UT). In the middle panel the temporal evolution of a coronal mass ejection is obvious which was captured with the Large Angle Spectroscopic Coronagraph (LASCO) C2 (at 13:54 UT, 14:06 UT, 14:30 UT *Brueckner et al.*, 1995). The bottom panel shows the advancing CME captured with LASCO C3 at later times (14:42 UT, 15:18 UT, 15:42 UT). As can be seen, the active region on the Sun (indicated by an arrow in the top

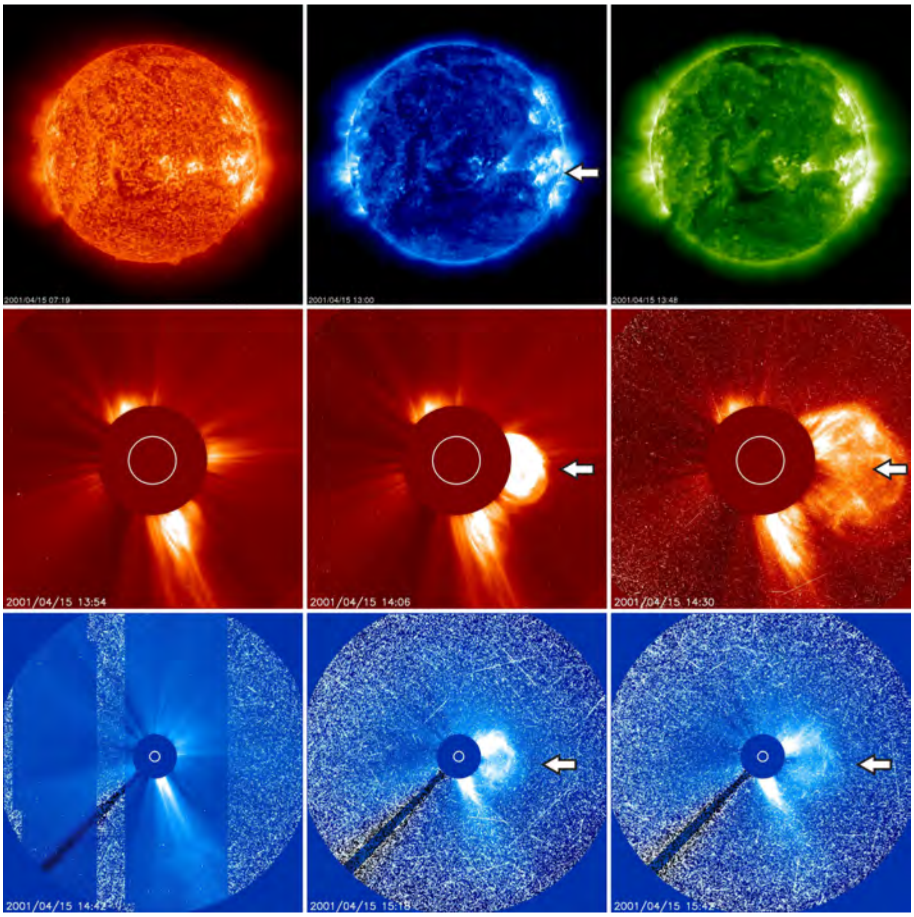

FIGURE 2.7: Images of the active solar region (top panel) observed with the EIT telescope (*Delaboudinière et al.*, 1995) on April 15th, 2001 (at 304 Å, 171 Å, and 195 Å) before the evolution of the CME giving rise to GLE 60. The middle and bottom panels show the evolving CME (indicated by arrows) captured with the LASCO C2 and LASCO C3 coronagraphs (*Brueckner et al.*, 1995) on-board SOHO. From left to right and top to bottom, the images were captured at 07:19 UT, 13:00 UT, 13:48 UT, 13:54 UT, 14:06 UT, 14:30 UT, 14:42 UT, 15:18 UT, and 15:42 UT.

panel) was located on the western hemisphere. From this region, a CME was launched (indicated by arrows in the middle and bottom panel) spanning several tens of degrees in heliolongitude and heliolatitude. Comparison with the extension of the Sun, indicated by the white circles in the centers of the coronagraph images, shows the enormous size of the CME. This CME was fast enough to accelerate coronal particles to relativistic energies and it was magnetically well connected to Earth. Therefore, this event resulted in the 60th ground level enhancement measured on Earth.

2.2.1 Data on SEP events and GLEs

Data on solar energetic particle events and ground level enhancements are available from two different sources, interplanetary and ground-based observations. The interplanetary observations are in general limited to non-relativistic energies, whereas ground-based instruments are only sensitive to relativistic primary particles. In measurements performed on ground, secondary particles produced in interactions of high-energetic primaries with atoms in the atmosphere are detected. In contrast, measurements using instruments on-board spacecrafts and satellites have the big advantage that galactic and solar particles are directly detected.

Data from interplanetary observations

One of the most important data sources in space is the Geostationary Operational Environmental Satellites[7] (GOES) operated by the National Oceanic and Atmospheric Administration (NOAA). These geosynchronous satellites orbit in the equatorial plane at about 36000 km above ground and measure e.g. X-rays, energetic electrons, protons and alpha particles. Other data such as interplanetary magnetic field measurements are available at the Space Physics Interactive Data Resource[8] (SPIDR, *Zhizhin et al.*, 2008). Further information on solar energetic particles is provided by the Solar and Heliospheric Observatory[9] (SOHO) and the Advanced Composition Explorer[10] (ACE), where data from many devices like coronagraphs, telescopes, or spectrometers are available. As already mentioned, one disadvantage of the currently operated instruments on-board spacecrafts is that they do not cover a wide enough energy range. For example the uppermost differential energy channel for protons aboard GOES-11 covers the range from 510 MeV to 700 MeV. This barely overlaps with the range above 450 MeV ground-based detectors are sensitive to. Therefore, these instruments alone cannot be used to precisely describe and forecast radiation levels on Earth, especially during GLEs. Nonetheless, important additional information and insights during such events can be derived.

Data from ground based observations - The Neutron Monitor Network

On Earth, a variety of continuous measurements are performed to monitor the intensity of secondary particles generated in collisions of high-energetic primary galactic or solar cosmic ray nuclei with atoms in the atmosphere. As already mentioned, only relativistic primaries with kinetic energies above 450 MeV per nucleon give rise to detectable secondary particle fluence rates at sea-level. Among others, the secondary particles consist of neutrons, protons, muons, and pions which are routinely measured.

The most important and most useful instruments for cosmic radiation and space weather observations on Earth are Neutron Monitors (NM). As discussed in more detail in *Pioch*

---

[7] http://www.oso.noaa.gov/goes/

[8] http://spidr.ngdc.noaa.gov/spidr/

[9] http://sohowww.nascom.nasa.gov/

[10] http://www.srl.caltech.edu/ACE/

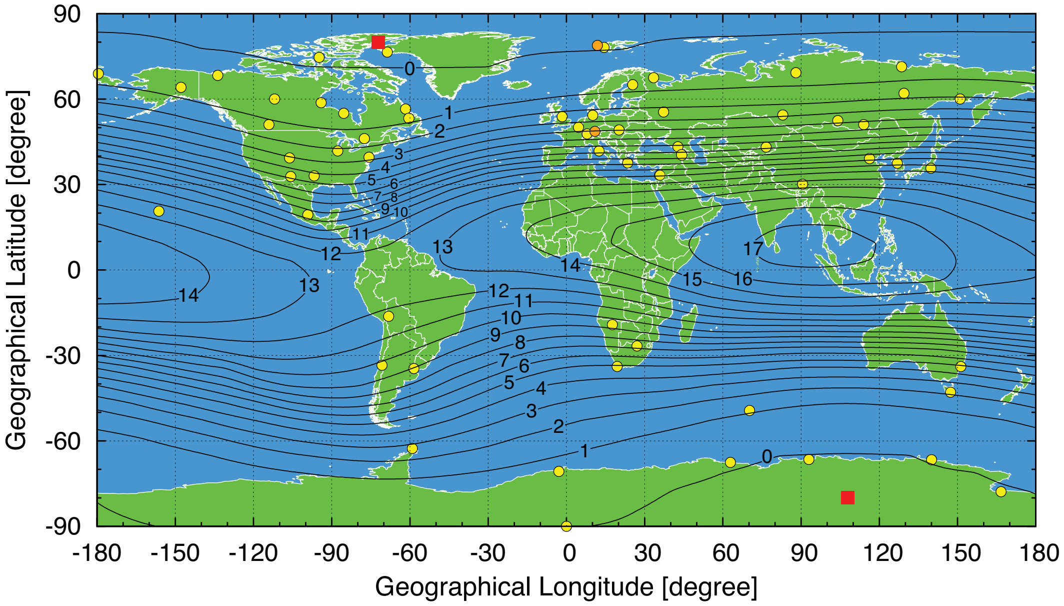

Figure 2.8: Geographic positions of various Neutron Monitor stations which are either in operation or whose data are still available (yellow dots). Positions of the two Bonner Sphere spectrometers operated by the HMGU which provide their data to the Neutron Monitor Data Base (NMDB) are shown as orange dots. Isolines indicate the vertical effective cutoff rigidity in GV (see Section 2.1.2 and Figure 2.5) and red squares indicate the positions of the magnetic poles in 2010.

(2008); *Pioch et al.* (2011b), Neutron Monitors are mainly sensitive to secondary neutrons which account for about 95% of the count rate but also protons ($\approx 3.5\%$), charged pions, and muons ($\approx 1.5\%$) contribute to the overall count rate. A single Neutron Monitor count rate only provides information about the integral intensity of cosmic radiation, and no spectral information can be derived. By simultaneously analysing the count rates of several Neutron Monitor stations which are located at various altitudes and geographical latitudes (i.e. at different cutoffs), information on the primary cosmic ray spectrum, the angular distribution, and the temporal variation of the primary particles outside the magnetosphere can be obtained. This global Neutron Monitor network is the only tool available to get information about spectra of relativistic solar protons during GLEs and the related acceleration mechanisms in the rigidity range from 1 GV to about 17 GV. In Figure 2.8 locations of NM stations at various geographic positions and cutoff rigidities are shown as yellow dots. Some of these stations are not in operation any more but their data are still available.

Primarily two different types of detectors are in operation, the IGY type and the standardized NM64 type. The so-called NM64 supermonitor was developed in the 1960s (*Hatton and Carmichael*, 1964; *Hatton*, 1971) and is nowadays the most commonly used detector. Both devices, however, were developed to study the high-energy hadronic component of cosmic radiation. Low-energy neutrons result from moderation in the soil and other material surrounding the monitor and hence do not provide useful information about secondary and primary cosmic radiation. Therefore, the devices are designed to be mainly sensitive to neutrons with energies above several tens of MeV. In case of the NM64, the outer volume of the detector consists of Polyethylene (PE), the so-called reflector, where low-energy neutrons are either reflected or absorbed. The inner part contains a big volume of lead, the producer, serving as target for higher energetic neutrons to produce further neutrons in spallation reactions with lead nuclei. These neutrons are finally moderated by the inner PE moderator to be efficiently detected in big BF_3 proportional counter tubes via $^{10}B(n,\alpha)^7Li$ reactions. Details about the geometry and the corresponding response of the NM64 type Neutron Monitor to neutrons and protons are discussed in *Pioch* (2008); *Pioch et al.* (2011b). *Clem and Dorman* (2000) additionally determined the monitor's response to muons and pions.

Data from NM stations are available through a variety of databases such as IZMIRAN[11] or the Australian Antarctic Data Center[12] (AADC). Of note is the recently released Neutron Monitor Data Base[13] (NMDB) which comprises 28 NM stations from 16 institutes and provides high-resolution data in near real-time.

At the Helmholtz Zentrum München (HMGU), two Bonner sphere spectrometers (BSS) are continuously operated at the Zugspitze mountain, Germany, and in Ny-Ålesund on Spitsbergen, Norway (shown as orange dots in Fig. 2.8). The spectrometers measure the spectral fluence rate distribution of secondary cosmic ray neutrons as a function of time and hence provide additional information to Neutron Monitors. The instruments have been maintained and their data have been analyzed throughout the present work (a description in every detail follows in chapter 3). *Pioch et al.* (2011b) showed that data obtained by means of the BSS and NM measurements are largely consistent. Therefore, it is planned to provide the BSS data to the Neutron Monitor Data Base on a routine basis.

Data from ice core samples

Another very interesting source of data on large GLEs is polar ice. Studies during the past 20 years have shown that impulsive nitrate peaks in polar ice are related to major solar proton events and hence provide a well-conserved record over several thousands of years. The initial research on this relationship was done by *Zeller et al.* (1986) and *Dreschhoff and Zeller* (1990) who found large spikes in nitrate concentration in two ice cores drilled in the Antarctic region which coincided with the time of major solar proton events.

Solar protons striking the Earth's polar atmosphere cause ionization. Secondary electrons from these ionization processes dissociate molecular nitrogen and generate nitrate radicals, so-called odd nitrogen[14] denoted by NO_y (for example via $N + O_2 \rightarrow NO + O$). Large portions of the nitrogen oxides are further oxidized to nitric acid (HNO_3), some of which becomes attached to aerosols or incorporated in snow crystals. By gravitational sedimentation the nitric acid is transported downwards to the troposphere and finally conserved in polar ice. The precipitation into polar ice occurs on a time scale of about 6 weeks (details on this process may be found in *Shea et al.* (2006) and references therein).

The two Antarctic ice cores analyzed by *Dreschhoff and Zeller* (1990) only cover a time period of 1905-1991. In 1992 another very long core was drilled at Summit, Greenland, especially dedicated to high-resolution nitrate studies. This core, 125.6 m in length, covers

---

[11] http://cr0.izmiran.rssi.ru/common/links.htm

[12] http://data.aad.gov.au/aadc/gle/

[13] http://www.nmdb.eu/

[14] Odd nitrogen includes NO, NO_2, NO_3, HN_2O_5, N_2O_5, HNO_3, HO_2NO_2, $ClONO_2$, $BrONO_2$

a time period of 1561-1991. *McCracken et al.* (2001a,b,c) analyzed both the Arctic and the Antarctic ice cores and demonstrated that nitrate events are highly correlated with periods of solar-terrestrial disturbance, with a probability of chance correlation being less than 10^{-9}. Furthermore, the seven largest GLEs observed since continuous monitoring of cosmic radiation started in 1936 were shown to be in one-to-one correlation with ice core data. The probability of this occurring by chance was estimated to be less than 10^{-6}. Therefore, the work of *McCracken et al.* (2001a,b,c) eliminated most of the doubts and uncertainties in the association between impulsive nitrate and major solar proton events.

In order to get useful information from the deposited nitrate found in drilled polar ice cores, *McCracken et al.* (2001a) established a conversion relationship of nitrate concentration and omnidirectional proton fluence on top of the atmosphere. In this approach, the total nitrate concentration N_t [ng/cm^2] in a single impulsive event summed over n time samples contained in the event is given as

$$N_t = \rho \cdot L \cdot \sum_n C_n \;\propto\; \mathit{\Gamma} \cdot \mathit{\Phi}, \tag{2.12}$$

where ρ denotes the ice density and C_n (in units of ng per g water) the nitrate concentration of the nth sample with length L. The conversion factor $\mathit{\Gamma}$ connects the omnidirectional fluence $\mathit{\Phi}$ [cm^{-2}] of protons with kinetic energies >30 MeV to the amount of nitrate in an ice core sample. Lower energetic protons cause ionizations and NO_y production in the uppermost atmosphere and contribute to auroral appearances. Most of this high altitude NO_y is destroyed by photo dissociation and is unlikely to be transported to the troposphere. The conversion factor in Equation 2.12 is an explicit function of time and geographical latitude accounting for annual variations of the NO_y transport in the atmosphere and different efficiencies of the precipitation in Arctic and Antarctic regions. Using various ground-based measurements and observations in interplanetary space, *Shea and Smart* (1990, 1993) provided values for the omnidirectional fluences of the seven largest GLEs observed in the period 1942-1989 in order to finally derive the conversion factor. Taking an average factor, a total number of 70 impulsive nitrate events were identified having a >30 MeV omindirectional fluence $\geq 2\times10^9$ cm^{-2}. A complete list of fluence values derived for these events and another 55 with fluences in the range of 1 - 2×10^9 cm^{-2} is given in *McCracken et al.* (2001a,b). It should be noted that the nitrate peaks of the 70 largest events were five standard deviations above the mean background level, which allows to exclude fluctuations in the nitrate concentration that may be attributed to meteorological reasons. Apart from short-term fluctuations, the nitrate concentration in polar ice shows a pronounced annual wave-like variation due to seasonal changes in the polar atmosphere. The date of occurrence of all investigated nitrate events has been determined using this annual variation of nitrate in the samples. By measuring the samples' electric conductivity, the dates of occurrence have been further inter-calibrated with the occurrence of well-dated volcanic eruptions.

The largest impulsive nitrate deposition on the 450 years record in the Arctic ice core was dated to late 1859. This event is associated with the first observation of a solar flare by *Carrington* (1860) and *Hodgson* (1860) on September 1, 1859. For this so-called Carrington event, an omnidirectional fluence (>30 MeV) of 1.88×10^{10} cm^{-2} was derived, having almost twice the fluence of the second largest in 1895. The Carrington event was by far the most intense GLE and geomagnetic storm ever documented. *Green and Boardsen* (2006) summarized data on this event using scientific measurements, newspapers, ship logs, and other records available. They found aurorae in all colors and forms being reported at geographical latitudes below 50° and a several hours lasting blood red aurora even at $\approx 18°$ latitude.

Using the fluence value derived by *McCracken et al.* (2001a) for the Carrington event, in the frame of the present work a plausible worst case scenario for a GLE was constructed. In this scenario secondary particle fluence rates in the Earth's atmosphere, related dose rates, and accumulated doses for aircrews along selected flights were calculated (see Chapter 6).

2.2.2 Modeling GLEs using Neutron Monitors

As stated in the previous section, information on GLE proton spectra at relativistic energies can be obtained using the global Neutron Monitor network. Such spectra were used in the present work to study the radiation environment in the lower atmosphere due to solar cosmic radiation (see Chapter 6). For this reason, the modeling of SEP events and the procedure of deducing spectral, temporal, and spatial characteristics of solar protons from NM count rate increases during GLEs, as well as the uncertainties arising are discussed in the following.

As pointed out in section 2.2.1, Neutron Monitors are mainly sensitive to secondary neutrons and, to a minor degree, to protons and other secondaries generated in collisions of cosmic ray nuclei with atoms in the atmosphere. An increase in the fluence rate of primary protons at a Neutron Monitor's location gives rise to enhanced secondary particle fluence rates and hence triggers an increase in the detector's count rate. Apart from the Monitor's response to secondary particles and the altitude of the NM station, the corresponding count rate, therefore, depends on the intensity and the spectral distribution of primary particles impinging onto the atmosphere.

The galactic cosmic ray background responsible for a Neutron Monitor's count rate during calm conditions exhibits an isotropic angular distribution. Accordingly, the momentum direction of particles outside the magnetosphere is of no importance, and the influence of the magnetosphere on the GCR particle intensity and spectral distribution on top of the atmosphere is well described by the vertical effective cutoff rigidity at the location considered (see section 2.1.2). In contrast, solar proton spectra during SEP events are usually anisotropic, in particular during the initial phase of the event. Since a particle with given rigidity and momentum direction outside the magnetosphere only has access to a certain geographic location, in GLE analyses this direction must be taken into account in addition to the cutoff rigidity. To address this issue, *McCracken et al.* (1962, 1968) introduced the asymptotic viewing or asymptotic arrival direction of a particle with access to a certain location as the particle's direction of motion in space prior to any deflection in the magnetosphere. Similar to the computation of cutoff rigidities described in section 2.1.2, asymptotic viewing directions are determined via backward calculation of the trajectory of a negatively charged particle in the magnetospheric field. Usually only particles starting in vertical direction on top of the atmosphere are considered. The direction of the mirror particle at the exit point of the magnetopause defines the viewing direction (details may be found in *Shea and Smart*, 1982; *Cooke et al.*, 1991). In Figure 2.9 (left) trajectories of particles with rigidities $1 \leq R \leq 20$ GV are exemplary shown for the NM stations in Barentsburg and Apatity. For conceptual purposes, asymptotic directions of approach can be plotted on an extended

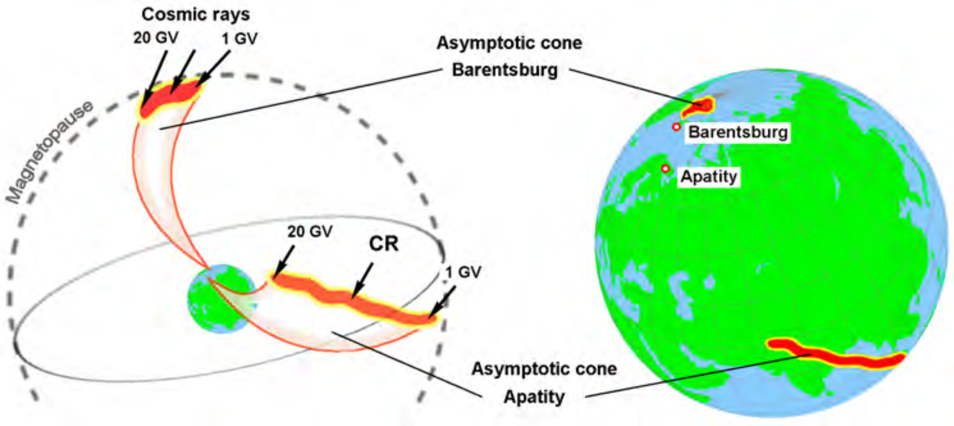

FIGURE 2.9: Illustration of the asymptotic cone of acceptance. On the left particle trajectories ($1 \leq R \leq 20$ GV) are shown for the NM stations in Barentsburg and Apatity. On the right the corresponding asymptotic directions are shown as projections on an extended orthographic globe (courtesy: *E.V. Vashenyuk and Yu.V. Balabin*).

orthographic projection of the Earth and thus are given by pairs of geocentric coordinates, i.e. latitude and longitude (ϕ, λ) as shown in Figure 2.9 (right). The set of asymptotic arrival directions for all rigidities allowing access to a particular site defines the so-called asymptotic cone of acceptance. As can be seen in Figure 2.9, although the NM stations of Barentsburg and Apatity are geographically close to each other, the polar station in Barentsburg samples radiation from very high latitudes of the celestial sphere, whereas the sub-polar station in Apatity only accepts particles from equatorial regions. Hence, the asymptotic cone of acceptance basically turns ground-based cosmic ray detectors into directional instruments, and the global Neutron Monitor network can be considered as a multidirectional solar proton spectrometer in the relativistic energy range.

In order to characterize the anisotropic flux of solar protons during SEP events, the so-called pitch angle distribution $f(\alpha, t)$ is used. This distribution is assumed to be rotationally symmetric around the incoming or apparent source direction of the event which is approximately given by the Sun-Earth magnetic field line. The pitch angle $\alpha[(\phi, \lambda), R]$ for a particular site is taken as the angle between the apparent source direction and the asymptotic viewing direction (ϕ, λ) at rigidity R. Along the apparent source direction, the particle intensity is assumed to be maximal and decreasing with increasing pitch angle. Various dependencies of the intensity on the pitch angle can be assumed. Some studies have found that solar particle anisotropies can be described by a Gaussian in pitch angle (e.g. *Smart et al.*, 1971; *Debrunner and Lockwood*, 1980), others have shown that an exponential function fits rather well to observations (e.g. *Beeck and Wibberenz*, 1986; *Humble et al.*, 1991), but also a linear relationship has been successfully applied (e.g. *Matthiä*, 2009; *Matthiä et al.*, 2009a,b). The convolution of the pitch angle distribution with all asymptotic directions for a specific geographic position finally gives the vertical flux of primary particles on top of the atmosphere above the vertical effective cutoff rigidity at this location.

Knowing the asymptotic cones of acceptance for all Neutron Monitor stations considered and assuming a certain pitch angle distribution describing the anisotropy of a GLE, information on the spectral, temporal, and spatial characteristics of the event can be deduced from measured count rate increases. The basic underlying technique has been developed over many years (*Smart et al.*, 1971; *Shea and Smart*, 1982) and many subsequent improvements have been made such as applying more accurate representations of the magnetospheric field (*Flückiger and Kobel*, 1990; *Flückiger et al.*, 2006) or taking non-vertical directions of incidence at the atmosphere into account (*Cramp et al.*, 1997; *Vashenyuk et al.*, 2007).

The response of a sea-level Neutron Monitor to the anisotropic solar proton flux with differential intensity $j(R,t)$ $[cm^{-2}s^{-1}sr^{-1}MeV^{-1}]$ and pitch angle distribution $f(\alpha,t)$ arriving in vertical direction on top of the atmosphere at time t can be expressed by

$$\Delta N(t) = \sum_{R_C}^{\infty} S(R)j(R,t)f(\alpha,t)\Delta R\,, \tag{2.13}$$

where $\Delta N(t)$ denotes the corresponding count rate increase, R the rigidity, and R_C the vertical effective cutoff rigidity. $S(R)$ is the specific yield function describing the influence of the atmosphere and relating the count rate to all components of the primary and secondary particle spectra (see e.g. *Stoker*, 1994). Equation 2.13 finally needs to be solved for as many NM stations as possible by applying a least square fitting procedure minimizing the differences between calculated and observed count rate increases. This allows to determine the primary solar proton parameters, i.e. the differential energy spectrum, the apparent source direction, and the pitch angle distribution outside the magnetosphere for several time intervals during the GLE event. Especially for an accurate determination of the spectral characteristics, responses of stations widely separated in both latitude and longitude must be included. Moreover, also stations which did not record increases must be taken into account, since they place bounds on the spectra at very high energies (see e.g. *Cramp et al.*, 1997).

Considering the difficulties involved in modeling SEP events in terms of calculating accurate asymptotic cones, assuming a proper anisotropy distribution and yield function, and including an adequate set of NM stations, it is not surprising that in principle many different functions of the differential solar proton intensity $j(R,t)$ can reproduce the observed count rate increases equally well. For this reason, differential proton spectra deduced by various authors can differ significantly from each other which implies large uncertainties for the GLE spectra.

2.2.3 Examples of GLE spectra

Various approaches for the differential proton spectra during GLEs have been proposed to fit the observed count rate increases of Neutron Monitors according to Equation 2.13. As argued at the beginning of section 2.2, energetic protons in large SEP events are believed to be accelerated in shocks driven by fast coronal mass ejections. *Ellison and Ramaty* (1985) developed a model for shock acceleration and derived an equation for the differential spectra of electrons and ions. These spectra with respect to the kinetic energy (E_k) are given by a power law in momentum p with an exponential turnover at high energies:

$$j(E_k) = dJ/dE_k \ \propto \ p^{-\gamma} \cdot \exp\left(-\frac{E_k}{E_0}\right). \tag{2.14}$$

E_0 denotes the energy where the turnover becomes important resulting in a steepening at high energies.

Xapsos et al. (2000) have shown that many GLE observations can well be described by a Weibull distribution for the proton spectra:

$$j(E_k) = dJ/dE_k = j_0 \tau \alpha E_k^{\alpha-1} \exp(-\tau E_k^{\alpha}), \tag{2.15}$$

where τ, α, and j_0 are constant parameters that may be determined by a fitting procedure to both interplanetary and ground-based observations. Also the Weibull distribution shows a steepening at high energies. This steepening effect can be understood as a natural limit of the acceleration mechanism due to an incapacity of the solar plasma to accelerate particles to very high energies, i.e. there is progressively more resistance against attaining higher energies in the plasma.

Another spectral form taking this steepening effect into account is a modified power law with respect to the rigidity (*Cramp et al.*, 1997):

$$dJ/dR \propto R^{-\gamma-\delta\gamma(R-1)}, \tag{2.16}$$

where $\delta\gamma$ describes the change of the power law exponent per GV, thus resulting in an increase of the slope with increasing rigidity.

Rather frequently, however, spectra are described by pure power laws in rigidity or kinetic energy:

$$dJ/dR \propto R^{-\gamma} \tag{2.17}$$

$$dJ/dE_k \propto E_k^{-\gamma} \tag{2.18}$$

In many cases, the spectra during GLEs change with time, and different forms of the spectra outlined above may be chosen for different time intervals during a GLE in order to accurately describe Neutron Monitor observations (e.g. *Vashenyuk et al.*, 2008, 2009b).

The modeling procedure of GLEs and the deduced spectral characteristics outlined in this section are exemplary illustrated in the following for GLE 69 which occurred on January 20, 2005. This GLE is related to a X7.1 class solar flare at 67°W on the Sun and, thus, was well connected to Earth. The onset time of the solar X-ray flare was at 06:36 UT, and about 15 minutes later the first relativistic protons reached the Earth giving rise to increased count rates of ground-based cosmic ray detectors. In the top panel of Figure 2.10 measurements with several NM64-type Neutron Monitors are shown. Depicted are relative count rates of two south-polar Neutron Monitor stations (South Pole and Terre Adelie at 0.0 GV cutoff), two sub-polar stations on the northern hemisphere (Apatity and Oulu at 0.65 and 0.8 GV, respectively), and a mid-latitude station in Switzerland (Jungfraujoch at 4.5 GV). With a maximum count rate increase of more than 4800% in the time interval from 6:50 UT to 6:55 UT at the South Pole station, GLE 69 was ranked among the largest ever recorded. Yet, it was also one of the most anisotropic events in years with very high count rate increases detected only by stations in the southern polar region.

In the bottom panel of Figure 2.10 proton spectra deduced from NM observations by *Bütikofer et al.* (2006) and *Vashenyuk et al.* (2005, 2007) are shown for the initial phase (≈ 7:00 UT) and the main phase (≈ 8:00 UT) of the event in the energy region from 500 MeV to 10 GeV. Obviously, rather large discrepancies between the deduced spectral

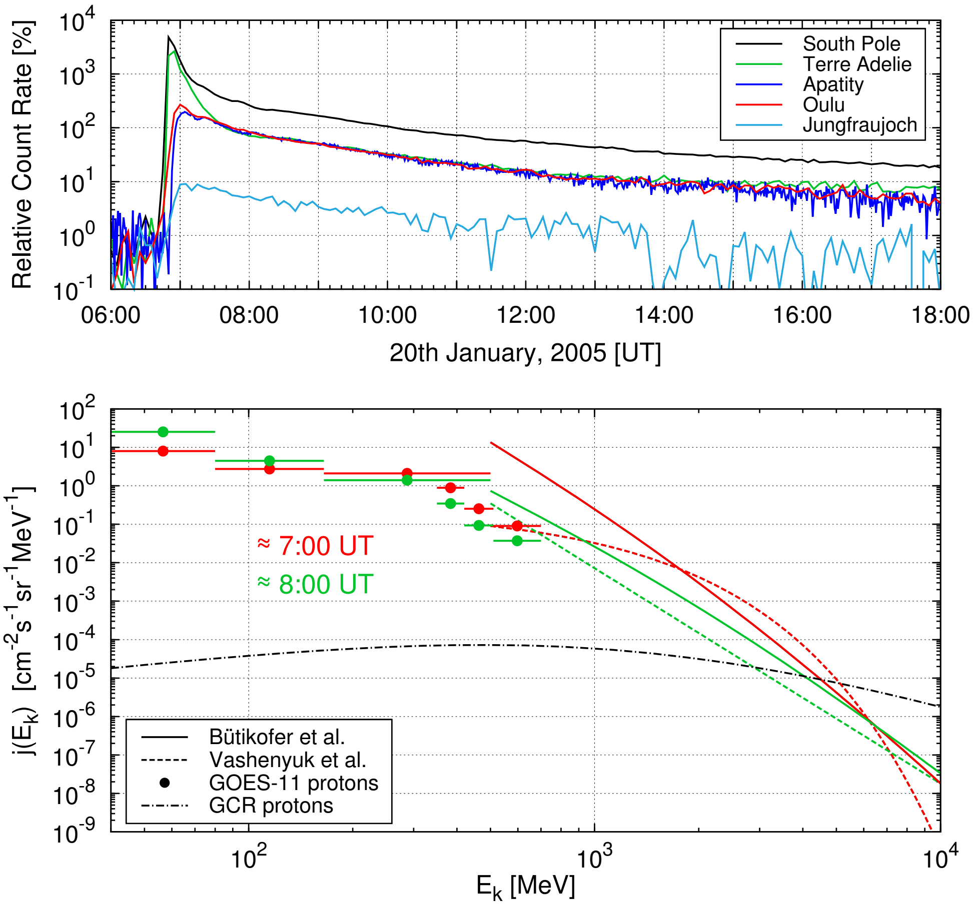

FIGURE 2.10: Relative count rate increases recorded by selected Neutron Monitor stations during GLE 69 on January 20, 2005 (top panel). The bottom panel shows the spectral characteristics deduced in the energy region from 500 MeV to 10 GeV by *Bütikofer et al.* (2006) and *Vashenyuk et al.* (2005, 2007, 2009a) for about 7:00 and 8:00 UT during the event. For comparison, proton measurements aboard the GOES-11 satellite and the flux of galactic cosmic ray protons are also shown.

characteristics are observed in terms of both spectral shape and absolute intensity. While *Bütikofer et al.* (2006) assumed a power law dependence of the proton intensity on rigidity (Eq. 2.17), *Vashenyuk et al.* (2005) used a modified power law (Eq. 2.16) with very different parameters during the initial and the main phase. For comparison, measurements aboard the GOES-11 satellite and the GCR proton flux in January 2005 according to the model of Burger/Usoskin (see section 2.1.1) are also depicted in Figure 2.10.

Especially during the initial phase the proton spectrum by *Bütikofer et al.* (2006) appears to overestimate GOES-11 data significantly, i.e. by almost a factor of 100. Spectra given by *Vashenyuk et al.* (2005) and the main phase spectrum by *Bütikofer et al.* (2006) are much closer to GOES data but still not fully consistent. Nevertheless, considering that the uppermost differential proton channel (510 - 700 MeV) on GOES-11 barely overlaps with the relativistic energy region ground-based detectors are sensitive to, discrepancies are highly probable and also expected. For this reason, the agreement of interplanetary and ground-observations is satisfactory. Concerning discrepancies between the spectra deduced from

NM count rates, it was already stated that basically a variety of combinations of pitch angle distributions, asymptotic cones, and differential spectra reproduce the NM count rate increases equally well. Thus, for none of the spectra shown in Figure 2.7 absolute correctness can be claimed.

Comparison of the GLE spectra with the galactic cosmic ray background (black dash-dotted line) makes the strongly enhanced primary proton flux obvious. Proton intensities may exceed those of galactic origin by many orders of magnitude below a few GeV. Therefore, dose assessment studies during GLEs are required, in particular for aircrews. Uncertainties in the differential proton spectra deduced from NM observations, however, result in rather large uncertainties for calculations of secondary particle fluence and dose rates in the lower atmosphere. These issues are addressed in every detail in Chapter 6.

CHAPTER

3

BONNER SPHERE MEASUREMENTS

After the discovery of the neutron by *Chadwick* (1932) many attempts have been made towards the development of instruments that allow to determine the energy distribution of these neutral particles. For this new field of neutron spectrometry several approaches have been suggested up to the 1960s. This includes spectrometry of recoil nuclei or charged particles released in neutron-induced nuclear reactions. Other techniques are based on neutron-induced activation of certain materials or measurements of the neutron velocity using the time-of-flight method.

Bramblett, Ewing, and Bonner (1960) introduced a new method with the multi-sphere neutron spectrometer, which subsequently became known as the Bonner sphere spectrometer (BSS). Such spectrometers consist of a thermal neutron detector centered in a number of moderating spheres of different diameters. With Bonner sphere spectrometers neutron fluence rates can be measured over a very broad energy range from thermal energies up to several tens of GeV. Furthermore, they exhibit a nearly isotropic response due to their spherical construction, and they can be operated continuously to monitor neutron fields. These are the main reasons why Bonner sphere spectrometers and the corresponding unfolding techniques to derive spectral information have been further improved during the last decades. Nowadays, BSS systems can be routinely applied for radiation protection at high-energy accelerators and ion therapy treatment facilities or for monitoring secondary neutrons from cosmic radiation. The latter has been done by the Helmholtz Zentrum München (HMGU) in order to supplement the global Neutron Monitor network and to obtain information on potential changes in neutron fluence and dose rates during ground level enhancements.

After a short description of the basic features of BSS systems, detailed information on the locations of the HMGU spectrometers is given. Subsequently, calculations of the response functions using the GEANT4 simulation toolkit with different state-of-the-art high-energy hadronic models are described. In the last part of this chapter a detailed analysis of the impact of different response functions on unfolded fluence and dose rates in Bonner sphere spectrometry is carried out. The results presented in this chapter have already been published in *Pioch et al.* (2010).

3.1 Features of Bonner sphere neutron spectrometers

A basic Bonner sphere consists of a spherical volume of material serving as moderator to slowdown incident neutrons. The resulting slow (thermal) neutrons are finally detected by a sensor centered in the sphere. The most appropriate detectors for this purpose are based on measuring the energies of charged products from neutron-induced nuclear reactions, but also others such as activation foils (e.g. *Fernández et al.*, 2007; *Garny et al.*, 2009) may be applied. Commonly used nuclear reactions are e.g. the ^{6}Li(n,α)^{3}H reaction in ^{6}Li-doped scintillation crystals (e.g. *Mares and Schraube*, 1994) or the ^{10}B(n,α)^{7}Li and ^{3}He(n,p)^{3}H reactions in proportional counters filled with the corresponding gas. At energies below a few hundred keV the cross sections of all these reactions are inverse proportional to the neutron velocity. The ^{3}He(n,p) reaction, however, exhibits the largest with a value of 5330 barn at thermal energies, followed by the ^{10}B(n,α) (3840 barn) and the ^{6}Li(n,α) (940 barn) reactions. Hence, the most efficient detectors applicable in Bonner spheres are proportional counters filled with ^{3}He gas.

In order to make use of the high thermal cross section and the corresponding high detection probability, incident neutrons have to be moderated via elastic scattering within a reasonably small volume. For this purpose, material containing a large fraction of hydrogen has to be used. Following classical collision theory (see e.g. *Turner*, 1995), the energy transfer Q in a collision of a neutron with kinetic energy E_k and a nucleus with mass number A is given as

$$Q = E_k \cdot \frac{4A}{(A+1)^2} \cdot \cos^2(\phi), \tag{3.1}$$

where ϕ is the scattering angle. Accordingly, the maximum possible energy transfer in a direct collision ($\phi = 0$) is $Q_{max} = E_k$ for hydrogen nuclei. Moreover, elastic scattering is isotropic in the center of mass system below 10 MeV with a mean energy transfer of $Q_{mean} = \frac{1}{2} Q_{max}$. This means a neutron loses on average half its kinetic energy per collision with a hydrogen nucleus and, thus, can be moderated within a small volume. The outer shell of Bonner spheres is, therefore, almost solely made of polyethylene (PE) which consists of $(CH_2)_n$ polymer chains.

The assembly of a PE moderator and a thermal neutron sensor providing a high sensitivity and allowing a good γ-ray discrimination is used in many other systems. Examples are neutron survey meters (e.g *Mares et al.*, 2002) or long counters. The specific feature characterizing the Bonner sphere spectrometer is the use of many different sized moderators in parallel. With increasing sphere diameter the degree of moderation and the number of capture reactions in PE increase with the H(n,γ) reaction being most important. Accordingly, in small spheres only low-energy neutrons have a high probability to reach the detector, whereas high-energy neutrons tend to escape. In larger spheres, on the other hand, the low-energy neutrons are either reflected or absorbed in (n,γ) reactions, whereas higher energetic neutrons have a reasonable probability to be thermalized and detected in the center. For this reason, the sensitivity of each sphere peaks at a certain neutron energy, and the measured count rates contain information on the neutron fluence rate present at that energy. Application of an unfolding procedure finally enables one to derive any spectral fluence rate distribution over a wide range of energy.

The use of a pure moderator only, however, results in very low responses above 20 MeV due to the rather large mean free path length of neutrons at these energies in PE. In particular for monitoring neutron fields near accelerators and in the Earth's atmosphere, much higher neutron energies have to be accurately measured. For this reason, shells with high atomic number material such as lead, iron, tungsten, or copper may be embedded in certain spheres (see e.g. *Wiegel and Alevra*, 1994, 2002; *Mares et al.*, 1998). Neutron-induced spallation reactions in these shells lead to neutron multiplication, where the major part of secondary neutrons generated results from evaporation processes. These neutrons with average energies of 1 -2 MeV can well be thermalized by an inner layer of PE covering the proportional counter. This in turn leads to a strongly increased response at high energies.

3.2 Spectrometers operated by the HMGU

The Helmholtz Zentrum München has been continuously operating two extended Bonner sphere spectrometers employing spherical ^{3}He proportional counters (SP90 Centronic Ltd.; 3.3 cm diameter; 172 kPa partial pressure) to measure secondary neutrons from cosmic radiation. The spectrometers consist of 13 basic Bonner spheres with pure PE moderators of different diameters (2.5, 3, 4, 5, 5.5, 6, 7, 8, 9, 10, 11, 12, and 15 inches). In two spheres with 9 inch outer diameter, lead shells of 0.5 and 1.0 inch thickness, respectively, are embedded serving as measurement channels in the high-energy region. Additionally, one bare ^{3}He proportional counter is operated to detect thermal neutrons resulting from moderation in the environment of the spectrometers.

Schraube et al. (1997, 1999) carried out the first promising measurements of secondary neutrons from cosmic radiation with one of the prescribed BSSs on the Zugspitze mountain, Germany. Since 2005 this system has been continuously operated in a laboratory at the Environmental research station (UFS) "Schneefernerhaus" at an altitude of 2660 m near the summit of the Zugspitze. In 2006 the spectrometer had been moved into a measurement shed with pitched roof on a terrace of the UFS, because accumulated snow on the roof of the lab strongly influenced the measurements of cosmic ray neutrons. The geographical position of the UFS is 47°25'N 10°59'E corresponding to a vertical effective cutoff rigidity of about 4.0 GV as calculated in the frame of the present work (see Section 2.1.2). The successful application of this spectrometer was demonstrated during a Forbush decrease by *Leuthold et al.* (2007).

The second BSS system has been continuously operated since June 2007 at the Koldewey station in Ny-Ålesund, Spitsbergen. The Koldewey station belongs to the Alfred Wegener Institute (AWI) and is part of the French-German arctic research base (AWIPEV). Ny-Ålesund is located at sea-level at a geographic position of 78°55'N 11°55'E corresponding to a vertical effective cutoff of 0.0 GV. Results from the BSS measurements in the polar region in comparison with the nearby operated Barentsburg Neutron Monitor are presented in *Pioch* (2008); *Pioch et al.* (2011b), and some additional information on the statistics and the time resolution during potential GLEs may be found in *Rühm et al.* (2009b).

Both systems have been maintained and the data have been analyzed throughout the present work. The measurements have been shown to be mutually consistent in terms of both unfolded fluence and ambient dose equivalent rates (*Pioch*, 2008; *Rühm et al.*, 2008, 2009a,b). The electronics of the BSS at the Zugspitze mountain was updated in the frame of the present work with a more stable equipment which is also used at the Koldewey station. For data acquisition both systems are now equipped with compact pre-amplifier/amplifier modules (ACHEM7F, Canberra). Amplified and shaped pulses from each ^{3}He proportional counter are further analyzed by Multiports (MP2-6E, Canberra) providing an independent analog-digital converter and multichannel analyzer for each measurement channel. The corresponding pulse height spectra are recorded in five and 60 minute intervals, respectively, in order to allow high-resolution analyses during potential GLEs. The systems are remotely operated via Internet, and the locally saved data are downloaded on a routine basis in order to determine count rates of each sphere as a function of time via integration of the pulse height spectra over a sphere-specific region of interest.

Of note is that due to the high atmospheric shielding at sea-level the polar BSS in Ny-Ålesund on average exhibits a factor of seven lower count rates than the BSS at mountain altitudes. For this reason, a set of new Bonner spheres was designed in the frame of the present work allowing to employ bigger spherical ^{3}He counters with 5.08 cm outer diameter manufactured by LND Inc. (LND-2705; 983 kPa partial pressure). As described in the next section, a GEANT4 simulation program was developed to calculate the response functions of the BSSs with small detectors, which also served as basis for the calculations with big detectors. First test measurements using LND detectors were performed at the UFS in June 2011 and reasonable consistency was found with the continuously operated BSS using smaller detectors (for details see *Ackermann*, 2011).

3.3 Calculation of BSS neutron responses using GEANT4

What follows is a description of the procedure to determine the response functions of Bonner spheres to neutrons by means of Monte Carlo calculations. Additionally to the neutron detection efficiencies, a complete set of proton response functions was calculated. Since a discussion of the proton responses is not necessary for the results presented in this and the subsequent chapter, they are presented in Appendix C.2.

For the prescribed BSS systems with SP90 detectors two complete sets of neutron response functions were calculated using the three-dimensional Monte Carlo simulation toolkit GEANT4 v. 8.2 (*Agostinelli et al.*, 2003; *Allison et al.*, 2006) with main focus on the high-energy region, where different state-of-the-art hadronic models were applied. GEANT4 was developed at CERN and is freely available as source code[1] written in C++. Application of this object oriented software technology provides a high degree in transparency allowing the user to change and combine any parts of the code according to his demands. This in turn

---

[1] http://geant4.cern.ch/

requires detailed knowledge at the user side, especially about the physics, and it is the user's responsibility to make sure the problem is properly modeled.

However, in this chapter the focus should be kept on results and not the detailed Monte Carlo (MC) techniques. Moreover, as will be seen in subsequent chapters, various particle transport calculations were performed in the present work. For this reason, general considerations on all GEANT4 calculations are given in Appendix B, including information on the basic MC method, GEANT4 specific modeling techniques, random number generation, and other issues. Furthermore, the physics applied are extensively summarized, described, and discussed there. Nonetheless, to allow for a coherent discussion, all necessary information on the hadronic framework of GEANT4 used for the BSS neutron response calculations is summarized in the following.

In GEANT4 certain physical processes can be assigned to certain particle types, and several models can be assigned to certain processes. Therefore, it is clearly distinguished between processes and models. Processes describe a particular initial or final state and have a well-defined cross-section or mean lifetime in case of decay. On the other hand, models describe the production of secondary particles. During run time the models are used by certain processes in order to determine the secondaries generated in an event and to calculate their momenta. This approach gives the possibility to apply multiple models for the same process. That is particularly the case in the hadronic framework of GEANT4 where a variety of models is available. All hadronic transport models can be categorized in data-driven, parametrization-driven, and theory-driven modeling approaches. The data-driven hadronic models mainly deal with the detailed transport of low-energy neutrons and isotope production. The low- and high-energy parametrized models include fission, capture, elastic, and inelastic scattering reactions. At high energies above several 10 - 100 MeV, the simulation of hadronic interactions relies on theoretical models since experimental cross section data are scarce. All these models can be arranged in complementary or alternative manner (see Table B.1 for a complete overview and *GEANT4 Collaboration*, 2009a,b).

3.3.1 Low-energy neutron transport and thermal scattering

The low-energy neutron transport in GEANT4 is mainly treated in a data-driven approach. For this purpose various cross section datasets are available in the G4NDL neutron data library. Results presented in the following were obtained using G4NDL v. 3.10 which is mainly based on the ENDF/B-VI cross section evaluation (*McLane*, 1991; *MacFarlane*, 1994a). This evaluation is complemented with others such as the Japanese evaluations JENDL3.2 (*Nakagawa et al.*, 1995) and JENDL-HE (*Fukahori et al.*, 2002) including extensions to 150 MeV for several isotopes.

Below 20 MeV neutron energy high-precision models are available in GEANT4, which either use these data to sample the corresponding double differential reaction cross sections or rely on theoretical approaches when no data are available. The high-precision modeling of neutrons includes elastic scattering based on the free gas approximation, inelastic scattering with tabulated final state information, capture, and fission.

At neutron energies below 4 eV scattering processes have to be treated differently, and the free gas approximation used in the high-precision models does not give an accurate description. At thermal neutron energies the specific thermal motion of the scattering nucleus gains importance. In molecules of the scattering material translational motion as well as vibration and rotation of the chemically bound atoms may be excited. This in turn highly affects the neutron scattering cross section and the final state characteristics such as energy gain or loss and the scattering angle. For this reason, thermal scattering cross sections (S(α, β) matrix, see App. B) for neutron scattering on bound hydrogen nuclei in water and polyethylene (PE) are adapted in GEANT4 from the low-energy extension of ENDF/B-VI (*MacFarlane*, 1994b). A detailed description of the thermal scattering law, the corresponding cross section, and the sampling method is given in Appendix B.

3.3.2 High-energy neutron transport and intra-nuclear cascade (INC) models

At high energies only very few experimental data are available, and the modeling of neutron interactions fully relies on theory in GEANT4 as in any other MC code. Of large importance for the results of neutron transport simulations is the energy range between a few hundreds of MeV to about 10 GeV where spallation processes are induced. The first, very fast step of a spallation process is handled by intra-nuclear cascade (INC) models. These describe the initial collision with a target nucleus which is heated and, in turn, ejects several rather fast nucleons and heavier compounds (e.g. α particles, deuterons). In the subsequent pre-equilibrium stage the nucleus again emits nucleons and/or is split by fission reactions before a slower stage follows, the de-excitation step. This phase is characterized by evaporation of nucleons with average energies of 1 - 2 MeV. The residual nucleus then is still highly excited and emits γ-rays to further cool down (see Appendix B and e.g. *Walters*, 1999).
In particular for the determination of the Bonner sphere response functions including lead shells, spallation processes are of main importance since the heavy Pb nuclei provide a large target for incident neutrons. Throughout the present work two state-of-the-art INC models were used above 20 MeV energy, the Bertini model included in the GEANT4 INC framework `G4CascadeInterface` and the Binary INC model contained in `G4BinaryCascade`. As outlined above, spallation processes consist of a variety of reactions and only a small part is treated in an INC model. Both INC frameworks in GEANT4 come along with their own models for the pre-equilibrium stage, fission, Fermi break-up, evaporation, and final nucleus de-excitation to describe spallation processes. For simplicity, however, it is only referred to the Bertini (BERT) and Binary (BIC) INC models throughout the present work, but one should keep in mind that this includes several other models. In the following, certain features and differences of the two INC models used are described.

Bertini INC

According to *Bertini* (1963, 1969) a heavy nucleus may be described by three concentric spherical shells approximating the continuously changing nuclear density and the corresponding potential. The target nucleus is assumed to consist of a completely degenerate Fermi gas, and the nucleons follow a Fermi gas energy distribution which is a function of the local nucleon density in each nuclear shell. A projectile particle entering the nucleus is tracked by solving the Boltzmann equation of motion on average. The reaction cross sections defining the interaction locations inside the nucleus and the momenta of secondary particles are calculated for free particles and modified with respect to the local Fermi potential. Following the Pauli principle, reactions in which the secondary particles have an energy below the local Fermi level are suppressed. After an initial collision, the INC finally terminates when the energy of all nucleons involved drops below the corresponding Fermi energy in each nuclear shell. The remnant nucleus is further treated with specific de-excitation models (see Appendix B, *Heikkinen and Stepanov*, 2003; *Heikkinen*, 2009; *GEANT4 Collaboration*, 2009a).

Binary INC

The approach in the Binary Cascade framework is very different from the prescribed Bertini INC model. The BIC is a hybrid model of a classical cascade code and a quantum molecular dynamics (QMD) model. Like in QMD, each participating nucleon is modeled as a Gaussian wave package. The nucleus consists of nucleons explicitly positioned in space in a manner that is consistent with the nuclear density distribution, the Pauli's exclusion principle, and the total nuclear mass. Therefore, each nucleon has its own Fermi momentum, and interactions take place as binary collisions between the projectile or scattered nucleons and an individual other nucleon in the target nucleus. Like in the Bertini INC, free hadron-hadron reaction cross sections are used to define collision locations in the nucleus and to calculate the corresponding momenta of all particles involved. The tracking inside the nucleus is accomplished by numerical integration of the Boltzmann equation of motion. The Binary INC progresses after an initial collision until the average energy of all participants in the nucleus drops below a given nucleus-specific threshold. The remnant nucleus is then also further treated via de-excitation models (see e.g. *Lara and Wellisch*, 2001; *Folger et al.*, 2004). These models differ somewhat from those used in the Bertini INC framework.

As outlined above, very different approaches for modeling the target nucleus and the actual collisions inside the nucleus are embedded in the INC frameworks `G4CascadeInterface` and `G4BinaryCascade`, respectively. Moreover, different criteria for the termination of an initial INC are implemented, and the remaining excited nuclei are further treated by different de-excitation models. As a consequence, differences in the simulation results are expected. Both cascade models have been validated with experimental data in terms of comparing double differential cross sections ($d\sigma/d\Omega dE$) for isotope production or nucleon yields. For both models satisfying and reasonable agreement with measurements may be found for various angles, energies, and target materials. Such validations as well as several successful applications of the models in sophisticated experiments can be found in e.g. *Heikkinen and Stepanov* (2003); *Folger et al.* (2004); *Heikkinen* (2009); *Apostolakis et al.* (2009) and references therein.

3.3.3 Specific details of neutron transport calculations

The geometry and material composition of the 13 basic Bonner spheres, the two spheres with lead shells, and the bare SP90 ^{3}He proportional were implemented in GEANT4 as realistically as possible. The counter wall was modeled as a 0.5 mm thick stainless steel

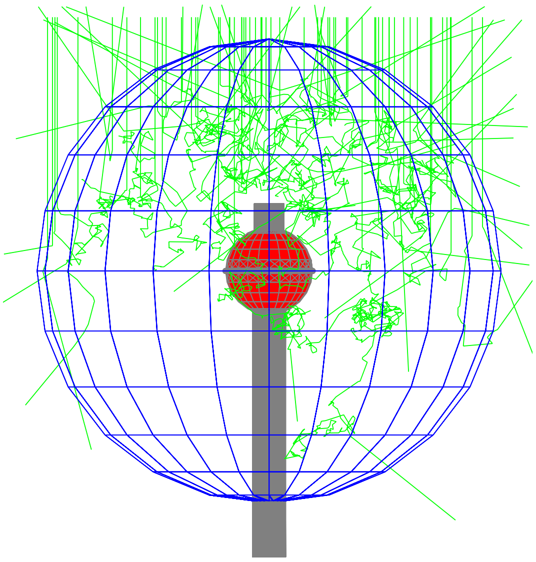

FIGURE 3.1: Illustration of a 7 inch Bonner sphere irradiated in GEANT4 with a parallel beam of 1 MeV neutrons impinging vertically from the top (green tracks). The geometry of the ^{3}He proportional counter in the center of the PE sphere is shown in gray with the effective detection volume in red.

shell (98% and 2% C by mass) with a 1.5 mm steel ring in the equatorial plane, a 9.25 cm long steel tube at the bottom (1.27 cm diameter, 0.5 mm thick wall) and a 0.95 cm long steel cap on top (1.14 cm diameter, 0.5 mm thick wall). Applying the perfect gas law, the ^{3}He atom density inside the spherical proportional counter with 172 kPa partial pressure is 4.25×10^{19} cm^{-3}. As an example, Figure 3.1 shows the geometry of the 7 inch PE sphere with the ^{3}He counter in the center as modeled in the GEANT4 calculations. The mass density of PE was assumed to have a constant value of 0.95 g/cm^3 and that of lead a value of 11.337 g/cm^3. For steel and Pb the corresponding natural isotopic abundances given by the database of the National Institute of Standards and Technology[2] (NIST) were used (*Bièvre et al.*, 1984). The response of each Bonner sphere was calculated for a parallel beam of mono-energetic neutrons in the energy range from 1 meV to 10 GeV (3 - 10 per decade), homogeneously covering the full cross sectional area of the corresponding sphere (see Fig. 3.1).

In all calculations the neutron fluence $\Phi(\epsilon_i)$ was scored in the effective detection volume of the ^{3}He proportional counter in certain energy intervals ϵ_i using an energy-binned fluence scorer. The scorer was modified to allow calculation of the statistical uncertainty in each bin. In order to determine the response function of each sphere and the bare detector, the total ^{3}He cross section $\sigma_{tot}(\epsilon_i)$ from the ENDF/B-VII evaluation (*Chadwick et al.*, 2006) was binned and convoluted with the calculated neutron fluences in the corresponding energy bins. The total ^{3}He cross section is strongly dominated by the ^{3}He(n,p) absorption cross section at thermal energies. Above about 1 MeV neutron energy, however, the elastic scattering cross section gains importance. At these energies nuclei may strip off their electronic shell due to elastic neutron-nucleus collisions. Such reactions lead to pulses in the detector and are therefore taken into account, although they have only minor influence on the results. The response of a sphere irradiated with a primary mono-energetic neutron fluence $\Phi_p(E)$ at

---

[2] http://www.nist.gov/pml/data/index.cfm

energy E is finally given as

$$R(E) = \frac{N_T}{\Phi_p(E)} \cdot \sum_i \sigma_{tot}(\epsilon_i) \cdot \Phi(\epsilon_i), \tag{3.2}$$

where N_T denotes the number of ^{3}He atoms in the proportional counter. The primary fluence $\Phi_p(E) = N/A_{sphere}$ is given as the number of mono-energetic neutrons N per cross sectional area A_{sphere} of the sphere considered. The response data obtained from the MC calculations were then interpolated to generate response functions with 130 energy points in logarithmic equidistant intervals from 1 meV to 10 GeV. A complete set of response functions for a BSS system is called response matrix.

3.4 Calculated BSS neutron responses

Figure 3.2 shows the neutron response functions of selected Bonner spheres, as obtained using the GEANT4 Bertini and Binary intra-nuclear cascade frameworks (GEANT4-BERT, GEANT4-BIC) above 20 MeV neutron energy. In the top panel responses of the 5, 8, and 12 inch PE spheres are depicted over the full energy range considered. The bottom panel shows responses of the two 9 inch spheres with lead shells (0.5 and 1 inch thickness) and the 15 inch PE sphere above 0.1 MeV in order to pronounce differences in the high-energy region. These three spheres are mainly sensitive to high-energy neutrons and thus most important for the unfolding procedure at high energies as discussed in subsequent sections. The complete sets of neutron response matrices are shown in Appendix C.2.

For comparison Figure 3.2 includes results calculated with the MCNP code v. 4A below 20 MeV neutron energy (*Briesmeister*, 1993) and a combination of the HMCNP/LAHET codes at higher energies (*Prael and Lichtenstein*, 1989). In these calculations the low-energy neutron transport was based on the ENDF/B-III and ENDF/B-IV evaluations (*Garber*, 1975). The LAHET code system at high energies uses its own representation of the Bertini or ISABEL cascade models for the simulation of inelastic hadron-nucleus interactions. At the de-excitation stage of nuclear reactions, a pre-equilibrium model and a Fermi break-up model were applied. Details about the MCNP/LAHET calculations are described in *Mares et al.* (1991, 1998); *Mares and Schraube* (1998) and *Sannikov et al.* (1997). The simulations are consistent with those of the present work in terms of material densities and compositions, but slightly different cross section datasets were applied in the low-energy region, and the ^{3}He proportional counter was modeled as simple spherical volume in the earlier works.

It is obvious from Figure 3.2 that only minor differences occur in the energy range below about 20 MeV resulting from the different cross section datasets and slightly different geometries. Significant differences, however, appear for energies above 20 MeV where no experimental data are available and all MC codes rely on theoretical approaches.

In case of the pure PE spheres (top panel), the GEANT4-BERT INC model clearly results in the highest values of the response functions, while the GEANT4-BIC model results in a similar energy dependence, but consistently lower values. The response functions for PE spheres obtained with MCNP/LAHET are also rather low and similar to those obtained with the GEANT4-BIC model up to an energy of about 1 GeV. For higher energies, however, they decrease in contrast to those obtained with both GEANT4 models.

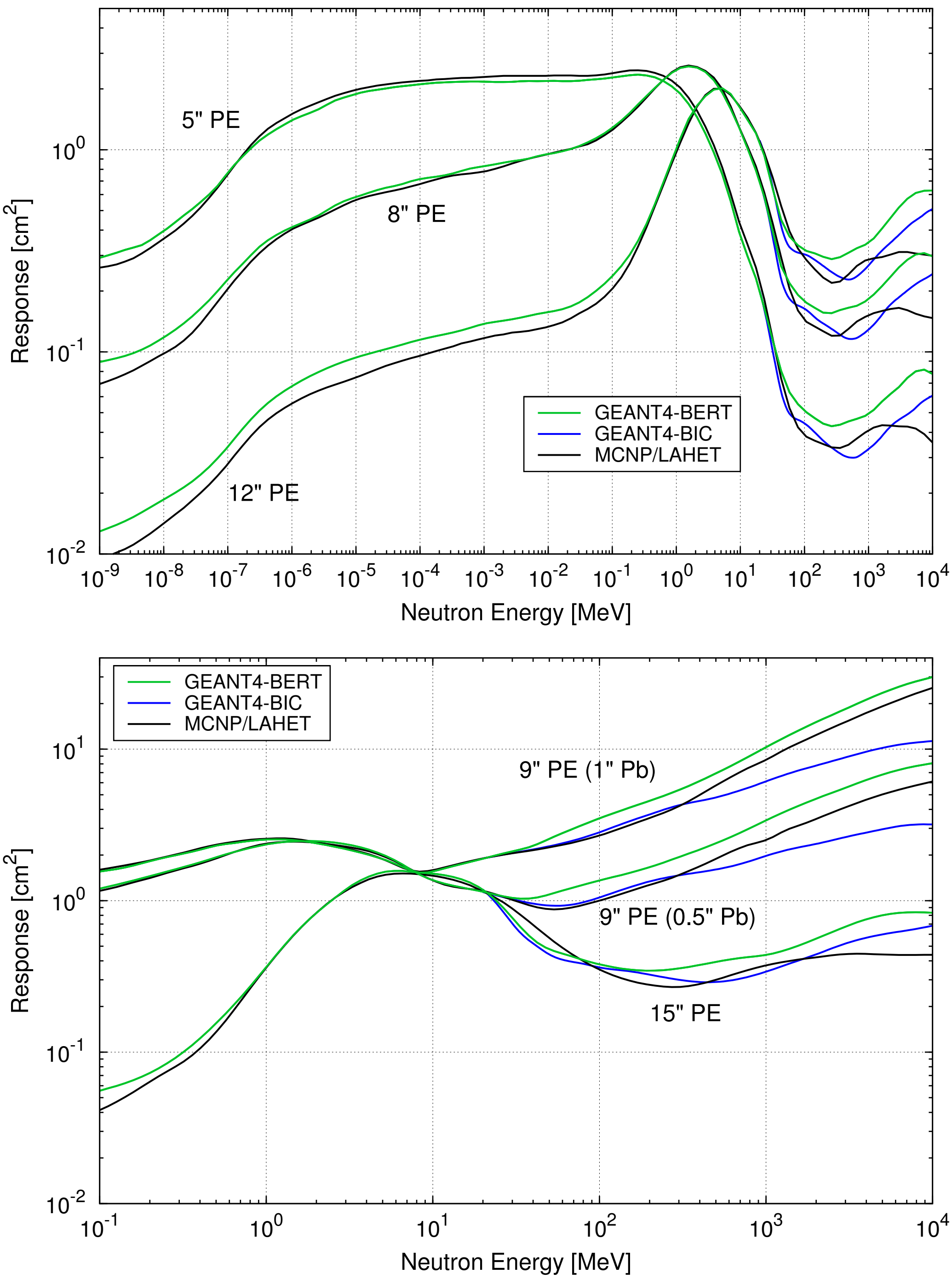

FIGURE 3.2: Neutron response functions of selected Bonner spheres calculated with the GEANT4 Bertini and Binary INC models above 20 MeV. The top panel shows responses of the 5, 8, and 12 inch PE spheres from thermal energies to 10 GeV. The bottom panel shows responses above 0.1 MeV energy for the two 9 inch spheres with lead shells (0.5 and 1 inch thickness) and the 15 inch PE sphere. For comparison calculations of *Mares et al.* (1991); *Mares and Schraube* (1998); *Mares et al.* (1998); *Sannikov et al.* (1997) using the MCNP/LAHET codes are also shown (see also App. C.2).

For the spheres containing lead shells (bottom panel), similar features are observed. Major differences become obvious only above about 20 MeV, and use of the GEANT4-BERT INC model again provides the highest values for the response. In contrast to the responses of pure PE spheres, those obtained with MCNP/LAHET are almost as high and do not decrease with increasing neutron energy above 1 GeV. More specifically, they are very similar to the GEANT4-BIC responses up to an energy of about 300 MeV. Above this energy the GEANT-BIC INC provides values more than a factor of two lower than those obtained with the other codes.

3.5 Impact of different responses on unfolded fluence and dose rates

While this finding is interesting for itself and asks for an experimental calibration at high energies, it must not necessarily mean that it is important in terms of unfolded spectral fluence rates as well as in terms of dose quantities.

3.5.1 Measurements considered

To investigate this in more detail, measurements of secondary neutrons from cosmic radiation at the UFS and the Koldewey station were used. Additionally, measurements performed behind a typical shielding at the hadron therapy facility GSI in Darmstadt, Germany, were considered (see e.g. *Rollet et al.*, 2009; *Wiegel et al.*, 2009). In this experiment a 400 MeV/n carbon ion beam was focused on a thick carbon target resembling typical workplace conditions in high-energy stray fields found near ion therapy treatment sites and accelerators. Exemplary, the monthly count rates measured at the UFS in February 2009 and those measured at the GSI (normalized to the beam current) are shown in Figure 3.3 as a function of sphere diameter (so-called measurement vector).

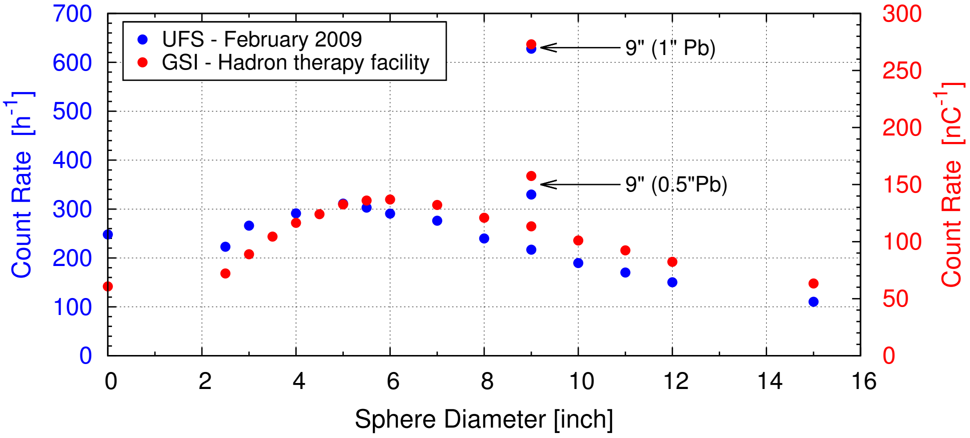

FIGURE 3.3: Count rates of all Bonner spheres as measured at the UFS in February 2009 and at the hadron therapy facility GSI, Darmstadt (normalized to beam current, *Wiegel et al.*, 2009). Count rates shown at zero inch correspond to readings of the bare detector.

Assuming Poisson statistics, the relative statistical uncertainty of a single measurement is given as $1/\sqrt{N}$, where N denotes the number of counts collected over a certain time period. In all three measurements taken into account in this section the statistical uncertainties of all spheres were well below 1%.

3.5.2 Unfolding procedure

The three prescribed measurement vectors were used to study the impact of the three different response matrices (GEANT-BERT, GEANT4-BIC, MCNP/LAHET) on unfolded fluence and ambient dose equivalent rates. Assuming 100% electronic efficiency, the count rate ζ of a Bonner sphere with response function $R(E)$ in a certain neutron field with spectral fluence rate distribution $\dot{\Phi}(E)$ is given as

$$\zeta = \int_0^\infty R(E) \frac{d\dot{\Phi}(E)}{dE} dE \; . \tag{3.3}$$

In any unfolding procedure the spectral fluence rate distribution is deduced from the measured count rates by solving the inversion problem of this equation for each sphere considered. Throughout the present work the unfolding code MSANDB developed by *Matzke* (1988, 2002, 2003) was used, which is a modified version of the SAND-II code (*McElroy et al.*, 1967). Taking the readings and the associated uncertainties of all spheres into account, this code iteratively searches for the global minimum of a χ^2 value which is defined as the logarithmic ratio of measured count rates and those calculated with Equation 3.3. To accurately find the minimum, 'a priori' physical information about the neutron spectrum must be provided by the user. This start or 'a priori' spectrum represents a first estimate of all spectral features expected at the measurement location. Based on this input and the response matrix, MSANDB iteratively adjusts the neutron fluence rate distribution to be consistent with the detectors' readings. To terminate the iteration process after a certain loop, a maximum iteration number can be given. A detailed description of the mathematics and the use of MSANDB is given in Appendix C.1.

For all three measurements considered in this section, a start spectrum including all typical features expected in high energy neutron fields (see below) and an iteration number of 300 was used.

3.5.3 Differences in unfolded fluence rates

The unfolded spectral fluence rate distributions for the measurements performed at the UFS in February 2009 are shown in Figure 3.4. The inset in this figure summarizes the results for the measurements at the hadron therapy facility GSI. The spectra are shown in lethargy representation $d\dot{\Phi}/d\ln(E) = E \cdot d\dot{\Phi}/dE$, in which equal areas below the curve correspond to equal neutron fluence rates.

Comparison of both measurements reveals that the spectral features are very similar as a result of the physics involved, although the source of neutrons and the general measurement conditions are very different. In both cases a thermal peak is observed at energies below 0.4 eV resulting from neutron moderation in material surrounding the spectrometer

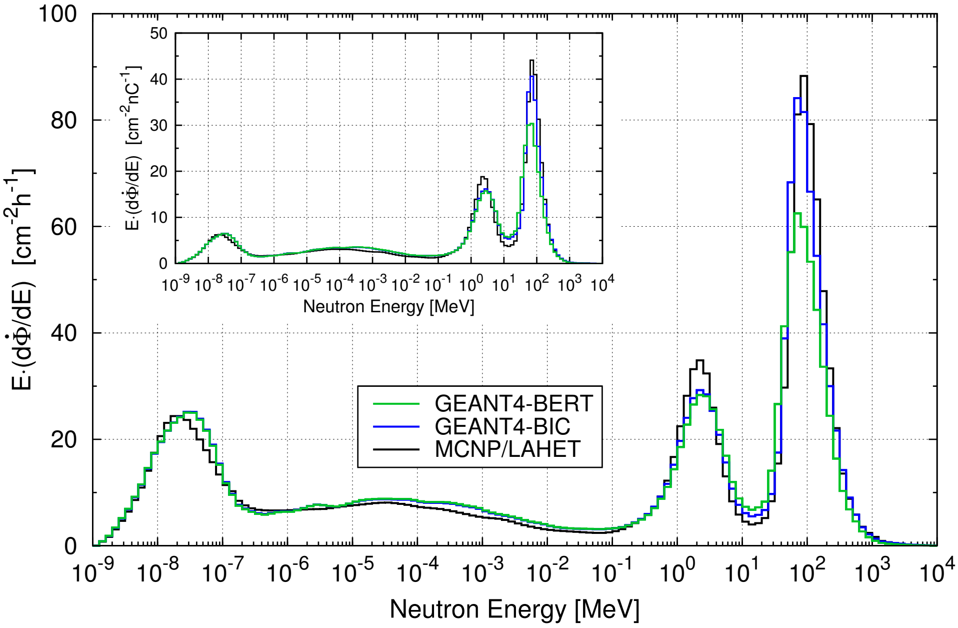

FIGURE 3.4: Spectral neutron fluence rate distributions unfolded with MSANDB using the count rates shown in Fig. 3.3 for the UFS in February 2009 and three different response matrices. The inset depicts the results for the measurements performed at the hadron therapy facility GSI.

(e.g. floor, shielding). Neutrons in thermal equilibrium with the surrounding material follow a Maxwell-Boltzmann distribution centered around the corresponding temperature. In the epithermal region between 0.4 eV and 0.1 MeV elastic scattering is the dominating interaction mechanism. According to classical collision theory, both the average and the maximum energy transfer of a neutron is proportional to the neutron's kinetic energy (see Eq. 3.1). Higher energetic neutrons, thus, suffer large energy-losses in collisions resulting in a steeply decreasing differential neutron flux with increasing kinetic energy. This in turn leads to a nearly horizontal course of the neutron spectrum in the lethargy representation. In the energy interval from 0.1 to 20 MeV a second peak emerges, the evaporation peak. This peak results from nuclei that are left in highly excited states due to spallation processes and, as a consequence, evaporate neutrons with average energies of 1 - 2 MeV to cool down. A third peak appears around 100 MeV, the so-called cacscade peak. In case of cosmic radiation, the primary spectra responsible for the neutron production steeply decrease with increasing energy above several hundreds of MeV/n and, accordingly, the neutron spectra do. As shown by *Rollet et al.* (2009), the neutron spectra produced by bombardment of a thick carbon target with 400 MeV/n carbon ions also steeply decrease above approximately 200 MeV. Additionally, the total cross sections of nearly all isotopes exhibit a broad minimum above about 100 MeV (see e.g. *Abfalterer et al.*, 2001), and convolution of the steeply decreasing neutron spectra with the broad cross section minimum finally results in the cascade peaks observed (a discussion of cosmic ray neutron spectra follows in every detail in Chapter 5.4).
It is clearly visible in Figure 3.4 that using different response matrices results in rather small differences in the unfolded fluence rates below 20 MeV since basically all responses agree in the low-energy region. On the other hand, major differences occur at higher energies. The

TABLE 3.1: Neutron fluence rates deduced from measurements performed at the UFS in February 2009 using three different response matrices (see Figs. 3.2 and 3.4). Percent values describe relative differences to the MCNP/LAHET results.

	FLUENCE RATE [cm^{-2}h^{-1}] / [%]		
Energy [MeV]	GEANT4-BERT	GEANT4-BIC	MCNP/LAHET
$\leq 4{\cdot}10^{-7}$	78.4 / 3.8	78.7 / 4.1	75.6 / 0
$4{\cdot}10^{-7} < E \leq 0.1$	80.4 / 13.4	79.7 / 12.4	70.9 / 0
$0.1 < E \leq 20$	69.1 / -2.4	68.6 / -1.8	70.8 / 0
> 20	107.4 / -18.0	128.6 / -1.8	131.0 / 0
Total	335.4 / -3.7	355.7 / 2.1	348.3 / 0

height of the cascade peak around 100 MeV is much lower for the GEANT4-BERT than that for GEANT4-BIC and MCNP/LAHET response matrices due to the highest response values obtained by GEANT4-BERT in that energy range (see Fig. 3.2).

In order to quantify these differences, the spectral neutron fluence rates unfolded using the three response matrices were integrated over the four prescribed characteristic energy regions (< 0.4 eV; 0.4 eV - 0.1 MeV; 0.1 - 20 MeV; > 20 MeV). The differences in the integrated fluence rates were very similar for all measurements considered. Using the count rates measured at the UFS, however, resulted in the largest differences in terms of both unfolded spectra and corresponding dose quantities. Therefore, these measurements give an upper limit for typical uncertainties involved in Bonner sphere spectrometry due to different response matrices, but neglecting potential differences arising from the use of unfolding codes other than MSANDB. The following discussion is, therefore, restricted to fluence rates unfolded from the UFS measurements.

As can be deduced from the numerical values given in Table 3.1, for all codes and models the total neutron fluence rates obtained do not differ much (< 4 %) relative to the standard MCNP/LAHET response functions calculated earlier. A closer look, however, reveals that the GEANT4-based response functions result in somewhat larger epithermal neutron fluence rates (12 - 13%) than those obtained with the MCNP-based response function. In contrast, at energies above 20 MeV the neutron fluence rate is significantly lower when based on GEANT4-BERT (about 18%). This is a direct consequence of the highest response values obtained with the GEANT4 Bertini INC at these energies (see Fig. 3.2). Altogether, the neutron spectra obtained from the GEANT4 response functions appear somewhat softer than those obtained from the MCNP/LAHET response function.

3.5.4 Differences in ambient dose equivalent rates

The H*(10) values corresponding to the previously discussed fluence rates were obtained using fluence to ambient dose equivalent conversion coefficients from *Pelliccioni* (2000) and references therein as recommended by *ICRP* (Publ. 74, 1997). A detailed description of these coefficients as well as supplementary information on dosimetry is given in Appendix A.2.

TABLE 3.2: Neutron ambient dose equivalent rates deduced from measurements performed at the UFS in February 2009 using three different response matrices (see Figs. 3.2 and 3.4). Percent values describe relative differences to the MCNP/LAHET results.

	AMBIENT DOSE EQUIVALENT RATE [nSv h^{-1}] / [%]		
Energy [MeV]	GEANT4-BERT	GEANT4-BIC	MCNP/LAHET
$\leq 4{\cdot}10^{-7}$	0.81 / 3.8	0.82 / 4.3	0.79 / 0
$4{\cdot}10^{-7} < E \leq 0.1$	0.97 / 13.8	0.96 / 13.0	0.85 / 0
$0.1 < E \leq 20$	26.8 / -2.3	26.5 / -3.4	27.4 / 0
> 20	38.7 / -12.6	44.7 / 1.1	44.2 / 0
Total	67.3 / -8.3	73.0 / -0.4	73.3 / 0

Differences in fluence rates at thermal and epithermal energies are not of major concern as they do not contribute much to total neutron ambient dose equivalent or effective dose. The different fluence rates in the cascade region, on the other hand, may have some relevance. Use of response functions calculated with the GEANT4 Bertini INC results in significantly lower neutron dose rates at energies above 20 MeV (about 12.6%). As a consequence, the total neutron ambient dose equivalent rate is about 8% lower than that calculated with the GEANT4 Binary INC or the MCNP calculations. In contrast, the results obtained with GEANT4 Binary INC and MCNP/LAHET appear quite consistent in terms of both total neutron ambient dose equivalent rate and contributions from high-energy neutrons.

As also discussed in *Pioch et al.* (2010), an overall uncertainty in dose rates below 10% is fully satisfying for radiation protection. Nonetheless, an experimental calibration as described in the next chapter is required and always reasonable for scientific purposes.

CHAPTER

4

BSS CALIBRATION IN HIGH-ENERGY NEUTRON FIELDS

In the previous chapter it has been shown that major differences in Bonner sphere response functions occur above 20 MeV due to different hadronic models used for the computation. This is particularly the case for Bonner spheres including lead shells. The differences in high-energy responses result in an uncertainty of about 18% in the unfolded fluence rates and an uncertainty of about 13% in the ambient dose equivalent rate at high energies.

In high-energy neutron fields, which are e.g. present at flight altitudes or behind the shielding of particle accelerators and hadron therapy facilities, it is highly favored to measure fluence and dose rates as precisely as possible. The only way of determining which of the calculated response functions discussed in Chapter 3 describe reality best is comparison to measurements performed in preferably quasi-monoenergetic neutron fields with known spectral fluence rate distribution. So far, calibration measurements with a BSS were only performed in neutron fields with energies ranging from thermal up to 14.8 MeV (*Alevra et al.*, 1992; *Thomas et al.*, 1994). Especially at higher energies, where major differences in the calculated response functions are observed, quasi-monoenergetic neutron fields are rather scarce. One of the most suitable facilities worldwide providing neutron fields with energies up to 400 MeV using the ^{7}Li(p,n)^{7}Be reaction is the cyclotron facility at the Research Center for Nuclear Physics (RCNP) in Osaka, Japan. At this facility a unique calibration measurement for the BSS systems described in Chapter 3 was carried out in quasi-monoenergetic neutron fields with peak energies of 244 and 387 MeV. The results of this measurement, which are also published in *Pioch et al.* (2011a), are presented in the following.

4.1 RCNP cyclotron facility and experimental setup

At the Research Center for Nuclear Physics (RCNP) of the University in Osaka, Japan, protons are pre-accelerated in an AVF cyclotron and then injected into a ring cyclotron where they are accelerated up to energies of 400 MeV with a maximum beam current of about 1 μA (see e.g *Miura et al.*, 1993; *Saito et al.*, 1995; *Ninomiya et al.*, 2004).
For the calibration measurements with Bonner sphere spectrometer presented in this chapter proton beams with nominal energies of 246 and 389 MeV were generated and focused on a 10.0±0.05 mm thick ^{nat}Li (7.6% ^{6}Li and 92.4% ^{7}Li) target situated in a beam swinger magnet inside a vacuum chamber (see Fig. 4.1). Neutrons were produced by ^{7}Li(p,n)^{7}Be reactions with a cross section of about 35 mb/sr at peak energies (in lab system) as measured by *Iwamoto et al.* (2010, 2011). These quasi-monoenergetic neutrons with nominal peak energies of 244 and 387 MeV were extracted to the 100 m long time-of-flight (TOF) tunnel through an iron collimator with 10×12 cm^2 aperture size embedded in a concrete wall of 1.5 m thickness (4.5 m distance to target). The resulting neutron beam homogeneously covered a minimum solid angle of 2.18×10^{-4} sr assuming a rotationally symmetric beam with radius 5.0 cm at the end of the collimator. During the measurements the primary proton beam intensity was continuously monitored by a Faraday cup, and a clearing magnet within the collimator (not shown in Fig. 4.1) served to reject charged particles from the neutron beam. At the neutron experimental facility of the RCNP both target and collimator can be moved. This allows measurements at various emission angles up to 30°.

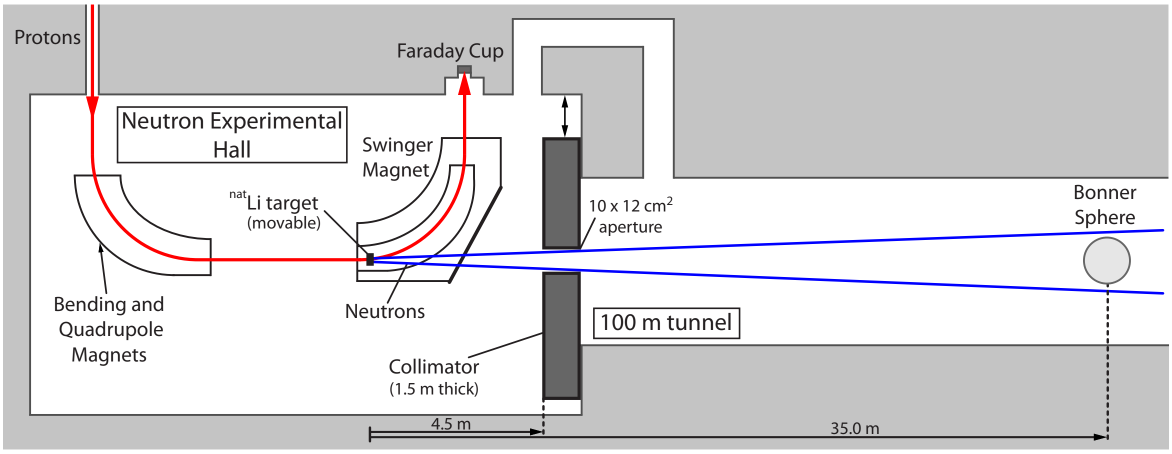

FIGURE 4.1: Sketch of the neutron experimental facility and experimental setup at the RCNP.

As shown in the sketch of the experimental setup in Figure 4.1, the BSS measurements were carried out at a distance of 35 m from the target. At this distance the beam's minimum radius was about 29.17 cm which guaranteed a homogeneous irradiation of even the biggest sphere with 19.05 cm radius. The BSS measurements were performed at 0° and 30° emission angles in order to get rid of contributions from low-energetic neutrons applying a subtraction method first proposed by *Nolte et al.* (2002). However, it turned out that at 30° emission the low-energy part of the neutron spectra changed significantly compared with 0°. Therefore, subtraction of 30° from 0° measurements could not be applied. Nevertheless, the results obtained at 0° emission could properly be used for calibration purposes as discussed below. For the sake of completeness, the 30° measurements are presented in Appendix C.4.

4.2 Time-of-flight measurements

In order to characterize the neutron energy spectra produced in ^{7}Li(p,n) reactions, *Iwamoto et al.* (2011) performed a time-of-flight (TOF) measurement using organic liquid scintillators NE213 of three different sizes (2×2, 5×5, and 10×10 inch^2). For both beam energies the spectra were measured at seven emission angles (0°, 2.5°, 5°, 10°, 15°, 20°, and 30°). At 0° emission neutron fluence rates were determined down to 2 MeV and down to 10 MeV at other angles. The neutron flight time was given as the time between the beam chopper signal and the detector signal. Neutron fluence rate distributions were measured independently with each of the three scintillators at a scintillator-specific distance from the target and combined afterwards. The maximum flight path in the TOF measurements was 65 m in case of 246 MeV and 95 m in case of 389 MeV proton beam energy, respectively, in order to obtain a good energy resolution in the high-energy region. A 390 MeV neutron has a velocity of about 70% of the speed of light and travels the distance of 95 m within approximately 450 ns. With a time resolution of the TOF measurement system below 100 ns the neutron flight times can well be recorded. Further details and general considerations on the TOF measurements at the RCNP may be found in *Taniguchi et al.* (2007).
Figure 4.2 shows as an example the differential neutron fluence rates per solid angle ($j(E) = d^2\dot{\Phi}/d\Omega dE$, see Appendix A.1) normalized to the beam current at 389 MeV proton beam energy and 0°, 5°, 10°, 20°, and 30° emission angles. A closer look at the 0° spectrum reveals interesting details on the nuclear physics of ^{7}Li(p,n) reactions and shows the accuracy of the TOF method applied. Neutrons in the peak of this spectrum result from transitions to the ground and first excited state of ^{7}Be as well as from transitions to the

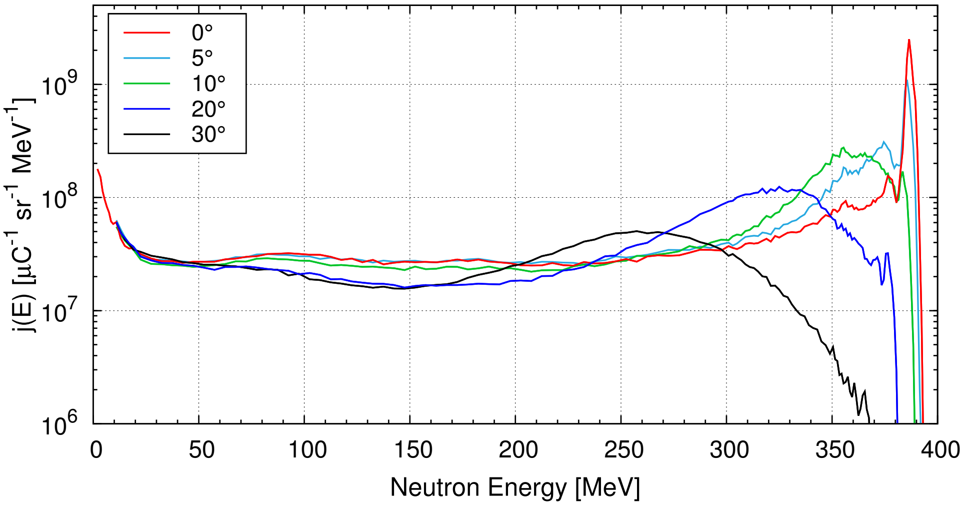

FIGURE 4.2: Differential neutron spectra measured with the TOF method at 389 MeV beam energy and 0°, 5°, 10°, 20°, and 30° emission angles (*Iwamoto et al.*, 2011).

ground state of ^{6}Be. The small peaks about 10 and 30 MeV below the peak energy arise from transitions to highly excited states of ^{7}Be. From 50 MeV below the peak to about 100 MeV ranges the so-called quasi-free region. This region is characterized by a broad peak due to elastic collisions of incident protons with single nucleons near the nuclear surface (*Wang et al.*, 1994). The continuum part from 20 - 100 MeV mainly results from three-body break-up processes ^{7}Li(p,n^{3}He)^{4}He (*Baba et al.*, 1999), and the region below 20 MeV is dominated by neutron evaporation.

As is evident from the comparison of spectra measured at different angles in Figure 4.2, the intensity of the peak neutrons rapidly decreases with increasing emission angle, and almost no peak neutrons are produced at 30° emission. On the other hand, both height and shape of the broad peak in the quasi-free region significantly changes with increasing emission angle. The changes in the neutron spectra do not only affect the energy region covered by the TOF method but rather the whole range down to thermal neutron energies. This evidently shows that for the calibration of the BSS subtraction of 30° from 0° measurements should not be applied in order to prevent the calibration results from being strongly biased due to a subtraction of the low-energy part of the spectra which might be influenced by an artifact (also see discussion in Appendix C.4).

The TOF spectra for 0° emission used in the present work for calibration of the BSS are shown for both beam energies in Figure 4.3. The energy resolution in the TOF measurements was 1 - 3 MeV (solid lines in Fig. 4.3). In contrast, the resolution chosen for calibration of the BSS was ten bins per decade since a much larger range down to meV needed to be covered. Therefore, the TOF spectra were re-binned by scoring the corresponding fluences in vacuo with the chosen resolution in a GEANT4 simulation (dashed lines in Fig. 4.3). The sharp peaks around 244 MeV and 387 MeV with peak intensities of about 10^{10} neutrons/(srμC) are obvious in Fig. 4.3. At both beam energies about half of the total neutron flux in

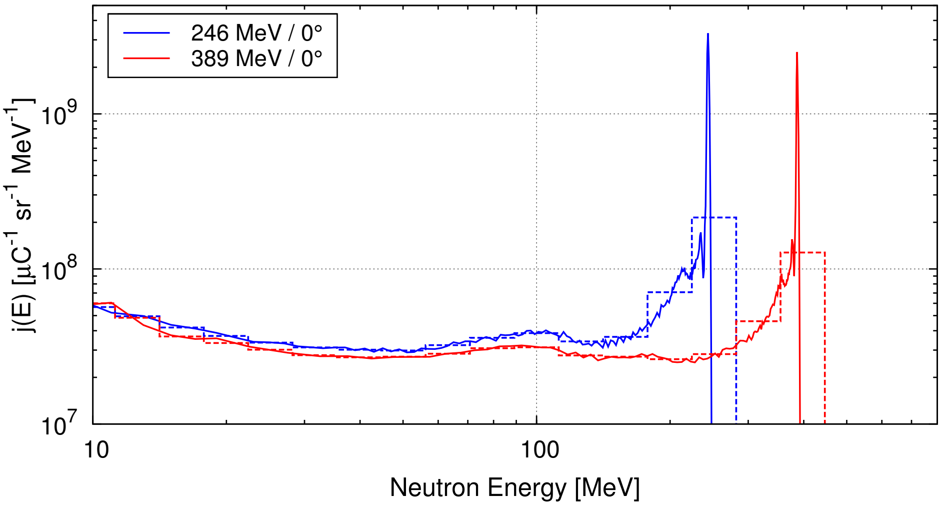

FIGURE 4.3: Differential neutron spectra for 0° as measured with the TOF method at 246 and 389 MeV beam energy (solid lines, *Iwamoto et al.*, 2011). The dashed lines show the same spectra re-binned to a resolution of ten bins per decade. These spectra were used in the energy range shown for calibration of the BSS.

the energy range covered by the TOF method results from peak neutrons ($E > 234$ and $E > 342$ MeV). Statistical uncertainties in the TOF measurements were below 0.16% in the peak region and 1 - 3% at lower energies.

It should be noted, however, that also for the TOF measurements the detectors' response functions must be known in order to obtain absolute fluence rate values. The neutron detection efficiencies of the NE213 scintillators were calculated by *Satoh et al.* (2006b) using the SCINFUL-QMD code, which extends the SCINFUL code developed earlier by *Dickens* (1988) with a quantum molecular dynamics (QMD) model. Calculated NE213 responses were also compared to experimental data and good agreement was found (*Satoh et al.*, 2006a). Nonetheless, uncertainties due to the calculated NE213 response functions imply a systematic uncertainty of 15% for the TOF data (*Iwamoto et al.*, 2011).

Apart from the uncertainties discussed above, the TOF measurements should be treated carefully in the energy region below 10 MeV since the discrimination threshold of NE213 scintillators lies within this range. Therefore, in the present work the TOF data were only used above 10 MeV for both 246 and 389 MeV beam energy as shown in Figure 4.3.

4.3 Bonner sphere measurements and unfolding procedure

The spectral fluence rate distributions of neutrons produced by the 246 MeV and 389 MeV proton beams were measured at 35 m distance from the target (see Fig. 4.1). Each sphere was vertically aligned with the beam axis defined by the center of the collimator (141.5 cm above the floor). Depending on sphere diameter and beam energy, the proton beam intensity was varied between 10 nA and 1 μA in order to keep potential dead-times of the ^{3}He proportional counter well below 1%. Furthermore, according to the detector's reading, irradiation time of each sphere was chosen to achieve statistical uncertainties well below 1%.

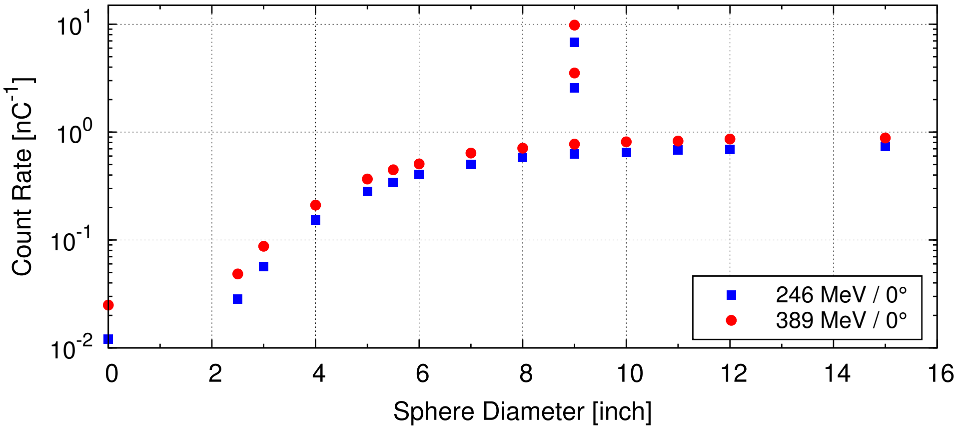

FIGURE 4.4: Count rates measured with the BSS at a distance of 35 m from target and 0° emission angle at nominal proton beam energies of 246 and 389 MeV. Statistical uncertainties are well below 1% for each sphere at both energies.

The resulting measured count rates, normalized to the corresponding beam current, are shown in Figure 4.4 as a function of sphere diameter for both beam energies and 0° emission angle. The shape of this figure already reflects the spectral neutron fluence rate distribution present during the measurements. E.g. the comparatively low count rates of the bare ^{3}He proportional counter (zero inch diameter in Fig. 4.4) indicate a very low contamination of the neutron beam with room-scattered thermal neutrons. In contrast, the continuously increasing count rates with increasing sphere diameter indicate large fluence rates of high-energetic neutrons.

The count rates shown in Figure 4.4, together with the three response matrices described in Chapter 3, were used to unfold the corresponding spectral neutron fluence rate distributions using the MSANDB unfolding code (*Matzke*, 1988, 2002, 2003, see Chap. 3 and App. C.1) with a resolution of ten energy bins per decade. For all BSS measurements, as 'a priori' start spectra the re-binned TOF spectra shown in Figure 4.3 were used at energies above 10 MeV. These spectra were extended down to 1 meV with a course proportional to $1/E$, i.e. almost no 'a priori' information was used in the low-energy region for the unfolding. These start spectra and a preset maximum iteration number of 500 gave very accurate and stable results.

4.4 Unfolded BSS spectra and comparison with TOF measurements

The unfolded spectral neutron fluence rate distributions using the detector count rates shown in Figure 4.4 and the three different sets of response matrices described in Chapter 3 are shown in Figure 4.5 for 246 MeV in the top panel and for 389 MeV proton beam energy in the bottom panel, respectively. In both figures the differential neutron fluence rate $\mathrm{d}\dot{\Phi}/d\ln(E)$ at 35 m distance from the target and 0° emission angle is shown in log-log scale as a function of neutron energy in order to make the low-energy part of the spectra clearly visible. Additionally, the insets in Figure 4.5 show the spectra in true lethargy representation, i.e. in log-lin scale. For comparison, the results of the TOF measurements for both beam energies and 0° emission are also depicted (red lines in Figure 4.5).

Apparently, the unfolded spectra agree rather well below 10 MeV whatever response matrix is used. This reflects that the response matrices show only minor differences at low neutron energies resulting from slightly differing cross section datasets used for the calculations. Nevertheless, due to intrinsic mathematical constraints involved in any iterative unfolding procedure such as MSANDB, changes in response functions at high energies lead to minor changes in the unfolded fluxes at low energies, too. Therefore, in the unfolded fluence rates using the two GEANT4-based response matrices minor differences are observed although the response functions below 20 MeV are identical (see Fig. 3.2).

Note that all unfolded spectra show a small peak at thermal energies resulting from room-scattered neutrons and a small evaporation peak around 2 MeV which is expected in high-energy neutron fields like those generated at the RCNP. The evaporation peak and the thermal peak agree very well at both beam energies for all response matrices. It should be emphasized that for the unfolding procedure a start spectrum proportional to $1/E$ was used below 10 MeV and the TOF spectra above. This means that using three different response matrices with almost no information on the spectral neutron fluence rate distribution at low energies

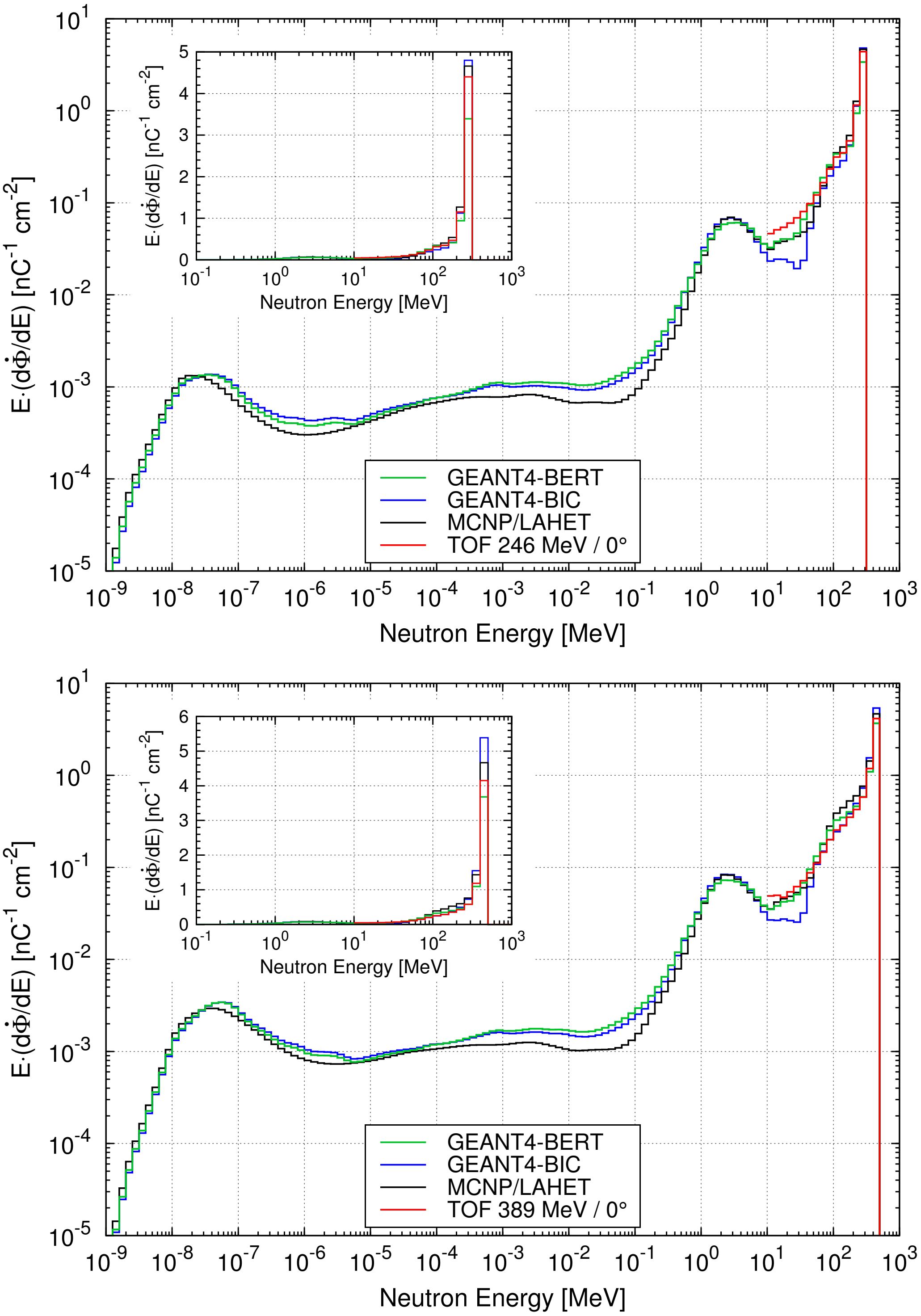

FIGURE 4.5: Unfolded spectral neutron fluence rate distributions using three sets of response matrices (GEANT4-BERT, GEANT4-BIC, MCNP/LAHET) in comparison with measured TOF spectra for 246 MeV (top panel) and 389 MeV (bottom panel) proton beam energy at 0° emission. The insets in both panels show the same curves in lethargy representation (log-lin scale).

results in nearly the same unfolded spectra. Moreover, a sensitivity analysis of unfolded spectra was performed in the frame of the present work in terms of using different start spectra below 10 MeV, where e.g. a thermal and an evaporation peak were included. Additionally, the maximum iteration number was varied between 200 and 800 iteration loops in order to check the stability of the deconvolution procedure. All changes encountered in the integral spectral fluence rates due to these changes in the input parameters were less than 3%. Furthermore, below 20 MeV all response calculations, and thus unfolding itself, are based on experimentally evaluated cross sections. Therefore, the spectral neutron fluence rate distributions produced by bombardment of a 1.0 cm thick ^{nat}Li target with 246 MeV and 389 MeV protons at the RCNP can be regarded as accurately determined at energies below 10 MeV. Together with the TOF measurements at higher energies, this fully characterizes the neutron spectra present during the measurements down to neutron energies of about 1 meV. Although the fluence rates of low-energetic neutrons ($E < 10$ MeV) are by orders of magnitude lower than those around the peak energies, an accurate determination over the whole range of energy is essential for calibration purposes.

In contrast to the low-energy part of the spectra, at neutron energies above 10 MeV major differences between the unfolded BSS neutron spectra occur at both beam energies, depending on the response matrix used. This is due to significantly differing response functions above 20 MeV, in particular for the two Bonner spheres with lead shells (see Fig. 3.2). Compared to the TOF data, the BSS spectra unfolded using the GEANT4-BERT and MCNP/LAHET response functions agree very well at energies between 10 MeV and about 40 MeV at 389 MeV beam energy, whereas minor differences to TOF data are observed at 246 MeV. This may be attributed to the unfolding procedure itself since MSANDB tends to produce smooth and rather narrow peaks (see e.g. *Wiegel et al.*, 2009). In contrast, the BSS spectra unfolded with the GEANT4-BIC response matrix show a pronounced dip in this energy region. This results from somewhat different shapes of the GEANT4-BIC responses at energies higher than 40 MeV affecting the deconvolution process at lower energies.

For energies ranging from 40 MeV to the nominal maximum neutron energies of 244 and 387 MeV, all spectra basically have a similar shape. In case of 246 MeV beam energy the unfolded neutron flux using GEANT4-BIC responses is slightly lower than the TOF spectrum in the energy range from 40 to 200 MeV but the peak fluence rate around the maximum energy is very well reproduced. At this beam energy, the MCNP/LAHET spectrum agrees best with the TOF spectrum above 40 MeV, whereas results obtained with the GEANT4-BERT matrix underestimates the peak fluence rate. In case of 389 MeV beam energy, on the other hand, results using the GEANT4-BIC response matrix agree best above 40 MeV but the the peak intensity is slightly overestimated. At this beam energy unfolding with the MCNP/LAHET response matrix results in higher fluence rates above 40 MeV with respect to TOF data but the peak intensity agrees rather well. The GEANT4-BERT spectrum is somewhat lower than the 389 MeV TOF spectrum at the maximum energy but overall this spectrum matches best.

In terms of calibration of the BSS, however, the peak fluence rates around the maximum neutron energies of 244 and 387 MeV are of main interest. The lethargy representations of the spectra (insets in Fig. 4.5) allow a much more quantitative comparison to TOF data since in this representation equal areas below the curve correspond to equal neutron fluence rates, and the differences in the peak fluence rates discussed above are more clearly visible. In case of 246 MeV beam energy best agreement with TOF data is obtained using the GEANT4-BIC and MCNP/LAHET responses. In contrast, at 389 MeV neutron fluence rates unfolded with the GEANT-BERT response matrix are closest to TOF data. This already shows that it might be somewhat difficult to find out which of the three response matrices describes the real BSS response most accurately since at different beam energies different responses seem to agree best.

4.5 Monte Carlo calculations inside the TOF tunnel

In order to cross-check the unfolded BSS spectra and estimate neutron fluence rates at thermal and epithermal energies resulting from room-scattered neutrons inside the TOF tunnel, a GEANT4 simulation was performed. For this purpose, GEANT4 v. 9.3 (*Agostinelli et al.*, 2003; *Allison et al.*, 2006) and the G4NDL cross section library v. 3.13 was used (see also Appendix B).

4.5.1 Details of GEANT4 calculations

The collimator was modeled as an iron frame with 10×12 cm^2 aperture and 10 cm in thickness embedded in a 1.5 m thick concrete wall. The concrete walls of the 100 m long TOF tunnel were assumed to have a thickness of 1 m, and the tunnel was filled with air at standard conditions. All material densities, compositions, and isotopic abundances were taken from the database of the National Institute of Standards and Technology[1] (NIST).

TOF data above 10 MeV combined with mean unfolded BSS spectra in the energy range from 0.1 to 10 MeV were used for both beam energies as source spectra. These spectra were shot from a point source at the target's position and homogeneously distributed within a solid angle of 3.5×10^{-3} sr, i.e. about five times the solid angle covered by the collimator. Finally, the resulting neutron fluences were scored at the measurement position of the BSS at 35 m distance from the target in a spherical volume with 15 inch diameter using an energy-binned fluence scorer that was modified to allow calculation of the uncertainty in each bin. Taking the number of source particles shot per steradian and the solid angle covered by the scorer into account, collected fluences were finally normalized in order to obtain absolute values comparable to those obtained in the measurements.

All available high-precision models for the low-energy neutron transport (< 20 MeV), including thermal scattering on hydrogen contained in concrete, were applied (see Appendix B). Above 20 MeV, the Bertini INC was used. It should be noted, however, that high-energetic neutrons scored at a distance of 35 m from the source are almost solely neutrons directly from the source which were not yet subject to any interaction. This is a consequence of the very small solid angle covered by the scoring region, since the probability of secondary high-energy neutrons produced in the collimator to cross the scorer is very low. Thus, for the calculation of low-energy neutron fluence rates inside the TOF tunnel the influence of the high-energy transport model applied is negligible. This was confirmed by various test calculations using the Binary INC above 20 MeV neutron energy.

In order to illustrate the fluences inside the TOF tunnel, Figure 4.6 shows energy-integrated

---

[1] http://www.nist.gov/pml/data/index.cfm

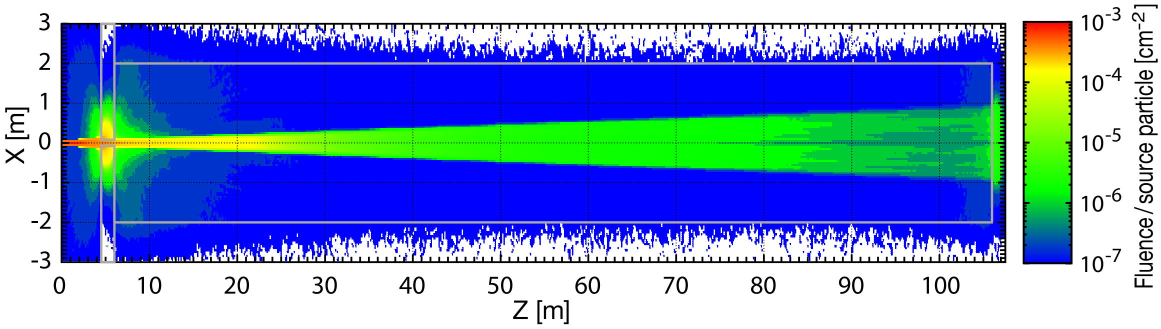

FIGURE 4.6: Illustration of integral neutron fluences per source particle scored in a GEANT4 simulation of the TOF tunnel at 246 MeV proton beam energy (mesh size 2×2×2 cm^3). Solid gray lines indicate boundaries of concrete walls and collimator. In the white areas zero fluence was scored.

neutron fluences per source particle collected with a mesh flux scorer (mesh size 2×2×2 cm^3). Depicted are resulting fluxes at 246 MeV beam energy scored in a horizontal plane centered in the collimator. The geometry of the collimator and the TOF tunnel used in GEANT4 (gray solid lines) as well as the source geometry can be seen. Considering the logarithmic color code, Figure 4.6 illustrates the comparatively low off-beam fluence indicating fairly little contamination with room-scattered low-energy neutrons inside the TOF tunnel. This is in good agreement with the unfolded BSS fluence rates in Figure 4.5 where thermal and epithermal neutron fluxes are by orders of magnitude lower than those at peak energies.

4.5.2 Comparison of unfolded and calculated spectra at low energies

The spectral neutron fluence rate calculated with GEANT4 at the measurement position of the BSS inside the TOF tunnel is shown in Figure 4.7 as differential neutron fluence rate $d\dot{\Phi}/d\ln(E)$ in log-log scale as a function of neutron energy. Since qualitatively and quantitatively similar results were obtained at both beam energies, the following discussion is exemplary restricted to 246 MeV beam energy. For comparison, the range of unfolded spectra given by the three different response matrices is shown as gray region in Figure 4.7 for energies below 10 MeV. Additionally, the source spectrum used in the GEANT4 calculation composed of the TOF spectrum above 10 MeV and the average unfolded spectrum between 0.1 and 10 MeV is also shown (red line).

As already stated above, scored high-energy neutrons are direct neutrons from the source resulting in exactly the same calculated fluence rates above 10 MeV (blue line in Fig. 4.7) as the TOF source spectrum (red line in Fig. 4.7). Concerning lower energetic fluences, it should be noted that at the RCNP high atomic number materials such as Fe are mainly present in the neutron experimental hall (e.g. beam swinger magnet) and around the collimator (see Fig. 4.1). For this reason, evaporation processes induced by high-energy protons and neutrons are expected to occur mainly before and within the collimator. Neutrons with energies around 1 - 2 MeV are able to reach the scoring region in 35 m distance with high probability because their mean free path in air at standard conditions is about 100 m. Therefore, an evaporation peak had to be included in the source spectrum of the GEANT4 calculations in order to accurately estimate epithermal and thermal neutron fluence rates inside the TOF tunnel. It

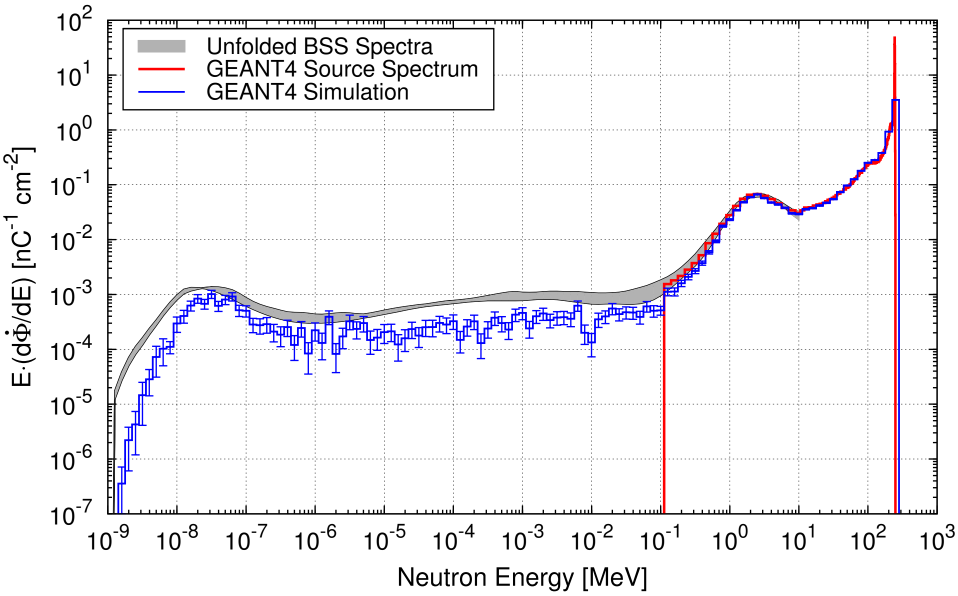

FIGURE 4.7: Comparison of unfolded BSS spectra below 10 MeV (gray region, see Fig. 4.5) and spectrum calculated with GEANT4 (blue line) at 35 m distance from the target and 246 MeV proton beam energy. The red line shows the source spectrum used in the particle transport simulation.

is obvious from Figure 4.7 that shooting TOF data above 10 MeV and an evaporation peak (measured by BSS) from the target's position and transporting these neutrons through the collimator to the measurement position of the BSS results in epithermal and thermal neutron fluxes which agree rather well with the unfolded BSS spectra at low energies. This in turn indicates an overall consistency of the BSS spectra over the whole energy region considered. The remaining systematic underestimation of less than 25% of the calculated compared with the unfolded fluxes at energies below 0.1 MeV may well be explained by the fact that not only evaporation but also lower-energetic neutrons are produced in regions before the collimator. Since e.g. the mean free paths of thermal neutrons in air at standard conditions is about 25 m, most of the epithermal and thermal neutrons produced before the collimator are scattered on the way to the scoring position. Nevertheless, minor contributions to low-energy neutron fluxes inside the TOF tunnel are expected.

4.6 Calibration of BSS in terms of detector readings

One way of calibrating the Bonner sphere spectrometer at high energies is to compare the detector readings of each sphere with count rates calculated using the TOF spectra and the corresponding Bonner sphere response function.

4.6.1 Contributions of low-energetic neutrons

In order to calculate count rates only corresponding to the TOF data above 10 MeV shown in Figure 4.3, the actual detector readings have to be corrected for contributions from neutrons with energies below 10 MeV. These were estimated according to Equation 3.3 using the unfolded neutron fluence rates shown in Figure 4.5 and the Bonner sphere response functions. In Figure 4.8 the relative contributions of low-energy neutrons ($E < 10$ MeV) to the measured detector readings are shown as a function of sphere diameter for 246 MeV proton beam energy. The inset in this figure summarizes the results for 389 MeV proton beam energy.

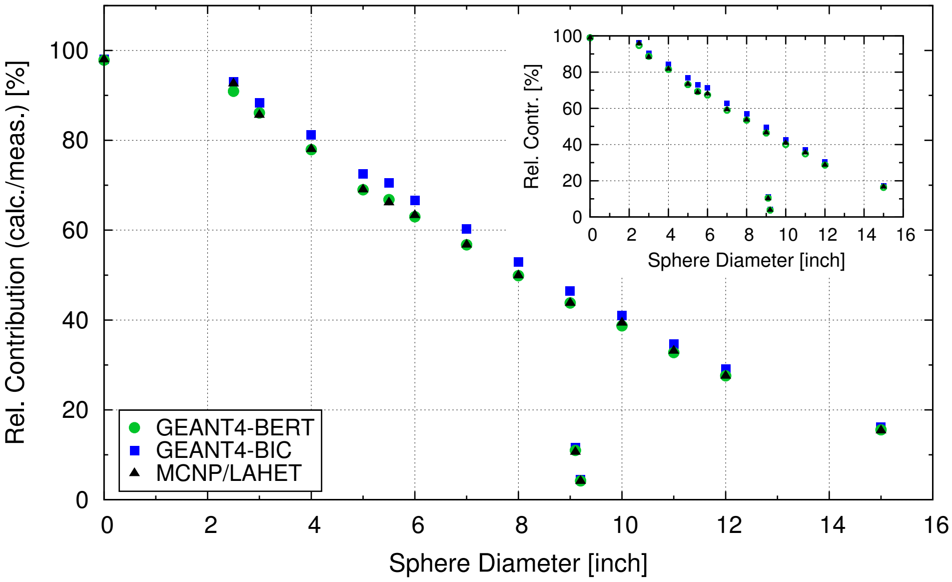

FIGURE 4.8: Relative contributions of low-energy neutrons ($E < 10$ MeV) to the measured detector readings of all spheres for 246 MeV beam energy. Contributions were estimated for all three sets of response matrices separately. The inset summarizes the results for 389 MeV proton beam energy.

At both beam energies the contributions were estimated for all three sets of response matrices separately. The minor differences in the contributions for the three different response matrices mainly result from the minor differences in the unfolded spectra below 10 MeV discussed in previous sections.

It is evident from this figure that although neutron fluence rates at energies below 10 MeV are small compared to peak fluxes at the maximum energies (see Fig. 4.5), the contributions to the detector count rates are very high for all small and medium-sized PE spheres. This simply reflects the fact that these spheres are mainly sensitive to low-energy neutrons. At both beam energies the relative contributions of low-energy neutrons rapidly decrease with increasing sphere diameter and hence increasing sensitivity to high-energy neutrons. Nonetheless, even for the rather large sphere with 12 inch diameter about 30% of the measured count rates result from neutrons with energies below 10 MeV. Only for the two 9 inch spheres with lead shells and the 15 inch PE sphere more than 80% of the count rates are caused by high-energy neutrons ($E > 10$ MeV). For this reason, an accurate calibration in the high-energy neutron fields of the RCNP is considered most reasonable and meaningful for these three spheres.

4.6.2 Comparison of measured and calculated count rates

Subtraction of the low-energy contributions shown in Figure 4.8 from the measured detector readings allows correction with respect to the low-energy part of the spectral neutron fluence rate distributions at both beam energies. The remaining count rates can then be compared to those calculated using the TOF data and the Bonner sphere response functions (Eq. 3.3). This in turn allows calibration of the BSS in terms of choosing the response matrix which agrees best with the independently measured TOF spectra.

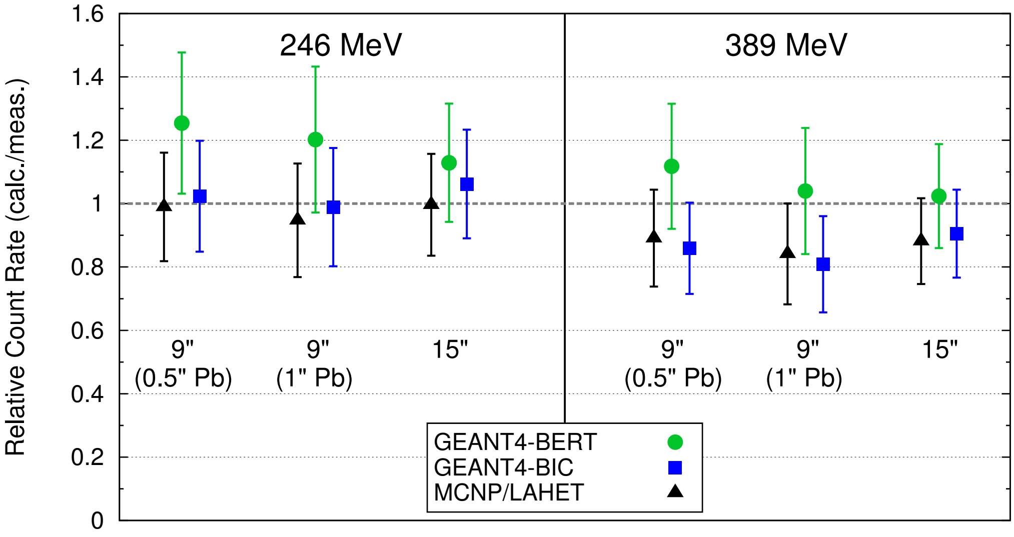

FIGURE 4.9: Ratio of count rates calculated using TOF data and three different response functions to measured and for low-energy contributions corrected count rates for the two 9 inch spheres with lead shells and the 15 inch PE sphere. On the left side results are depicted for 246 MeV and on the right side for 389 MeV proton beam energy.

In Figure 4.9 the ratios of calculated and measured count rates are shown for the three spheres which are most sensitive to high-energy neutrons, i.e. the two 9 inch spheres with lead shells and the 15 inch PE sphere. On the left side of this figure the results are depicted for 246 MeV and on the right side for 389 MeV proton beam energy.

The uncertainties shown were estimated assuming 5% uncertainty of the BSS response functions at energies below 10 MeV based on low-energy calibration measurements (*Alevra et al.*, 1992; *Thomas et al.*, 1994), and taking the standard deviation of the unfolded integral low-energy fluxes ($E < 10$ MeV), the statistical uncertainties of the BSS measurements ($< 1\%$), as well as the systematic and statistical uncertainties of the TOF data into account. The overall statistical uncertainties were finally calculated using standard Gaussian error propagation. Additionally, a 5% systematic uncertainty for the BSS data was assumed based on an inter-comparison of BSS measurements performed in high-energy stray fields at the hadron therapy facility GSI in Germany (*Wiegel et al.*, 2009). This error reflects typical systematic uncertainties arising from the application of different unfolding codes in Bonner sphere spectrometry as well as the use of different input parameters for the deconvolution procedure such as start spectra and iteration numbers. It should be noted, however, that the systematic uncertainty basically depends on the neutron spectra measured and, therefore, it may slightly differ in the high-energy neutron fields of the RCNP. Nonetheless, this value is expected to give a reasonable estimate for the systematic uncertainty involved in the BSS measurements presented in the present work. Since all statistical uncertainties are very low for both TOF and BSS data, the error bars shown in Figure 4.9 predominantly reflect the systematic uncertainty of 15% involved in the TOF measurements (*Iwamoto et al.*, 2011) and that of 5% involved in the BSS measurements.

For the sake of completeness, in Figure 4.10 the ratios of calculated and measured count rates are shown for all PE spheres with diameter up to 12 inch and the bare ^{3}He detector. The top panel summarizes the results for 246 MeV and the bottom panel for 389 MeV beam energy. Obviously, also for all smaller PE spheres the same trend is observed as for the

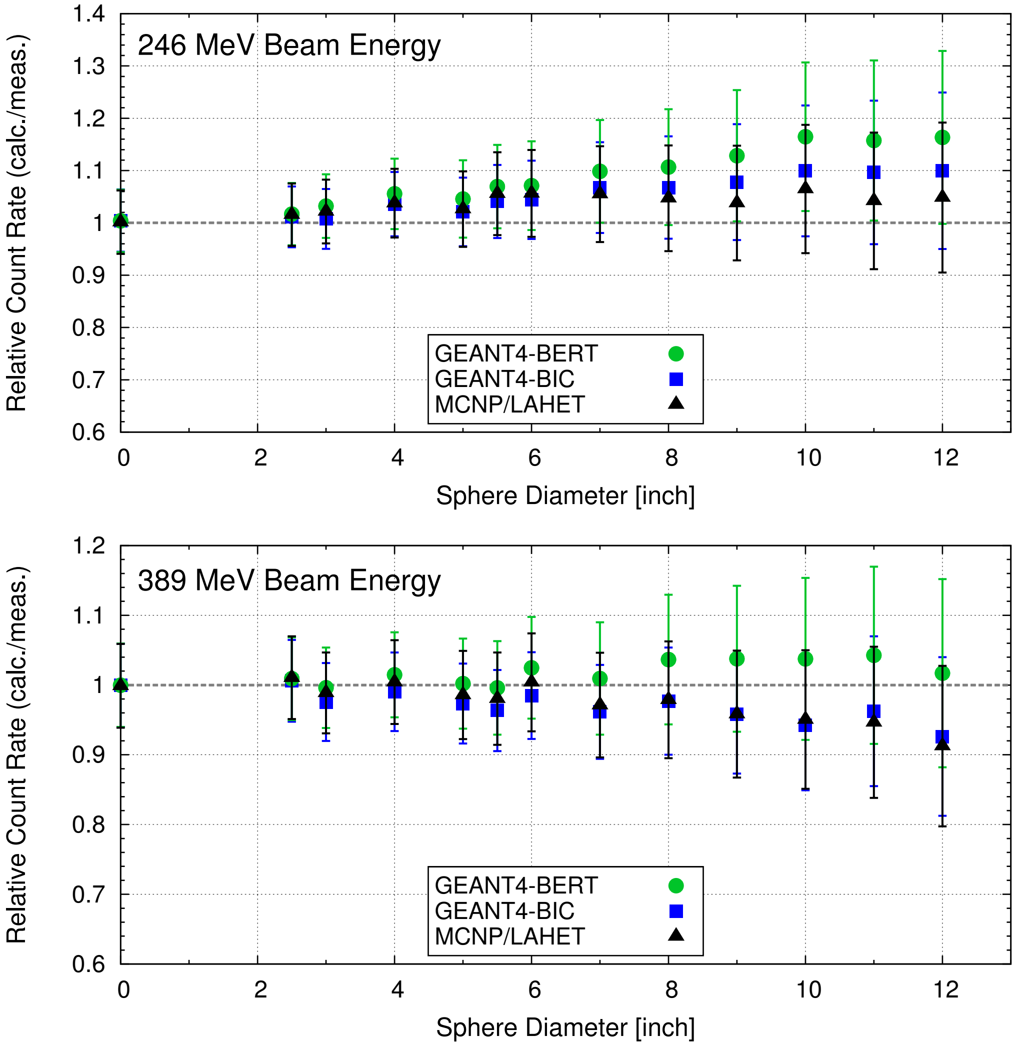

FIGURE 4.10: Ratio of count rates calculated using TOF data and three different response functions to measured and for low-energy contributions corrected count rates for all PE spheres up to 12 inch diameter and the bare ^{3}He proportional counter (zero inch). The top panel shows results for 246 MeV and the bottom panel for 389 MeV beam energy.

Bonner spheres which are more sensitive to high-energy neutrons. Due to the fact that the very small spheres almost solely detect low-energy neutrons, the differences resulting from different response matrices decrease with decreasing sphere size. The same is valid for the associated uncertainties since the 15% systematic uncertainty of the TOF data contributes only to a minor degree.

Taking the uncertainties into account, the overall agreement of measured count rates and those calculated using TOF data is completely satisfying for all three sets of response functions. As it was also the case in the inter-comparison of unfolded BSS and TOF spectra discussed in Section 4.4, however, at different beam energies different response matrices appear to agree best with the actually measured count rates. At 246 MeV beam energy calculations using the GEANT4-BIC and the MCNP/LAHET matrix match very well with the measurements for all Bonner spheres. At 389 MeV, on the other hand, the GEANT4-BERT response functions reproduce measurements best. Therefore, it appears that the hadronic interaction models applied in the GEANT4-BERT hadronic framework handle neutron interactions at energies above about 200 MeV somewhat more accurately, whereas the models in MCNP/LAHET and GEANT4-BIC may be better at lower energies.

4.7 Calibration of BSS in terms of response values

Another approach for calibration of the BSS is to determine measured response values using TOF data and measured count rates that were corrected for contributions from low-energy neutrons. To be more specific, the measured count rates were corrected with respect to neutrons with energies below 10 MeV by subtraction of the mean low-energy count rates calculated based on unfolded fluence rates and the three response matrices (see Fig. 4.8). The remaining count rates ζ_{corr} divided by the integral fluence rates of the TOF spectra $\dot{\Phi}_{TOF}$ finally give measured response values for each sphere i in the energy region covered by the TOF method:

$$R_{meas,i}(E_{eff,i}) = \frac{\zeta_{corr,i}}{\dot{\Phi}_{TOF}} = \frac{\zeta_{corr,i}}{\int_{10MeV}^{E_{max}} \frac{d\dot{\Phi}_{TOF}(E)}{dE} dE}. \tag{4.1}$$

Due to the fact that every Bonner sphere has a different sensitivity in this energy range, these response values correspond to sphere-specific effective energies $E_{eff,i}$. Taking each sphere's response (R_i) and the spectral TOF fluence rate distribution into account, the effective energies can be estimated as

$$E_{eff,i} = \frac{\int_{10MeV}^{E_{max}} E \cdot R_i(E) \cdot \frac{d\dot{\Phi}_{TOF}(E)}{dE} dE}{\int_{10MeV}^{E_{max}} R_i(E) \cdot \frac{d\dot{\Phi}_{TOF}(E)}{dE} dE}. \tag{4.2}$$

As a result of the very similar shapes of the three different response functions, the effective energies calculated for each sphere agree within a few percent.

In the top panel of Figure 4.11 the measured response values are shown for the two 9 inch spheres with lead shells and the 15 inch PE sphere at the corresponding mean effective energies in comparison with mono-energetic response calculations. The bottom panel of this figure shows measured responses for the 5, 8, and 12 inch PE spheres. In Table 4.1 numerical values of the mean effective energies and the measured responses are listed for 246 MeV and 389 MeV proton beam energy for all spheres larger than 4 inch, as the uncertainties for the very small spheres are much larger than 30%. The uncertainties in the mean effective energies arise from the three different response functions, and those for the measured response values were estimated as discussed in the previous section.

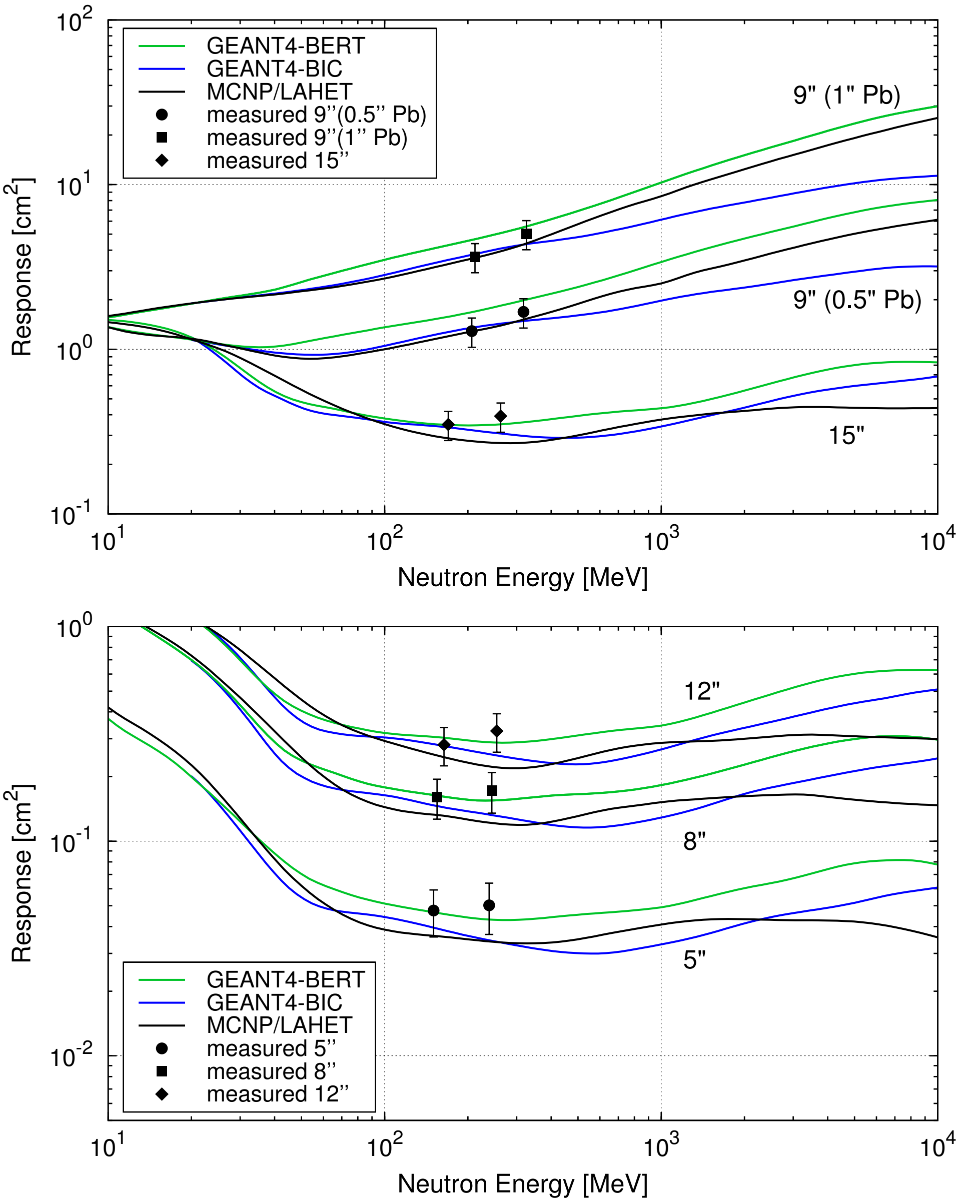

FIGURE 4.11: Measured response values at assigned mean effective energies calculated with Equation 4.2 for 246 MeV and 389 MeV proton beam energy in comparison with mono-energetic MC calculations. In the top panel response values are shown for the two 9 inch Bonner spheres with lead shells and the 15 inch PE sphere. The bottom panel depicts measured responses of the 5, 8, and 12 inch PE spheres.

TABLE 4.1: Measured response values at assigned mean effective energies calculated with Equation 4.2 for 246 MeV and 389 MeV proton beam energy. Response values obtained for the bare detector, the 2.5, and the 3 inch PE spheres are not shown since the deduced uncertainties are much larger than 30%.

	246 MeV BEAM ENERGY		389 MeV BEAM ENERGY	
Sphere [inch]	eff. Energy [MeV]	Response [cm^2]	eff. Energy [MeV]	Response [cm^2]
4	148.7 ±4.82%	0.0181 ±30.45%	238.1 ±4.69%	0.0196 ±35.01%
5	150.2 ±4.32%	0.0475 ±24.74%	238.6 ±4.55%	0.0502 ±26.85%
5.5	150.9 ±3.57%	0.0618 ±23.84%	239.2 ±4.17%	0.0707 ±24.85%
6	152.1 ±3.64%	0.0811 ±22.95%	240.2 ±4.83%	0.0844 ±24.29%
7	153.6 ±4.18%	0.1187 ±21.81%	243.1 ±4.50%	0.1352 ±22.21%
8	154.6 ±3.69%	0.1604 ±21.12%	244.1 ±4.22%	0.1720 ±21.48%
9	156.7 ±3.69%	0.1960 ±20.72%	247.4 ±4.15%	0.2171 ±20.91%
9 (0.5 Pb)	206.6 ±0.65%	1.2875 ±20.14%	317.8 ±1.22%	1.6856 ±20.18%
9 (1.0 Pb)	212.1 ±0.45%	3.6481 ±20.11%	325.3 ±0.98%	5.0314 ±20.16%
10	159.2 ±4.21%	0.2202 ±20.52%	250.1 ±4.47%	0.2552 ±20.62%
11	160.9 ±4.67%	0.2548 ±20.35%	251.4 ±3.91%	0.2827 ±20.45%
12	163.8 ±3.81%	0.2814 ±20.26%	254.3 ±3.81%	0.3259 ±20.32%
15	169.8 ±3.41%	0.3490 ±20.15%	262.5 ±3.73%	0.3925 ±20.20%

Especially at 246 MeV proton beam energy the measured responses of the two 9 inch spheres with lead shells agree remarkably well with the GEANT4-BIC and MCNP/LAHET response functions. At 389 MeV beam energy the measurements indicate slightly higher detection efficiencies and are much closer to the GEANT4-BERT response functions.

In case of pure polyethylene spheres nearly the same trend is observed. For the small and medium-sized PE spheres, however, the inter-comparison of measured and calculated count rates presented in the previous section is less meaningful, because these spheres are rather sensitive to low-energy neutrons. Nevertheless, the comparison for the smaller spheres in the bottom panel of Figure 4.11 again shows the consistency of the calibration measurements performed in the high-energy neutron fields of the RCNP. It may, therefore, be concluded that the Bertini model appears to overestimate neutron yields in spallation reactions, at least in the energy range up to approximately 200 MeV, whereas the other two codes and models appear to handle these reactions rather accurately. In contrast, at energies above about 200 MeV the Bertini model seems to give rather correct results, but also the other models are consistent with the measurements considering the uncertainties involved.

4.8 Summary of calibration measurements

To put it in a nutshell, a detailed comparison of neutron spectra measured with the BSS and unfolded using three different response matrices with the spectra obtained by the TOF method was done. It turned out that at 246 MeV beam energy the unfolded BSS neutron fluence rates using the response matrix calculated with the GEANT4 Binary INC model and the MCNP/LAHET code agree best with the TOF measurements around the nominal peak energies. In contrast, at 389 MeV proton energy the peak intensities given by the TOF method were closer to unfolded BSS fluence rates using the response matrix calculated with the GEANT4 Bertini INC model.

For the actual calibration of the BSS two different approaches were applied. First, measured count rates of all Bonner spheres were corrected with respect to contributions from neutrons with energies below 10 MeV using unfolded fluence rates and the corresponding response functions. The remaining count rates resulting from high-energy neutrons ($E > 10$ MeV) finally were compared to calculated count rates using the independently measured TOF spectra and the response functions of the Bonner spheres. In the second approach, count rates corrected for neutrons with energies below 10 MeV and the TOF spectra were used to obtain measured response values. Those were finally compared with response values based on mono-energetic calculations using different MC codes and INC models. In both approaches remarkable overall agreement of the measurements and basically all response calculations was obtained considering the uncertainties involved in the determination of high-energy neutron fluence rates. This in turn confirms all response calculation at high energies. As it was already the case in the inter-comparison of BSS and TOF neutron spectra, however, a closer look revealed that at 246 MeV beam energy the GEANT4-BIC and the MCNP/ LAHET responses appear to give a more accurate estimate for the real responses of the Bonner spheres. At 389 MeV, on the other hand, measurements seem to match better with the GEANT4-BERT response matrix. This in turn indicates that the GEANT4 Bertini INC model is likely to handle high-energy hadronic interactions more accurately at energies above approximately 200 MeV, whereas the other two may be better at lower energies. In terms of Monte Carlo calculations in general, this is a very interesting and important finding, which is addressed again in Chapter 5.

The Bonner sphere measurements in the high-energy neutron fields of the RCNP revealed that basically all three calculated response matrices are almost equally consistent with measurements, depending somewhat on the energy and the material. Nevertheless, it may be concluded that for radiation protection purposes either the GEANT4-BIC or the MCNP/LAHET response matrix should be used because both were shown to be consistent with response measurements at high energies and both give nearly the same conservative estimate for the ambient dose equivalent in high-energy neutron fields as discussed in Chapter 3.

The results of the BSS measurements in quasi-monoenergetic neutron fields presented in this chapter are published in *Pioch et al.* (2011a). Furthermore, it should be noted that during the composition of the present work complementing Bonner sphere response measurements were carried out in neutron fields generated by 140 and 200 MeV proton beams at the RCNP in Osaka, Japan. Due to the fact that the final evaluation of time-of-flight data provided by the Japanese colleagues takes several months, these data could not be included. They are expected to be published as soon as the final TOF data are available.

CHAPTER

5

COSMIC RADIATION IN THE EARTH'S ATMOSPHERE

One major goal of the present work was the calculation of secondary cosmic radiation in the lower atmosphere by means of Monte Carlo transport simulations in order to estimate the radiation exposure at aircraft altitudes. This comprises both exposure due to galactic cosmic radiation as well as due to solar cosmic radiation during solar energetic particle events or ground level enhancements. To address this issue in detail, in the following chapter secondary cosmic ray particle fluence rates induced in the Earth's atmosphere by GCR nuclei are extensively discussed and compared with results of other authors as well as with several high-precision measurements (Section 5.4). This, in turn, serves as validation for the transport simulations, which is necessary to ensure accuracy of the calculations during ground level enhancements. To allow for a coherent discussion, a complete description of the characteristics of the Earth's atmosphere (Section 5.1), the physical processes responsible for the production of secondary particles (Section 5.2), and the MC calculations performed in the present work (Section 5.3) are given in the first part of this chapter. Furthermore, a detailed comparison of calculated secondary neutron spectra at sea-level with Bonner sphere measurements in Ny-Ålesund, Spitsbergen, follows in Section 5.5. This includes detailed studies of the influence of different soil types on neutron spectra as well as influences of the hydrogen content in and on the soil. Additionally, the last section of this chapter (Sec. 3) focuses on potential measurements of ground level enhancements with the polar BSS and the corresponding potential changes in neutron intensities and spectral characteristics during such events.

5.1 The Earth's atmosphere

For the computation of secondary particle fluence rates and the corresponding dose quantities the transport of primary cosmic radiation through the Earth's atmosphere needs to be simulated. The atmosphere reaches several thousand kilometers into interplanetary space with a mean total mass of about 5.148×10^{18} kg (*Trenberth and Smith*, 2005). More than 99.99% of this mass is contained in the lower atmospheric layers below about 100 km, which comprises the Troposphere, the Stratosphere, the Mesosphere, and parts of the Thermosphere (see e.g. *Lutgens et al.*, 2009). The lower atmosphere is mainly composed of N_2, O_2, and Ar which account for about 75%, 23%, and 1.3% by mass, respectively. Apart from these constituents, the atmosphere contains minor fractions of C ($\approx 0.012\%$ by mass) bound in CO_2, CO, or CH_4 and traces of other elements such as He, Ne, or Kr. Water content in the atmosphere is highly variable but even during cloudy conditions the hydrogen fraction is only in the order of $10^{-5}\%$. The exact mass fraction of each constituent, however, depends on altitude.

In the present work a dry atmosphere composed of N_2, O_2, and Ar was considered up to an altitude of 100 km. The altitude profiles of composition, density, temperature, and pressure were adapted from the empirical atmospheric model[1] NRLMSISE-00 developed by *Picone et al.* (2002) which is an update of the widely used MSISE-90 model[2] (*Hedin*, 1991).

For the calculation of secondary particle fluence rates induced in the atmosphere by primary cosmic radiation it is essential to have a measure for the air mass overburden at the point of interest. This is particularly important for any inter-comparison of simulation results obtained by different authors or for a comparison with experimental data. The parameter describing the air mass above a point of interest is the atmospheric depth d given as the ratio of mass per area. The atmospheric depth at an altitude h is related to the pressure $p(h)$ for a given gravitational acceleration $g(h)$ according to

$$d = \frac{m(h)}{A} = \frac{F_g(h)}{A \cdot g(h)} = \frac{p(h)}{g(h)} = \int_h^\infty \rho(h')dh', \tag{5.1}$$

where $m(h)$ is the mass of air above the point of interest, $\rho(h)$ is the air density, and F_g the gravitational force on area A. Throughout the present work, the gravitational acceleration is assumed to be constant with a value of $g = 9.81$ m/s^2.

The profiles of atmospheric depth, pressure, temperature, and density in the Earth's atmosphere depend on the geographic latitude and show a strong seasonal variation. In Figure 5.1 example profiles are shown as given by the NRLMSISE-00 model from sea-level to 20 km altitude in comparison with the U.S. Standard Atmosphere 1976 (*COESA*, 1976) which models medium latitudes on the northern hemisphere. Apparently, significant differences in all parameters occur for different latitudes and times at a given altitude. For this reason, globally and seasonally averaged profiles (red lines in Fig. 5.1) were used in the GEANT4 particle transport calculations presented in this chapter which agree very well with the Standard Atmosphere.

It is obvious from Figure 5.1 that the differences in atmospheric depth, pressure, and density are especially pronounced at commercial aircraft altitudes from 9 - 13 km. As a consequence,

---

[1] http://modelweb.gsfc.nasa.gov/atmos/nrlmsise00.html

[2] http://omniweb.gsfc.nasa.gov/vitmo/msis_vitmo.html

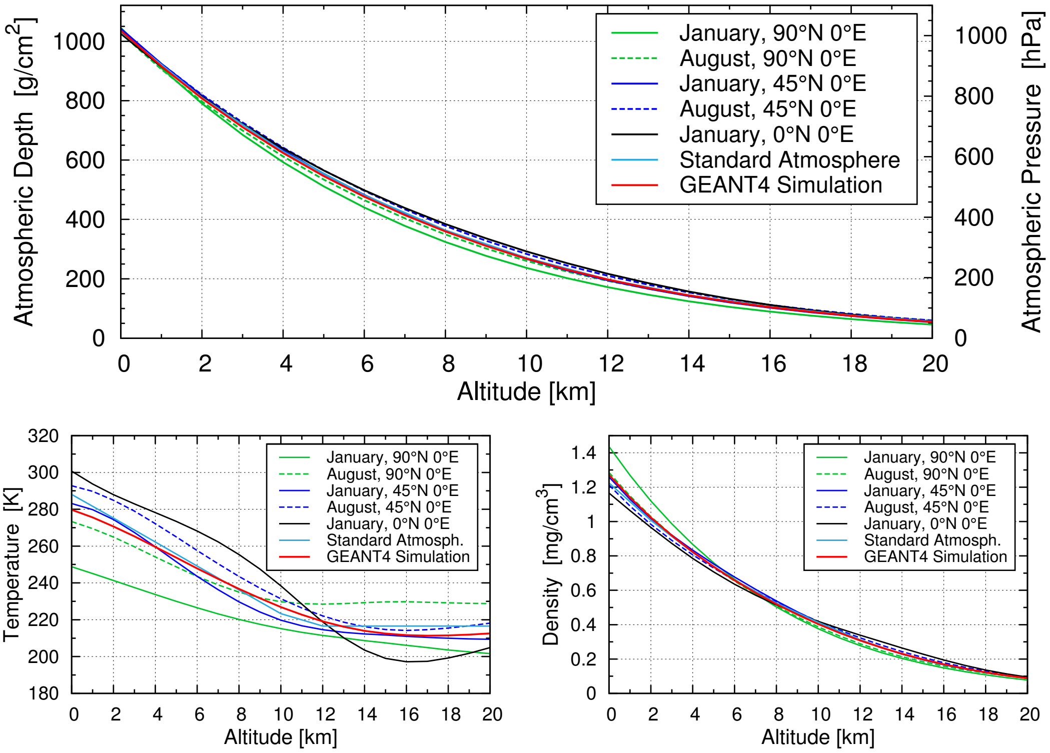

FIGURE 5.1: Seasonal and latitudinal variations in the profiles of atmospheric depth, pressure (top), temperature (bottom left), and density (bottom right) from sea-level to 20 km altitude according to the NRLMSISE-00 model (*Picone et al.*, 2002) in comparison with the U.S. Standard Atmosphere 1976 (*COESA*, 1976). Red lines show the profiles used in GEANT4 simulations.

a certain altitude may correspond to different atmospheric depths depending on the model used for the atmosphere. The atmospheric depth, however, is a measure for the air mass overburden at a specific point and, thus, describes the shielding against primary cosmic radiation provided by the mass contained above that point. Therefore, simulation results from different atmospheric models or measurements are only comparable at certain atmospheric depths. This is not necessarily true for a particular altitude which may correspond to a very different air mass overburden and shielding. In case results from other authors were only given at a specific altitude, they were converted to depth according to the U.S. Standard Atmosphere in order to allow for a quantitative inter-comparison.

The Standard Atmosphere was chosen as a reference since it is also used in aviation, where the nominal elevation of an airplane is expressed in flight levels (1 FL $=$ 100 ft $\approx$ 30.48 m). Airplanes fly at constant pressure, and the corresponding nominal altitude above sea-level is calculated with respect to the U.S. Standard Atmosphere. The real elevation of an aircraft, therefore, may significantly differ from the nominal altitude, depending on the local atmospheric conditions.

5.2 Extensive air showers in the atmosphere

The characteristics of primary cosmic radiation were summarized in Chapter 2, including a detailed description of composition, intensity, and energy distribution. Furthermore, the modulation by solar activity in the Heliosphere and the influence of the Earth's Magnetosphere were extensively discussed there.

When primary cosmic ray nuclei impinge on the atmosphere, a complex field of secondary cosmic radiation is generated in hadronic and electromagnetic interactions with atoms and molecules in the air. Among others, neutrons, protons, muons, pions, electrons, positrons, and photons are produced in a broad energy range. High-energetic secondaries on their part may produce further particles or decay according to their mean lifetime and velocity. As a consequence, so-called extensive air showers develop in cascade processes. A single relativistic hadron may create millions of secondaries spreading several tens of square kilometers in lateral extension and ranging from top of the atmosphere down to sea-level. The particles involved in the evolution of such a shower can be divided according to the particle species into the hadronic, the electron-photon, and the muonic component (see e.g. *Grieder*, 2001).

Primary cosmic ray nuclei striking the Earth's atmosphere are subject to strong interactions with atmospheric nuclei and induce spallation reactions. As a result, high-energetic nucleons, alpha particles, and heavier fragments as well as pions, kaons, and hyperons are created. At sufficiently high energies primary and secondary particles further excite atmospheric nuclei, which in turn evaporate nucleons with average energies $\leq$ 10 MeV. The resulting hadronic cascade constitutes the core of the extensive air shower.

A relativistic primary proton ($E > 1$ GeV) undergoes about 12 hadronic interactions while penetrating the atmosphere down to sea-level. This corresponds to a mean interaction length of about 80 g/cm^2. For a heavy nucleus with mass number A $\approx$ 25, on the other hand, the mean interaction length is only about 20 g/cm^2 (*Allkofer*, 1975). Thus, the first interaction, in which the projectile nucleus is usually completely fragmented occurs at much higher altitudes than for protons. Additionally, much more interactions occur along the way ($\approx$ 50), and there is almost no chance for a heavy primary cosmic ray particle to fully traverse the atmosphere and survive to sea-level.

Apart from hadronic interactions, primary cosmic ray nuclei are subject to electromagnetic interactions and lose energy in excitation and ionization processes with electrons of atoms and molecules in the air. The electromagnetic energy loss of charged particles per unit path length is well described by the Bethe-Bloch formula below several GeV/n (see e.g *Turner*, 1995). A relativistic primary proton traversing the whole atmosphere loses approximately 2.2 GeV energy in ionization and excitation reactions. Radiative energy loss through emission of Bremsstrahlung or Čerenkov radiation, on the other hand, is negligible for heavy charged particles.

For the overall development of an extensive air shower and the creation of further particle generations the pion triplet (π^+, π^-, π^0) produced in hadronic interactions is of major importance. With a mean lifetime of about 26 ns (*Nakamura et al.*, 2010), charged pions decay into muons and neutrinos via $\pi^+ \rightarrow \mu^+ + \nu_\mu$ and $\pi^- \rightarrow \mu^- + \overline{\nu}_\mu$. Due to the time dilation effect, the mean lifetime at relativistic energies is significantly longer in the terrestrial reference system, and above about 100 GeV charged pions themselves may interact with nuclei before they decay. Thus, charged pions markedly contribute to the hadronic component.

Furthermore, the $\pi^{\pm}$ decay processes give rise to the muon component. Muons lose only about 2 GeV of energy in ionizations (*Allkofer*, 1975), and most of them are able to reach sea-level due to time dilation although their mean lifetime at rest is rather short ($\approx$ 2.2 μs). Some of them, however, decay into electrons, positrons, and neutrinos via $\mu^{+} \rightarrow e^{+} + \nu_{e} + \overline{\nu}_{\mu}$ and $\mu^{-} \rightarrow e^{-} + \overline{\nu}_{e} + \nu_{\mu}$.

Neutral pions decay into two photons ($\pi^{0} \rightarrow 2\gamma$) with a mean lifetime of approximately 10^{-16} s. These may interact via photo effect, Compton effect, pair production, and photonuclear reactions producing further electrons, positrons, and photons. Positrons in turn annihilate with electrons, and electrons deposit their energy via Bremsstrahlung, ionization, excitation, emission of Čerenkov radiation, or nuclear reactions. As a result, an electromagnetic cascade is induced, the electron-photon component of the air shower.

Due to the competition of production, absorption, and decay of secondary cosmic ray particles, the overall particle intensity is not constant but highly depends on atmospheric depth. In the vertical development of an extensive air shower an increase in particle number occurs during the first 100 g/cm^{2}. At greater atmospheric depth, a continuous decrease in intensity is observed as a result of absorption and decay processes. *Pfotzer* (1936a,b) was the first to observe the maximum at an atmospheric pressure of 8 cmHg corresponding to an altitude of about 16 km in the U.S. Standard Atmosphere. This maximum in secondary cosmic ray particle intensity was subsequently termed the Pfotzer maximum.

The exact atmospheric depth of the Pfotzer maximum slightly varies for each particle species due to particle-specific production and interaction mechanisms. These differences in integral secondary particle intensities as well as the spectral fluence rate distributions of all particles contributing to the total dose rates due to cosmic radiation are discussed in subsequent sections by means of particle transport calculations in the atmosphere.

5.3 Particle transport calculations using GEANT4

All calculations of secondary cosmic radiation performed within the frame of the present work were done with GEANT4 v. 9.3 and the G4NDL data library v. 3.13. The simulation of the radiation environment in the lower atmosphere due to cosmic radiation is a deep penetration problem as the mass equivalent of the whole atmosphere corresponds to about 10 m of water. Furthermore, the computing time for the simulation of extensive air showers increases exponentially with increasing energy of the primary particle. Therefore, such calculations are rather CPU time consuming. To obtain results within a reasonable computing time and with satisfactory statistics even at sea-level, the components of secondary cosmic radiation were computed in parallel on six Intel Core i7 machines with four physical CPUs and eight threads each.

However, to keep the focus in this chapter on valuable results, only the most important points of the particle transport calculations are outlined in the following. A detailed summary of GEANT4 specific modeling techniques, the physics, random number generation, and the parallelization of calculations may be found in Appendix B.

5.3.1 Geometry and scoring

The Earth's atmosphere was modeled in a cubic geometry with a base area of 5000×5000 km^2. A dry atmosphere composed of N_2, O_2, and Ar was considered. The influence of discarding the minor fractions of other constituents such as CO_2 or Ne was studied during this work, and it was found that differences in the simulation results are negligible. The atmosphere was modeled up to an altitude of 100 km, where the real atmospheric profiles of composition, temperature, density, and pressure were resembled by a stack of 100 layers with constant parameters. As stated at the beginning of this chapter, globally and seasonally averaged profiles for these parameters given by the NRLMSISE-00 model (*Picone et al.*, 2002) were used (red lines in Fig. 5.1). In order to accurately approximate the continuously increasing pressure and density with increasing atmospheric depth, each layer corresponded to an increment in atmospheric depth of only about 10 g/cm^2, and the slab thicknesses were calculated based on Equation 5.1. The geometry used in the GEANT4 calculations is illustrated in Figure 5.2 as a section of 200×200×100 km^3 where blue lines indicate boundaries of the atmospheric layers. The extensive air shower shown in this figure was initiated by a 100 GeV proton vertically incident on top of the atmosphere (red vertical line).

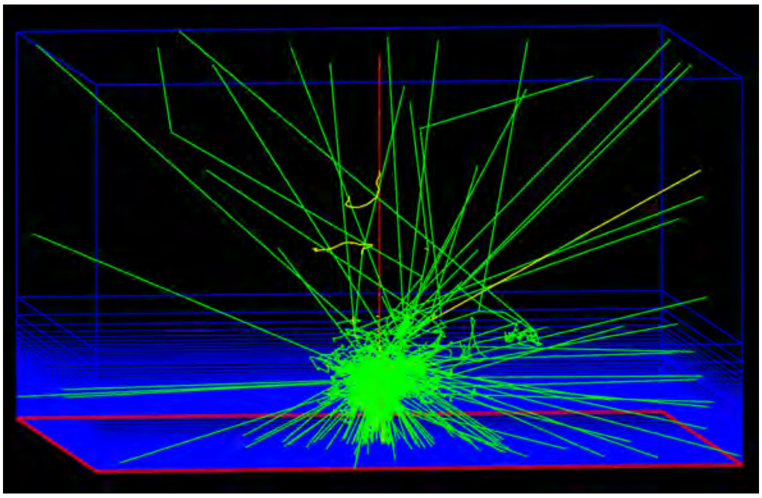

FIGURE 5.2: Illustration of the geometry used in GEANT4 calculations as a section of 200×200×100 km^3. The extensive air shower was initiated by a 100 GeV proton vertically incident on top of the atmosphere at 100 km altitude (red vertical line). Yellow tracks correspond to trajectories of negatively charged particles, red tracks to positively charged, and green tracks to neutral particles. Blue boxes represent atmospheric layers considered in the simulation, and the red box depicts the surface of the Earth.

For the determination of ambient dose equivalent and effective dose due to cosmic radiation, the secondary particle fluences of neutrons, protons, negative and positive muons, electrons, positrons, photons, and all kinds of pions were scored. As discussed in more detail in Chapter 6, these particle species are most important in terms of their contributions to total effective dose. For each particle type a total number of 46 tube-shaped scorers were distributed between 0.25 g/cm^2 ($\approx$ 60 km altitude) and 1030 g/cm^2 (sea-level).

Scorer thicknesses corresponding to 1.0 g/cm^2 were chosen in order to avoid averaging of the fluences over a wide range in atmospheric depth. This is in particular important near sea-level, where the conditions rapidly change with increasing atmospheric depth. Moreover, the lateral dimension of the scorers was half the full extension of the simulated atmosphere (i.e. 2500 km) to avoid boundary effects such as particles escaping from the geometry. Secondary particle spectra induced in the atmosphere by primary cosmic radiation cover a broad range in energy depending on the particle species. To make sure the full range is covered, neutrons were collected in the range from 10^{-11} MeV to 10^7 MeV and all other particles from 10^{-2} MeV to 10^7 MeV. For this purpose, energy-binned fluence scorer were applied which were modified to allow determination of the statistical uncertainty in each bin (see also Chapter 3 and *GEANT4 Collaboration*, 2009b).

In order to compare and validate results of particle transport calculations with experimental data, a zenith angle dependence of secondary particle intensities has to be taken into account in addition to the dependence on the kinetic energy. This is necessary because most instruments, in particular the very precise ones, only accept particles with certain zenith angles. Accordingly, the scoring in GEANT4 also has to be restricted to particles with momentum directions within a certain solid angle. For this purpose, a scoring filter was developed which allows to count not only particles of certain type and kinetic energy. By calculating the zenith angle between momentum direction and surface normal vector of each particle entering, crossing, or being produced in a scoring region, an adjustable filter criterion for the zenith angle was implemented in the GEANT4 code. This finally allows a validation of the MC results by comparison with measurements given as differential particle intensities per solid angle in units of particles/(cm^2·s·sr·MeV).

Furthermore, it should be noted that secondary particle spectra near sea-level are strongly influenced by the soil. This is particularly the case for neutrons with energies below several tens of MeV which follow an isotropic angular distribution and where elastic scattering is the dominating interaction process. In order to calculate free-in-air particle spectra at very high atmospheric depths, back scattering from layers below the Earth's surface has to be taken into account. In case all particles are stopped and killed directly on the Earth's surface, the scored integral particle fluences are strongly reduced leading to an artificial bias in the results. Test calculations showed that a layer of about 400 m filled with air at sea-level conditions is necessary to avoid influences on scored neutron fluences due to the soil-atmosphere interface. For the free-in-air particle spectra presented in the following this additional slab of air was considered (red box in Figure 5.2). More realistic simulations studying the impact of the soil and the hydrogen content in and on the soil are discussed in the last part of this chapter.

From the assumptions made on the geometry of the atmosphere in the present work, minor inaccuracies with respect to reality may arise. Due to the flat geometry chosen in contrast to the real spherical shape, minor differences in the path lengths occur for primaries starting in non-vertical directions. The path length to reach a certain altitude is about 2% shorter in the flat geometry for a primary particle starting with a zenith angle of 50° and about 5% shorter for 75°. The impact of these small differences on the secondary particle intensities at certain altitudes are expected to be much less, because secondaries are produced in a broad spatial area in cascade processes. Hence, the exact location of the initial reaction is less important. Furthermore, primaries starting in non-vertical direction have much longer path lengths with respect to vertical incidence, anyway. A primary starting with 60° zenith angle, for example, already has twice the path length to reach a certain altitude. Accordingly, the contributions to the radiation environment at aircraft altitudes and below are only of minor importance since they tend to induce particle showers at much lower atmospheric depths. Therefore, the overall discrepancies in secondary particle intensities below about 20 km arising from the simulation of a flat atmosphere are expected to be negligible.

Another inaccuracy with respect to reality may arise from the large lateral extension of the flat geometry when considering secondary particle fluences at different cutoff rigidities. In reality a 5000×5000 km^2 section of the atmosphere would sample radiation over a rather broad range in cutoff. However, to model particle intensities at the exact cutoff rigidities, the transport through the Earth's magnetosphere would have to be simulated, and all possible incoming directions on top of the atmosphere would have to be considered. It is, therefore, nearly impossible to exactly model the real conditions and calculate secondary particle intensities with high statistical precision down to sea-level. As discussed in detail in Chapter 2.1.2, the commonly used approach is to use the vertical effective cutoff rigidity, which has been shown by *Smart and Shea* (2003a,b) to provide an accurate approximation for the primary particle intensities on top of the atmosphere, in particular for studies of the radiation environment in the lower atmosphere and at aircraft altitudes. The big size of the geometry in the present work was simply chosen because otherwise too many primary particles starting with high zenith angles can escape. Increase of the atmosphere's lateral extension from 500 km to 5000 km increased integral particle intensities at very high altitudes above 25 km by about 5 - 8%, whereas almost no influence was observed at lower altitudes. In the real isotropic field of primary cosmic radiation, however, particles with very high zenith angles impinge onto the atmosphere. Their contributions at high altitudes were, thus, taken into account by choosing a rather large geometry. Nonetheless, small differences to reality might occur due to the approximation with the vertical effective cutoff since particles arriving in non-vertical direction can have a very different cutoff.

5.3.2 Physics

The simulation of the complex radiation field of secondary cosmic radiation in the atmosphere and the concomitant deep penetration problem in calculations down to sea-level requires a well-tuned assignment of the physics in GEANT4. All possible processes over the full range of energy have to be taken into account for all particle species involved. Since most of the energy in an extensive air shower is delivered by hadronic interactions, special attention has to be payed to these processes. Primary galactic cosmic ray spectra for protons and He nuclei were considered in the energy range from 10 MeV to 10 TeV. The resulting secondary particles, in particular neutrons, have to be transported down to 10^{-11} MeV. This means that a total range in energy of 17 orders of magnitude has to be accurately covered in the simulation. In the following the physics applied in the particle transport calculations in the Earth's atmosphere are summarized. A more detailed description of the underlaying models and modeling techniques may be found in Appendix B.

At energies above 10 GeV the Quark Gluon String Precompound (QGSP) model was applied which models inelastic hadronic collisions of neutrons, protons, pions, and kaons. This model is composed of several components handling various parts of a high-energy interaction. The Quark-Gluon String component models the formation of strings in an initial hadron-nucleon collision inside a nucleus. The subsequent fragmentation of strings into hadrons is handled by the Quark-Gluon String fragmentation model. The de-excitation of the remnant nucleus after the initial collision is finally handled by the precompound component. Further information on the QGSP model may be found in *GEANT4 Collaboration* (2009a).

As it was already the case in the calculations of the response functions of Bonner spheres presented in Chapter 3, the energy range from 20 MeV to 10 GeV, where spallation processes are induced, is very important. Also for the particle transport simulations in the atmosphere two different intra-nuclear cascade models were used, namely the Bertini model included in the GEANT4 INC framework `G4CascadeInterface` and the Binary INC model contained in `G4BinaryCascade`. Both INC frameworks can handle incident protons, neutrons, pions, kaons, and hyperons and come along with their own models for the pre-equilibrium stage, fission, Fermi break-up, evaporation, and final nucleus de-excitation to describe spallation processes. For simplicity, however, it is only referred to the Bertini (BERT) and Binary (BIC) INC models in the following. Specific features and differences of these hadronic frameworks were summarized in Chapter 3.3, and a more detailed description is given in Appendix B.

The detailed transport of low-energy neutrons and isotope production was treated in a data-driven approach using the G4NDL cross section library v. 3.13 and the high-precision models (`G4NeutronHP`). These cross sections are mainly based on the ENDF/B-VI evaluation (*McLane*, 1991; *MacFarlane*, 1994a), and the high-precision modeling of neutrons contains elastic scattering based on the free gas approximation, inelastic scattering with tabulated final state information, capture, and fission.

A major weakness of the hadronic framework offered in GEANT4 is the incapacity of modeling inelastic nucleus-nucleus collisions at energies above 10 GeV per nucleon. This in turn means that the transport of He nuclei is restricted to energies below 40 GeV which is by far not sufficient for the simulation of galactic cosmic radiation. So far, only the Japanese Monte Carlo code PHITS (*Niita et al.*, 2010) is able to handle nucleus-nucleus collisions at higher energies with its JQMD/JAM model. *Koi et al.* (2003) developed an interface between GEANT4 and the JQMD/JAM model of the PHITS code. Unfortunately, this interface is not part of the official GEANT4 collaboration work and, thus, not part of the official GEANT4 release. However, *Sihver et al.* (2008) explicitly studied the differences in simulation results of cosmic radiation in the atmosphere when replacing He nuclei by free nucleons (2p2n approximation) and transporting them with regular GEANT4 physics instead of using the interface to the JQMD/JAM model. They found that results in secondary particle fluences are only influenced at very high altitudes above about 40 km. At these altitudes in the 2p2n approximation neutron fluences are strongly enhanced above a few hundreds of MeV due to primary source neutrons which have not yet suffered a significant energy loss. At altitudes below about 20 km, on the other hand, the 2p2n approximation has been found to be in very good agreement with results from the JQMD/JAM model. Therefore, in the frame of the present work the 2p2n approximation was used to determine the radiation environment in the lower atmosphere.

For electromagnetic interactions the well-validated standard physics offered in GEANT4 was used. This comprises standard handling of basic processes for electrons, positrons, photons, and ions including Compton scattering, photoelectric effect, pair production, muon-pair production for photons, δ-electron production, Bremsstrahlung, Čerenkov radiation, and annihilation. Bremsstrahlung, capture, and annihilation for muons as well as ionization processes for muons, electrons, positrons, and other charged particles were explicitly assigned in addition since they are handled in separate GEANT4 classes. The same is valid for multiple scattering of muons, electrons, positrons, and other charged particles. Based on the theory of *Lewis* (1950), special GEANT4 classes deliver corrections for path lengths and lateral displacements of multiply scattered charged particles. Further details on the electromagnetic physics applied may be found in Appendix B.

In order to increase the computational efficiency, a certain production cutoff in range can be set for electrons, positrons, and photons. In particular for simulating the rather large geometry of the Earth's atmosphere this has to be considered. In any material the cutoff value is translated to an energy below which the continuous slowing down approximation is used and no secondary particles are produced. The particle then looses its remaining kinetic energy continuously along the track (see e.g. *GEANT4 Collaboration*, 2009b). In the atmosphere the density of the same material strongly varies in different parts of the geometry, and basically the whole geometry is of interest. It is, therefore, not feasible to set an overall cutoff in range as the mean free path of a particle with given energy strongly varies within the geometry. Instead, it is much more feasible to set an overall cutoff in atmospheric depth. For this reason, in each of the 100 atmospheric layers corresponding to about 10 g/cm^2 an overall production cut value of 0.5 g/cm^2 was translated to a layer-specific cut in range. This allows to increase the simulation performance by approximately 10% without loosing necessary information.

5.3.3 Primary cosmic ray spectra

Calculated secondary particle spectra induced by galactic cosmic rays crucially rely on the primary spectra. In Chapter 2.1.1 an extensive comparison of models describing the galactic cosmic ray particle intensities near Earth with high-precision measurements was done. It turned out that the local interstellar spectrum by *Burger et al.* (2000) and the model for the heliopsheric modulation developed by *Usoskin et al.* (2005, 2011) agrees best with measurements of protons and helium nuclei near Earth at all heliospheric modulation strengths. Therefore, these proton and helium spectra were used in the present work to calculate secondary particle fluxes and the corresponding dose quantities at modulation potentials of 250 MV, 465 MV, 800 MV, 1200 MV, and 1500 MV, i.e. covering a complete solar cycle. Due to the small particle numbers and the very short mean free paths, galactic cosmic ray nuclei heavier than He do not significantly contribute to the radiation environment in the lower atmosphere. Their contributions were, therefore, discarded in the present work.

For the calculation of secondary cosmic radiation during GLEs, primary proton spectra derived from various authors were used. Specific characteristics of GLE spectra such as spectral shape and intensity are discussed in the corresponding sections. In contrast to the differential galactic primary spectra used, which are given as a function of kinetic energy E_k (see Equation 2.7), differential proton spectra during GLEs are usually given as a function of rigidity R. To simulate these spectra they have to be converted into a function of kinetic energy. Applying basic relativistic calculus, the rigidity is connected to the total energy E of a particle via

$$R = \frac{pc}{|q|} = \frac{\sqrt{E^2 - m_0^2 c^4}}{Ze} = \frac{\sqrt{E_k(E_k + 2E_0)}}{Ze}, \tag{5.2}$$

where m_0 denotes the rest mass and E_0 the rest energy (also see Appendix A.1). With this equation a differential spectrum with respect to the kinetic energy $j(E_k)$ can finally be calculated from a rigidity spectrum $j(R)$:

$$j(E_k) = \frac{dJ(E_k)}{dE_k} = \frac{dJ(R)}{dR} \cdot \frac{dR(E_k)}{dE_k} = j(R) \cdot \frac{E_k + E_0}{Ze\sqrt{E_k(E_k + 2E_0)}}. \tag{5.3}$$

In order to implement primary spectra in kinetic energy in GEANT4, they were binned and read from a file during initialization of a run. The binned spectra were then integrated and normalized to unity. The resulting probability distribution $P(E_k)$ between zero and one resembles the amount of flux contained in each energy bin E_k^i. By throwing a random number $\eta \in [0, 1[$ the primary spectra were then sampled during runtime:

$$P(E_k) = \eta \qquad \Rightarrow \qquad E_k \in [E_{k,min}^i, E_{k,max}^i[. \tag{5.4}$$

Within each bin the spectrum was assumed to be uniform, and the kinetic energy E_k for each primary in the simulation was finally determined by throwing a second random number $\kappa \in [0, 1[$ to define an energy between the boundaries of the energy bin:

$$E_k = E_{k,min}^i + \kappa \cdot (E_{k,max}^i - E_{k,min}^i). \tag{5.5}$$

In this way both the proton and helium spectra were sampled in a single run. As argued in the previous section, the 2p2n approximation of alpha particles had to be used due to a lack of models describing nucleus-nucleus collisions at sufficiently high energies. Therefore, similar to the approach of sampling a single spectrum, proton and helium spectra were shot according to the probability distribution given by the corresponding integral intensities (j_{proton}, j_{helium}). To be more specific, a random number $\varepsilon \in [0, 1[$ was thrown to decide which of the two spectra serves to determine the kinetic energy of the next primary:

$$\varepsilon = \begin{cases} < \frac{j_{proton}}{j_{proton}+j_{helium}} & \Rightarrow \quad \text{proton spectrum} \\ \geq \frac{j_{proton}}{j_{proton}+j_{helium}} & \Rightarrow \quad \text{helium spectrum} \end{cases} \tag{5.6}$$

If the helium spectrum was chosen, either a proton or a neutron was shot with equal probabilities.

For the computation of secondary particle spectra at different vertical effective cutoff rigidities the corresponding cutoff values in kinetic energy were calculated using Equation 5.2, and the primary spectra were only sampled at higher energies. In this way, calculations were performed covering the whole range of cutoff rigidities from 0 GV to 17 GV.

5.3.4 Source and normalization of results

For the specification of the source in the GEANT4 calculations as well as for the normalization of the Monte Carlo results certain boundary conditions have to be fulfilled. If not stated otherwise, an isotropic primary radiation field impinging on the atmosphere was simulated. An isotropic flux on a flat surface requires a special sampling of momentum directions and start coordinates of primary particles. This is due to the fact that a flat surface is only exposed to the full flux of particles having a momentum direction parallel to the surface's normal vector. The flux of particles arriving from non-vertical directions is reduced by the cosine of the zenith angle θ between incoming direction and normal vector. In optics the analog phenomenon is known as Lambert's cosine law.

In order to account for the cosine law, the momentum directions given in polar coordinates (θ, ϕ) on the unit sphere have to be sampled with random numbers $\zeta_1, \zeta_2 \in [0, 1[$ as described e.g. in *Ferguson* (2000)

$$\phi = \zeta_1 \cdot 2\pi \tag{5.7}$$

$$\theta = \arcsin\left(\sqrt{\zeta_2}\right). \tag{5.8}$$

The corresponding Cartesian coordinates are then easily calculated via regular coordinate transformation.

After the definition of a primary's momentum according to the prescribed method, a random location on top of the atmosphere has to be chosen in order to resemble an isotropic particle flux. For this purpose, the start coordinates were homogeneously distributed on a flat disk with radius $r = 3000$ km on top of the atmosphere. Choosing a source size smaller than the full geometry additionally reduces boundary effects such as particles escaping from the geometry. The Cartesian start coordinates (x, y) can then be sampled during runtime with independent random numbers $\zeta_3, \zeta_4 \in [0, 1[$ as follows

$$x = r \cdot \sqrt{\zeta_3} \cdot \cos(2\pi\zeta_4) \tag{5.9}$$

$$y = r \cdot \sqrt{\zeta_3} \cdot \sin(2\pi\zeta_4). \tag{5.10}$$

The cosine law described above also has to be considered in the normalization of the simulation results. Both galactic and solar primary cosmic ray spectra are generally given as differential spectra with respect to the solid angle $j(E_k, \Omega, t) = d^4N/(dtdAd\Omega dE_k)$. Taking the cosine law into account, the normalization factor for an isotropic flux on a flat surface is given as

$$\int_{E_{min}}^{E_{max}} \int_0^{2\pi} \int_0^{\pi} j(E_k, \Omega, t) \cos(\theta) \sin(\theta) d\theta d\phi dE_k = \tag{5.11}$$

$$= \pi \cdot \int_{E_{min}}^{E_{max}} j(E_k, t) dE_k = \pi \cdot \dot{\Phi}_p \ ,$$

where $\dot{\Phi}_p$ denotes the total primary fluence rate in units of particles/(cm^2 s) given by the sum of all primary spectra considered in the simulation (i.e. proton and helium spectra in case of galactic cosmic rays). The output ϕ in units of particles/cm^2 of each fluence scorer is finally normalized to obtain a meaningful particle fluence rate $\dot{\Phi}$ according to

$$\dot{\Phi} = \frac{\pi \cdot \dot{\Phi}_p \cdot \phi}{(N_p/A)}, \tag{5.12}$$

where $A = \pi \cdot r^2$ denotes the cross sectional area of the source ($r = 3000$ km) and N$_p$ the number of primary particles simulated in a single run.

5.4 Secondary particles induced by galactic cosmic radiation

In the following paragraphs the results of the particle transport calculations for galactic cosmic radiation performed with GEANT4 and two different intra-nuclear casccade models at high energies (Bertini and Binary INC) are presented. A detailed inter-comparison with computations using the FLUKA Monte Carlo code by *Roesler et al.* (1998, 2002) and *Heinrich et al.* (1999) is carried out. Additionally, predictions of secondary cosmic ray particle spectra from the PHITS-based Analytical Radiation Model in the Atmosphere[3] (PARMA) developed by *Sato et al.* (2006, 2008) are compared. In both the FLUKA and the PHITS calculations different models for the heliospheric modulation and, accordingly, different primary spectra were used. While *Roesler et al.* (1998) used proton and He spectra given by the *Badhwar and O'Neill* (1996) model, *Sato et al.* (2008) used a modified version of the primary GCR model of *Nymmik et al.* (1992) for all ion species up to Nickel. Differences in these primary spectra were extensively studied in Chapter 2.1, and it was shown that the *Badhwar and O'Neill* (1996) and the *Nymmik et al.* (1992) models predict much higher H and He intensities near Earth than observed. The modified version used by *Sato et al.* (2008), on the other hand, agrees very well with the model of *Burger et al.* (2000) and *Usoskin et al.* (2005, 2011) used in the GEANT4 calculations (*T. Sato* priv. comm.). Numerical values of the modulation potential, however, depend on the models, and there is no well-defined relation among them. Thus, minor uncertainties in secondary particle spectra due to slightly differing solar modulation potentials may arise. If not stated otherwise, values of the modulation parameter are based on the reconstruction of *Usoskin et al.* (2005, 2011) in the following.
Since the primary GCR intensity on top of the atmosphere is largest at solar minimum conditions ($\phi \approx 465$ MV) and 0 GV vertical effective cutoff rigidity, the inter-comparison of results obtained by the different MC codes and the two hadronic interaction models in GEANT4 is carried out for these conditions. Accordingly, differences in the results of all codes and models are pronounced most with respect to other solar and geomagnetic conditions. As a result of the deep penetration problem, differences in secondary particle spectra strongly vary with atmospheric depth. Since one major goal of the present work was to determine dose rates at aircraft altitudes, the features of secondary particle spectra induced by galactic cosmic radiation are exemplary discussed for an atmospheric depth of 250 g/cm^2 ($\approx$ 10.5 km a.s.l.), and the vertical development in the atmosphere is discussed by means of energy integrated fluence rates.

5.4.1 Protons

As described in more detail in Chapter 6, protons significantly contribute to the overall effective dose at aircraft altitudes. In principal, atmospheric protons originate from three different sources. First, primary protons are able to reach certain atmospheric depths if their kinetic energy is sufficiently high to outweigh energy losses due to electromagnetic and hadronic interactions. Therefore, this component is dominating at very high altitudes where the mass shielding provided by the atmosphere is rather low. To survive down to sea-level a primary

---

[3] http://phits.jaea.go.jp/expacs

proton must have a minimum kinetic energy of about 2.5 - 3 GeV. On the other hand, the threshold kinetic energy to reach typical aircraft altitudes of 10 km ($\approx$ 265 g/cm^2) is only about 1 GeV for protons (see e.g. *Grieder*, 2001). Accordingly, primary protons significantly contribute to the total proton flux and the corresponding dose equivalent in aviation. The second source of protons in the atmosphere is the fragmentation of heavy galactic cosmic ray nuclei in collisions with atoms in the air. As already stated at the beginning of this chapter, the mean free path of heavy ions in air is in the order of 15 - 30 g/cm^2, and nearly all of them are completely fragmented in the first collision. These fragmentation processes, could not be included in the computation of secondary cosmic radiation due to a lack of nucleus-nucleus interaction models at sufficiently high energies. This component, however, only slightly contributes to the overall proton flux at very low atmospheric depths, whereas the radiation environment at aircraft altitudes and below is almost unaffected. Additionally to the two prescribed sources, protons are generated in inelastic collisions of energetic primary and secondary particles with nuclei in the atmosphere. This includes break-up processes, as well as evaporation from highly-excited target nuclei. For protons with momenta less than 1 GeV/c, these processes are a major source at high atmospheric depths (see e.g. *Nakamura et al.*, 2010).

In the top panel of Figure 5.3 omnidirectional proton fluence rates calculated in the present work using the Bertini INC (GEANT4-BERT) and the Binary INC (GEANT4-BIC) model are compared with results from *Roesler et al.* (1998) and *Sato et al.* (2008) at 250 g/cm^2, solar minimum ($\phi \approx 465$ MV), and a vertical effective cutoff rigidity $R_C = 0$ GV. The spectral fluence rate distributions are shown in lethargy representation ($d\dot{\Phi}/d\ln(E)$) in order to pronounce the spectral features as well as the differences between the calculations. As pointed out above, protons with kinetic energies above about 1 GeV are predominantly primary protons at this altitude, hence showing the characteristic course of a power law in kinetic energy ($\propto E_k^{-\gamma}$ see Chap. 2.1). At lower energies losses per unit path length due to electromagnetic interactions increase with decreasing energy. This results in a strongly decreasing proton flux at low energies.

Obviously, proton spectra obtained from all MC codes are largely consistent at typical aircraft altitudes. This is particularly true for energies below 1 GeV where electromagnetic interactions dominate. In contrast, at higher energies some differences are observed. Comparison of the two GEANT4-based calculations shows the impact of different hadronic models on the simulation results, where the Binary INC model leads to significantly enhanced proton fluence rates at high energies. The somewhat larger fluence rates obtained by *Roesler et al.* (1998) with the FLUKA code may be due to different hadronic models and somewhat larger primary proton intensities predicted by the *Badhwar and O'Neill* (1996) model.

With increasing atmospheric depth, however, the differences in the calculations become more pronounced. This is obvious from the bottom panel of Figure 5.3 which shows the energy integrated fluence rates as a function of atmospheric depth at solar minimum and 0 GV cutoff. The largest differences in integral fluxes of more than a factor of three at sea-level occur between the two GEANT4 calculations. This reveals that the hadronic interaction model used for the computation has the the biggest impact. On the other hand, minor differences in the geometry of the atmosphere or different primary GCR spectra are less important, at least at high atmospheric depths.

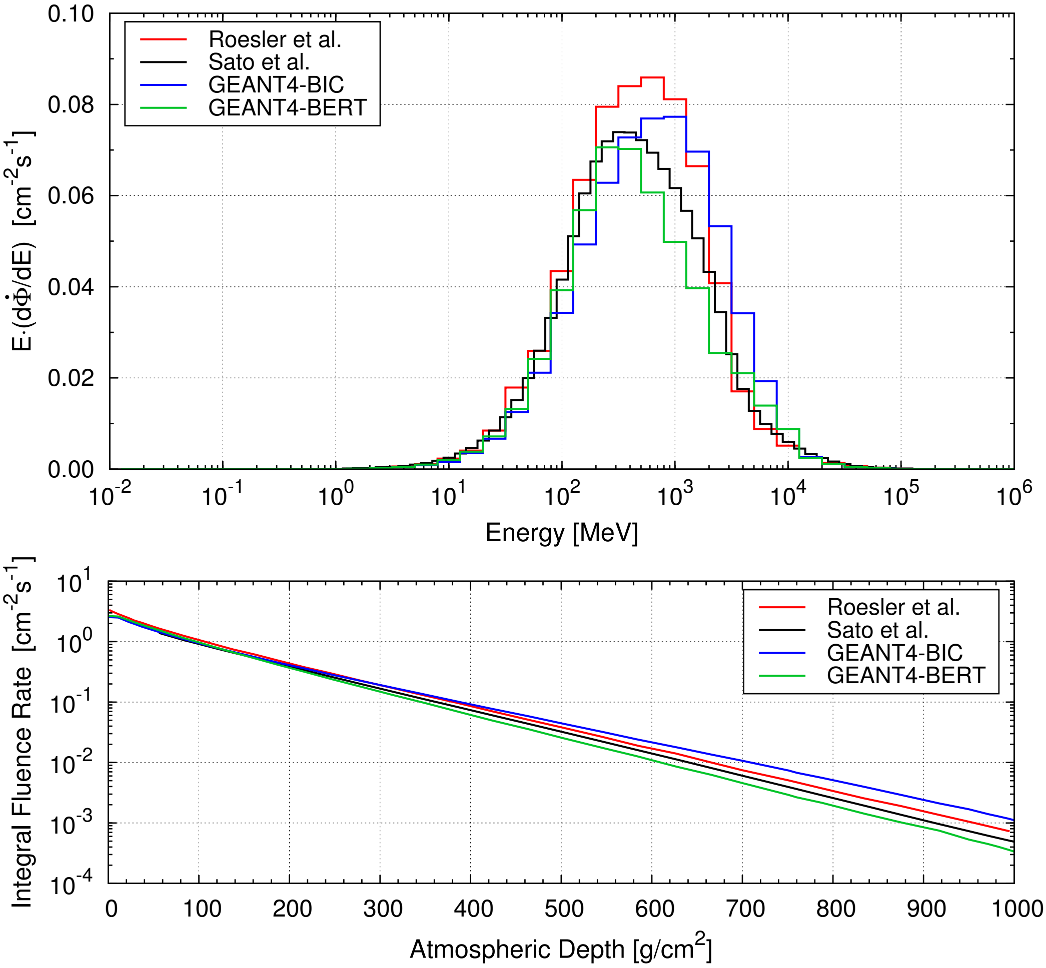

FIGURE 5.3: Omnidirectional fluence rate of protons at an atmospheric depth of 250 g/cm^2 ($\approx$ 10.5 km), 0 GV cutoff rigidity, and solar minimum conditions (top panel). Transport calculations from the present work using GEANT4 are compared with FLUKA (*Roesler et al.*, 1998) and PHITS-based results (*Sato et al.*, 2008). The bottom panel shows energy integrated fluence rates as a function of atmospheric depth.

The only way of determining which of the GEANT4 hadronic frameworks might give the best estimate for the proton intensities in the atmosphere is a comparison with experimental data. Several accurate measurements have been performed for atmospheric protons e.g. by *Kocharian et al.* (1959) or *Barber et al.* (1980). To check the consistency of MC simulations with experimental data, recently performed high-precision measurements with the Balloon-borne Experiment with a Superconducting Spectrometer (BESS) reported in *Sanuki et al.* (2003) were chosen as an example. This high-resolution spectrometer was designed to precisely study primary cosmic rays on top of the atmosphere (*Sanuki et al.*, 2000; *Haino et al.*, 2004), but it was also in operation on ground for studies of atmospheric cosmic ray events. The differential proton intensities reported in *Sanuki et al.* (2003) were measured at the Mt. Norikura Observatory of the University of Tokyo, Japan. The observatory is located at an altitude of 2770 m above sea-level corresponding to 742 g/cm^2. The vertical effective

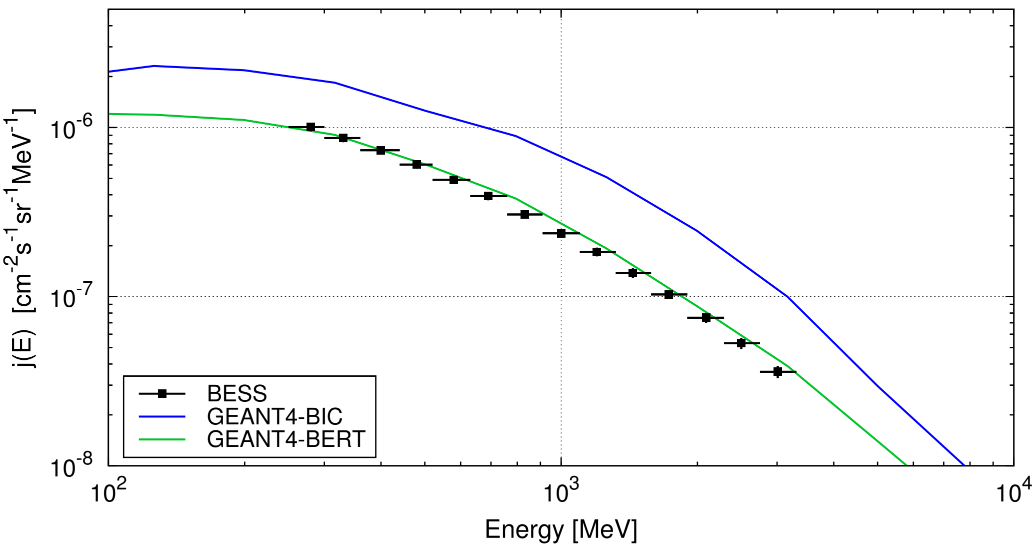

FIGURE 5.4: Differential proton intensities with zenith angle $\cos(\theta) \geq 0.95$ measured at 742 g/cm^2, 11.2 GV cutoff, and $\phi = 691$ MV with the BESS spectrometer by *Sanuki et al.* (2003) in comparison with MC calculations from the present work.

cutoff for this location is 11.2 GV, and the measurements were performed during September 1999 at a moderate solar modulation strength of $\phi = 691$ MV following *Usoskin et al.* (2011). The zenith angle θ for protons in this experiment was limited to $\cos(\theta) \geq 0.95$, corresponding to approximately 18.2°. In order to accurately compare MC calculations from the present work with the BESS measurements, all these conditions were exactly simulated. The comparison of measured differential proton intensities $j(E) = d^2\dot{\Phi}/(dEd\Omega)$ and those calculated in the present work is shown in Figure 5.4, where the excellent agreement of results obtained with the Bertini INC interaction model is evident. Results using the Binary INC, on the other hand, significantly overestimate the observations. From this comparison, several important conclusions can be drawn. First of all, it shows an overall accuracy of the particle transport calculations and the validity of the assumptions made on the simulated geometry, the composition and density profile of the atmosphere, as well as the source spectra with the 2p2n approximation for He nuclei and the corresponding sampling method of primaries during the simulation. Since the cutoff for the experiment is with a value of 11.2 GV rather high, it can additionally be concluded that the concept of the vertical effective cutoff provides an accurate approximation, at least for atmospheric protons with zenith angles $\cos(\theta) \geq 0.95$. Moreover, especially in the 2p2n approximation used in the present work, protons are most important for the simulation of all other particle species. At the atmospheric depth considered, the integral proton fluxes given by the two GEANT4 models differ by a factor of about 2.5 (also see bottom panel of Fig. 5.3). Given the fact that such large differences are only observed in protons fluxes, the comparison with the high-precision BESS measurements strongly indicates that the Bertini INC model provides a much better estimate for secondary cosmic ray particles in the atmosphere. As discussed subsequently, however, the differences in proton fluxes do not necessarily translate to the same differences in fluence rates of all other particles.

5.4.2 Neutrons

The most important secondary particles in terms of contributions to effective dose in the lower atmosphere are neutrons. These are generated in spallation reactions induced by inelastic collisions of primary GCR particles with nuclei in the atmosphere. In such reactions, fast neutrons with energies above about 10 MeV and evaporation neutrons with energies between several tens of keV and 10 MeV are produced.

The fast neutrons result from direct interactions of incident primary particles with nuclei and can either be fragments of the projectile or nucleons emitted from the target as a result of intra-nuclear cascades. The production of high-energetic neutrons is, therefore, mainly in forward direction. The resulting spectral fluence rate resembles the course of the primary spectrum, i.e. it steeply decreases with increasing energy following a power law in energy. Since the fast neutrons can carry a large fraction of the projectile's energy, they significantly contribute to the hadronic cascade in an extensive air shower. After an initial collision, the remaining target nucleus is left in an highly excited state and lowers its excessive energy by evaporation of nucleons with energies of 10^{-3} - 10 MeV. In contrast to fast neutrons created in the initial collision, evaporation neutrons follow an isotropic angular distribution. As uncharged particles, neutrons do not lose energy in ionization processes but are only subject to strong interactions. Furthermore, due to the rather long neutron mean lifetime of about 885.7 s at rest (*Nakamura et al.*, 2010), decay into protons is almost negligible. Therefore, neutrons produced in the atmosphere can easily reach sea-level.

In the top panel of Figure 5.5 omnidirectional neutron fluence rates calculated in the present work are compared with results from *Roesler et al.* (1998) and *Sato et al.* (2008) (250 g/cm^2, solar minimum, 0 GV cutoff). In the lethargy representation three characteristic spectral features are obvious. At energies above about 10 - 20 MeV the so-called cascade peak emerges. This peak results from a convolution of the spectrum of fast neutrons which steeply decreases with increasing energy and a broad minimum of the total interaction cross section of all elements constituting the atmosphere, i.e. N, O, and Ar (see e.g. *Abfalterer et al.*, 2001). A second peak appears around 1 - 2 MeV, the evaporation peak, which is a direct result of the evaporation processes described above. Evaporated neutrons follow a Maxwell-Boltzmann distribution in the energy range of 10^{-3} - 10 MeV, with a maximum around 1 - 2 MeV. In the epithermal region below about 0.1 MeV elastic scattering is the dominating interaction mechanism. Following classical collision theory, both the average and the maximum energy transfer of a neutron is proportional to the neutron's kinetic energy (see Eq. 3.1). Higher energetic neutrons, thus, suffer large energy-losses in collisions resulting in a steeply decreasing differential neutron flux with increasing kinetic energy. This in turn leads to a nearly horizontal course of the neutron spectrum in the lethargy representation. As low-energy neutrons interact with the nitrogen isotope ^{14}N, they produce the cosmogenic nuclide ^{14}C via $^{14}_{7}\mathrm{N(n,p)}^{14}_{6}\mathrm{C}$. At low energies the cross section of this reaction is inverse proportional to the neutron's velocity and has a rather high value of approximately 1.9 barn at thermal energies. Free-in-air neutron fluence rate distributions, thus, do not contain thermal neutrons as they are all converted to ^{14}C.

Additionally to the prescribed macroscopic spectral features, a resonance-like fine structure is noticeable in the evaporation peaks of the highly resolved calculations from the present work and from *Roesler et al.* (1998). These structures are mainly related to maxima and

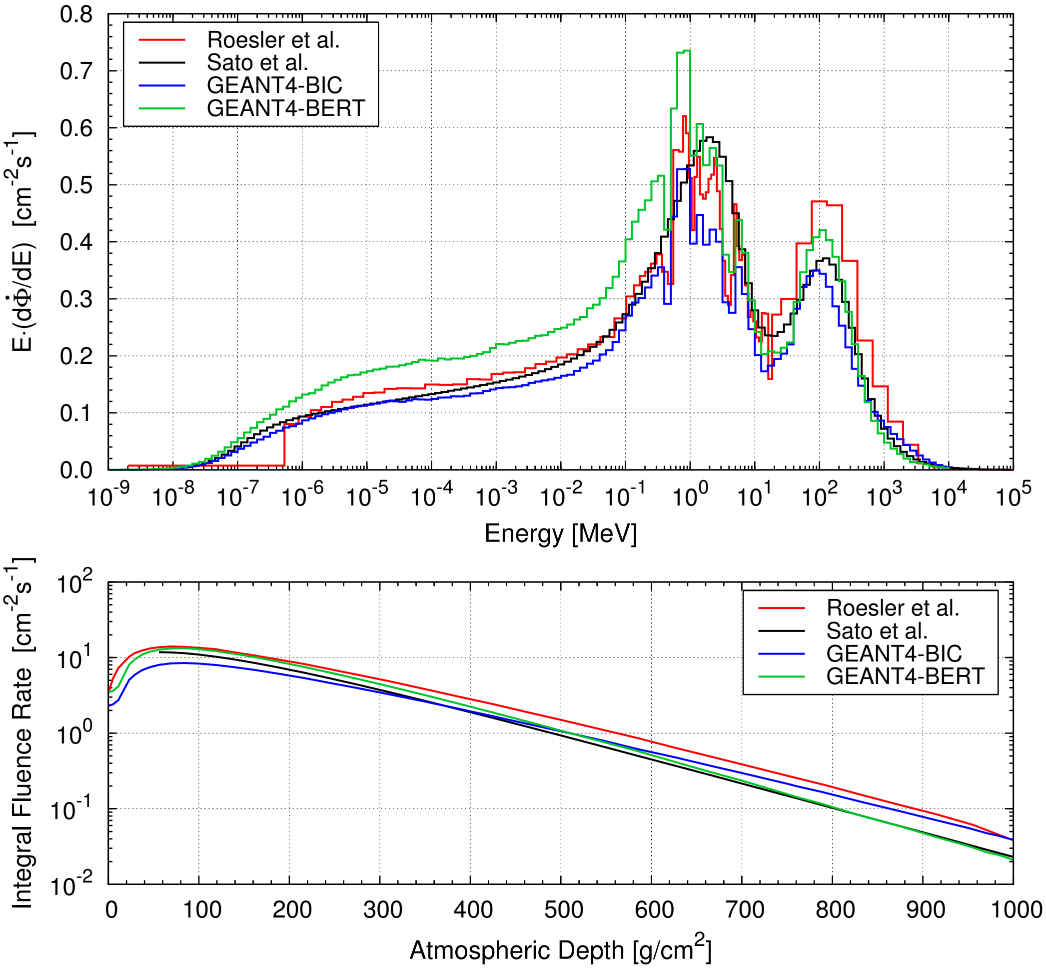

FIGURE 5.5: Omnidirectional fluence rate of neutrons at an atmospheric depth of 250 g/cm^2 (≈ 10.5 km), 0 GV cutoff rigidity, and solar minimum conditions (top panel). Transport calculations from the present work using GEANT4 are compared with FLUKA (*Roesler et al.*, 1998) and PHITS-based results (*Sato et al.*, 2008). The bottom panel shows energy integrated fluence rates as a function of atmospheric depth.

minima in reaction cross sections of nitrogen and to a minor degree of Oxygen. The dips in neutron fluence rates around 500 keV, 1.2 MeV, and 4 MeV, for example, are related to pronounced maxima in the ^{14}N absorption cross section.

The overall agreement of all MC codes shown in Figure 5.5 is fully satisfying from epithermal up to relativistic energies, although the Bertini INC seems to result in somewhat higher fluence rates with respect to the Binary INC at the altitude shown. Particularly in case of atmospheric secondary neutrons, however, it must be emphasized that the differences in calculated fluence rates by using different MC codes and hadronic models strongly depend on atmospheric depth. This becomes obvious from the bottom panel of Figure 5.5 which shows the energy integrated fluence rates as a function of atmospheric depth. Below about 100 g/cm^2 the characteristic increase in the flux is observed as a result of the developing hadronic cascade. The Pfotzer maximum around 80 - 85 g/cm^2 (≈ 17 - 18 km) agrees very well for all codes and models. On the other hand, with increasing depth the different codes seem to model neutron production in the evolving cascade differently. This becomes manifest in the comparison of the two GEANT4 results, where the integral fluxes intersect each other at about 500 g/cm^2 ($\approx$ 6 km). At high altitudes the GEANT4-BERT results agree very well with results from *Roesler et al.* (1998), whereas they are fully consistent with claculations from *Sato et al.* (2008) at sea-level. Concerning the GEANT4-BIC results, the situation is reversed. This behavior is only observed at secondary neutrons and may be attributed to somewhat different neutron yields in hadronic interactions modeled by the Binary and the Bertini INC hadronic frameworks of GEANT4.

Also for the validation of neutron fluence rates, a comparison with measurements is required. Unfortunately, accurate experimental data covering the whole energy region are scarce for neutrons due to a lack of precise instruments. As described in Chapter 3, Bonner sphere spectrometers are rather suited for that purpose. *Goldhagen et al.* (2004) measured the energy spectrum of cosmic ray induced neutrons on an airplane over a wide range in altitude and latitude using an extended BSS. Figure 5.6 shows as an example the spectrum reported by *Goldhagen et al.* (2004) for 201 g/cm^2 (11.9 km), 4.3 GV cutoff rigidity, and solar minimum conditions (ϕ = 405 MV) in comparison with spectra calculated by means of GEANT4 applying the Bertini or the Binary INC model, respectively. Apparently, for the conditions shown both calculations agree rather well with experimental data in terms of both spectral shape and absolute intensity.

In Table 5.1 measured energy-integrated neutron fluence rate values for all geomagnetic conditions and altitudes as reported by *Goldhagen et al.* (2004) are contrasted with results of the present work. Calculated neutron intensities were interpolated to obtain values at the specific atmospheric depths and cutoffs. Furthermore, fluxes at sea-level were computed with a granite soil and 5 cm of water on top in order to approximately take influences of the envi-

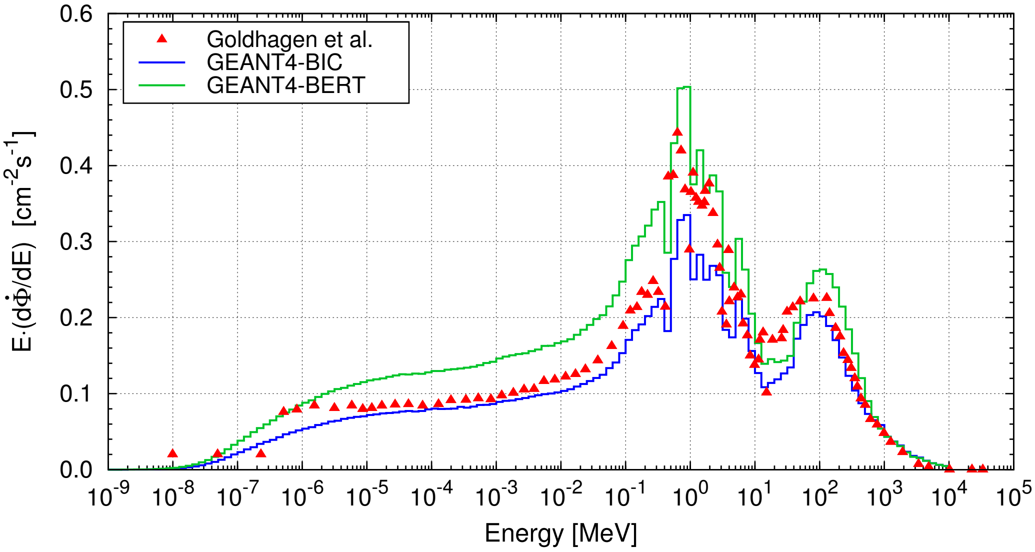

FIGURE 5.6: Neutron spectrum measured by *Goldhagen et al.* (2004) during solar minimum (ϕ = 405 MV) at 201 g/cm^2 (11.9 km) and 4.3 GV cutoff rigidity in comparison with spectra calculated by means of GEANT4 applying the Bertini or the Binary INC model, respectively.

TABLE 5.1: Integral neutron fluence rates measured by *Goldhagen et al.* (2004) at various locations in comparison with calculated quantities.

Atm. Depth [gcm^{-2}]	Altitude [km]	Cutoff [GV]	INTEGRAL NEUTRON FLUENCE RATE [cm^{-2}s^{-1}]		
			Goldhagen	GEANT4-BERT	GEANT4-BIC
53.3	20.3	11.6	1.24	1.38	0.87
56	20.0	0.8	9.8	12.43	7.75
101	16.2	0.7	9.5	12.61	8.15
201	11.9	4.3	3.4	4.32	2.96
1030	0.0	2.7	0.0126	0.0131	0.0235

ronment at low energies into account (see section 5.5). From this comparison it turns out that integral quantities obtained with both GEANT4 hadronic models reasonably agree with the measurements. The Binary INC calculations are largely compatible with measurements at medium and high altitudes but significantly overestimate the neutron flux at sea-level. Vice versa, calculations using the Bertini INC agree very well with measurements at sea-level and very low atmospheric depths, but significantly overestimate the observations at medium to high altitudes.

Unfortunately, *Goldhagen et al.* (2004) do not provide uncertainties for the experimental data. Based on the work presented in Chapters 3 and 4, however, the uncertainty associated with BSS data is expected to be in the order of at least 10%. Uncertainties in responses result in a about 5% uncertainty in integral fluence rates (see Chapter 3) and another 5% systematic uncertainty may arise from differences in various unfolding procedures (see Chapter 4). An unknown uncertainty due to averaging over certain atmospheric depths and cutoffs may add to this. Therefore, it can be concluded that both hadronic frameworks and INC models (Bertini, Binary) used in the present work are consistent with the experimental data reported by *Goldhagen et al.* (2004). A more detailed comparison of calculated and measured neutron fluence rate distributions at sea-level follows in section 5.5 by using BSS measurements performed in the present work.

5.4.3 Charged pions

As argued in section 5.2, pions are of major importance for the overall development of an extensive air shower since they give rise to the muon and also the electron-photon component. Therefore, fluence rates of charged pions are discussed next, although their direct contributions to effective dose rates in the atmosphere are of minor importance.

The top panel of Figure 5.7 shows spectra of charged pions calculated with GEANT4 in comparison with data from *Roesler et al.* (1998) at 10.5 km altitude, 0 GV cutoff, and solar minimum. Charged pions are mainly produced in inelastic p-p collisions of primary protons with single protons in the nuclear potentials of target nuclei. In such reactions, a larger number of positive elementary particles is produced, because the collision partners have a positive charge excess which is transferred to secondary components (see e.g. *Gaisser*, 1990). The characteristic enhancement of positively with respect to negatively charged pions at low atmospheric depths where most of the pions are produced is well reproduced by all MC codes and models as can be seen in the top panel of Figure 5.7. Pions created in high-energy collisions can carry a large fraction of the projectile's momentum. Thus, the pion spectra show a similar course as the primary proton spectra at high energies. Since the lifetime of charged pions at rest is with a value of about 26 ns (*Nakamura et al.*, 2010) rather short, the low-energy part of the spectra is dominated by the decay of slow pions into muons via $\pi^+ \rightarrow \mu^+ + \nu_\mu$ and $\pi^- \rightarrow \mu^- + \overline{\nu}_\mu$. The decay processes are also the reason for the poor statistics in the MC results with respect to other secondary particle species, which may also be the reason for the outlier in the spectrum of *Roesler et al.* (1998) at about 100 MeV.

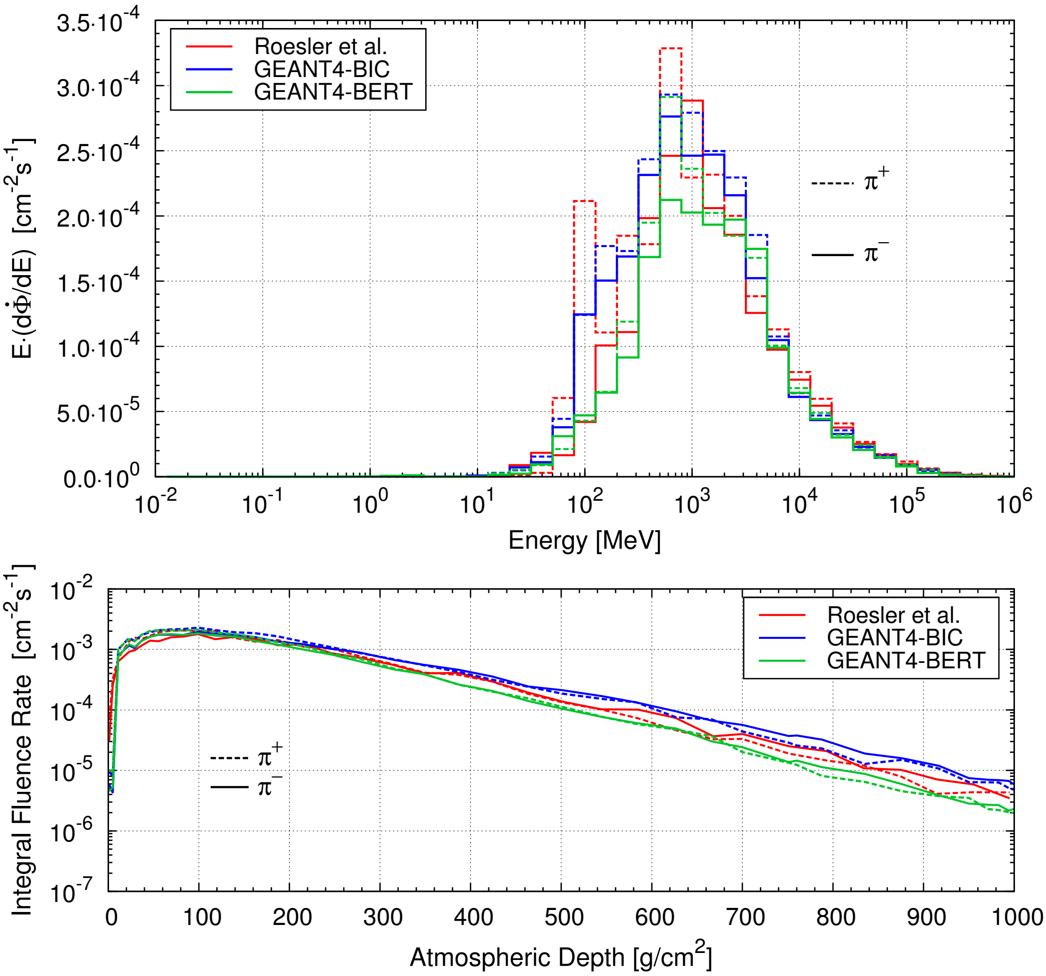

FIGURE 5.7: Omnidirectional fluence rate of charged pions at an atmospheric depth of 250 g/cm^2 ($\approx$ 10.5 km), 0 GV cutoff rigidity, and solar minimum conditions (top panel). Transport calculations from the present work using GEANT4 are compared with results obtained with FLUKA (*Roesler et al.*, 1998). The bottom panel shows energy integrated fluence rates as a function of atmospheric depth.

The comparison of both spectral characteristics (top panel) and energy-integrated fluence rates as a function of atmospheric depth (bottom panel in Fig. 5.7) reveals that results from all calculations are consistent. Pion intensities obtained with the GEANT4-BIC model appear somewhat enhanced at low altitudes which may be attributed to the much higher proton fluence rates given by the Binary INC model. The results of *Roesler et al.* (1998) lie between both GEANT4 calculations again indicating that different primary spectra and geometries play a minor role in the calculation of secondary cosmic radiation.

5.4.4 Muons

Atmospheric muons are a direct consequence of $\pi^{\pm}$ decay since contributions from muon-pair production of photons are very small. Their spectra, accordingly, resemble the course of the pion spectra at high energies. Due to the fact that pions with energies above about 100 GeV undergo hadronic interactions, the muon spectra are somewhat steeper at very high energies. Furthermore, due to the enhancement of positively charged pions, also the positivle charged muon component is somewhat enhanced with respect to negative muons. All these features can be seen in the top panel of Figure 5.8, where results from the present work are compared with FLUKA (*Roesler et al.*, 1998) and PHITS (*Sato et al.*, 2008) calculations. Low-energy muons ($<$ 1 GeV) are subject to electromagnetic interactions such as emission of Bremsstrahlung, ionization, or annihilation in case of μ^{+}. Although major parts of the muons can survive down to sea-level due to time dilation, the low-energy part of the muon spectra is further reduced by decay of muons into electrons and positrons via $\mu^{+} \rightarrow e^{+} + \nu_e + \overline{\nu}_{\mu}$ and $\mu^{-} \rightarrow e^{-} + \overline{\nu}_e + \nu_{\mu}$ (mean lifetime at rest $\approx$ 2.2 μs).

Comparison of both spectral fluence rate distribution (top panel) and energy-integrated muon fluxes (bottom panel in Fig. 5.8) shows remarkable consistency of all MC codes and models over the whole vertical profile of the atmosphere. This indicates that both production and decay processes of pions are modeled in a very coherent manner by all MC codes. Furthermore it can be concluded that the excessive pions observed using the Binary INC with respect to the Bertini INC must be almost completely converted in hadronic interactions. This, in turn, may additionally contribute to the strongly enhanced proton and neutron fluence rates calculated with GEANT4-BIC at sea-level.

Although basically all calculations agree very well, a comparison of calculated muon fluxes with experimental data is straightforward, in particular because many precise muon measurements have been performed during the last decades. As reference measurements, the high-precision experimental muon data reported in *Kremer et al.* (1999) were chosen. These data were measured in the frame of the Cosmic Anti-Particle Ring Imaging Čerenkov Experiment (CAPRICE97), employing a superconducting magnet spectrometer. Also CAPRICE97 was primarily dedicated to balloon-borne cosmic ray studies. The muon data chosen for intercomparison with MC results were measured in Fort Summer, New Mexico, at an altitude of 1270 m (868 g/cm^2) and a cutoff of 4.2 GV during solar minimum conditions in April/May

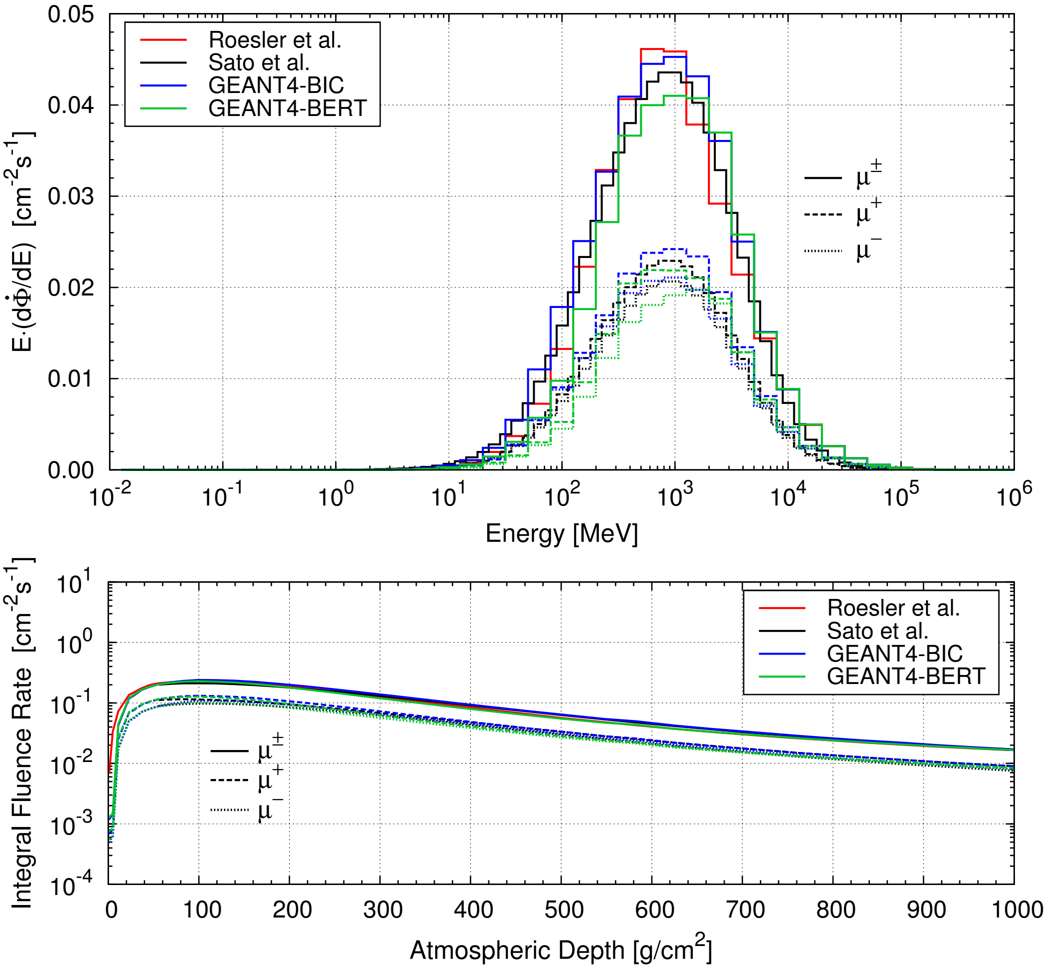

FIGURE 5.8: Omnidirectional fluence rate of muons ($\mu^+ + \mu^-$) at an atmospheric depth of 250 g/cm^2 ($\approx$ 10.5 km), 0 GV cutoff rigidity, and solar minimum conditions (top panel). Transport calculations from the present work using GEANT4 are compared with FLUKA (*Roesler et al.*, 1998) and PHITS-based results (*Sato et al.*, 2008). For PHITS and GEANT4 calculations, μ^+ and μ^- fluence rates are also shown individually. The bottom panel shows energy integrated fluence rates as a function of atmospheric depth.

1997 ($\phi \approx$ 408 MV). The zenith angles were restricted to $\cos(\theta) \geq 0.99$ corresponding to approximately 8°. All these conditions were exactly taken into account in the GEANT4 calculations. These calculations are contrasted with the near-vertical CAPRICE97 data in Figure 5.9 as differential intensities with respect to the momentum $j(p) = d^2\dot{\Phi}/(d\Omega dp)$. Since both GEANT4 results agree very well, the agreement is remarkable for both. The results obtained with the Bertini INC model, however, agree slightly better with the measurements, which is especially the case around the maximum of the distribution at muon momenta of 200 - 2000 MeV/c. This again shows an overall accuracy of the simulation results and indicates that the Bertini model may provide a somewhat more accurate estimate of the radiation environment in the lower atmosphere.

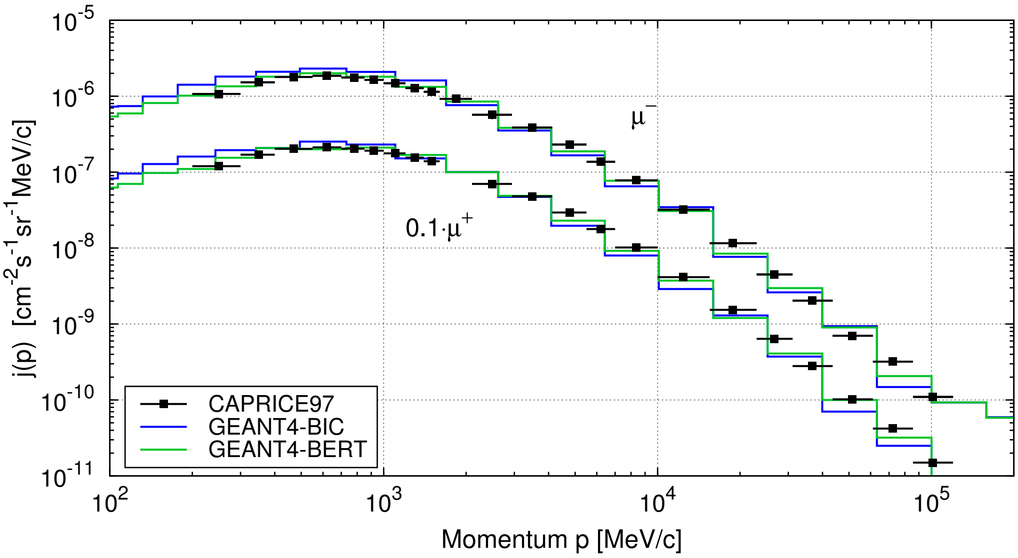

FIGURE 5.9: Near-vertical ($\cos(\theta) \geq 0.99$) differential μ^+ and μ^- intensities with respect to the momentum measured at 868 g/cm^2 ($\approx$ 1270 m), 4.2 GV cutoff, and $\phi = 408$ MV with the CAPRICE97 spectrometer by *Kremer et al.* (1999) in comparison with MC calculations from the present work. Results for μ^+ were scaled with a factor of 0.1 to allow distinction.

5.4.5 Electrons and positrons

In electromagnetic cascades of extensive air showers a variety of electrons and positrons are generated. Example spectra at the same conditions as the particles described previously are depicted in the top panel of Figure 5.10.

Muon decay plays only a minor role in the overall production of $e^{\pm}$ and is only responsible for the very high energy part of the spectra (*Grieder*, 2001). Electron and positron spectra differ quite a lot from each other since the production of positrons fully relies on decay of short-lived particles such as muons and pair-production by high-energy photons. Positrons are further subject to annihilation leading to the decrease below about 20 MeV. Knock-on electrons, on the other hand, are produced in ionization processes of all charged particles in the cascade. Compton electrons further add to this component, which all in all leads to the maximum around 2 - 4 MeV. Contributions of photo-electrons are very low, since the total interaction probability for photons in low proton number material such as N_2 and O_2 is highly dominated by Compton scattering (see e.g. *Turner*, 1995).

The calculated spectral fluence rate distributions in the top panel of Figure 5.10 and the vertical intensity profile shown in the bottom panel agree very well for all codes and models shown. This is expected since electromagnetic processes are very well validated in most MC codes.

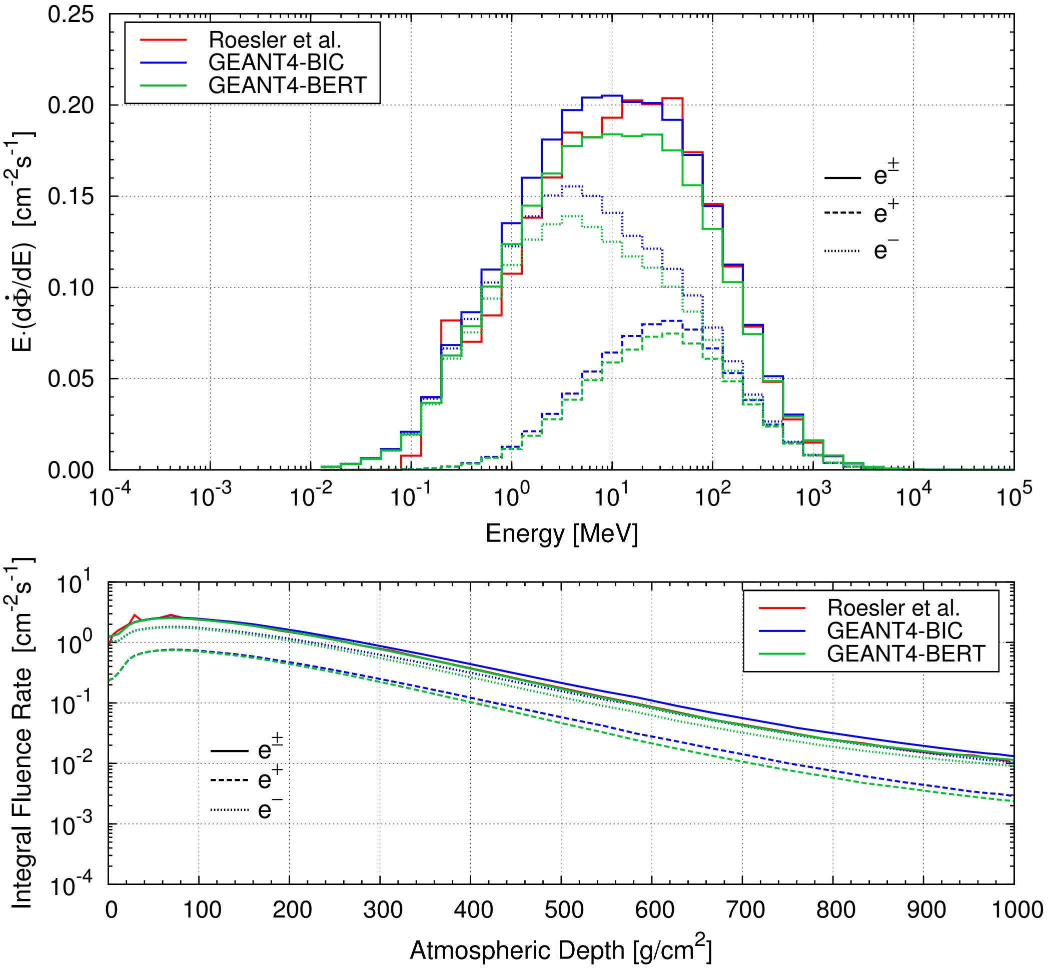

FIGURE 5.10: Omnidirectional fluence rate of electrons and positrons at an atmospheric depth of 250 g/cm^2 ($\approx$ 10.5 km), 0 GV cutoff rigidity, and solar minimum conditions (top panel). Transport calculations from the present work using GEANT4 are compared with FLUKA (*Roesler et al.*, 1998). The bottom panel shows energy integrated fluence rates as a function of atmospheric depth.

5.4.6 Photons

Also photons are produced in a variety of processes in electromagnetic cascades of extensive air showers. The resulting spectral distribution spans energies from several tens of keV to GeV. Example spectra calculated with GEANT4 are depicted in the top panel of Figure 5.10 for 10.5 km altitude, 0 GV cutoff, and solar minimum in comparison with the work of *Roesler et al.* (1998).

The main gamma sources at energies above 10 MeV are decay of π^0 and emission of Bremsstrahlung by electrons and positrons, but also Čerenkov radiation adds at these energies. Bremsstrahlung from e$^-$ is dominating in the range of 1 - 10 MeV, resulting in the plateau where the electron spectrum has a pronounced maximum (see Fig. 5.10). Positron fluence rates in this energy region are already one order of magnitude lower than electron fluxes due to annihilation processes. Annihilation radiation, on the other hand, leads to the sudden increase between 511 keV and the plateau. The photon fluence rates at low energies

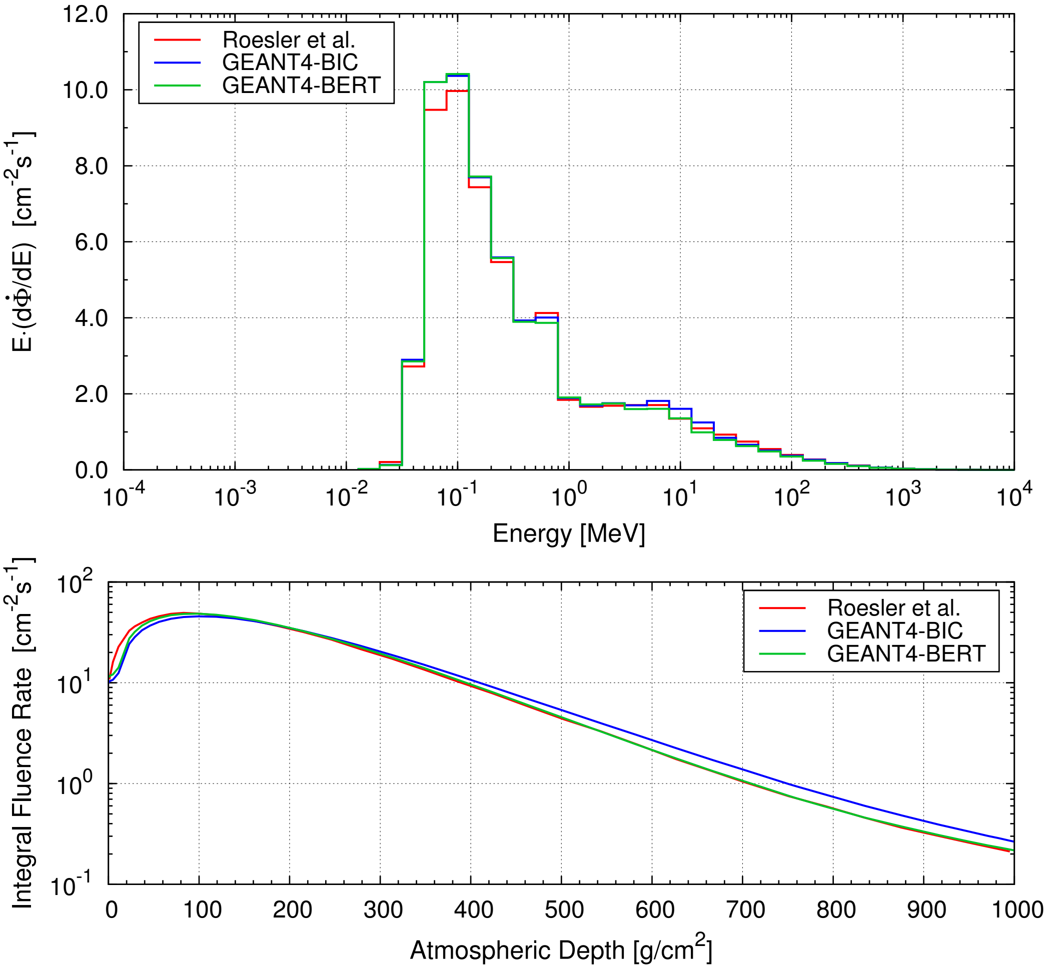

FIGURE 5.11: Omnidirectional fluence rate of photons at an atmospheric depth of 250 g/cm^2 ($\approx$ 10.5 km), 0 GV cutoff rigidity, and solar minimum conditions (top panel). Transport calculations from the present work using GEANT4 are compared with FLUKA (*Roesler et al.*, 1998). The bottom panel shows energy integrated fluence rates as a function of atmospheric depth.

between several tens of keV and 511 keV, which dominate the photon spectrum in terms of absolute photon numbers, result from gamma emission by highly excited remnant nuclei in the atmosphere. As may be found in *Lederer et al.* (1978), energy differences in nuclear levels are in the order of several tens to hundreds of keV. Excited nuclei in the atmosphere tend to stepwise cool down by emitting a lot of lower energetic gammas instead of a few high energetic ones. The latter are rarely produced when a nucleus relaxes in a single step into a low-energy level or the ground state. The overall photon fluence rate produced in the prescribed mechanisms is finally lowered and shaped by all kinds of photon reactions such as photo effect, Compton effect, e$^{\pm}$ pair production above 1.022 MeV, photo-nuclear reactions, and $\mu^{\pm}$ pair production above about 212 MeV.

As obvious from Figure 5.11, the calculated spectral fluence rate distributions in the top panel of Figure 5.10 and the vertical intensity profile shown in the bottom panel agree very well for all codes and models as photon physics are well understood and well validated in all MC codes. Furthermore, a variety of data on photo-nuclear reactions as well as data for photon emission from excited nuclei is implemented in the physics of all codes.

5.5 Neutrons at sea-level and comparison with BSS measurements

As already pointed out at the beginning of this chapter, the spectral fluence rate distribution of secondary neutrons from cosmic radiation on Earth is strongly influenced by geometrical effects such as e.g. the soil and the hydrogen content in and on the soil. In order to compare calculations with the continuous Bonner sphere measurements in Ny-Ålesund, Spitsbergen, carried out throughout the present work (see Chapter 3), these influences have to be taken into account. Due to the fact that the particle transport calculations in the Earth's atmosphere are very CPU time consuming, extensive studies of this kind are hardly manageable within a reasonable time in case calculations are done starting on top of the atmosphere.

For this reason, the following calculations were performed in two steps. In the first step primary galactic cosmic radiation was simulated starting on top of the atmosphere, and the directional fluxes of all secondary particles were calculated in downward and upward direction by restricting the scoring to zenith angles in the ranges of $0° \leq \theta < 90°$ and $90° \leq \theta < 180°$, respectively. Since the neutron fluence rates at sea-level almost solely result from high-energy protons and neutrons generated at lower atmospheric depths, in the second step the downward directed neutron and proton spectra were shot from an atmospheric depth of 917 g/cm^2 corresponding to an altitude of approximately 1 km above sea-level. The momentum directions of source neutrons and protons were uniformly distributed in downward direction in the second step, i.e. in a solid angle of 2π. The transport calculations from 1 km down to sea-level require much less CPU time which, in turn, allows to study the impact of geometrical effects such as the soil and hydrogen content on the neutron spectra. All these computations were again performed applying the two different INC models available in GEANT4 (Bertini and Binary).

The directional neutron spectra scored for the stepwise approach at 917 g/cm^2, 0 GV cutoff, and solar minimum ($\phi = 420$ MV) are depicted in Figure 5.12 together with the omnidirectional neutron flux. The inset in this figure shows the corresponding proton spectra. Due to the fact that the relative contributions of up- and downward directed neutron and proton fluence rates to the corresponding total particle flux are nearly identical for both INC models, the spectra are not shown for both models separately. Instead, the depicted spectral fluxes are normalized to the maximum omnidirectional fluence rate of the cascade peak in case of neutrons and to the omnidirectional peak fluence rate of protons in order to exemplary illustrate the directional components of the spectra.

The neutron spectra in Figure 5.12 reveal the expected characteristics of fluence rates with nearly all high-energy neutrons in the cascade peak being directed downwards and only a very small fraction of neutrons with energies above 20 MeV having a zenith angle above 90°. These upward directed neutrons result from scattering processes of high-energy neutrons which were already produced with rather large zenith angles. Since evaporation neutrons with energies between 0.1 and 20 MeV follow an isotropic angular distribution, the corresponding up- and downward fluxes are nearly identical. Only a very small excess in

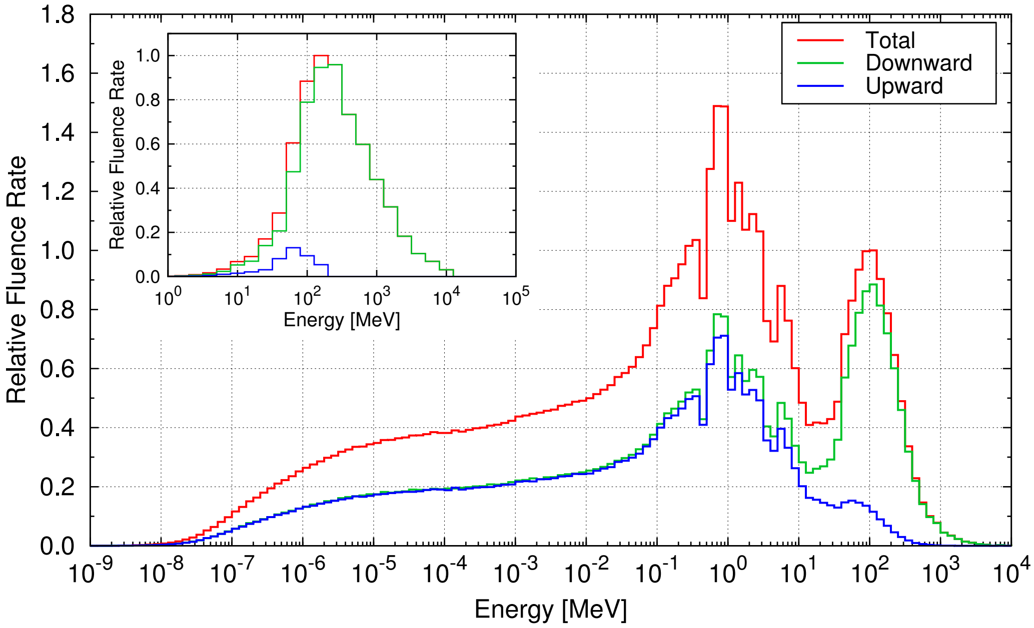

FIGURE 5.12: Relative up- and downward directed neutron fluence rates at 917 g/cm^2, 0 GV cutoff, and solar minimum in comparison with the omnidirectional spectrum. The inset shows the corresponding proton spectra. Neutron spectra are normalized to the maximum omnidirectional fluence rate of the cascade peak and proton spectra to the omnidirectional peak fluence rate.

downward direction is observed resulting from momentum transfer in forward direction of projectile particles inducing evaporation processes. Expectedly, below 0.1 MeV the neutron flux is completely isotropic as a result of elastic scattering processes. Thus, both directional components are identical at low neutron energies. In case of proton spectra, on the other hand, only a very small upward flux is observed at energies below 200 MeV due to slightly scattered secondary protons produced in hadronic interactions with large zenith angles.
The accuracy and validity of the stepwise approach for the calculation of neutron spectra at sea-level was cross-checked with a direct calculation starting with primary cosmic radiation on top of the atmosphere. As can be seen in Figure 5.13, the omnidirectional neutron fluence rates determined in the stepwise approach agree very well with the direct calculations. Differences in energy-integrated neutron fluence rates on Earth were found to be less than 1%, i.e. both approaches were fully consistent within the statistical uncertainties of the MC simulations. It should be noted, however, that the excellent agreement of both approaches may also result from the very simple cubic geometry considered. As stated above, in the stepwise calculation the downward spectra were homogeneously distributed in a solid angle of 2π. The major part of the downward-directed neutron fluence rate in the cascade peak as well as the proton fluence rate shown in Figure 5.12 has a near-vertical momentum direction with rather small zenith angles. Since in the flat geometry only omnidirectional particle fluence rates were scored, inaccuracies due to an isotropic distribution of high-energy primary neutrons and protons in the stepwise calculation are negligible. On the hand, when large obstacles such as e.g. mountains are to be included in the geometry, the correct angular distribution would have to be considered.

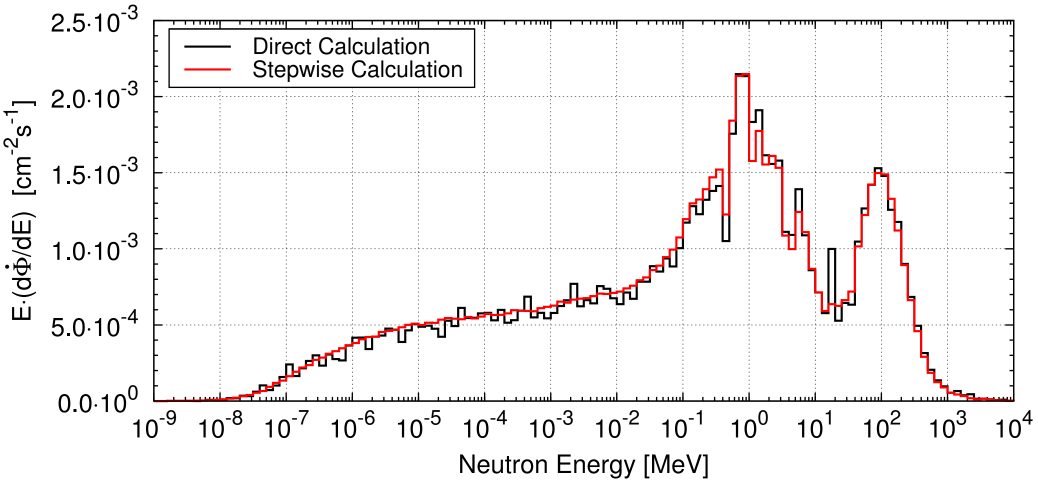

FIGURE 5.13: Comparison of direct and stepwise calculation of omnidirectional neutron fluence rates at sea-level. In the direct calculation primary cosmic radiation was transported starting on top of the atmosphere (100 km), whereas in the stepwise approach the downward neutron and proton spectra from Fig. 5.12 were transported from 1 km down to sea-level. All calculations are based on the Bertini INC model for solar minimum conditions and 0 GV cutoff rigidity.

As stated above, the neutron and proton fluence rates with zenith angles in the range of $0° \leq \theta < 90°$ were used to study the impact of geometrical effects on the neutron spectra at sea-level, 0 GV cutoff rigidity, and solar minimum conditions at a modulation potential of $\phi = 420$ MV. One major goal of these simulations was to find out which of the INC models applied in the particle transport calculations agrees best with measurements of secondary neutrons from cosmic radiation. For this inter-comparison average data measured in January 2011 with the polar Bonner sphere spectrometer in Ny-Ålesund, Spitsbergen, discussed in Chapter 3 were used. Due to the fact that neither the exact composition nor the average mass density of the soil is known for this measurement location, a very basic composition of silica sand was assumed in a first attempt, where the dry soil was composed of 75% SiO_2 and 25% Al_2O_3 by mass having an overall density of 2.785 g/cm^3. In a series of calculations using both INC models, respectively, the weight fraction of water in this soil type was varied between 0 (dry soil) and 1 (pure water). To be more specific, a water weight fraction of 0.2 corresponds to a soil with 20% H_2O, 60% SiO_2, and 20% Al_2O_3. The related overall densities were accordingly adjusted taking the water content into account. With these different soil conditions the impact on calculated neutron fluence rates were determined directly on ground, i.e. at an atmospheric depth of 1030 g/cm^2.

In order to compare the simulation results with measurements, the BSS data have to be normalized to the corresponding sea-level pressure of approximately 1010 hPa used in the calculations. This is necessary because the detector readings of the Bonner spheres are subject to changes in the airmass overburden at the measurement location and, thus, depend on changes in the local and temporal meteorological conditions. This airmass may well be estimated during calm atmospheric conditions by measuring the local pressure p. The count rate N of each sphere can then be corrected according to

$$dN = -\alpha N dp \qquad \Rightarrow \qquad N_{corr} = N \cdot e^{-\alpha(p_0 - p)} \quad , \tag{5.13}$$

where N_{corr} denotes a sphere's count rate normalized to the reference pressure p_0 and α the so-called barometric coefficient describing the mass shielding provided by the atmosphere. Since the barometric coefficient cannot be experimentally determined with the BSS with sufficiently high precision, a value of $\alpha = 0.741$ %/mbar was taken as measured by the nearby operated Neutron Monitor in Barentsburg[4] (see also *Pioch et al.*, 2011b).

Apart from the prescribed pressure correction, the BSS data have to be corrected for contributions from atmospheric protons in order to obtain spectra that only result from secondary neutrons. As described in detail in Appendix C.3, for this purpose the Bonner sphere response functions to protons calculated in the present work with GEANT4 and proton spectra at sea-level simulated with GEANT4 were used to estimate contributions to the detector readings of each sphere. At sea-level, 0 GV cutoff rigidity, and solar minimum conditions this proton correction finally leads to a reduction of the unfolded integral fluence rate in the cascade peak of BSS measurements of approximately 8%. Given the fact that fluence rates of other charged particles such as pions are by orders of magnitude smaller at sea-level than neutron and proton fluxes, contributions from other secondary particle species to the detector readings can well be neglected.

In Figure 5.14 results from the outlined GEANT4 particle transport calculations are contrasted with the proton- and pressure-corrected BSS measurements carried out during January 2011 in Ny-Ålesund, Spitsbergen. The top panel depicts simulation results obtained using the Bertini INC model and the bottom panel those using the Binary INC model. As extensively discussed in Chapter 4, the unique calibration measurements for the Bonner sphere system performed in quasi-monoenergetic neutron fields of 244 and 387 MeV at the RCNP in Osaka, Japan, revealed that the Bonner sphere response functions calculated with both the Bertini and the Binary INC model are largely consistent with the independent high-precision time-of-flight measurements. However, it turned out that the Bertini model appears to give more accurate results at the higher beam energy and, therefore, may handle high-energy hadronic interactions slightly better. This very important result of the present work, in turn, indicates that the Bertini INC model might give somewhat more correct results for the simulation of cosmic radiation in the Earth's atmosphere, since in this case the INC models influence simulation results up to energies of 10 GeV. The inter-comparison of calculated and measured atmospheric protons discussed in Section 5.4.1 already confirmed this finding where the near-vertical proton flux calculated with the Binary INC model significantly overestimated experimental data.

In order to additionally confirm this in case of atmospheric neutrons, the BSS spectra shown in Figure 5.14 were unfolded using both the GEANT4-BERT and the GEANT4-BIC response matrices, respectively. The unfolding itself was done using the MSANDB unfolding code (*Matzke*, 1988, 2002, 2003, see App. C.1), 500 iteration loops, and an 'a priori' spectrum including all expected spectral features.

---

[4] http://cr0.izmiran.rssi.ru/brbg/main.htm

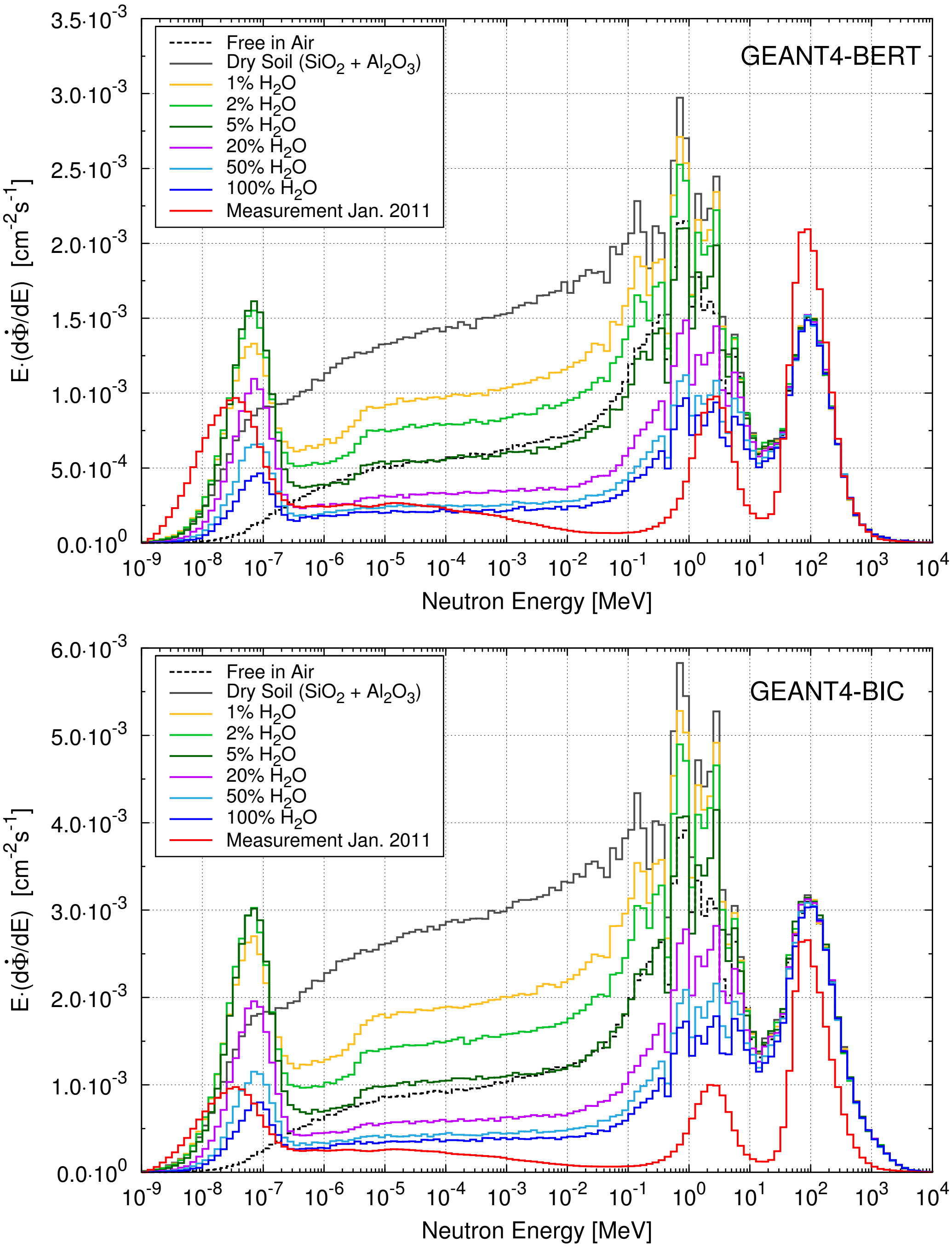

FIGURE 5.14: Influence of different water weight fractions in silica sand soil (SiO_2 Al_2O_3) on neutron spectra at sea-level, 0 GV cutoff rigidity, and solar minimum conditions in comparison with BSS measurements carried out during January 2011 in Ny-Ålesund, Spitsbergen. The top panel depicts simulation results obtained using the Bertini INC model and the bottom panel those using the Binary INC model.

TABLE 5.2: Integral neutron fluence rates at sea-level, 0 GV cutoff rigidity, and solar minimum conditions calculated with GEANT4 using two different INC models in comparison with proton-corrected BSS measurements carried out during January 2011 in Ny-Ålesund, Spitsbergen. Neutron spectra were unfolded using the corresponding response matrices calculated with the Bertini and the Binary INC model, and calculations of the spectra were performed using silica sand soil with 20% water weight fraction as an example.

GEANT4 WITH BERTINI INC

Energy [MeV]	BSS Measurement [$cm^{-2}s^{-1}$]	MC Simulation [$cm^{-2}s^{-1}$]	Relative Deviation [%]
$\leq 4\cdot10^{-7}$	$2.99\cdot10^{-3}$	$2.25\cdot10^{-3}$	-25
$4\cdot10^{-7} < E \leq 0.1$	$2.26\cdot10^{-3}$	$4.33\cdot10^{-3}$	+91
$0.1 < E \leq 20$	$2.10\cdot10^{-3}$	$5.18\cdot10^{-3}$	+146
> 20	$3.73\cdot10^{-3}$	$3.11\cdot10^{-3}$	-16
Total	$1.11\cdot10^{-2}$	$1.48\cdot10^{-2}$	+33

GEANT4 WITH BINARY INC

Energy [MeV]	BSS Measurement [$cm^{-2}s^{-1}$]	MC Simulation [$cm^{-2}s^{-1}$]	Relative Deviation [%]
$\leq 4\cdot10^{-7}$	$3.01\cdot10^{-3}$	$4.09\cdot10^{-3}$	+36
$4\cdot10^{-7} < E \leq 0.1$	$2.23\cdot10^{-3}$	$7.77\cdot10^{-3}$	+248
$0.1 < E \leq 20$	$2.08\cdot10^{-3}$	$1.02\cdot10^{-2}$	+390
> 20	$4.51\cdot10^{-3}$	$7.54\cdot10^{-3}$	+67
Total	$1.18\cdot10^{-2}$	$2.96\cdot10^{-2}$	+151

The comparison of the free in air (black dashed lines) neutron spectra in Figure 5.14 with the spectra calculated on dry silica sand soil (dark-gray lines) illustrates the rather huge impact of the ground. Expectedly, high-energy neutrons are completely unaffected by any geometrical effects, whereas the evaporation peak is enhanced by approximately 50% with respect to free in air computations due to a much higher density of high atomic number material in the soil. This in turn leads to an increase in epithermal neutron fluence rates of more than a factor of two. This increase consequently propagates down to thermal energies and finally results in a formation of a small thermal peak even on dry ground which is not observed in calculations in the atmosphere as a result of thermal neutron absorption on nitrogen.

Comparison of the simulations with different water weight fractions contained in the soil demonstrates the impact of hydrogen on the neutron spectra. With increasing water content the evaporation peak is stepwise reduced, since less high atomic number nuclei constitute the soil where evaporation processes might be induced by high-energy neutrons and protons. Furthermore, the higher the water weight fraction in the soil the higher the degree in moderation as a result of elastic scattering processes. Both the maximum and the average energy transfer in elastic neutron-proton collisions is much higher in wet with respect to dry soil as a result of nearly equal neutron and proton masses (see also Eq. 3.1). This additionally reduces the height of the evaporation peak. Moreover, this effect predominantly shapes and stepwise reduces the neutron flux in the epithermal region with increasing water content. Below 4 eV the calculations clearly illustrate the influence of thermal scattering on hydrogen nuclei bound in H_2O. Even at a very small water weight fraction of only 1%, thermal scattering leads to a sudden decrease in flux around 4 eV. On the other hand, the thermal peak gets more pronounced reflecting thermal equilibrium of the neutrons with the surrounding soil and, thus, following a distinctive Maxwell-Boltzmann distribution. At water fractions between 1 - 5% thermal scattering processes lead to a small increase in the peak height, whereas at higher water fractions the peak is strongly reduced due to H(n,γ) capture reactions.

All these features are observed with both INC models, but neutron fluence rates calculated with the Binary INC are about twice as high as those using the Bertini model as a results of strongly different atmospheric neutron and proton intensities given by both models. In order to quantitatively compare simulated and measured neutron spectra, numerical fluence rate values integrated over the four characteristic energy regions are listed in Table 5.2. Note that the slightly different values for the measurements result from using the response matrices calculated with the Bertini and the Binary INC models, respectively.

Furthermore, it should be noted that calculated neutron fluence rates at energies below 20 MeV are not only influenced by large-scale geometrical effects such as the soil and the water fraction within. Additionally, also small-scale factors such as the housing of the spectrometer and the positioning of the spheres relative to each other may have an impact, since e.g. large PE spheres may be an additional source of thermal neutrons. Therefore, minor discrepancies of simulated and measured spectra may arise at low energies. The main impact on the measured spectra, however, results from the large-scale geometry around the spectrometer which can not exactly be taken into account without precisely knowing the soil composition, its density, and its humidity in a rather large spatial area around the spectrometer. Therefore, the calculated values in Table 5.2 exemplary correspond to silica sand soil with 20% water weight fraction. Due to the fact that the simulation results above 20 MeV are not influenced by any geometrical effects, an inter-comparison of calculations and measurements is most meaningful at these energies. In the high-energy region the simulated spectra using the Bertini INC only differ by about 16% from measurements, whereas those using the Binary INC differ by about 67%. Also the total integral neutron fluence rates given by the Bertini INC are much closer to experimental data than those given by the Binary INC model. It can therefore again be concluded that the neutron spectra at sea-level calculated using the Bertini INC model are somewhat more accurate.

In addition to the calculations of neutron spectra at sea-level and the analysis of the impact of different water weight fractions in silica sand soil presented above, a series of calculations was performed with granite soil. The composition and density of granite was taken from the database of the National Institute of Standards and Technology[5] (NIST). On top of the granite soil an extra layer of water was modeled whose vertical extension was varied. This allows to estimate the influence of different soil types on the calculated neutron spectra and the impact of hydrogen on top of the soil resembling a snow cover. The results of these calculations are

---

[5] http://www.nist.gov/pml/data/index.cfm

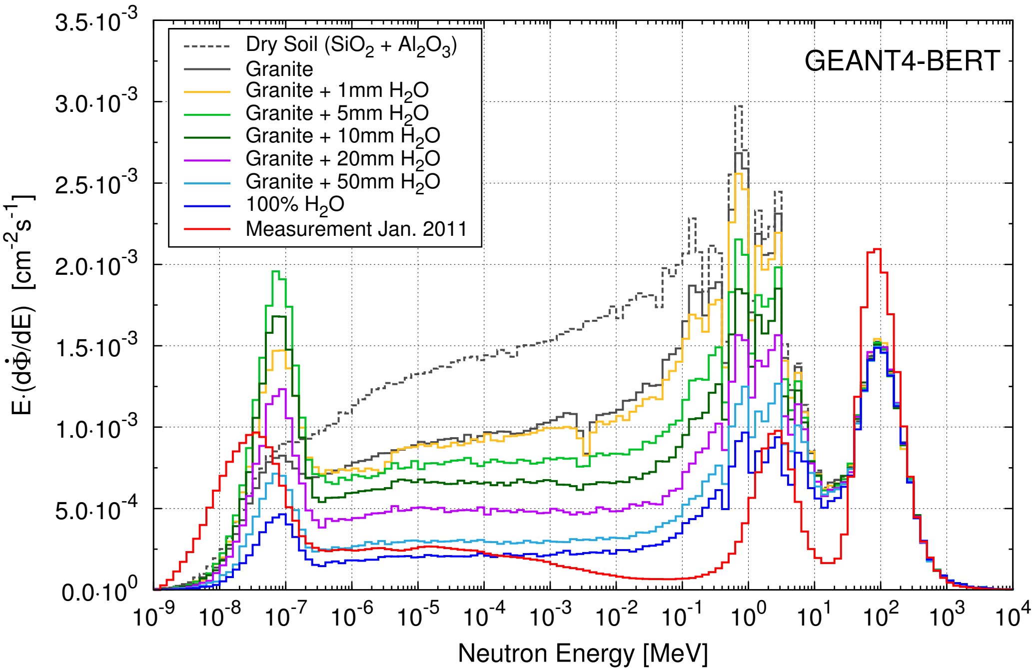

FIGURE 5.15: Neutron spectra at sea-level, 0 GV cutoff rigidity, and solar minimum conditions calculated above a granite soil with the Bertini INC model in comparison with BSS measurements carried out during January 2011 in Ny-Ålesund, Spitsbergen. On top of the granite soil an extra layer of water with different vertical extension was simulated resembling a snow cover.

contrasted with BSS measurements in Figure 5.15. Since also in these calculations the simulated neutron fluxes using the Binary INC model significantly overestimated experimental data, in Figure 5.15 only the results using the Bertini model are depicted. As neutron fluence rates are significantly lower for the granite soil, the comparison of the simulation results for dry silica sand (gray dashed lines in Figure 5.15) and granite soil (solid gray lines) clearly demonstrates how sensitive simulated neutron spectra are at energies below 20 MeV on the exact soil composition and its density. The particle transport calculations for various thicknesses of the water layer basically have the same influence on the neutron spectra at low energies as observed when varying the hydrogen content in the soil (see discussion above). However, all the spectra shown in Figures 5.14 and 5.15 clearly demonstrate that the large-scale geometrical effects including the soil composition, density, hydrogen content in the soil, and water on the soil have to be considered in every detail. Furthermore, also the small-scale factors such as the housing and other geometrical features may have to be modeled in every detail in order to possibly achieve a complete consistency of BSS measurements and transport calculations at low energies. At energies above 20 MeV, on the other hand, neutron spectra are completely unaffected by any geometrical parameters. Therefore, the detailed comparison with experimental data carried out in this section clearly revealed that neutron spectra at sea-level calculated with the Bertini INC model match much better with observations. This, in turn, is in agreement with the inter-comparison of calculated proton spectra with measurements discussed in Section 5.4.1 as well as with the calibration measurements of the BSS performed in high-energy neutron fields presented in Chapter 4.

5.6 Potential measurement of a GLE with BSS

In the previous sections secondary particle spectra and intensities induced by galactic cosmic radiation were extensively discussed. Apart from the galactic component, one major goal of the present work was to study increased radiation levels in the lower atmosphere caused by solar protons during ground level enhancements. The mechanisms leading to these events, their occurrence rate, and the techniques to derive their temporal, spatial, and spectral characteristics were addressed in detail in Chapter 2.2. In particular considering that two Bonner sphere spectrometers are continuously operated by the HMGU in order to get information on potential changes in secondary neutron spectra and related dose rates during GLEs (see Chapter 3), the question arises whether and how the spectral neutron fluence rates may possibly be affected.

In the following this question is addressed exemplary for GLE 69 which occurred on January 20, 2005. With a maximum count rate increase of more than 4800% in the time interval from 6:50 UT to 6:55 UT at the South Pole Neutron Monitor station (see Fig. 2.10), this GLE was ranked amongst the most intense events in decades, but also amongst the most anisotropic events. Moreover, in Chapter 2.2.3 the spectral characteristics of GLE 69 as derived from the global Neutron Monitor network by various authors were inter-compared and contrasted with interplanetary observations. The primary proton spectra reported in *Vashenyuk et al.* (2005, 2007, 2009a) were shown to be largely consistent with both space-born and ground-based observations. Thus, these were chosen to calculate secondary particle spectra in the Earth's atmosphere.

According to *Vashenyuk et al.* (2009a) the primary proton intensity $j(E_k)$ in units of $[1/(\mathrm{m}^2 \cdot \mathrm{s} \cdot \mathrm{sr} \cdot \mathrm{GeV})]$ for the prompt component of GLE 69 at about 7:00 UT on January 20, 2005 has an exponential dependence on kinetic energy with a turnover above 490 MeV:

$$j(E_k) = 2.5 \cdot 10^6 \cdot \exp(-E_k/0.49). \tag{5.14}$$

For the delayed GLE component at about 8:00 UT a simple power law in kinetic energy was found to agree rather well with Neutron Monitor observations:

$$j(E_k) = 7.2 \cdot 10^4 \cdot E_k^{-5.6}. \tag{5.15}$$

In Figure 5.16 the prompt and the delayed component are contrasted with the mean galactic cosmic ray background during January 2005 following *Usoskin et al.* (2005, 2011).

Apart from the spectral characteristics of GLEs, the exact angular distribution of primary protons on top of the atmosphere needs to be known for an accurate estimation of the secondary particle intensities induced in the Earth's atmosphere. As described in more detail in Chapter 2.2.2, the pitch angle distribution serves to describe the anisotropy of a GLE outside the magnetosphere. The pitch angle is defined as the angle between the apparent source direction (i.e. approximately the Sun-Earth magnetic field line) and the asymptotic viewing direction for a given site and magnetic rigidity. Convolution of the pitch angle distribution and the asymptotic cone gives the vertical particle intensity on top of the atmosphere above the vertical effective cutoff at a particular location. In many GLEs a rather high degree in isotropy is found even in the prompt component and, therefore, an isotropic particle distribution on top of the atmosphere is a good approximation (see also *Bütikofer and Flückiger*,

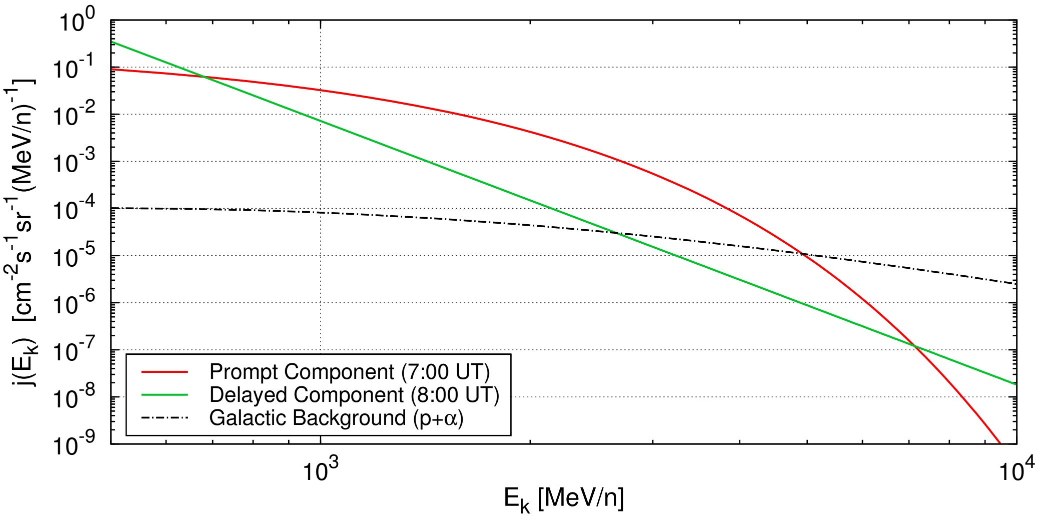

FIGURE 5.16: Prompt (≈ 7:00 UT) and delayed (≈ 8:00 UT) component of the solar proton spectra during GLE 69 on January 20, 2005, as derived by *Vashenyuk et al.* (2005, 2007, 2009a). Solar spectra are compared with the mean galactic cosmic ray background during January 2005 following *Usoskin et al.* (2005, 2011) (see also Fig. 2.10).

2011). During the initial phase of very anisotropic events such as GLE 69, on the other hand, solar protons may arrive almost solely from a specific direction at given locations, because protons with given rigidity and momentum direction outside the magnetosphere follow specific trajectories. The maximum secondary particle intensity is then induced in the atmosphere in case solar protons arrive from near-vertical directions. The possible range in secondary particle intensities in the atmosphere resulting from the assumption of isotropic and vertical incoming directions of primary protons was estimated for the spectrum of the prompt component shown in Figure 5.16, whereas the spectrum of the delayed component was only isotropically considered. During the whole duration of GLE 69 no increases in count rates were recorded with ground-based detectors above 10 GV vertical effective cutoff. Accordingly, the rigidity range of solar proton was restricted to the interval from 0.5 GV to 10 GV in the particle transport calculations.
Note that the main focus of this section is on secondary neutrons in order to study potential measurements with the BSS systems operated throughout the present work. Therefore, the following discussion is restricted to this particle species. Furthermore, as it is much more likely to measure a GLE with the polar BSS in Ny-Ålesund, Spitsbergen due to the very low effective cutoff at this location, secondary neutron spectra are considered for 0.0 GV cutoff at sea-level.

In Figure 5.17 the omnidirectional fluence rate distributions of sea-level neutrons are shown during the initial (07:00 UT) and the main phase (8:00 UT) of GLE 69. As stated above, the prompt component was also calculated for vertical incidence on top of the atmosphere (red lines). Note that these spectra were only computed with GEANT4 using the Bertini INC model, because it was found in the previous section of this Chapter that this model is likely to give somewhat more accurate results at sea-level. In order to demonstrate the enhanced neutron intensities with respect to the mean galactic cosmic ray background in January 2005

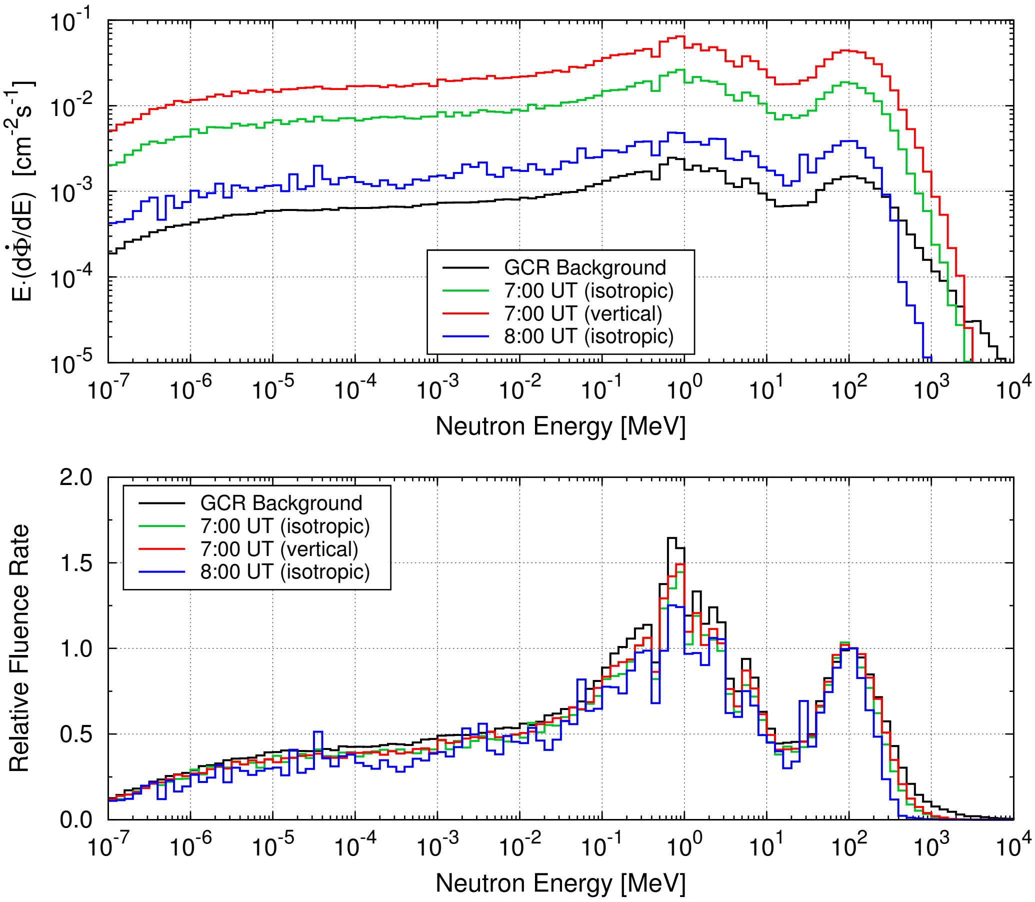

FIGURE 5.17: Omnidirectional fluence rate distributions of secondary neutrons at sea-level and various times during GLE 69 on January 20, 2005 in comparison with the spectrum induced by galactic cosmic radiation. In the bottom panel the spectra are normalized to the maximum flux in the cascade peak.

at a modulation strength of about 788 MV (*Usoskin et al.*, 2011), the top panel of Figure 5.17 shows neutron spectra in log-log scale. To pronounce the spectral differences, the bottom panel shows the spectra normalized to the corresponding maximum flux in the cascade peak in log-lin scale.

To cross-check the calculated integral fluence rates with Neutron Monitor observations, the neutron fluence rates shown in Figure 5.17 were folded with the neutron response function of NM64 type Neutron Monitors presented in *Pioch* (2008); *Pioch et al.* (2011b). This allows to estimate expected count rate increases in a ground-based Neutron Monitor under the presumption that the Monitor's asymptotic cone of acceptance was directed along the incoming direction of solar protons at the magnetopause. For comparison, the south-polar Neutron Monitor station Terre Adelie was chosen. This 9-NM64 type monitor is located at sea-level at 66.65°S 140°E corresponding to 0.0 GV cutoff. During GLE 69 the Terre Adelie station was fully exposed to both the prompt and the delayed component, which makes this monitor perfectly suited. In the time interval from 06:55 to 07:00 UT an increase of 2650% was observed, whereas from 07:45 to 08:00 UT it was only about 83% (see also Fig. 2.10). This compares to a calculated increase with respect to the calculated galactic cosmic ray background of 2510% using the neutron spectrum for vertical incidence (red line in Fig. 5.17) during the initial phase and to an increase of 92% assuming an isotropic distribution for the delayed GLE component (blue line).

This excellent agreement shows the accuracy and consistency of the primary proton spectra as derived by *Vashenyuk et al.* (2009a) as well as an overall consistency of the calculations of secondary neutrons at sea-level. In addition this demonstrates that in fact solar protons may arrived in near-vertical direction above the Terre Adelie station during the initial phase of the event, because the increase calculated with the isotropic prompt component (green line) is only about half that for vertical incidence. As e.g. reported by *Plainaki et al.* (2007), at the beginning of the January 2005 event solar protons indeed arrived in narrow beams near Earth, and only south polar Neutron Monitor stations had asymptotic viewing cones fully intersecting with the arrival direction of the event.

Concerning changes in the neutron spectra induced by solar protons during GLE 69 compared with those induced by the galactic component, it is obvious from Figure 5.17 that the spectra are very similar in shape. As secondary particle spectra in the Earth's atmosphere are already in equilibrium around the Pfotzer maximum at an atmospheric depth below 100 g/cm^2, this is expected. The only part of the neutron spectra being affected by differences in the primary proton spectra during a GLE, is the very high-energy part above several tens to hundreds of MeV. These neutrons are produced in break-up processes and direct collisions of incident high-energy protons with single nucleons in air nuclei during the first step of spallation reactions (also see App. B). Thus, the very high-energy part of secondary neutron spectra resemble the course of the primary proton spectra. Since spectra during GLEs are much steeper than the galactic cosmic ray spectra, also the secondary neutron fluence rate distributions are much steeper at very high energies. However, the resulting differences in absolute fluence rates are very small, and it is, thus, very difficult to resolve such spectral features with a Bonner sphere spectrometer.

To research this in more detail, expected detector readings for all spheres of the BSS in Ny-Ålesund were calculated for the prompt component of GLE 69 with vertical incidence on top of the atmosphere. In Figure 5.18 the hypothetical relative count rate with respect to the galactic background is shown for each Bonner sphere. Apparently, also in the Bonner spheres an average count rate increase of about 2550% would have been observed during the initial phase of the event around 7:00 UT if the spectrometer's viewing direction fully intersected with the incoming direction of solar protons at the magnetopause. Differences in the count rate increases of different spheres basically indicate changes in the neutron spectra with respect to GCR. The somewhat smaller increase triggered in the spheres containing lead shells is thus a direct consequence of the more steeply decreasing secondary neutron spectra during the GLE. Given the fact that the relative count rates of all spheres agree within less than 3%, such changes are hardly resolvable with a BSS due to the intrinsic statistical fluctuations in the detector readings. Note that for a hypothetical 10-fold enhanced neutron intensity during a time period of 1 hour the statistical precision given by the readings of the small ^{3}He proportional counters employed in the BSS is in the order of 5% (also see *Rühm et al.*, 2009b). As the count rate increase during the first hour of the very intense January 2005 event was e.g. only about a factor of six to seven at the Terre Adelie station (also see Fig. 2.10), this shows that resolving the small changes in the neutron spectra during GLEs

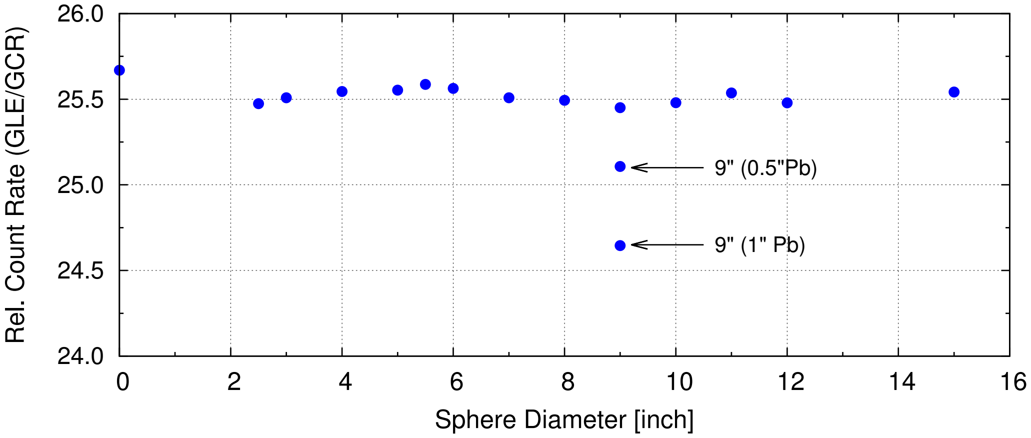

FIGURE 5.18: Expected relative increase in detector readings of the Bonner sphere spectrometer in Ny-Ålesund with respect to galactic cosmic radiation during the maximum phase of GLE 69 on January 20, 2005.

is expected to be very difficult, at least with a time resolution of much less than 1 hour favored and required for GLE analyses. For measurements of integral neutron intensities and effective doses, on the other hand, the precision of the BSS is adequate. Furthermore, GLEs are not predictable in their intensity and there are well-founded indications that very intense events can occur as discussed in Chapter 6.3. During such an intense GLE, in turn, the BSS in Ny-Ålesund may be suited to derive information on changes in neutron spectra with a time resolution equal to or less than one hour. Additionally, it is planned to replace the detectors currently operated with bigger ones increasing the statistical precision by a factor of two. This will further improve the situation.

Note that in principal the calculated count rates shown in Figure 5.18 could be used to unfold the corresponding neutron spectrum. However, it turned out that the deconvolution procedure using the MSANDB code in combination with this artificial measurement vector calculated from the free in air neutron spectra shown Figure 5.17 is very sensitive to any changes in the ‘a priori’ spectrum. To be more specific, the calculated neutron spectra could only be reproduced if they were already used as start spectra. In this case, exactly the same neutron fluence rate distributions were obtained after the unfolding. As this is basically no unfolding from which useful information could be extracted, the results are not shown in the following. However, this must not necessarily mean that MSANDB is not suited or not accurate enough, but a real measurement vector during a GLE is required for further investigations.

CHAPTER

6

AIRCREW RADIATION DOSIMETRY

In the previous chapter spectral fluence rate distributions of secondary particles induced in the Earth's atmosphere by cosmic radiation were extensively discussed. Consequently, the question arises how these particle fluence rates translate to dose quantities. This is of particular importance in commercial aviation, where the exposure of crews to cosmic radiation is recommended by the *ICRP* (1990, Publication 60) to be regarded occupational. Based on these recommendations, international and national regulations and directives have been released, in particular in the European Union (*EU*, 1996). In Germany, the dosimetry of flying personnel is regulated by law in §103 of the German Radiation Protection Ordinance. According to this regulation, monitoring of effective dose for aircrews due to cosmic radiation is obligatory in case the yearly accumulated dose is likely to exceed 1 mSv. Since effective dose is not directly measurable, computer programs are used to estimate dose values along any flight route. Most of such programs, therefore, rely on calculated spectral fluence rate distributions of all secondary cosmic ray particles that are relevant in terms of radiation protection. Furthermore, the particle spectra have to be determined for all solar modulation strengths and all geographic positions, in order to derive the corresponding effective doses along arbitrary flight routes.

As described in Chapter 5, two complete sets of spectra for all components of secondary galactic cosmic radiation were calculated in the frame of the present work with GEANT4 using two different INC models. Their application in aircrew dosimetry is addressed in the first part of this chapter. Subsequently, dose rates and accumulated doses for aircrews during ground level enhancements are discussed by means of GLE 42 which occurred on September 29, 1989. Based on this GLE, a plausible worst case scenario is presented at the end of this chapter for the well-known Carrington event in 1859. Note that all dosimetric background knowledge necessary for the discussion in the following chapter is summarized in Appendix A.2.

6.1 Doses in aviation due to galactic cosmic rays

As shown in Chapter 5, differences in spectral fluence rate distributions are observed for certain particle species as a result of different theoretical models handling high-energy hadronic interactions. These differences do not necessarily have an impact on dose quantities, in particular at typical cruising altitudes of commercial aircrafts.

To investigate this in more detail, the secondary particle spectra calculated with GEANT4 using the Bertini and the Binary INC model, respectively, were converted to effective dose and ambient dose equivalent rates. As discussed in Appendix A.2, for the determination of ambient dose equivalent and effective dose following *ICRP* (Publ. 60, 1990, referred to as ICRP-60) fluence-to-dose conversion coefficients from *Pelliccioni* (2000) and references therein were used. Recently, the radiation weighting factors for neutrons and protons were revised in *ICRP* (Publ. 103, 2007, referred to as ICRP-103), with the most important change being the reduction of the weighting factor for protons from 5 to 2. Effective dose rates following ICRP-103 were obtained using conversion coefficients based on *Sato et al.* (2007) for protons and neutrons. However, the final values used in the following, which will also be included in the next ICRP publication, were kindly provided by *T. Sato* in private communication.

To give an example for effective dose rates due to galactic cosmic radiation as calculated in the present work, Figure 6.1 shows values following ICRP-103 for all secondary particle species which are important in terms of radiation protection. Depicted are hourly dose rates as a function of atmospheric depth during solar minimum conditions at 0 GV vertical effective cutoff rigidity. These values correspond to the spectra and intensity-depth profiles discussed in Chapter 5.4 and, thus, represent maximum dose rates, to illustrate upper limits.

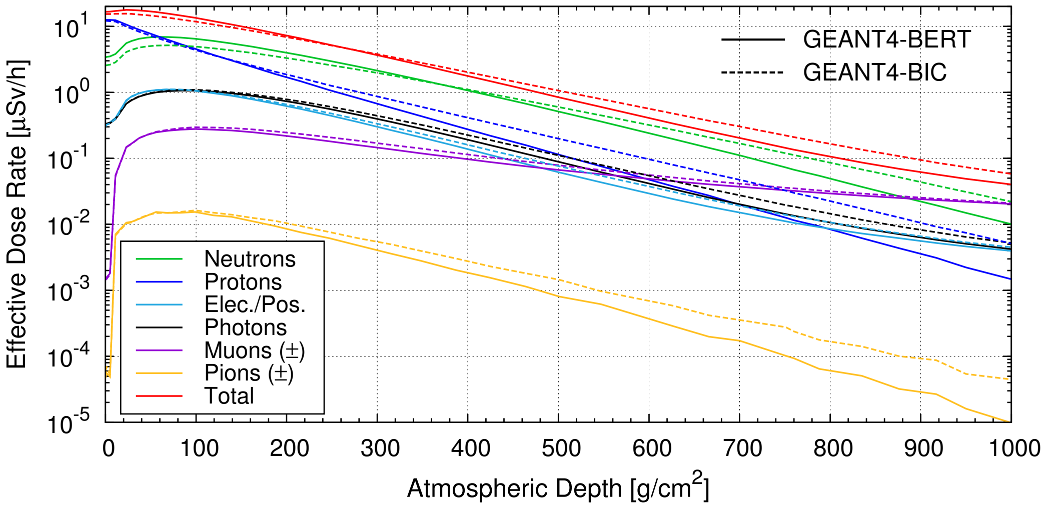

FIGURE 6.1: Hourly effective dose rates (following ICRP-103) from secondary particles induced by galactic cosmic radiation as a function of atmospheric depth. Solid lines correspond to secondary particle spectra calculated with GEANT4 and the Bertini INC model for solar minimum conditions and a vertical effective cutoff rigidity of 0 GV; dashed lines correspond to those calculated with the Binary INC model (see Chapter 5.4 for details).

The dose rates shown in Figure 6.1 clearly reflect the vertical profiles of secondary particle intensities in the Earth's atmosphere. During solar minimum and at 0 GV cutoff the total effective dose rate in the atmosphere ranges from approximately 19 μSv/h at an atmospheric depth of about 40 g/cm^2 ($\approx$ 22 km) to approximately 0.04 μSv/h at sea-level. As argued previously, differences in calculated secondary particle intensities due to different hadronic interaction models strongly depend on atmospheric depth and particle species. In particular for neutrons, protons, and pions large differences were observed. As a consequence, also the associated dose rates based on fluence rate calculations using the Bertini INC (solid lines in Fig. 6.1) differ significantly from those based on the Binary INC model (dashed lines). However, at atmospheric depths from 150 - 350 g/cm^2 corresponding to typical cruising altitudes of 9 - 13 km for long-haul flights in commercial aviation, all calculated secondary particle spectra agree rather well. Thus, both models result in nearly the same total effective dose rates of approximately 5 - 8 μSv/h. At lower atmospheric depths, on the other hand, large differences are observed in the individual neutron, proton, and pion dose rates of even more than a factor of three. Nonetheless, the total effective dose rates agree within about 30% even at sea-level. This is a result of the different relative contributions of individual secondary particle species to the total dose rate at different altitudes.

To illustrate this behavior, Figure 6.2 shows the relative contributions of individual particle types to total effective dose according to ICRP-103 as a function of altitude. These contributions were determined based on calculations with the Bertini model for solar minimum conditions and 0 GV cutoff. Note that charged pions were discarded due to their negligibly small associated dose rates (see Fig. 6.1). Apparently, below about 6 km altitude, corresponding to an atmospheric depth of approximately 500 g/cm^2, where the differences in neutron and proton fluence/dose rates become more pronounced, their contributions to to-

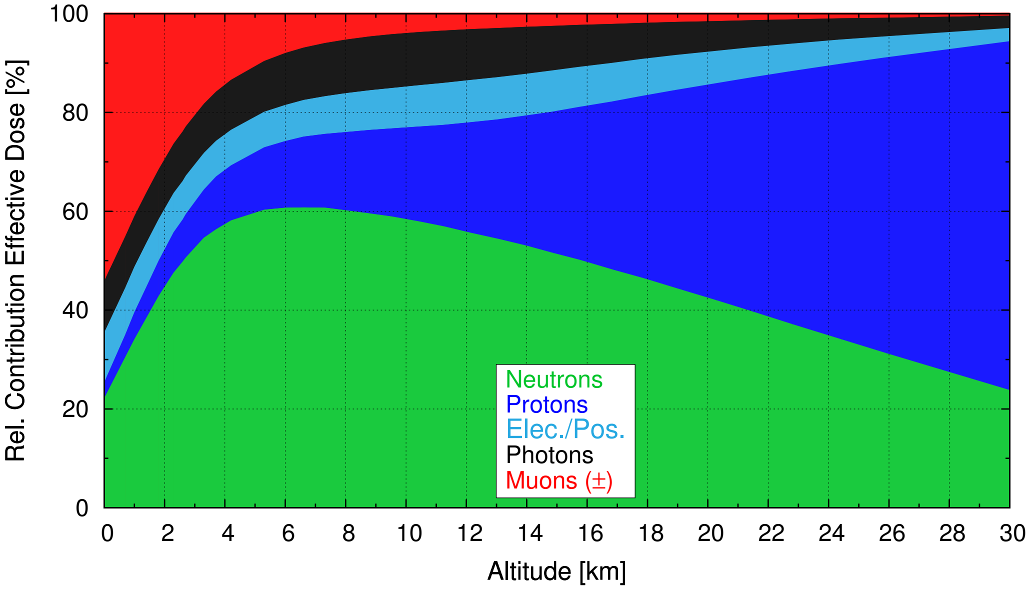

FIGURE 6.2: Relative contributions of individual secondary particle species to total effective dose following ICRP-103 as a function of altitude at 0 GV cutoff (based on GEANT4 calculation using the Bertini INC model).

tal effective dose rapidly decrease. Contributions from muons, on the other hand, rapidly increase at low altitudes reaching a value of more than 50% at sea-level. Since calculated muon spectra and consequently the associated dose rates are nearly identical for both INC models, the total effective dose rates along the whole vertical profile of the atmosphere are very similar.

Apart from this, Figure 6.2 clearly demonstrates the importance of the neutron component in aircrew dosimetry which accounts for more than 55% of the total effective dose rate at typical aircraft altitudes. Protons only contribute to about 20% in aviation and all other particle species to approximately 20%. Of note is, that the relative contributions of neutrons are reduced by about 10%, whereas proton contributions are enhanced by about 10% when radiation weighting factors according to ICRP-60 are applied. Concerning contributions to total ambient dose equivalent, on the hand, neutrons account for approximately 65% and protons only about 10%.

6.1.1 Comparison of effective dose with EPCARD

As stated at the beginning of this chapter, monitoring of the effective dose of aircrews is mandatory in Germany, and the corresponding dose values are determined by computer programs. Most of them are based on calculated spectral fluence rate distributions of secondary cosmic radiation in the Earth's atmosphere covering all cutoff rigidities and solar modulation strengths. A widely used program for this purpose is the European Program package for the Calculation of Aviation Route Doses[1] (EPCARD). This code was developed at the Helmholtz Zentrum München by *Schraube et al.* (2002) and further improved by *Mares et al.* (2009). All legal requirements for the determination of effective dose along any flight route are fulfilled by this program package. Note that for this reason, EPCARD is legally bound to calculate dose using radiation weighting factors according to ICRP-60. In any comparison with data from the present work carried out in the following, values for effective dose were, thus, estimated with conversion coefficients from ICRP-60.

The basis for the calculation of effective dose and ambient dose equivalent in EPCARD are secondary particle spectra calculated by *Roesler et al.* (1998, 2002) and *Heinrich et al.* (1999). These spectra were already inter-compared and shown to be consistent with results from the present work (see Chapter 5.4). The primary galactic spectra used in the calculations by *Roesler et al.* (1998, 2002) and *Heinrich et al.* (1999) as well as the modulation potential describing solar activity and the related impact on the GCR intensity and spectral distribution near Earth are based on the theory of *Badhwar and O'Neill* (1994, 1996). As discussed in more detail in Chapter 2.1.1, this model was designed to derive the solar potential from the Climax Neutron Monitor and it was revised already two times in *O'Neill* (2006) and *O'Neill* (2010). The main reasons for the revisions may be the significant overestimation of proton and helium intensities near Earth with respect to measurements and the potential uncertainties arising from using only one Neutron Monitor count rate to determine the solar potential. Modulation potentials from the very early version of the Badhwar/O'Neill model, therefore, fluctuate quite a lot. Furthermore, there is no well-defined correlation between the values given by this model and the one of *Usoskin et al.* (2005, 2011) used in

---

[1] http://www.helmholtz-muenchen.de/epcard-portal/

the present work, in which the modulation strength is derived from monthly averaged count rates of all available Neutron Monitor stations. This, in turn, means that a given time may correspond to very different modulation parameters in the two models. Accordingly, for an inter-comparison of dose values from the present work with EPCARD certain time periods have to be chosen rather than certain solar potentials. In order to cover a full solar cycle, May 1990 (solar maximum) and July 2006 (solar minimum) were selected. Following *Usoskin et al.* (2005, 2011), the modulation strengths during these months were 1435 MV and 443 MV, respectively, whereas the model of *Badhwar and O'Neill* (1994, 1996) predicts values of 1689 MV and 588 MV.

Calculation of aviation route doses

To accurately estimate doses along any flight route using secondary cosmic ray particle spectra calculated in the present work with GEANT4, the corresponding values have to be computed at any given solar potential, geographic position (i.e. cutoff rigidity), and altitude. As discussed in Chapter 5, secondary cosmic ray particle spectra were computed for solar potentials of 250 MV, 465 MV, 800 MV, 1200 MV, and 1500 MV, whereas the vertical effective cutoff rigidities were considered in steps of 1 GV from 0 - 6 GV and in steps of 2 GV from 6 - 17 GV cutoff. For all these conditions secondary particle fluence rates were scored at 46 different atmospheric depths from 0.25 - 1030 g/cm^2. In order to calculate doses for any flight, all the particle spectra were converted to effective dose rates (ICRP-60 and ICRP-103) and ambient dose equivalent rate as described in Appendix A.2. The vertical profiles, i.e. the dose rates as a function of atmospheric depth, were approximated by a least-squares fitting procedure using the open-source software Gnuplot[2], which employs a standard numerical fitting algorithm based on works of *Levenberg* (1944) and *Marquardt* (1963). In Figure 6.1 such vertical profiles of effective dose rates for all particle species considered are exemplary shown for 0 GV cutoff and 465 MV modulation potential. The dependence of dose rates $\dot{D}$ on atmospheric depth d for neutrons, electrons, positrons, photons, muons, and charged pions is well represented by the following function

$$\dot{D}(d) = \alpha \cdot d^{\beta} \cdot \exp(-\gamma \cdot d), \tag{6.1}$$

where the parameters α, β, γ were determined with the prescribed fitting procedure. Proton dose rates, on the other hand, only depend exponentially on atmospheric depth and can well be described by

$$\dot{D}_{proton}(d) = \alpha \cdot \exp(-\gamma \cdot d). \tag{6.2}$$

The individual fitting parameters of each particle species were embedded in a computer program for all combinations of cutoff and solar activity calculated with GEANT4. Dose values at any solar potential and cutoff rigidity can then be determined by linear interpolation between neighboring values. This finally allows to estimate accumulated doses along any flight profile.

A flight profile is given by so-called way-points defining the time, the altitude, and the geographic position of an airplane. The nominal altitude, hereby, is expressed in flight levels,

---

[2] http://www.gnuplot.info/

i.e. in hundreds of feet (100 ft ≈ 30.48 m). To avoid differences in the inter-comparison of results from the present work with EPACRD arising from the use of different flight routes, the complete flight profiles given by EPCARD in a time resolution of one minute were read from an ASCII file. EPCARD determines the geographical position of an airplane between two neighboring way-points by grand circle navigation, whereas the flight level is assumed to be constant between two way-points. Based on EPCARD dump outputs, which were kindly provided by *V. Mares* in private communication, the minutely flight profiles including time, altitude, geographic position, and the related vertical effective cutoff rigidity were used to estimate dose quantities based on secondary cosmic ray particle spectra calculated in the present work.

Comparison of dose rates along the Greenwich meridian

In order to compare typical dose rates for aircrews with values given by EPACRD in a more quantitative and meaningful manner than in terms of accumulated doses, an artificial flight was constructed. Starting at the geographic South Pole, this flight was bound for the North Pole along the Greenwich meridian with constant altitude at FL 390 corresponding to approximately 200 g/cm^2 or 11.9 km. This covers a range in vertical effective cutoff rigidity from 0 GV to nearly 15 GV (see Fig. 2.5). In Figure 6.3 the resulting effective dose rates as a function of geographical latitude as estimated in the present work (GEANT4-BERT and GEANT4-BIC) are contrasted with values given by EPCARD. To cover a full typical solar cycle, dose rates were determined for solar minimum (July 2006, red lines) and maximum (May 1990, blue lines) conditions. It should be emphasized that all values shown in this figure are based on ICRP-60, and the corresponding quantities according to ICRP-103 are reduced by approximately 35%.

Figure 6.3 ostensively reflects effective dose rates expected due to galactic cosmic radiation along 0° geographical longitude. As described in detail in Chapter 2.1.2, the geomagnetic dipole axis is shifted with respect to the center of the Earth. This results in the highest vertical effective cutoff rigidities around 12° N (see Fig. 2.5), and consequently the dose rates around this latitude are lowest. Apart from this, Figure 6.3 also reflects expected changes in dose rates during a typical solar cycle. As solar modulation predominantly affects the low-energy part of primary galactic cosmic ray spectra, minimum values around 12° N corresponding to about 14.5 GV cutoff are rather similar at solar minimum and maximum. Near the poles, on the other hand, dose rates are reduced by about 50% during solar maximum conditions.

Concerning differences in estimated dose rates, it is obvious from Figure 6.3 that all values are in extraordinary agreement. The two GEANT4 based calculations agree within less than 5% throughout the solar cycle along the whole flight profile. As discussed previously in this chapter, this results from the rather good agreement of secondary particle spectra at typical flight altitudes calculated with both INC models. In turn, this shows that differences in hadronic interaction models and Monte Carlo codes only play a minor role in aircrew dosimetry. Compared with EPCARD, minor differences are observed at low geographical latitudes. This may reflect a somewhat different spectral shape of the primary GCR spectra used in the calculations by *Roesler et al.* (1998, 2002) and *Heinrich et al.* (1999) in combination with a slightly different consideration of the influence of the cutoff on primary spectra.

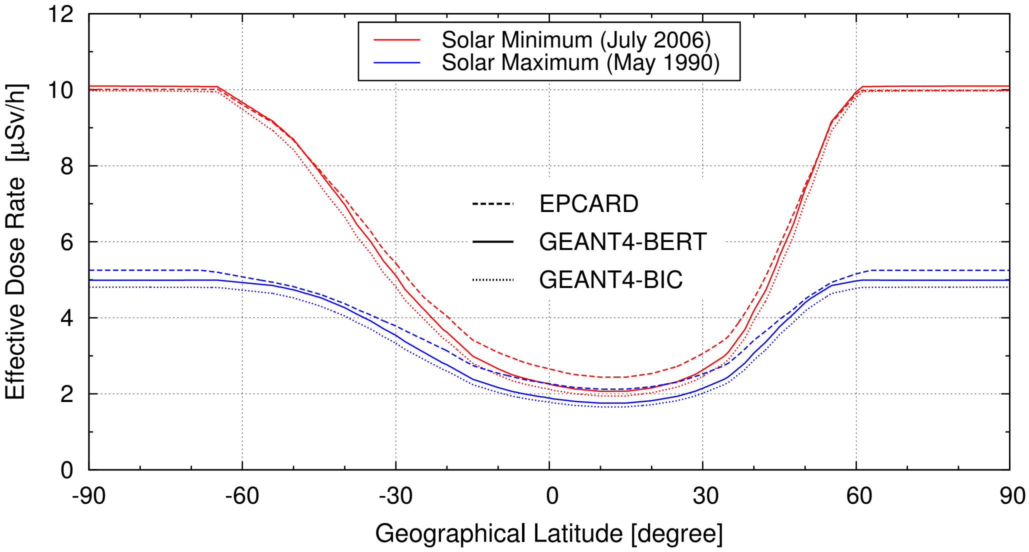

FIGURE 6.3: Comparison of effective dose rates (ICRP-60) as a function of geographical latitude based on secondary cosmic ray particle spectra calculated using the GEANT4-BERT and the GEANT4-BIC INC models with values given by EPCARD. Dose rates are shown for an artificial flight performed at FL 390 ($\approx$ 200 g/cm^2 or 11.9 km) along the Greenwich meridian during solar minimum (July 2006, red lines) and maximum (May 1990, blue lines) conditions.

The resulting maximum deviation of less than 15% between results from the present work and values predicted by EPCARD is fully satisfying in terms of radiation protection. However, it must be emphasized that any discrepancies compared to EPCARD also depend on the time period chosen and, to a minor degree, on the altitude. Differences of 10 - 20% can easily occur at different times due to uncertainties in the related solar modulation strength.

Comparison of accumulated doses along selected flights

As already stated, the minor differences in dose rates between both GEANT4-based calculations and EPCARD also slightly depend on altitude. For this reason it is straightforward to compare accumulated doses along selected flight profiles, as the altitude changes during a flight. For this purpose two typical routes on the northern hemisphere from San Francisco to Paris and from Chicago to Beijing were chosen. On the southern hemisphere flights from Buenos Aires to Auckland and from Sydney to Johannesburg were considered. The corresponding two-dimensional route profiles are illustrated in Figure 6.4. All these flights, including the related flight levels, are based on realistic profiles covering the geographical regions which are most frequently traveled in commercial aviation.

The accumulated total effective and equivalent doses were determined for the four prescribed flights during solar minimum (July 2006) and solar maximum (May 1990) conditions. In Table 6.1 numerical values of the total accumulated effective doses (ICRP-60) are given as obtained using secondary particle spectra calculated with the Bertini and the Binary INC model, respectively. As a reference, accumulated doses given by EPCARD are also listed.

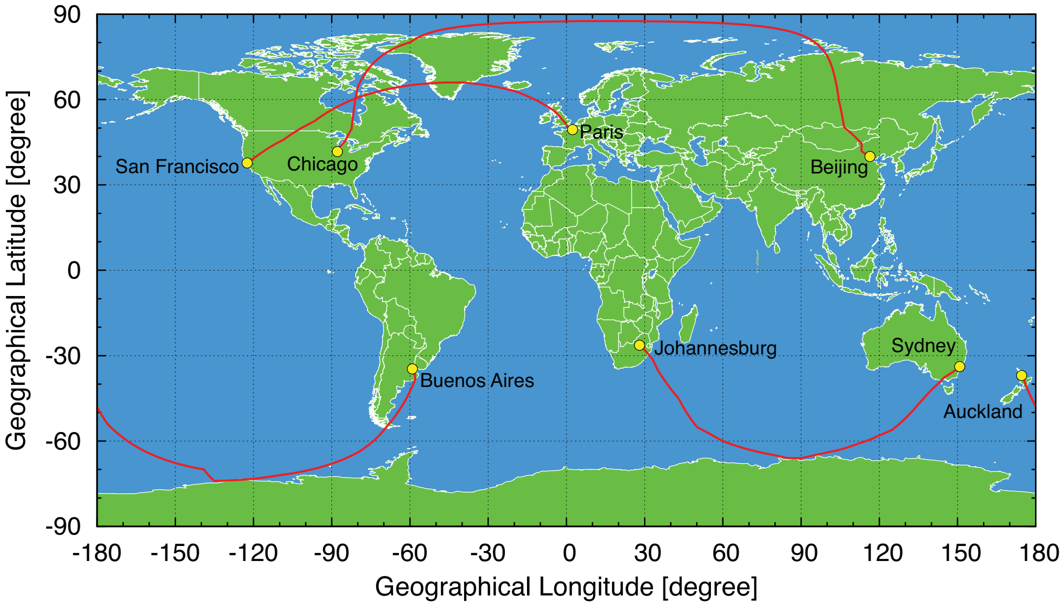

FIGURE 6.4: Illustration of the selected flight routes Chicago - Beijing, San Francisco - Paris, Sydney - Johannesburg, and Buenos Aires - Auckland.

TABLE 6.1: Numerical values for total accumulated effective doses (ICRP-60) due to GCR along selected flight routes. Doses given by EPCARD are compared with estimations based on particle spectra calculated in the present work (GEANT4-BERT, GEANT4-BIC).

ACCUMULATED EFFECTIVE DOSE IN JULY 2006 (SOLAR MINIMUM)

Flight	Duration [min]	Max. Altitude [km]	EPCARD [μSv]	GEANT4-BERT [μSv]	GEANT4-BIC [μSv]
Chicago - Beijing	791	11.3	77.5	75.3	78.3
San Francisco - Paris	555	11.9	75.8	75.2	75.1
Sydney - Johannesburg	825	11.9	83.9	81.6	83.8
Buenos Aires - Auckland	980	12.2	109.2	108.7	108.3

ACCUMULATED EFFECTIVE DOSE IN MAY 1990 (SOLAR MAXIMUM)

Flight	Duration [min]	Max. Altitude [km]	EPCARD [μSv]	GEANT4-BERT [μSv]	GEANT4-BIC [μSv]
Chicago - Beijing	791	11.3	45.8	41.3	41.5
San Francisco - Paris	555	11.9	41.2	38.6	37.6
Sydney - Johannesburg	825	11.9	48.9	45.1	45.0
Buenos Aires - Auckland	980	12.2	60.6	57.2	55.7

Obviously, all accumulated doses agree very well reflecting the consistency of dose rates inter-compared previously. For the solar conditions during July 2006, i.e. solar minimum, relative differences to EPCARD are less than 5%. During solar maximum conditions in May 1990 the differences are somewhat higher, but still less than 10%.

Concerning the two GEANT4 based dose estimations, the values for all flights are very similar. This again shows that differences in secondary particle spectra between computations with the Bertini and the Binary INC model are negligible in terms of accumulated doses during flights. In addition, the comparison of numerical values shows that none of the two models gives consistently higher doses. Therefore, none of the models can be prioritized in terms of providing a conservative dose estimation. Furthermore, it can be concluded that also differences in calculations concerning different primary GCR spectra and slightly different geometries as used in EPCARD are of minor importance. Thus, all methods of assessing route doses may be applied equally well in aircrew dosimetry.

6.1.2 Comparison of ambient dose equivalent with ICRU reference data

The International Commission on Radiation Units and Measurements has released so-called reference data for ambient dose equivalent rates in aviation in *ICRU* (2010, Report 84). This report aims on providing experimental data against which methods of assessing dose values using calculations may be compared for validation purposes.

The main basis of the ICRU reference data comprises approximately 20000 individual measurements of ambient dose equivalent on-board aircrafts since 1990. This dataset is summarized and compiled in a report of the European Radiation Dosimetry Group (EURADOS) published by the European Commission (*EC*, 2004). For the experimental determination of dose rates associated to the complex field induced by galactic cosmic radiation at aircraft altitudes, a variety of instruments was employed. The low-LET and non-neutron component was, amongst others, measured with tissue-equivalent proportional counters (TEPCs), ionization chambers, silicon-based detectors, and scintillation detectors. For measurements of the high-LET and the neutron component e.g. extended-range survey meters, Bonner sphere spectrometers, TEPCs, and passive detectors were applied. In order to allow interpretation and combination of results from different instruments, nearly all devices have been calibrated to ambient dose equivalent (H*(10)) in a variety of reference fields, which are traceable to national standards.

As discussed in more detail in *ICRU* (2010, Report 84), the relative standard deviation of H*(10) measurements simultaneously performed on-board aircrafts with different devices is in the order of 10%. Another 10 - 20% uncertainty adds to this for measurements carried out on different dates. This results from short-term changes in solar activity, the related variations in primary GCR intensity near Earth as well as related variations in the Earth's magnetic field affecting the cutoff rigidity at certain geographical positions. Therefore, the relative combined standard uncertainty for the dataset chosen by the *ICRU* (2010, Rep. 84) is reported to be in the order of 15 - 30%. This is largely consistent with a 25% uncertainty estimated by EURADOS (*EC*, 2004).

The prescribed large set of experimental data was fitted using a Bayesian approach (see

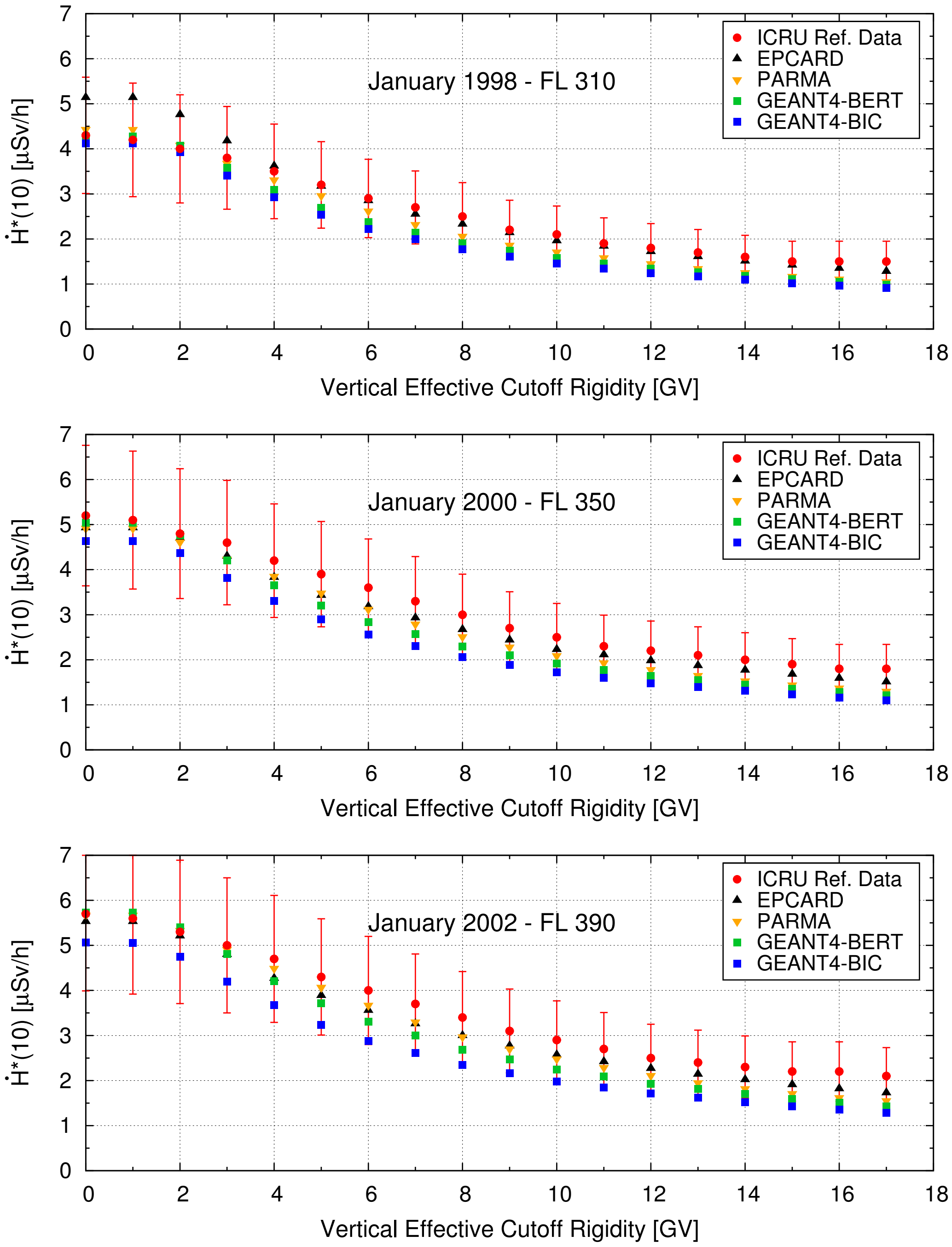

FIGURE 6.5: Comparison of reference ambient dose equivalent rates as given by *ICRU* (2010, Report 84) with calculations from the present work using GEANT4 with the Bertini and Binary INC model. Additionally, $\dot{H}^*(10)$ values estimated by EPCARD and PARMA (*Sato et al.*, 2006, 2008) are depicted in the top panel for January 1998 at FL 310, in the middle panel for January 2000 at FL 350, and in the bottom panel for January 2002 at FL 390.

also *Wissmann et al.*, 2010), in order to derive reference levels of ambient dose equivalent rates during solar cycle 23 for altitudes corresponding to FL 310, FL 350, and FL 390. These reference data cover the whole range of vertical effective cutoff rigidity from 0 GV to 17 GV and are assigned to the periods of January 1998, 2000, 2002. This corresponds to solar modulation strengths of 427 MV, 752 MV, and 977 MV (*Usoskin et al.*, 2005).

In Figure 6.5 reference ambient dose equivalent rates as given by *ICRU* (2010, Report 84) from 0 GV to 17 GV vertical effective cutoff rigidity are compared with values determined in the present work based on GEANT4 transport calculations. The top panel shows data for January 1998 at FL 310, the middle panel for January 2000 at FL 350, and the bottom panel for January 2002 at FL 390. In addition, dose rates predicted by EPCARD and the PHITS-based Analytical Radiation Model in the Atmosphere[3] (PARMA) developed by *Sato et al.* (2006, 2008) are also included. Note that the error bars shown for the reference dose rates are the 30% uncertainty as recommended in *ICRU* (2010, Rep. 84) for an inter-comparison.

It is obvious from Figure 6.5 that results from the present work agree remarkably well with the ICRU reference data at low cutoff rigidities. At rigidities above several GV, on the other hand, ambient dose equivalent rates appear to be somewhat underestimated. Dose rates based on particle spectra calculated with the Bertini model deviate up to 30% at very high cutoffs, depending on the time period and the flight level. Values based on calculations with the Binary INC model may even deviate by about 5% more, in particular at the higher flight levels shown in the middle and bottom panel of Figure 6.5. Nearly the same discrepancies as for GEANT4-BERT are observed with the PARMA model (*Sato et al.*, 2006, 2008) at low and high cutoffs, whereas at medium cutoffs PARMA is somewhat closer to the reference data. At cutoff rigidities above about 8 GV, ambient dose equivalent rates estimated with EPCARD match best with the measurements. Apart from the slight overestimation for the conditions shown in the top panel of Figure 6.5, EPCARD also agrees very well with the PARMA model and the GEANT4-based results at low cutoffs.

All $\dot{H}^*(10)$ values contrasted with the ICRU reference data in Figure 6.5 are based on particle transport calculations in the atmosphere. Uncertainties may, therefore, arise from different assumptions on the GCR primary spectra on top of the atmosphere as well as the characteristics of the transport code, the cross section dataset, and the models describing high-energy hadronic interactions. The main sources of uncertainty, however, result from differences in the method of accounting for variations in solar activity and the use of the vertical cutoff rigidity instead of taking the exact angular distribution of the cutoff into account. Dose rates derived with solar potentials for consecutive months can for example easily vary by about 20%. A sensitivity analysis in terms of varying the cutoff by ±0.3 GV additionally showed that about 10% uncertainty for dose rates may arise. This means that the range of uncertainty for all methods of assessing dose rates is in the order of 15 - 30%. This is the same range as estimated in *ICRU* (2010, Rep. 84) for the dataset from which the reference values were derived. Therefore, all dose rates shown in Figure 6.5 are consistent within the range of uncertainty.

Note that according to ICRU Reports 47 and 66 (*ICRU*, 1992, 2001) an overall uncertainty of 30% for a single measurement of operational quantities such as H*(10) is considered acceptable. Following ICRU Report 84 (*ICRU*, 2010) this means for aircrew dosimetry that

---

[3] http://phits.jaea.go.jp/expacs

"... the combined relative standard uncertainty should not exceed 30% for an assessment of an ambient dose equivalent equal to or greater than an annual dose of 1 mSv."
The maximum differences of calculated dose rates at high cutoffs of approximately 30% compared with the ICRU reference data only contribute little to the total accumulated dose for single flights. This is due to the rather small dose rates with respect to low cutoffs, and because most of the journeys in aviation are on the northern hemisphere below about 5 GV cutoff. Consequently, accumulated doses along flight routes determined by all methods of dose assessment using calculations shown in Figure 6.5 agree rather well. This was already demonstrated in the previous section of this chapter. Moreover, any differences in annual doses estimated by EPCARD, PARMA, and based on GEANT4 calculations are expected to be much less than 30%, because minor differences in dose rates at certain solar conditions and geographical positions are likely to cancel out. For this reason, any of the approaches to determine doses for aircrews presented in this section are equally well suited for radiation protection purposes.

6.2 Doses in aviation due to solar cosmic rays

Apart from the rather predictable exposure to radiation induced by galactic cosmic rays discussed in the previous section, sudden and randomly occurring bursts of energetic particles emitted from the Sun can lead to increased radiation levels at aircraft altitudes and on ground. General characteristics of such solar energetic particle (SEP) events and ground level enhancements (GLE), including related and accompanying phenomena, acceleration mechanisms on the Sun, and their occurrence rate were extensively summarized in Chapter 2.2. Furthermore, useful data sources from interplanetary and ground-based observations as well as the modeling techniques to derive spectral, temporal, and spatial characteristics of GLEs from Neutron Monitor count rates were discussed there.
Lantos and Fuller (2003) studied possible hazards for aircrews due to increased radiation levels during a total number of 64 GLEs. They found that only 18 of them were likely to exceed an accumulated dose equivalent of 30 μSv during typical long-haul flights. This is comparable to the dose equivalent received from GCR during solar maximum for similar flights (see Tab. 6.1). The vast majority of GLEs are, therefore, of minor importance in terms of contributions to total lifetime exposures of flight attendants and pilots. For the first five GLEs in the chronological list, however, *Lantos and Fuller* (2003) estimated route doses larger than 1 mSv and for the most intense event ever recorded on ground, GLE 5 which occurred on 23 February 1956, a dose equivalent of approximately 5 mSv was derived. This means that during a single flight the limit of 1 mSv annual effective dose may be exceeded, above which monitoring of aircraft crews is mandatory according to the European Directive (*EU*, 1996). It should be noted, that all the dose estimations exceeding 1 mSv for long-haul flights are subject to uncertainties larger than a factor of two, since only few ground-based measurements are available prior to 1960. In contrast, the largest GLE examined in the work of *Lantos and Fuller* (2003) after the February 1956 event, GLE 42 on September 29 1989, was well detected by numerous Neutron Monitors and other ground-based detectors. For this GLE an accumulated route dose for a flight from Paris to San Francisco of approximately 300 μSv was estimated.

Recently, the Working Group 11 of the European Radiation Dosimetry Group (EURADOS) decided to select GLE 42 for an inter-comparison of route doses determined by several institutes. All calculations required for this task were performed in the frame of the present work, and the data have been provided to EURADOS. After a short description of the characteristics of GLE 42, including the primary proton spectra and the time profile as defined in EURADOS/WG11, these results are presented. In addition to the investigations for EURADOS, the impact of the primary spectrum of solar protons on estimated dose rates and accumulated doses in aviation is also studied in the following.

6.2.1 Observations and characteristics of GLE 42

During the ground level enhancement on September 29, 1989, no indications of a solar flare on the Sun's visible disk were reported, as concisely reviewed and summarized by *Lovell et al.* (1998). On photographs published by *Swinson and Shea* (1990), flare activity with a looped prominence was seen behind the limb for more than ten hours during the event. The event itself was accompanied by intense radio and X-ray emission with a peak intensity of X9.8 observed on-board GOES satellites around 11:30 UT. However, *Cliver et al.* (1993) reported γ-ray emissions on the western hemisphere of the visible disk. They suggested a broad shock driven by a coronal mass ejection (CME) being responsible for these observations. As discussed in more detail in Chapter 2.2, a fast CME-driven shock, encompassing regions of the Sun's surface near the foot-point of the Sun-Earth magnetic field line ($\approx$ 60°W), is likely to accelerate coronal particles that, in turn, can travel to Earth along the field line and give rise to a GLE.

Ground-based observations

The enhanced solar proton flux during GLE 42 triggered increases in count rates of Neutron Monitors all over the world. With a maximum increase of about 404% recorded by the Calgary Neutron Monitor in the time interval from 12:55 UT to 13:00 UT, this event has been ranked amongst the most intense observed since February 1956. It was even detected by the Australian Neutron Monitor station Darwin, which is located in equatorial regions at a vertical effective cutoff rigidity of 14.2 GV. Moreover, as reported by *Swinson and Shea* (1990), increased count rates were also registered by underground muon telescopes such as Embudo which has a threshold rigidity of approximately 19 GV. *Lovell et al.* (1998) examined several other muon detectors and found an upper rigidity of 30 GV being consistent with all observations.

Figure 6.6 shows measurements with several Neutron Monitors during the September 1989 event. Depicted are relative count rate increases of four stations on the northern hemisphere (Calgary at 1.1 GV, Goose Bay at 0.6 GV, Climax at 3 GV, and Jungfraujoch at 4.5 GV) and one Antarctic station (Mawson at 0.2 GV). Apparently, two distinct peaks were observed by some Neutron Monitors, whereas others only recorded one. Amongst others, *Vashenyuk et al.* (1997) suggested different directions of approach due to particles following different paths through interplanetary space. They explained the delay between particle arrivals by a

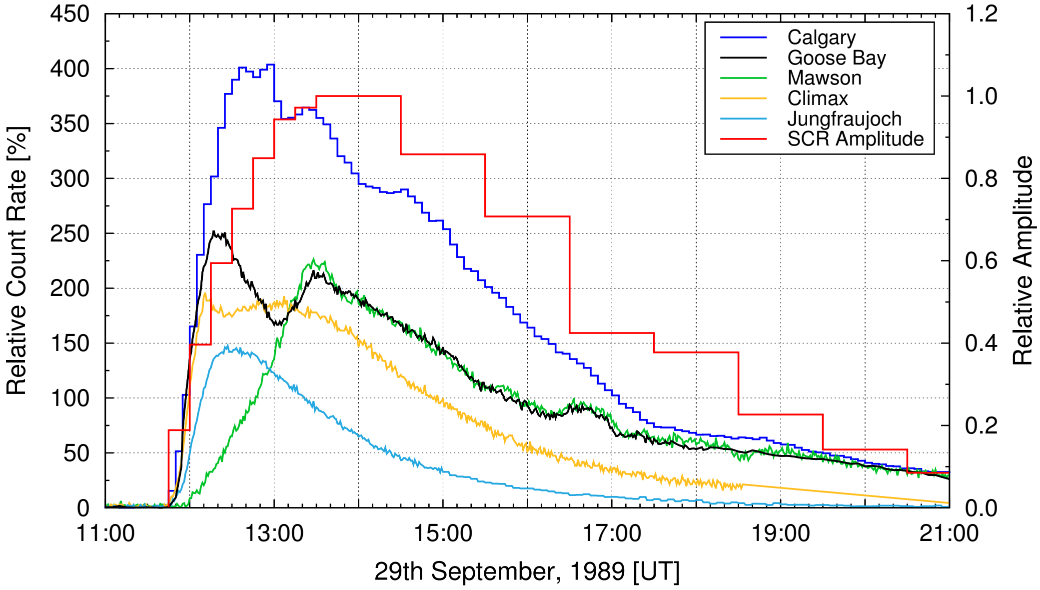

FIGURE 6.6: Relative count rate increases recorded by selected Neutron Monitor stations during GLE 42 on September 29, 1989. The red curve depicts the relative amplitude of solar cosmic ray flux as assumed for the EURADOS task.

looped structure of the interplanetary magnetic field with both foot points anchored on the Sun. As described in Chapter 2.2.2, ground-based cosmic ray detectors are inherently directional instruments due to the fact that charged particles of given rigidity and momentum direction follow specific paths in the magnetospheric field. This in turn defines the asymptotic viewing cone of a Neutron Monitor station. The fact that some stations observed only one peak, therefore, reflects the sensitivity of a Neutron Monitor to solar protons arriving from a specific direction of approach at the magnetopause. Furthermore, it indicates that the spectral distribution might have changed during the event. This is also suggested by *Lovell et al.* (1998) who found that the second peak was not recorded by any muon detector indicating a softening of the spectrum at later times.

Spectral characteristics

The spectral and temporal characteristics of solar protons during GLE 42, as well as the spatial anisotropy was analyzed by several research groups using the worldwide network of cosmic ray stations (see e.g. *Bieber and Evanson*, 1991; *Morishita et al.*, 1991; *Lovell et al.*, 1998). For the computation of doses to aircrews in the frame of the EURADOS/WG11 task, however, the spectrum derived by *Smart et al.* (1991) was selected. Consistent with other authors, the analyses by *Smart et al.* (1991) have shown that a modified power law for the relativistic solar proton flux agrees rather well with Neutron Monitor observations.

The differential intensity $j(R,t)$ with respect to the rigidity R in units of [1/(cm$^2\cdot$s$\cdot$sr$\cdot$GV)] is given as

$$j(R,t) = \begin{cases} A(t)\cdot R^{-\gamma} & \text{for } R < 2\text{GV} \\ A(t)\cdot R^{-[\gamma+\delta\gamma(R-2)]} & \text{for } R \geq 2\text{GV}, \end{cases} \tag{6.3}$$

where the power law exponent γ has a value of 3.0 and the change in the exponent per GV is $\delta\gamma = 0.3$ (for $R \geq 2$ GV). For the amplitude $A(t)$ at time t, a maximum value of 10.6 [1/(cm$^2\cdot$s$\cdot$sr$\cdot$GV)] was derived in the time interval from 13:30 UT to 14:30 UT. The complete amplitude-time profile is shown in Figure 6.6 (red line), where values are normalized to the maximum amplitude.

It should be noted that for the EURADOS investigations the spectral shape was presumed to be constant in time. Neglecting a potential softening of the spectrum during the event allows a conservative dose estimation which is required in radiation protection. Furthermore, a completely isotropic flux of solar protons near Earth was assumed for the whole duration of GLE 42. As for example shown by *Lovell et al.* (1998), GLE 42 in fact had a strongly pronounced isotropic component justifying this presumption for dose assessment. Moreover, *Bütikofer and Flückiger* (2011) studied differences in doses for aircrews in case an isotropic solar proton flux is assumed instead of accounting for anisotropy. They found that route doses during GLE 42 agree within approximately 10% for most of the flights considered. Only for two flights doses were enhanced by about 25% in the isotropic case. In terms of radiation protection, this again justifies the assumption of complete isotropy for the EURADOS investigations.

As discussed in every detail in Chapter 2.2.2, modeling GLEs using Neutron Monitor count rates is a rather tricky task. Difficulties arise e.g. from calculating accurate asymptotic cones of acceptance, assuming a proper pitch-angle distribution to describe anisotropy, as well as using an appropriate yield function. Therefore, many different functions of the differential solar proton intensity $j(R,t)$ can reproduce the observed count rate increases equally well. To estimate the impact of different primary proton spectra for GLE 42 on calculated dose rates at aircraft altitudes, a spectrum derived by *Dyer et al.* (2003a,b) was studied in addition to that of *Smart et al.* (1991). This spectrum is based on a Weibull fit of *Xapsos et al.* (2000) that was used by *Dyer and Lei* (2001) to calculate neutron fluxes and doses in the atmosphere. Because the original Weibull spectrum was fitted to space data with energies below 300 MeV only, it has been discovered that it was too soft to reproduce ground-based observations. Therefore, the differential intensity of solar protons was refitted by *Dyer et al.* (2003a,b) including Neutron Monitor observations to derive the spectral characteristics in the relativistic energy range above several hundreds of MeV. The final Weibull distribution for the differential solar proton flux $j(E_k,t)$ with respect to the kinetic energy E_k as derived for the maximum phase of the event around 14:30 UT is given as

$$j(E_k,t) = j_0(t)\tau\alpha E_k^{\alpha-1}\exp(-\tau E_k^{\alpha}), \tag{6.4}$$

where $\tau = 0.994$, $\alpha = 0.3158$ and the maximum amplitude $j_0 = 39800$ [1/(cm$^2\cdot$s$\cdot$sr$\cdot$MeV)]. Note that also for this spectrum complete isotropy and a constant shape was assumed during the event. As intensity-time profile for the Weibull spectrum the relative count rate increase of the Climax Neutron Monitor, normalized to the maximum increase, was used (see discussion later in this section).

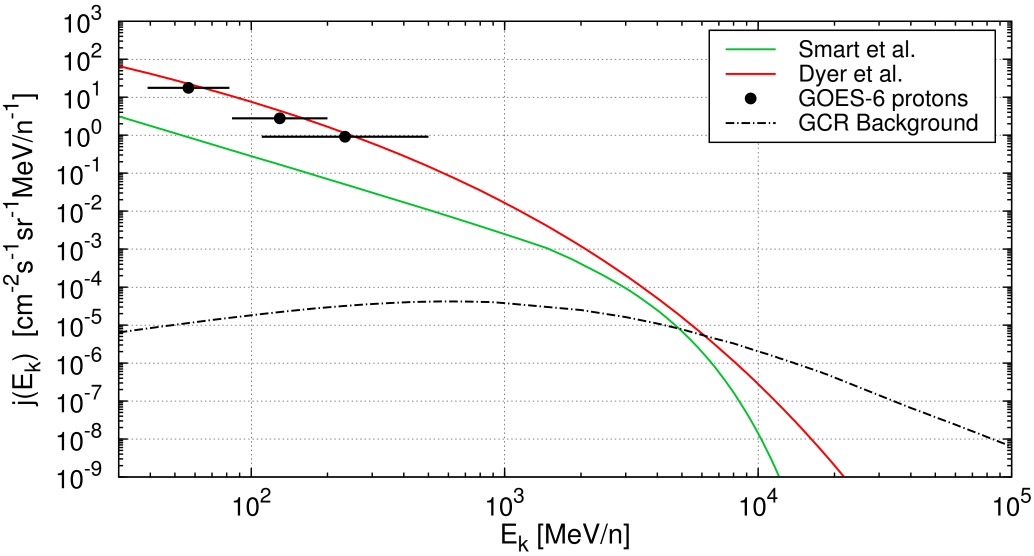

FIGURE 6.7: Differential solar proton flux during GLE 42 on September 29, 1989, as determined by *Smart et al.* (1991, green line) and used for the EURADOS investigations. The red line shows the spectrum derived by *Dyer et al.* (2003a,b) at the maximum phase of the event. For comparison, differential proton intensities measured on-board GOES-6 (black dots) and the galactic cosmic ray background in September 1989 (black dash-dotted line) are also depicted.

Both the spectrum reported in *Smart et al.* (1991) and the one reported in *Dyer et al.* (2003a,b) are shown in Figure 6.7 as differential intensity with respect to the kinetic energy. In addition, measurements on-board the GOES-6 satellite and the galactic cosmic ray background for September 1989 as given by the model of *Usoskin et al.* (2005) are also depicted. Apparently, rather large differences are observed for the solar spectra in terms of both spectral shape and absolute intensity. The dominant discrepancies at energies below about 500 MeV, however, do not have a significant impact on dose rates at aircraft altitudes as these protons and the secondaries generated only contribute to a minor degree to the radiation environment in the lower atmosphere. Differences at higher energies, on the other hand, can lead to significantly differing dose rates as will be discussed in subsequent paragraphs. Comparison of the solar spectra with proton measurements on-board GOES demonstrates the versatility of the Weibull fit allowing to reproduce both interplanetary and ground-based observations rather well.

6.2.2 Dose rates in aviation during GLE 42

The differential intensities of solar protons shown in Figure 6.7 were transported through the Earth's atmosphere using GEANT4, and all secondaries generated were computed as described in Chapter 5. Based on investigations of *Lovell et al.* (1998) a maximum rigidity cutoff of 30 GV was considered. All calculations were again performed applying either the Bertini or the Binary INC model at intermediate energies. As already stated previously, a completely isotropic flux of solar protons near Earth was assumed during the whole event. In this case the cutoff rigidity fully accounts for the influence of the magnetosphere on the primary proton intensity on top of the atmosphere. Secondary particle spectra and related dose quantities were determined in steps of 1 GV in the range of 0 - 6 GV and in steps of 2 GV at higher rigidities. Dose rates at any altitude or geographic position and accumulated doses for aircrews were then estimated as described in Section 6.1.

Although the spectral fluence rate distributions of secondary particles induced by solar protons are very similar in shape compared to those induced by galactic cosmic rays (also see Chap. 5.6), the contributions of individual particle species to the total fluence and dose rates are somewhat different. To illustrate this, Figure 6.8 shows the fractions of effective dose of individual particle species to total effective dose following ICRP-103 for the September 1989 event at 0 GV cutoff.

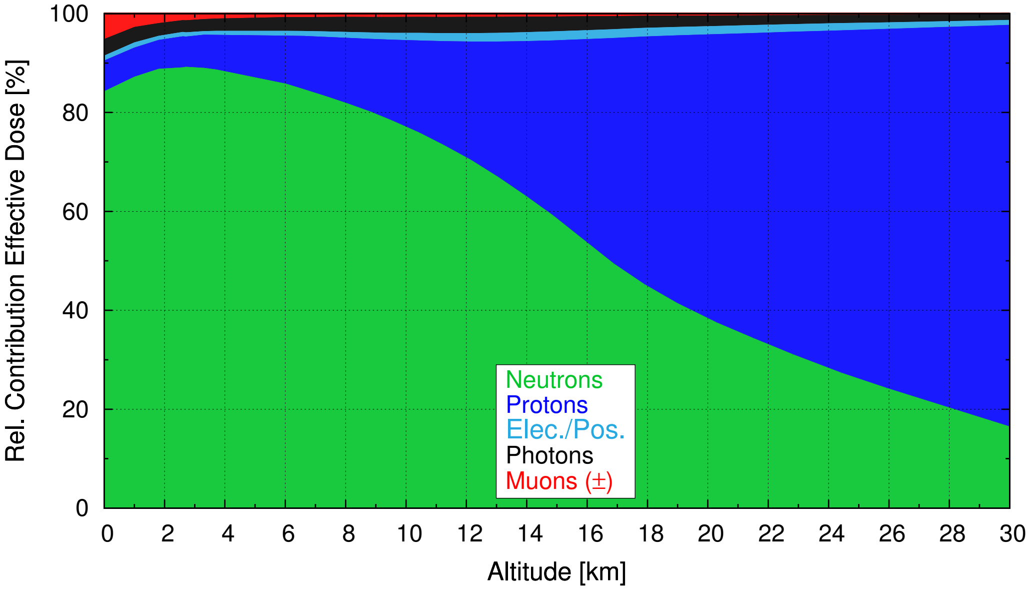

FIGURE 6.8: Relative contributions of individual secondary particle species to total effective dose (ICRP-103) during GLE 42 as a function of altitude. The corresponding fractions were calculated for 0 GV cutoff at the maximum phase of the event on September 29, 1989, with the primary solar proton spectrum of *Smart et al.* (1991).

Comparison with the analog figure for galactic cosmic radiation (Fig. 6.2) reveals that the relative contribution of the hadronic component is strongly enhanced during GLEs. While at altitudes above 20 km primary solar protons are the dominant species, neutrons account for more than 2/3 of the total particle flux and the dose at aircraft altitudes (9 - 13 km) and below. This basically reflects the significantly softer primary spectrum of solar protons with respect to GCR spectra. Protons in the energy range from several hundreds of MeV to a few GeV predominantly excite atmospheric nuclei in spallation reactions. Pion production, on the other hand, is rather low in this energy region due to the large pion rest mass of $\approx$ 140 MeV/c^2 (*Nakamura et al.*, 2010). As a result of the steeply decreasing solar spectra at high energies, the fractions of pions, muons as decay products, as well as photons, electrons, and positrons are much lower with respect to GCR.

In order to illustrate absolute values of dose rates at typical cruising altitudes during long-

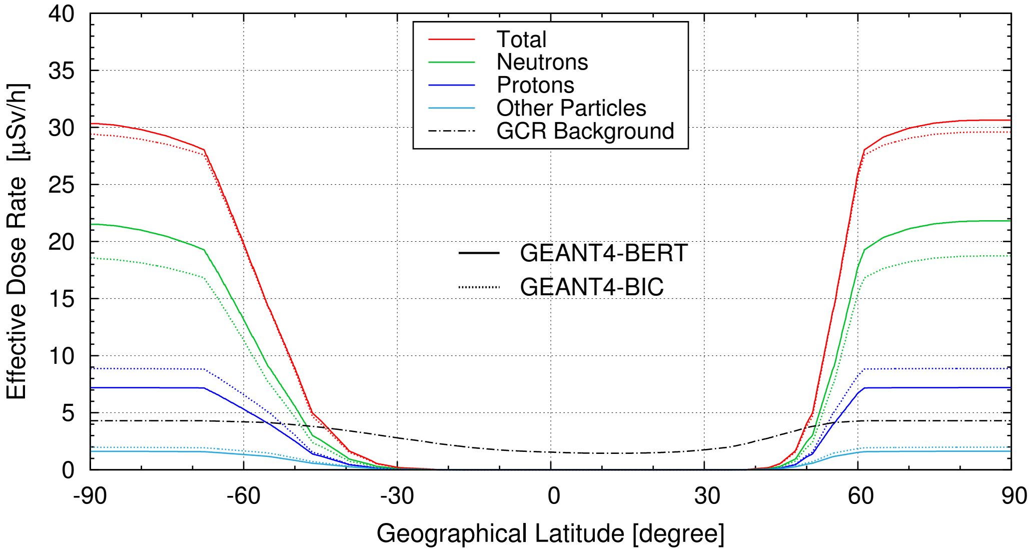

FIGURE 6.9: Effective dose rates (ICRP-103) along the Greenwich meridian at FL 390 during the maximum phase of GLE 42. Depicted are total and individual dose rates of neutrons, protons, and other species as obtained applying the Bertini or the Binary INC model in the GEANT4 calculations and using the solar spectrum of *Smart et al.* (1991). The dash-dotted line illustrates the GCR background during September 1989.

haul flights, Figure 6.9 shows effective dose rates (ICRP-103) along the Greenwich meridian at FL 390 during the maximum phase of GLE 42. Depicted are total and individual dose rates of neutrons, protons, and other species as obtained applying the Bertini or the Binary INC model in the GEANT4 transport calculations. In addition, the total effective dose rate due to galactic cosmic radiation during the solar maximum conditions in September 1989 is shown ($\phi \approx 1197$ MV). Note that all dose rates for GLE 42 in Figure 6.9 were estimated based on the proton spectrum of *Smart et al.* (1991) selected for the EURADOS inter-comparison. Values obtained using the spectrum of *Dyer et al.* (2003a,b) are a factor of approximately 5 higher as discussed in the subsequent paragraph.

It is obvious from Figure 6.9 that even considering an isotropic flux of solar protons resembling a worst case scenario, dose rates are only enhanced in polar and sub-polar regions during a GLE. This is a direct consequence of the steeply decreasing primary spectra leading to a much more pronounced gradient in particle fluence and dose rates with respect to the cutoff rigidity. At a vertical effective cutoff rigidity of about 5 GV the intensity of solar protons on top of the atmosphere is reduced by geomagnetic shielding to the level of the galactic background. Therefore, almost no enhancement in dose rates is observed from 50°N to 40°S. Note that the estimation of dose rates and route doses for aircrews during the September 1989 event is based on values for the vertical effective cutoff rigidity reported in *Smart and Shea* (1997) for that period. These are valid for calm geomagnetic conditions. With a K_p index of about 2 on September 29, 1989 (*Dyer et al.*, 2003b) disturbances in the geomagnetic field were rather low, indeed. For the sake of completeness, however, it should be mentioned that GLEs are often accompanied by geomagnetic storms, leading to strong disturbances in the magnetic field ($K_p \geq 5$). This in turn results in a suppression of the cutoff, allowing more lower energetic protons to enter the atmosphere at lower latitudes. Thus, dose rates and accumulated doses for aircrews may be further enhanced.

According to Figure 6.9 a maximum effective dose rate following ICRP-103 of approximately 30 μSv/h at FL 390 ($\approx$ 200 g/cm^2 or 11.9 km) is estimated for the EURADOS investigations at 0 GV cutoff. Note that *Bütikofer and Flückiger* (2011) estimated a maximum effective dose rate following ICRP-60 of approximately 27 μSv/h at 0 GV cutoff and an atmospheric depth of 250 g/cm^2. Exactly the same value for the dose rate at these conditions was determined in the present work. This strongly indicates consistency of the methods of dose assessment.

Concerning differences in dose rates arising from secondary particle spectra calculated with different INC models for hadronic interactions, it is obvious from Figure 6.9 that they are only of minor importance in terms of total dose rates. Although the secondaries induced by solar protons are strongly dominated by neutrons and protons (see Figs.6.8 and 6.9) and accordingly differences in individual intensities given by the Bertini and the Binary INC model are pronounced, they cancel out regarding total dose. As it was already the case for galactic cosmic radiation, this shows that differences in both INC models only play a minor role at aviation altitudes and that both models are equally well suited for aircrew dosimetry.

6.2.3 Accumulated doses along selected flights during GLE 42

Apart from the prescribed strong dependence on the cutoff, i.e. the geographic position, and the flight level, dose rates in the atmosphere and accumulated doses for aircrews during a GLE highly depend on the phase of the event. Therefore, the time profiles of all flights considered in the following were adjusted that the peak intensity of GLE 42 was experienced while cruising altitude at high latitudes was reached. As for galactic cosmic rays, two typical routes on the northern hemisphere from San Francisco to Paris and from Chicago to Beijing were chosen, and on the southern hemisphere flights from Buenos Aires to Auckland and from Sydney to Johannesburg were considered. The corresponding two-dimensional flight profiles are shown in Figure 6.4.

To illustrate the dose rates estimated for a typical long-haul flight during the September 1989 event, Figure 6.10 shows effective dose rates (ICRP-103) as a function of time for the polar flight from San Francisco to Paris. In the top panel results are depicted for the primary solar proton spectrum reported by *Dyer et al.* (2003a,b) and in the middle panel for the EURADOS investigations based on the primary spectrum of *Smart et al.* (1991). In the bottom panel the vertical effective cutoff rigidity and the flight level are shown in order to demonstrate the adjustment of the flight time for an estimation of maximum doses. Note that all dose rates in Figure 6.10 were obtained using the Bertini INC model. In addition to the dose rates shown in the top and middle panels (red lines), the assumed intensity-time profiles for GLE 42 are also depicted (black lines). In case of the EURADOS inter-comparison this profile was predefined by members of Working Group 11. For dose assessment based on the primary spectrum by *Dyer et al.* (2003a,b) the profile as defined by the count rate increase of the Climax Neutron Monitor, normalized to the maximum increase, was used. This NM was chosen as it registered both peaks and was fully exposed to the isotropic component in later phases of the event (see Fig. 6.6). Note that using intensity-time profiles given by other Neutron Monitors such as Calgary or Goose Bay influences dose estimates only by 10%.

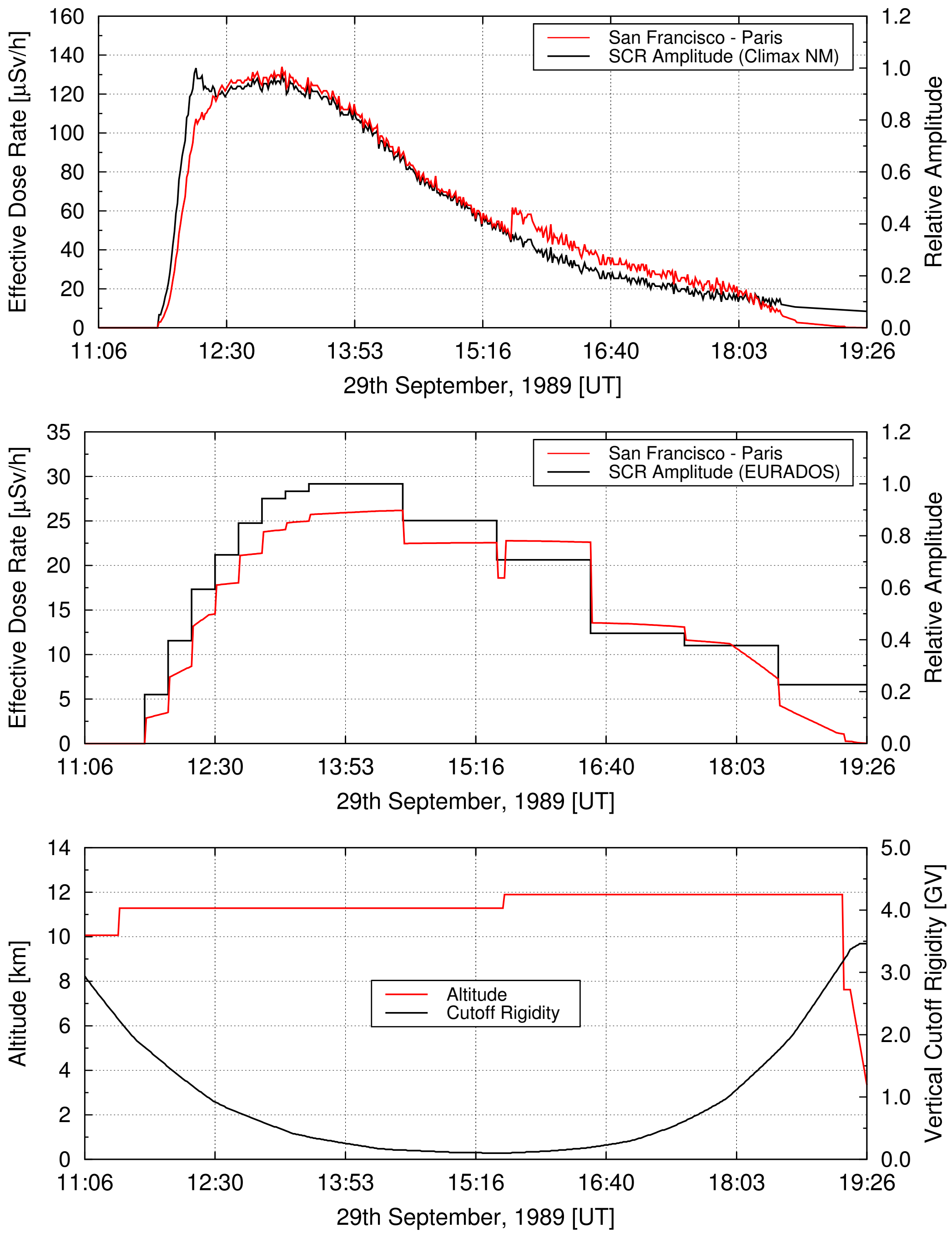

FIGURE 6.10: Effective dose rates (ICRP-103) estimated for a typical long-haul flight from San-Francisco to Paris during GLE 42 on September 29, 1989. In the top panel results are depicted for the primary solar proton spectrum reported by *Dyer et al.* (2003a,b) and in the middle panel based on the primary spectrum of *Smart et al.* (1991). Additionally, the intensity-time profiles as defined by the readings of the Climax Neutron Monitor (top panel, black line) and as assumed for the EURADOS investigation (middle panel, black line) are depicted. In the bottom panel the vertical effective cutoff rigidity and the altitude along the flight profile are shown.

Comparison of the dose rates estimated with the solar proton spectrum by *Dyer et al.* (2003a,b, top panel) and those estimated using the spectrum by *Smart et al.* (1991, middle panel panel) shows the impact of the primary spectrum on the procedure of dose assessment for aircrews during GLEs. Since the primary proton intensity given by *Dyer et al.* (2003a,b) is somewhat higher and the spectrum is much harder (see Fig. 6.7), the related maximum effective dose rate exceeds estimations for the EURADOS task up to a factor of 5. While a maximum effective dose rate of approximately 130 μSv/h is determined with the hard spectrum, a value of only 26 μSv/h is obtained with the softer. This basically reflects the difficulties and uncertainties involved in the techniques to derive the spectral characteristics of a GLE from ground-based observations, although both spectra are consistent with Neutron Monitor data. As for none of the primary spectra considered in the present work absolute correctness can be claimed, an uncertainty of a factor 5 in dose rates, retrospectively determined for GLEs, must presently be accepted.

Concerning accumulated effective doses for the four intercontinental flights outlined above, the differences obtained for the two primary spectra are somewhat smaller but still in the order of a factor of 3 - 4. This is a result of the different time-profile chosen for studies using the spectrum of *Dyer et al.* (2003a,b). The numerical values for accumulated effective doses (ICRP-103) are listed in Table 6.2 for both solar spectra and the two INC models applied in the particle transport simulations (GEANT4-BERT and GEANT4-BIC). In addition, the route doses due to galactic cosmic radiation in September 1989 are also contrasted.

Predominantly depending on the primary spectrum used for dose assessment, but also on the flight profile, route doses for the four flights considered range from approximately 90 μSv to more than 500 μSv. The differences and related uncertainties up to a factor of 4 arising from the use of different primary spectra appear somewhat large, but in fact they are very consistent with values reported by other authors for this event. For example *Bütikofer and Flückiger* (2011) estimated an accumulated effective dose following ICRP-60 of 109 μSv for the same flight from Chicago to Beijing. This compares to a value of 116 μSv determined in the present work using the primary proton spectrum of *Smart et al.* (1991). On the other hand, *Dyer et al.* (2003a) report an accumulated ambient dose equivalent of 571 μSv for a flight from London to Los Angeles. Based on the corresponding flight profile and the primary proton spectrum given by *Dyer et al.* (2003a), a largely consistent dose equivalent of 390 μSv was estimated in the present work. Also *Matthiä* (2009) and *Lantos and Fuller* (2003) report effective doses in the range of 100 - 400 μSv for typical intercontinental long-haul flights. This evidently shows the consistency of all results presented in this section with results of other authors. Furthermore, it confirms the range of uncertainty.

In terms of radiation protection the large uncertainties discussed above are basically not of major concern. The maximum route dose of about 0.5 mSv for the flight from Buenos Aires to Auckland is equal to five such flights during solar minimum conditions. Therefore, contributions of GLEs to lifetime exposures of flight attendants and pilots are rather small, even if the event is assumed to be intense. However, given the fact that GLEs are not predictable and several enhancements may be observed within a rather short period of time, retrospective dose assessment is required. Note that for example from August through October 1989 five GLEs occurred. Apart from the unpredictable occurrence rate, the intensity of GLEs strongly varies as well. Also for this reason dose assessment for GLEs is required, although the majority of events is no hazard in terms of doses for aircrews or on ground.

TABLE 6.2: Accumulated effective doses (ICRP-103) on selected flights during GLE 42 on September 29, 1989. Values are given for the solar spectra of *Dyer et al.* (2003a,b) and *Smart et al.* (1991), respectively. All dose estimates are based on calculations applying either the Bertini or the Binary INC model. In addition, the route doses due to galactic cosmic radiation in September 1989 are also listed.

ACCUMULATED EFFECTIVE DOSE DUE TO SOLAR PROTONS DURING GLE 42

Flight	SCR flux by Smart et al.		SCR flux by Dyer et al.	
	GEANT4-BERT [μSv]	GEANT4-BIC [μSv]	GEANT4-BERT [μSv]	GEANT4-BIC [μSv]
Chicago - Beijing	87.3	87.8	286.3	283.9
San Francisco - Paris	124.7	122.4	451.2	440.3
Sydney - Johannesburg	90.9	91.0	302.9	299.2
Buenos Aires - Auckland	136.5	133.8	518.6	504.2

ACCUMULATED EFFECTIVE DOSE DUE TO GCR IN SEPTEMBER 1989

Flight	Duration [min]	Max. Altitude [km]	GEANT4-BERT [μSv]	GEANT4-BIC [μSv]
Chicago - Beijing	791	11.3	35.8	35.1
San Francisco - Paris	555	11.9	33.3	31.6
Sydney - Johannesburg	825	11.9	38.9	37.9
Buenos Aires - Auckland	980	12.2	49.0	46.6

At this point it should be mentioned that the results of the GLE analysis presented in the previous section provide the basis for a potential GLE module in the European Program package for the Calculation of Aviation Route Doses (EPCARD). Using a typical but preferably hard spectrum as the one by *Dyer et al.* (2003a,b) and assuming an isotropic flux of solar protons near Earth allows, in most cases, a conservative dose estimation. This is favored for radiation protection purposes. Deriving the intensity-time profile of a GLE as well as the maximum amplitude from near real-time Neutron Monitor databases such as NMDB[4] allows dose estimation soon after the event. Uncertainties arising from this approach are expected to be in the same range as observed in the present work and are, thus, acceptable. However, additional investigations and calculations for different GLEs are required in order to fully develop a GLE module for EPCARD which may be routinely applied in aircrew dosimetry.

---

[4] http://www.nmdb.eu

6.3 The Carrington event - a plausible worst case scenario

Based on the analysis of GLE 42 presented in the previous section a plausible worst case scenario for the most intense ground level enhancement ever documented is constructed in the following. This event is associated with the first observation of a white-light solar flare by *Carrington* (1860) and *Hodgson* (1860) on September 1, 1859, and was therefore termed the Carrington event. Based on nitrate studies in polar ice *McCracken et al.* (2001a) derived a value for the omnidirectional fluence of solar protons of 1.88×10^{10} cm^{-2} during this enhancement, which is used as normalization factor to estimate plausible doses in aviation.

6.3.1 Observations during the Carrington event

The Carrington event was by far the most intense GLE and geomagnetic storm ever documented. Based on studies by *Chapman* (1957) and *Kimball* (1960), *Green and Boardsen* (2006) reviewed and compiled data on auroral observations during the storm in 1859. Using scientific measurements, newspapers, ship logs, and other records available, they found aurorae in all colors and forms being reported at geographical latitudes below 50° and a several hours lasting blood red aurora even at $\approx$ 18° latitude. Apart from these visual observations, the great geomagnetic storm in 1859 demonstrated the impact of space weather on technology for the first time in history. As concisely reviewed by *Nevanlinna* (2006), the ionospheric currents induced by the geomagnetic storm associated with the Carrington event were so strong that numerous magnetometers went off scale and major parts of the worldwide telegraph system were disrupted. Accounting for all available observations, *Smart et al.* (2006) suggest that the Carrington solar flare was the most important event of a period of enhanced solar activity starting before September 1859 and continuing days after the flare observation.

6.3.2 Estimation of the solar proton fluence during the Carrington event

As discussed in every detail in Chapter 2.2.1, studies initiated by *Zeller et al.* (1986) and *Dreschhoff and Zeller* (1990) have shown that large spikes in nitrate concentration found in polar ice coincide with the time of major solar proton events. An increase in proton intensity during a GLE leads to enhanced ionization rates in the atmosphere. The secondary electrons generated in these processes in turn dissociate molecular nitrogen. As a consequence nitrogen radicals, so-called odd nitrogen, is produced some of which becomes further oxidized and attached to aerosols or incorporated in snow crystals. By gravitational sedimentation the odd nitrogen is finally transported to the troposphere and well-conserved in polar ice to provide a record of GLEs over several thousand years.

In 1992 a very long ice core was drilled at Summit, Greenland, which was explicitly dedicated to high-resolution nitrate studies. This core, 125.6 m in length, covers a time period of 1561 - 1991. *McCracken et al.* (2001a,b,c) analyzed the Arctic ice core in addition to two cores drilled earlier in Antarctic regions. They found a one-to-one correlation of pronounced impulsive nitrate peaks with the seven largest GLEs observed on Earth since continuous monitoring of cosmic radiation started in 1936. The probability of this occurring by chance was estimated to be less than 10^{-6}. Therefore, the works of *McCracken et al.* (2001a,b,c) eliminated most of the doubts and uncertainties in the association between impulsive nitrate and major solar proton events.

Moreover, as discussed in Chapter 2.2.1, *McCracken et al.* (2001a) established a conversion relationship of nitrate concentration and omnidirectional fluence of protons with energies above 30 MeV striking the polar atmosphere (see Eq. 2.12). Using various ground-based measurements and observations in interplanetary space, *Shea and Smart* (1990, 1993) provided values for the omnidirectional fluences of the seven largest GLEs observed in the period 1942 - 1989 in order to finally derive a conversion factor for nitrate concentration and solar proton fluence. Taking an average factor, a total number of 70 impulsive nitrate events were identified having a > 30 MeV omindirectional fluence $\geq 2\times10^{9}$ cm^{-2}. A complete list of fluence values derived for these events and another 55 with fluences between 1×10^{9} cm^{-2} and 2×10^{9} cm^{-2} is reported in *McCracken et al.* (2001a,b).

The largest impulsive nitrate deposition on the 450 years record in the Arctic ice core was dated to late 1859. This nitrate deposition is, thus, associated with the first observation of a white-light solar flare by *Carrington* (1860) and *Hodgson* (1860) on September 1, 1859. For the Carrington event, an omnidirectional fluence (> 30 MeV) of 1.88×10^{10} cm^{-2} was derived, having almost twice the fluence of the second largest in 1895.

6.3.3 Estimation of possible doses during the Carrington event

Using the value for the solar proton fluence reported by *McCracken et al.* (2001a) as overall normalization factor allows to estimate possible dose values for the Carrington event. For this purpose, certain assumptions on the spectral characteristics and the intensity-time profile of the event have to be made. Assuming the spectral shape of large solar particle events as derived from ground-based observations during the past 60 years and using the value of the omnnidirectional solar proton fluence of 1.88×10^{10} cm^{-2} to normalize these spectra to the Carrington event has already been successfully applied e.g. by *Townsend et al.* (2003, 2004, 2006) and *Stephens et al.* (2005). These works focused on estimates of possible doses to crews in interplanetary space.

The same approach to construct a hypothetical but yet plausible worst-case scenario for a GLE is applied in the following, in order to estimate potential doses for aircrews in commercial aviation. For this purpose the spectral characteristics of GLE 42 as reported by *Smart et al.* (1991) and *Dyer et al.* (2003a,b) were used. These spectra were inter-compared in Figure 6.7 and extensively discussed in the previous section of this chapter. For the temporal characteristics of the hypothetical worst-case scenario the intensity-time profile as defined for the EURADOS investigations on GLE 42 was assumed (see Figs. 6.6 and 6.10). Furthermore, a completely isotropic flux of solar protons near Earth was considered.

Under the presumptions outlined above, the spectral fluence rate distributions $\dot{\Phi}(t)$ at time t during the event can easily be obtained from Equations 6.3 and 6.4 for the differential intensities of solar protons reported by *Smart et al.* (1991) and *Dyer et al.* (2003a,b, also see App. A.1). In combination with the energy- and time-integrated omnidirectional fluence of solar protons with energies > 30 MeV determined by *McCracken et al.* (2001a) this finally allows to derive an integral scaling factor Γ between a spectrum valid for GLE 42 and the worst case spectrum via integration over the duration $\mathit{\Delta} t$ of the event:

$$\mathit{\Gamma} \cdot \int_{\mathit{\Delta} t} \int_{30MeV}^{E_{max}} \frac{d\dot{\mathit{\Phi}}(t)}{dE} \, dEdt \overset{!}{=} 1.88 \cdot 10^{10} \mathrm{cm}^{-2}. \tag{6.5}$$

It is clear from this equation that the scaling factor highly depends on the spectral fluence rate distribution considered. Moreover, the integral over the energy and thus $\mathit{\Gamma}$ is strongly dominated by the assumption on the spectrum below several hundreds of MeV because the solar spectra steeply decrease with increasing energy. Based on the spectral fluence rate distribution of *Dyer et al.* (2003a,b) a factor of $\mathit{\Gamma} = 35.9$ is derived, whereas for the spectrum reported in *Smart et al.* (1991) an unrealistic high value of approximately 839 is obtained. The large difference between the scaling factors is a direct consequence of the much lower spectrum of *Smart et al.* (1991) at low energies. The comparison of both spectra with direct proton measurements on-board GOES in Figure 6.7 indicates that the spectrum by *Dyer et al.* (2003a,b), which is based on a Weibull fit of *Xapsos et al.* (2000) on interplanetary observations, might be somewhat more accurate in the low-energy region. This does not mean that the spectrum of *Smart et al.* (1991) is less appropriate or less suited for studies of the radiation environment in the lower atmosphere as it is only derived from ground-based observations at relativistic energies above approximately 450 MeV. Lower energy protons do not significantly contribute to secondary particle fluence and dose rates at aircraft altitudes. Therefore, a scaling factor of $\mathit{\Gamma} = 35.9$ was applied for both solar proton spectra, in order to estimate doses for aircrews during the Carrington-like worst case GLE.

Re-normalizing the spectra by *Smart et al.* (1991) and *Dyer et al.* (2003a,b) used in the analysis of GLE 42 to the integral fluence derived by *McCracken et al.* (2001a) for the Carrington event, thus, means to scale the accumulated effective doses for aircrews listed in Table 6.2 by the conversion factor of 35.9. This, however, only applies to dose values based on the spectrum by *Smart et al.* (1991). Route doses determined with the primary spectrum of *Dyer et al.* (2003a,b), on the other hand, are enhanced by more than this factor because values in Table 6.2 are based on the intensity-time profile of the Climax Neutron Monitor for GLE 42 and not on the profile defined in the EURADOS task which is also assumed for the worst case scenario.

The final accumulated effective doses following ICRP-103 for the four flights considered previously in this chapter are listed in Table 6.3 for both solar proton spectra and, for the sake of completeness, also for both INC models applied in the calculations of secondaries induced in the atmosphere. Apparently, depending on the assumptions made on the solar proton spectrum and to a minor degree depending on the flight routes, accumulated effective doses during the Carrington-like worst case scenario range from approximately 3 mSv to more than 28 mSv. This in turn means that the annual limit of 1 mSv effective dose, above which monitoring of aircrews is mandatory, may be by far exceeded during a single flight. Furthermore, if a comparatively hard spectrum as the one proposed by *Dyer et al.* (2003a,b) is used for dose assessment, even the annual limit of 20 mSv may be reached. The International Commission on Radiological Protection continues to recommend in Publication 103 (*ICRP*, 2007) that this annual limit for occupational exposure should be expressed as effective dose averaged over 5 consecutive years (i.e. 100 mSv in five years), under the condition that a single annual effective dose should not exceed 50 mSv. Note that an effective dose of approximately 20 mSv is similar to a dose received from two abdominal chest computer

TABLE 6.3: Hypothetical accumulated effective doses (ICRP-103) on selected flights during the Carrington event in 1859. Values are given for the solar spectra of *Dyer et al.* (2003a,b) and *Smart et al.* (1991), respectively. All dose estimates are based on calculations applying either the Bertini or the Binary INC model.

HYPOTHETICAL ACCUMULATED EFFECTIVE DOSE DUE TO SOLAR PROTONS ESTIMATED FOR THE CARRINGTON EVENT

Flight	SCR flux based on Smart et al.		SCR flux based on Dyer et al.	
	GEANT4-BERT [mSv]	GEANT4-BIC [mSv]	GEANT4-BERT [mSv]	GEANT4-BIC [mSv]
Chicago - Beijing	3.13	3.15	16.44	16.29
San Francisco - Paris	4.48	4.39	25.10	24.46
Sydney - Johannesburg	3.26	3.27	17.32	17.09
Buenos Aires - Auckland	4.90	4.80	28.55	27.75

tomographies (*Shrimpton et al.*, 2004). Nonetheless, the estimates of worst case route doses clearly demonstrate the necessity of retrospective dose assessment for GLEs, because there are well-founded indications that very intense events can occur.

Although the route doses estimated for the worst case scenario appear somewhat high, they are largely consistent with a dose equivalent of 4.5 mSv reported by *Lantos and Fuller* (2003) for a flight from Paris to San Francisco during the very intense ground level enhancement in February 1956 (GLE 4). With an omnidirectional proton fluence above 30 MeV of approximately 1×10^{9} cm^{-2} as reported by *Shea and Smart* (1990, 1993); *McCracken et al.* (2001a), the February 1956 event was about 20 times less intense than the Carrington event. In terms of dose assessment for aircrews during GLEs, however, the hardness of the spectrum as well as the intensity-time profile are much more important than the integral solar proton flux. As stated previously, *Smart et al.* (2006) suggest that the Carrington solar flare was the most important event of an episode of solar activity starting before September 1859 and continuing days after the flare observation. Accordingly, they propose an intensity-time profile spanning several days and not only several hours as assumed for the dose assessment presented above. Moreover, they found no statistically significant increase in ^{10}Be concentration for the year 1859. As this cosmogenic nuclide is produced in neutron- and proton-induced spallation reactions on nitrogen and oxygen nuclei (see e.g. *Yoshimori*, 2005), the absence of an increased concentration indicates a rather soft spectrum for the Carrington event. This in turn implies that doses estimated based on the spectrum by *Smart et al.* (1991) may be somewhat more realistic, as this spectrum is much softer with respect to the one reported by *Dyer et al.* (2003a,b).

The construction of the worst case scenario presented in this section may have some weaknesses from a scientific point of view, and estimated dose values are subject to uncertainties larger than a factor of 5. In order to estimate hypothetical but yet plausible maximum doses for aircrews during a worst case GLE, on the other hand, the assumptions made are feasible and reasonable from a dosimetric point of view.

CHAPTER

7

SUMMARY AND CONCLUSIONS

At typical aircraft altitudes of 9 - 13 km the intensity of secondary cosmic radiation is strongly enhanced with respect to sea-level conditions. As a consequence, pilots and aircrews are occupationally exposed to much higher radiation levels, and monitoring of effective dose for aircrews is mandatory according to European and German directives in case the annual dose is likely to exceed 1 mSv. One major goal of the present work, therefore, was the accurate characterization of the radiation environment in the lower atmosphere induced by cosmic radiation. This includes both galactic and solar cosmic rays during ground level enhancements. All available experimental data on differential intensities of secondary particles in the Earth's atmosphere are restricted in time, particle species, geographic position, altitude, and energy. As a consequence, a full characterization based on experimental data is hardly possible. This is particularly the case for ground level enhancements where experimental data are very scarce. An alternative approach is the computation of all secondary components of cosmic radiation by means of Monte Carlo (MC) codes. In the frame of the present work the MC simulation toolkit GEANT4 (*Agostinelli et al.*, 2003; *Allison et al.*, 2006) was chosen for this task.

For an accurate and comprehensive description of the radiation environment induced by galactic cosmic rays (GCR) several issues must be addressed. First, the differential intensities of primary cosmic ray protons and helium nuclei outside the magnetosphere have to be determined. This includes an adequate method to account for solar activity and the related modulation of primary spectra and intensities within the heliosphere. Second, the impact of the magnetosphere on primary cosmic ray spectra on top of the atmosphere has to be determined by computing the propagation of charged particles through the magnetospheric field. Third, primary spectra have to be transported through the Earth's atmosphere and the energy spectra of all components of secondary cosmic radiation have to be calculated. These secondary particle spectra finally can be converted to dose quantities such as effective dose and ambient dose equivalent to fully characterize the radiation environment in the lower atmosphere at arbitrary times, altitudes, and geographic positions.

In order to select an appropriate model predicting the differential intensities of primary hydrogen and helium nuclei near Earth, an extensive literature review was carried out. The predictions of various analytical approximations to the Parker's equation were compared with several precise measurements of primary GCR spectra. It turned out that the local interstellar spectrum given by *Burger et al.* (2000) in combination with the model for heliospheric modulation developed by *Usoskin et al.* (2005, 2011) reproduces proton and helium observations near Earth best (see Chapter 2.1.1). Consequently these primary GCR spectra were selected for the calculation of secondaries produced in the atmosphere.

A commonly used approach to approximate the influence of the magnetosphere on primary spectra on top of the atmosphere at various geographic positions is to consider particles arriving in vertical direction only. The influence of the magnetosphere on the isotropic GCR flux is then described by a single parameter, the vertical effective cutoff rigidity. To calculate this parameter in a grid covering the whole Earth the program package MAGNETOCOSMICS (*Desorgher*, 2004) was used. This program is based on the Monte Carlo simulation toolkit GEANT4 and allows to compute the propagation of cosmic ray particles through the magnetosphere by numerical integration of the Lorentz equation of motion for a negatively charged mirror-particle. For the description of the magnetospheric field due to external sources the model described in *Tsyganenko* (1989) was considered, whereas for the dipole-like geomagnetic field due to sources inside the Earth the very recently released 11th generation of the International Geomagnetic Reference Field[1] (IGRF-11, *Finlay et al.*, 2010b) was applied. This way vertical effective cutoff rigidities valid for the years 2010 to 2015 were calculated. Accounting for the vertical effective cutoff rigidity, the prescribed primary spectra for hydrogen and helium nuclei were finally transported through the Earth's atmosphere using GEANT4. The corresponding spectral fluence rate distributions of all secondary particle species were computed from 100 km altitude down to sea-level for all solar and geomagnetic conditions. As primary cosmic ray particles were considered up to a maximum energy of 10 TeV, the results of the particle transport calculations crucially rely on the hadronic interaction models applied. To estimate the uncertainties arising from the use of different intra-nuclear cascade (INC) models describing the initiation of spallation reactions, two alternative models from the hadronic framework of GEANT4 were applied, the Bertini and the Binary INC model. Comparison of simulation results with measurements of atmospheric protons, muons, and neutrons revealed that the Bertini INC model appears to give a somewhat more accurate description of the radiation environment in the lower atmosphere. In addition to measurements performed in the atmosphere, calculated neutron spectra at sea-level were extensively compared with continuous Bonner sphere measurements performed throughout the present work in Ny-Ålesund, Spitsbergen. For this purpose, the influence of the soil composition and density as well as the hydrogen content in and on top of the soil on calculated neutron spectra at sea-level was studied. Again best agreement with measurements was found for the spectra calculated with the Bertini INC model (see Chapter 5).

The spectral fluence rate distributions of secondary cosmic ray particles determined by means of particle transport calculations were then converted to effective dose and ambient dose

---

[1] http://www.ngdc.noaa.gov/IAGA/vmod/igrf.html

equivalent rates allowing to derive dose rates at any geographic position, altitude, and phase in the solar cycle. Furthermore, accumulated dose quantities along selected intercontinental long-haul flights were estimated and inter-compared with results given by the European Program package for the Calculation of Aviation Route Doses[2] (EPCARD) developed by *Schraube et al.* (2002) and *Mares et al.* (2009). Throughout a typical solar cycle as well as at all geomagnetic conditions excellent agreement was found. Additionally, values for ambient dose equivalent rates at various altitudes and phases in the solar cycle were compared in the full range of vertical effective cutoff rigidity (0 - 17 GV) with experimental reference data released by the *ICRU* (2010, Report 84). Results from the present work were found to be fully consistent within the range of uncertainty given by the ICRU (see Chapter 6.1.2). Concerning dose rates at aviation altitudes and route doses for aircrews derived from particle spectra calculated with the Bertini or the Binary INC model it turned out that differences in secondary particle spectra only play a minor role in aircrew dosimetry. This is due to the fact that the spectra and, thus, the related dose values given by both models agree rather well at aircraft altitudes. Moreover, small differences observed for certain particle species tend to cancel out in terms of total dose (see Chapter 6).

For the calculation of secondary particle spectra induced by solar energetic particles during ground level enhancements (GLE) a similar approach was chosen as for galactic cosmic rays. To estimate dose rates and route doses for aircrews during a typical but rather intense GLE, the event of September 29, 1989 (GLE 42) was selected. The spectral, temporal, and spatial characteristics of GLEs are usually derived from the global Neutron Monitor network. Difficulties in this procedure arise e.g. from calculating accurate asymptotic cones of acceptance, assuming a proper pitch-angle distribution to describe anisotropy, as well as using an appropriate yield function. Therefore, many different functions of the differential solar proton intensity can reproduce the observed count rate increases equally well. To estimate the impact of different primary proton spectra for GLE 42 on calculated dose rates at aircraft altitudes, spectra reported by *Dyer et al.* (2003a,b) and *Smart et al.* (1991) were studied. For radiation protection purposes a conservative dose assessment is required. Therefore, complete isotropy of the solar proton flux near Earth was assumed for the GLE analyses. Accumulated doses along selected long-haul flights in the range of 90 μSv to more than 500 μSv were estimated. Uncertainties hereby mainly arise from the solar proton spectra. Differences in the primary spectra result in uncertainties of route doses in the order of a factor of 3 - 5. The dose quantities obtained in the present work were inter-compared with values reported by various other authors and full consistency was found. This furthermore confirms the range of uncertainty in dose assessment during GLEs arising from uncertainties in the primary solar proton flux. Of note is that the results of the GLE analyses have been provided to the European Radiation Dosimetry Group (EURADOS) for an inter-comparison of doses estimated by several European research institutes (see Chapter 6.2).
Based on the analysis of GLE 42 a plausible worst case scenario for the most intense ground level enhancement ever documented was constructed at the end of the present work. This event is associated with the first observation of a white-light solar flare by *Carrington* (1860) and *Hodgson* (1860) on September 1, 1859, and was therefore termed the Carrington event.

---

[2] http://www.helmholtz-muenchen.de/epcard-portal/

Based on nitrate studies in polar ice, *McCracken et al.* (2001a) derived an omnidirectional fluence of solar protons ($E > 30$ MeV) of 1.88×10^{10} cm^{-2} during this enhancement. Using this value as overall normalization factor in combination with the spectral characteristics and the intensity-time profile of GLE 42 allows to estimate hypothetical but yet plausible dose values for the Carrington event. Depending on the assumptions made on the spectral characteristics and, to a minor degree, on the flight profile worst case route doses from approximately 5 mSv to 28 mSv were estimated (see Chapter 6.3).

Apart from the numerical and theoretical approach of characterizing the radiation environment in the lower atmosphere, two advanced Bonner sphere spectrometers (BSS) have been continuously operated throughout the present work to monitor secondary neutrons from cosmic radiation. The spectrometers consist of 13 basic Bonner spheres with pure polyethylene (PE) moderators of different diameters (2.5, 3, 4, 5, 5.5, 6, 7, 8, 9, 10, 11, 12, and 15 inches). In two spheres with 9 inch outer diameter lead shells of 0.5 and 1.0 inch thickness, respectively, are embedded serving as measurement channels in the high-energy region. Additionally, one bare ^{3}He proportional counter is operated to detect thermal neutrons resulting from moderation in the environment of the spectrometers. One of the prescribed BSS systems is located at the Environmental research station (UFS) “Schneefernerhaus” at an altitude of 2660 m near the summit of the Zugspitze mountain, Germany. The second instrument is located at the Koldewey station in Ny-Ålesund, Spitsbergen, at a distance of approximately 800 km to the geographic North Pole. Both spectrometers have been maintained and the data have been analyzed throughout the present work.

In order to derive information on neutron spectra with a BSS, the detection efficiency of each component of the spectrometer has to be determined by means of Monte Carlo techniques from thermal up to relativistic energies. In the frame of the present work the response of each Bonner sphere to neutrons as well as to protons was calculated with GEANT4. Also for this task the impact of different hadronic interaction models at high energies was studied. Differences in INC models resulted in differences in calculated response functions of more than a factor of two at very high energies. In order to determine the impact of these uncertainties on unfolded fluence and dose rates, measurements of secondary cosmic ray neutrons and stray neutron fields behind a shielding of the hadron therapy facility GSI in Darmstadt, Germany, were considered. It turned out that energy integrated fluence and dose rates unfolded using the response functions calculated with different hadronic interaction models and MC codes agree within less than 10% which is fully satisfying for radiation protection purposes. Unfolded fluence rates at energies above 20 MeV, on the other hand, were found to differ by about 20% (see Chapter 3).

The only way of determining which of the calculated responses agree best with the real detection efficiency of the BSS system is calibration in quasi-monoenergetic neutron fields with known spectral fluence rate distribution. For this purpose a unique calibration measurement was carried out at the Research Center for Nuclear Physics (RCNP) of the University in Osaka, Japan. At this facility neutron fields with energies up to 400 MeV can be generated using the ^{7}Li(p,n)^{7}Be reaction. For the calibration of the BSS systems proton beams with nominal energies of 246 and 389 MeV were focused on a 10.0 mm thick ^{nat}Li (7.6% ^{6}Li and 92.4% ^{7}Li) target, resulting in quasi-monoenergetic neutrons with peak energies of 244 and 387 MeV, respectively. At energies above 10 MeV the spectral fluence rate distributions were measured by means of the time-of-flight (TOF) method employing organic liquid scintillators NE213. At lower energies the neutron spectra were characterized with the Bonner sphere spectrometer. A detailed comparison of the neutron spectra measured with the BSS and unfolded using different response matrices with the spectra obtained by means of the TOF method was done. It turned out that at 246 MeV beam energy the unfolded BSS neutron fluence rates using the response matrix calculated with the GEANT4 Binary INC model agree very well with the TOF measurements around the nominal peak energies. In contrast, at 389 MeV proton energy the peak intensities given by the TOF method were closer to unfolded BSS fluence rates using the response matrix calculated with the GEANT4 Bertini INC model.

For the actual calibration of the BSS, two different approaches were applied. First, measured count rates of all Bonner spheres were corrected with respect to contributions from neutrons with energies below 10 MeV using unfolded fluence rates and the corresponding response functions. The remaining count rates resulting from high-energy neutrons ($E > 10$ MeV) finally were compared to calculated count rates using the independently measured TOF spectra and the response functions of the Bonner spheres. In the second approach, count rates corrected for neutrons with energies below 10 MeV and the TOF spectra were used to determine measured response values. Those were finally compared with response values based on mono-energetic calculations using different INC models and MC codes. In both approaches remarkable overall agreement of the measurements and basically all response calculations was obtained considering the uncertainties involved in the determination of high-energy neutron fluence rates. This in turn confirmed all response calculations at high energies (see Chapter 4). As it was already the case in the inter-comparison of BSS and TOF neutron spectra, however, a closer look revealed that at 246 MeV beam energy the responses calculated with the Binary INC model appear to give a more accurate estimate for the real responses of the Bonner spheres. At 389 MeV, on the other hand, measurements match better with the Bertini response matrix. This in turn appears to indicate that the GEANT4 Bertini INC model is likely to handle high-energy hadronic interactions more accurately at energies above approximately 300 MeV. This is in good agreement with the results from the particle transport calculations in the Earth's atmosphere, since in this case all simulation results are influenced by the INC model up to an energy of 10 GeV.

Publications from this Work in Peer-Reviewed International Journals and in Proceedings

Pioch, C., V. Mares, W. Rühm, H. Iwase, Y. Iwamoto, T. Sato, M. Hagiwara, D. Satoh, Y. Nakane, H. Nakashima, Y. Sakamoto, H. Yashima, T. Matsumoto, A. Masuda, J. Nishiyama, T. Itoga, C. Theis, E. Feldbaumer, L. Jägerhofer, A. Tamii, K. Hatanaka, and T. Nakamura (2011a). Calibration of a Bonner sphere spectrometer in quasi-mono-energetic neutron fields of 244 and 387 MeV. *Journal of Instrumentation*, 6:P10015. doi:10.1088/1748-0221/6/10/P10015.

Pioch, C., V. Mares, W. Rühm, E. Vashenyuk, and Y. Balabin (2011b). Measurement of cosmic ray neutrons with Bonner sphere spectrometer and neutron monitor at 79°*N*. *Nuclear Instruments and Methods in Physics Research, Section A*, 626–627:51–57. doi: 10.1016/j.nima.2010.10.030.

Pioch, C., V. Mares, and W. Rühm (2010). Influence of Bonner sphere response functions above 20 MeV on unfolded neutron spectra and doses. *Radiation Measurements*, 45(10):1263–1267. doi:10.1016/j.radmeas.2010.05.007.

Mares, V., **C. Pioch**, W. Rühm, H. Iwase, Y. Iwamoto, T. Sato, M. Hagiwara, D. Satoh, Y. Nakane, H. Nakashima, Y. Sakamoto, H. Yashima, T. Matsumoto, A. Masuda, J. Nishiyama, T. Itoga, C. Theis, E. Feldbaumer, L. Jägerhofer, A. Tamii, K. Hatanaka, and T. Nakamura (2012). Bonner sphere measurements in quasi-mono-energetic p-Li neutron fields of 244 and 387 MeV. *IEEE Transactions on Nuclear Science*, submitted.

Rühm, W., U. Ackermannn, **C. Pioch**, and V. Mares (2012). Spectral neutron fluence rate oscillations of cosmic radiation on the Earth's surface. *Journal of Geophysical Research (Space Physics)*, submitted.

Masuda, A., T. Matsumoto, H. Harano, J. Nishiyama, Y. Iwamoto, M. Hagiwara, D. Satoh, H. Iwase, H. Yashima, T. Nakamura, T. Sato, T. Itoga, Y. Nakane, H. Nakashima, Y. Sakamoto, C. Theis, E. Feldbaumer, L. Jägerhofer, **C. Pioch**, V. Mares, A. Tamii, and K. Hatanaka (2012). Response measurement of a Bonner sphere spectrometer for high-energy neutrons. *IEEE Transactions on Nuclear Science*, 59(1):161–166. doi: 10.1109/TNS.2011.2175406.

Iwamoto, Y., M. Hagiwara, D. Satoh, H. Iwase, H. Yashima, T. Itoga, T. Sato, Y. Nakane, H. Nakashima, Y. Sakamoto, T. Matsumoto, A. Masuda, J. Nishiyama, A. Tamii, K. Hatanaka, C. Theis, E. Feldbaumer, L. Jägerhofer, **C. Pioch**, V. Mares, and T. Nakamura (2011). Quasi-monoenergetic neutron energy spectra for 246 and 389 MeV ^{7}Li(p,n) reactions at angles from 0° to 30°. *Nuclear Instruments and Methods in Physics Research, Section A*, 629:43–49. doi:10.1016/j.nima.2010.12.022.

Iwamoto, Y., M. Hagiwara, D. Satoh, H. Iwase, H. Yashima, T. Itoga, T. Sato, Y. Nakane, H. Nakashima, Y. Sakamoto, T. Matsumoto, A. Masuda, J. Nishiyama, A. Tamii, K. Hatanaka, C. Theis, E. Feldbaumer, L. Jägerhofer, **C. Pioch**, V. Mares, and T. Nakamura (2010). Characterization of quasi-monoenergetic neutron energy spectra using the ^{7}Li(p,n) reactions at 246 and 389 MeV. In *Proceedings of the 10th Workshop on Shielding Aspects of Accelerators, Targets and Irradiation Facilities – SATIF-10, CERN, Geneva, Switzerland.*

Masuda, A., T. Matsumoto, H. Harano, J. Nishiyama, Y. Iwamoto, M. Hagiwara, D. Satoh, H. Iwase, H. Yashima, T. Nakamura, T. Sato, T. Itoga, Y. Nakane, H. Nakashima, Y. Sakamoto, C. Theis, E. Feldbaumer, L. Jägerhofer, **C. Pioch**, V. Mares, A. Tamii, and K. Hatanaka (2010). Response measurement of a Bonner sphere spectrometer for high-energy neutrons. *IEEE Nuclear Science Symposium Conference Record (NSS/MIC)*, pages 986–990. doi:10.1109/NSSMIC.2010.5873911.

Iwase, H., M. Hagiwara, Y. Iwamoto, D. Satoh, , H. Yashima, T. Itoga, T. Sato, Y. Nakane, H. Nakashima, Y. Sakamoto, T. Matsumoto, A. Masuda, J. Nishiyama, A. Tamii, K. Hatanaka, C. Theis, E. Feldbaumer, L. Jägerhofer, **C. Pioch**, V. Mares, and T. Nakamura (2010). Benchmark experiment of neutron penetration through iron and concrete shields using 243 and 387 MeV quasi-monoenergetic neutrons part I: Measurement and calculation of neutron depth-dose distribution. In *Proceedings of the 10th Workshop on Shielding Aspects of Accelerators, Targets and Irradiation Facilities – SATIF-10, CERN, Geneva, Switzerland.*

Rühm, W., V. Mares, **C. Pioch**, E. Weitzenegger, R. Vockenroth, and H. Paretzke (2009a). Measurements of secondary neutrons from cosmic radiation with a Bonner sphere spectrometer at 79°N. *Radiation and Environmental Biophysics*, 48:125–133. doi:10.1007/s00411-009-0219-y.

Rühm, W., V. Mares, **C. Pioch**, G. Simmer, and E. Weitzenegger (2009b). Continuous measurement of secondary neutrons from cosmic radiation at mountain altitudes and close to the north pole - a discussion in terms of H*(10). *Radiation Protection Dosimetry*, 136(4):256–261. doi:10.1093/rpd/ncp161.

Rühm, W., V. Mares, **C. Pioch**, E. Weitzenegger, and H. Paretzke (2008). Continuous measurements of secondary neutrons from cosmic radiation at low atmospheric and low geomagnetic shielding by means of Bonner sphere spectrometers. In *Proceedings of the 21st European Cosmic Ray Symposium, ECRS XXI, Košice, Slovakia*.

BIBLIOGRAPHY

Abfalterer, W., F. Bateman, F. Dietrich, R. Finlay, R. Haight, and G. Morgan (2001). Measurement of neutron total cross sections up to 560 MeV. *Physical Review C*, 63:044608. doi:10.1103/PhysRevC.63.044608.

Ackermann, U. (2011). *Verbesserung eines Bonner Vielkugelspektrometers zum Nachweis von sekundären Neutronen der kosmischen Strahlung*. Diploma thesis. Technische Universität München.

Agosteo, S., E. Dimovasili, A. Fasso, and M. Silari (2004). The response of a bonner sphere spectrometer to charged hadrons. *Radiation Protection Dosimetry*, 110(1-4):161–168.

Agostinelli, S., J. Allison, K. Amako, J. Apostolakis, H. Araujo, P. Arce, M. Asai, et al. (2003). Geant4 - a Simulation Toolkit. *Nuclear Instruments and Methods in Physics Research, Section A*, 506:250–303.

Alcaraz, J., B. Alpat, G. Ambrosi, H. Anderhub, L. Ao, A. Arefiev, P. Azzarello, et al. (2000a). Helium in near Earth orbit. *Physics Letters B*, 494:193–202.

Alcaraz, J., B. Alpat, G. Ambrosi, H. Anderhub, L. Ao, A. Arefiev, P. Azzarello, et al. (2000b). Protons in near Earth orbit. *Physics Letters B*, 472:215–226.

Alevra, A., M. Cosack, J. Hunt, D. Thomas, and H. Scharube (1992). Experimental determination of the response of four Bonner sphere sets to monoenergetic neutrons (II). *Radiation Protection Dosimetry*, 40(2):91–102.

Allison, J., K. Amako, J. Apostolakis, H. Araujo, P. Dubois, M. Asai, G. Barrand, et al. (2006). Geant4 Developments and Applications. *IEEE Transactions on Nuclear Science*, 53:270–278.

Allkofer, O. (1975). *Introduction to Cosmic Radiation*. Number 10 in Buchreihe der Atomkernenergie. Verlag Karl Thiemig München.

Amako, K., S. Guatelli, V. Ivanchenko, M. Maire, B. Mascialino, K. Murakami, L. Pandola, et al. (2006). Geant4 and its Validation. *Nuclear Physics B (Proceedings Supplements)*, 150:44–49.

Apostolakis, J., G. Folger, V. Grichine, A. Heikkinen, A. Howard, V. Ivanchenko, P. Kaitaniemi, et al. (2009). Progress in hadronic physics modelling in Geant4. In *Proceedings of the 8th International Conference on Calorimetry in High Energy Physics*, volume 160 of *Journal of Physics: Conference Series*. IOP Publishing. doi:10.1088/1742-6596/160/1/012073.

Asakimori, K., T. Burnett, M. Cherry, K. Chevli, M. Christ, S. Dake, J. Derrickson, et al. (1998). Cosmic-Ray Proton and Helium Spectra: Results from the JACEE Experiment. *The Astrophysical Journal*, 502:278–283.

Axford, W. (1982). Discovering the Earth's Magnetosphere. *Advances in Space Research*, 2:11–12.

Baba, M., Y. Nauchi, T. Iwasaki, T. Kiyosumi, M. Yoshioka, S. Matsuyama, N. Hirakawa, et al. (1999). Characterization of a 40 - 90 MeV ^{7}Li(p,n) neutron source at TIARA using a proton recoil telescope and a TOF method. *Nuclear Instruments and Methods in Physics Research, Section A*, 428:454–465.

Badhwar, G. (1997). The Radiation Environment in Low-Earth Orbit. *Radiation Research*, 148:3–10.

Badhwar, G. and P. O'Neill (1994). Long-term modulation of galactic cosmic radiation and its model for space exploration. *Advances in Space Research*, 14(10):10749–10757.

Badhwar, G. and P. O'Neill (1996). Galactic Cosmic Radiation Model and its Applications. *Advances in Space Research*, 17(2):27–217.

Barber, H., T. Bowen, D. Delise, E. Jenkins, J. Jones, R. Kalbach, and A. E. Pifer (1980). Predictions and measurements of mass spectra of the charged nucleonic component of cosmic rays at mountain altitude. *Physical Review D*, 22:2667–2687. doi:10.1103/PhysRevD.22.2667.

Beach, A., J. Beatty, A. Bhattacharyya, C. Bower, S. Coutu, M. DuVernois, A. Labrador, et al. (2001). Measurement of the Cosmic-Ray Antiproton-to-Proton Abundance Ratio between 4 and 50 GeV. *Physical Review Letters*, 87(27):271101. doi:10.1103/PhysRevLett.87.271101.

Beeck, J. and G. Wibberenz (1986). Pitch angle distributions of solar energetic particles and the local scattering properties of the interplanetary medium. *The Astrophysical Journal*, 311:437–450.

Bertini, H. (1963). Low-Energy Intranuclear Cascade Calculation. *Physical Review*, 131(4):1801–1820.

Bertini, H. (1969). Intranuclear-Cascade Calculation of the Secondary Nucleon Spectra from Nucleon-Nucleus Interactions in the Energy Range 340 to 2900 MeV and Comparisons with Experiment. *Physical Review*, 188(4):1711–1730.

Bieber, J. and P. Evanson (1991). Determination of energy spectra for the large solar particle events of 1989. In *Proceedings of the 22nd International Cosmic Ray Conference, ICRC XXII, Dublin*, volume 3, pages 129–132.

Bièvre, P., M. Gellte, N. Holden, and I. Barnes (1984). Isotopic abundances and atomic weights of the elements. *Journal of Physical and Chemical Reference Data*, 13(3):809–891.

Boezio, M., P. Carlson, T. Francke, N. Weber, Suffert, M. M. Hof, W. Menn, et al. (1999). The Cosmic-Ray Proton and Helium Spectra between 0.4 and 200 GV. *The Astrophysical Journal*, 518:457–472.

Boezio, M., P. Carlson, T. Francke, N. Weber, Suffert, M. M. Hof, W. Menn, et al. (2000). The Cosmic-Ray Electron and Positron Spectra Measured at 1 AU during Solar Minimum Activity. *The Astrophysical Journal*, 532(1):653–669. doi:10.1086/308545.

Bramblett, R., R. Ewing, and T. Bonner (1960). A new type of neutron spectrometer. *Nuclear Instruments and Methods*, 9:1–12.

Briesmeister, J. (1993). MCNP - A General Monte Carlo N-Particle Transport Code, Version 4A. *Technical Report LA-12625-M*, Los Alamos National Laboratory.

Brooks, F. and H. Klein (2002). Neutron spectrometry - a histrorical review and present status. *Nuclear Instruments and Methods in Physics Research, Section A*, 476:1–11.

Brueckner, G., R. Howard, M. Koomen, C. Korendyke, D. Michels, J. Moses, D. Socker, et al. (1995). The Large Angle Spectroscopic Coronagraph (LASCO). *Solar Physics*, 162:357–402. doi:10.1007/BF00733434.

Burger, R., M. Potgieter, and B. Heber (2000). Rigidity dependence of cosmic ray proton latitudinal gradients measured by the Ulysses spacecraft: Implications for the diffusion tensor. *Journal of Geophysical Research (Space Physics)*, 105(A12):27447–27455.

Bütikofer, R. and E. Flückiger (2011). Radiation doses along selected flight profiles during two extreme solar cosmic ray events. *Astrophysics and Space Sciences Transactions*, 7:105–109. doi:10.5194/astra-7-105-2011.

Bütikofer, R., E. Flückiger, L. Desorgher, and M. Moser (2006). Analysis of the GLE on January 20, 2005: an Update. In *Proceedings of the 20th European Cosmic Ray Symposium, ECRS XX, Lisbon, Portugal*.

Caballero-Lopez, R. and H. Moraal (2004). Limitations of the force field equation to describe cosmic ray modulation. *Journal of Geophysical Research (Space Physics)*, 109:1101.

Cane, H. and D. Lario (2006). An introduction to CMEs and energetic particles. *Space Science Reviews*, 123:45–56.

Carrington, R. (1860). Description of a singular appearance seen on the Sun on Spetember 1, 1859. *Monthly Notices of the Royal Astronomical Society*, 20:13–15.

Carter, L. and E. Cashwell (1975). *Particle-Transport Simulation with the Monte Carlo Method.* Prepared for the Division of Military Application, U.S. Energy Research and Development Administration.

Castagnoli, G. and D. Lal (1980). Solar modulation effects in terrestrial production of carbon 14. *Radiocarbon*, 22:153–188.

Chadwick, J. (1932). The Existence of a Neutron. *Proceedings of the Royal Society of London*, 136(830):692–708.

Chadwick, M., P. Oblozinsky, M. Herman, N. Greene, R. McKnight, D. Smith, P. Young, et al. (2006). ENDF/B-VII.0: Next Generation Evaluated Nuclear Data Library for Nuclear Science and Technology. *Technical Report UCRL-JRNL-225066*, Lawrence Livermore National Laboratory.

Chapman, S. (1957). *The aurora in middle and low latitudes*, volume 4 of *Annals of the International Geophysical Year, Part I.* Pergamon Press, London.

Clem, J. and L. Dorman (2000). Neutron Monitor Response Functions. *Space Science Reviews*, 93:335–359.

Cliver, E. (1995). Solar Flare Nomenclature. *Solar Physics*, 157:285–293. doi:10.1007/BF00680622.

Cliver, E., S. Kahler, and W. Vestrand (1993). On the origin of gamma-ray emission from the behind-the-limb flare on 29 September 1989. In *Proceedings of the 23rd International Cosmic Ray Conference, ICRC XXIII*, volume 3, pages 91–94.

COESA (1976). U.S. Standard Atmosphere 1976. *Technical Report NOAA Document S/T 76-1562*, Committee on Extension to the Standard Atmosphere (COESA), National Oceanic and Atmospheric Administration (NOAA), the National Aeronautics and Space Administration (NASA), U.S. Air Force.

Cooke, D., J. Humble, M. Shea, D. Smart, I. Lund, L. Rasmussen, B. Byrnak, et al. (1991). On Cosmic-Ray Cut-Off Terminology. *Il Nuovo Cimento*, 14(3):213–234.

Cramp, J., M. Duldig, E. Flückiger, J. Humble, M. Shea, and D. Smart (1997). The October 22, 1989, solar cosmic ray enhancement: An analysis of the anisotropy and spectral characteristics. *Journal of Geophysical Research (Space Physics)*, 102(A11):24237–24248. doi:10.1029/97JA01947.

Cucinotta, F., H. Wu, M. Shavers, and K. George (2003). Radiation Dosimetry and Biophysical Models of Space Radiation Effects. *Gravitational and Space Biology*, 16(2):11–18.

Debrunner, H. and J. Lockwood (1980). The spatial anisotropy, rigidity spectrum, and propagation characteristics of the relativistic solar particles during the event on May 7, 1978. *Journal of Geophysical Research (Space Physics)*, 85:6853–6850.

Delaboudinière, J., G. Artzner, J. Brunaud, A. Gabriel, J. Hochedez, F. Millier, X. Song, et al. (1995). EIT: Extreme-UV imaging telescope for the SOHO mission. *Solar Physics*, 162:291–312. doi:10.1007/BF00733432.

Desorgher, L. (2004). *User guide of the MAGNETOCOSMICS code. Technical report*, University of Bern.

Dickens, J. (1988). SCINFUL - A Monte Carlo Based Computer Program to Determine a Scintillator Full Energy Response to Neutron Detection for Energies between 0.1 and 80 MeV: User's Manual and FORTRAN Program Listing. *Technical Report ORNL-6462*, Oak Ridge National Laboratory.

Dreschhoff, G. and E. Zeller (1990). Evidence of individual solar proton events in Antarctic snow. *Solar Physics*, 127:333–346.

Dyer, C. and F. Lei (2001). Monte Carlo calculations of the influence on aircraft radiation environments of structures and solar particle events. *IEEE Transactions on Nuclear Science*, 48:1987–1995.

Dyer, C., F. Lei, S. Clucas, D. Smart, and M. Shea (2003a). Calculations and Observations of Solar Particle Enhancements to the Radiation Environment at Aircraft Altitudes. *Advances in Space Research*, 32(1):81–93. doi:10.1016/S0273-1177(03)00503-9.

Dyer, C., F. Lei, S. Clucas, D. Smart, and M. Shea (2003b). Solar Particle Enhancements of Single-Event Effect Rates at Aircraft Altitudes. *IEEE Transactions on Nuclear Science*, 50(6):2038–2045. doi:10.1109/TNS.2003.821375.

EC (2004). *European Commission. Cosmic Radiation Exposure of Aircraft Crew: Compilation of Measured and Calculated Data.* Report Radiation Protection 140 of the European Radiation Dosimetry Group, WG5.

Edward, B., S. Berry, and V. Hess (1942). Study of cosmic rays between New York and Chile. *Terrestrial Magnetism and Atmospheric Electricity*, 47(3):251–256. doi:10.1029/TE047i003p00251.

Ellison, D. and R. Ramaty (1985). Shock acceleration of electrons and ions in solar flares. *The Astrophysical Journal*, 298:400–408.

EU (1996). Council Directive 96/29/Euratom of 13 May 1996, Laying down Basic Safety Standards for the Protection of the Health of Workers and the General Public against the Dangers Arising from Ionizing Radiation. *Official Journal European Communities*, 39(L159):1–28. Council of the European Union.

Ferguson, C. (2000). General Purpose Source Particle Module for GEANT4/SPARSET: Technical Note. *Technical Report UoS-GSPM-Tech*, University of Southampton.

Fernández, F., T. Bouassoule, K. Amgarou, C. Domingo, M. J. Garcia, V. Lacoste, V. Gressier, et al. (2007). Monte Carlo calculations and validation of a gold foil-based bonner sphere system. *Radiation Protection Dosimetry*, 126:366–370.

Ferrari, A., M. Pelliccioni, and M. Pillon (1996). Fluence to Effective Dose and Effective Dose Equivalent Conversion Coefficients for Photons from 50 keV to 10 GeV. *Radiation Protection Dosimetry*, 67(4):245–252.

Ferrari, A., M. Pelliccioni, and M. Pillon (1997a). Fluence to Effective Dose and Effective Dose Equivalent Conversion Coefficients for Electrons from 5 MeV to 10 GeV. *Radiation Protection Dosimetry*, 62(9):97–104.

Ferrari, A., M. Pelliccioni, and M. Pillon (1997b). Fluence to Effective Dose and Effective Dose Equivalent Conversion Coefficients for Protons from 5 MeV to 10 TeV. *Radiation Protection Dosimetry*, 71(2):85–91.

Ferrari, A., M. Pelliccioni, and M. Pillon (1997c). Fluence to Effective Dose Conversion Coefficients for Muons. *Radiation Protection Dosimetry*, 74(4):227–233.

Ferrari, A., M. Pelliccioni, and M. Pillon (1997d). Fluence to Effective Dose Conversion Coefficients for Neutrons up to 10 TeV. *Radiation Protection Dosimetry*, 71(3):165–173.

Ferrari, A., M. Pelliccioni, and M. Pillon (1998). Fluence to Effective Dose Conversion Coefficients for Negatively and Positively Charged Pions. *Radiation Protection Dosimetry*, 80(4):361–370.

Ferrari, A., M. Pelliccioni, and R. Villari (2004). Evaluation of the influence of aircraft shielding on the aircrew exposure through an aircraft mathematical model. *Radiation Protection Dosimetry*, 108(2):91–105.

Finlay, C., S. Maus, C. Beggan, M. Hamoudi, F. Lowes, N. Olsen, and E. Thebault (2010a). Evaluation of candidate geomagnetic field models for IGRF-11. *Earth Planets and Space*, 62(10):787–804. doi:10.5047/eps.2010.11.005.

Finlay, C., S. Maus, C. D. Beggan, T. N. Bondar, A. Chambodut, T. A. Chernova, A. Chulliat, et al. (2010b). International Geomagnetic Reference Field: the eleventh generation. *Geophysical Journal International*, 183(3):1216–1230. doi:10.1111/j.1365-246X.2010.04804.

Flückiger, E., R. Bütikofer, L. Desorgher, and M. Moser (2006). Magnetosheath Effect and GLE Analysis. In *Proceedings of the 20th European Cosmic Ray Symposium, Lisbon, Portugal.*

Flückiger, E. and E. Kobel (1990). Aspects of combining models of the Earth's internal and external magnetic field. *Journal of Geomagnetism and Geoelectricity*, 42:1123–1136.

Folger, G., V. Ivanchenko, and J. Wellisch (2004). The Binary Cascade. *The European Physical Journal A*, 21:407–417.

Forbush, S. (1946). Three Unusual Cosmic-Ray Increases Possibly Due to Charged Particles from the Sun. *Physical Review*, 70:771–772. doi:10.1103/PhysRev.70.771.

Fukahori, T., Y. Watanabe, N. Yoshizawa, F. Maekawa, S. Meigo, C. Konno, N. Yamano, et al. (2002). JENDL High Energy File. *Journal of Nuclear Science and Technology Supplements*, 2:25–30.

Gaisser, T. (1990). *Cosmic rays and particle physics*. Cambridge University Press.

Garber, D. (1975). ENDF/B Documentation. *Technical Report BNL-17541*, Upton NY, National Nuclear Data Center, Brookhaven National Laboratory.

Garcia-Munoz, M., G. M. Mason, and J. A. Simpson (1975). The anomalous He-4 component in the cosmic-ray spectrum at below approximately 50 MeV per nucleon during 1972-1974. *The Astrophysical Journal*, 202:265–275. doi:10.1086/153973.

Garny, S. (2008). *Development of a Biophysical Treatment Planning System for the FRM II Neutron Therapy Beamline*. Ph.D. thesis, Technische Universität München.

Garny, S., V. Mares, and W. Rühm (2009). Response functions of a Bonner sphere spectrometer calculated with GEANT4. *Nuclear Instruments and Methods in Physics Research, Section A*, 604:612–617. doi:10.1016/j.nima.2009.02.044.

GEANT4 Collaboration (2009a). Physics Reference Manual. *Technical Report GEANT4 v.9.3*, CERN.

GEANT4 Collaboration (2009b). User's Guide for Application Developers. *Technical Report GEANT4 v.9.3*, CERN.

Gleeson, L. and W. Axford (1968). Solar Modulation of Galactic Cosmic Rays. *The Astrophysical Journal*, 154:1011. doi:10.1086/149822.

Goldhagen, P., J. Clem, and J. Wilson (2004). The Energy Spectrum of Cosmic-Ray induced Neutrons measured on an Airplane over a wide Range of Altitude and Latitude. *Radiation Protection Dosimetry*, 110:387–392. doi:10.1093/rpd/nch216.

Gopalswamy, N., S. Yashiro, G. Michalek, G. Stenborg, A. Vourlidas, S. Freeland, and R. Howard (2009). The SOHO/LASCO CME Catalog. *Earth, Moon and Planets*, 104:295–313. doi:10.1007/s11038-008-9282-7.

Green, J. and S. Boardsen (2006). Duration and extent of the great auroral storm of 1859. *Advances in Space Research*, 38:130–135.

Grieder, P. (2001). *Cosmic Rays At Earth: Researcher's Reference Manual and Data Book*. Elsevier, 1st edition.

Guatelli, S., A. Mantero, B. Mascialino, M. G. Pia, and V. Zampichelli (2007). Validation of Geant4 Atomic Relaxation against the NIST Physical Reference Data. *IEEE Transactions on Nuclear Science*, 54(3):594–603.

Haino, S., T. Sanuki, K. Abe, K. Anraku, Y. Asaoka, H. Fuke, M. Imori, et al. (2004). Measurements of Primary and Atmospheric Cosmic-Ray Spectra with the BESS-TeV Spectrometer. *Physics Letters B*, 594:35–46. doi:10.1016/j.physletb.2004.05.019.

Hatton, C. (1971). *The Neutron Monitor*, volume X. North-Holland Publishing Co., Amsterdam.

Hatton, C. and H. Carmichael (1964). Experimental Investigation of the NM-64 Neutron Monitor. *Canadian Journal of Physics*, 42:2443–2473.

Hedin, A. (1991). Extension of the MSIS thermosphere model into the middle and lower atmosphere. *Journal of Geophysical Research (Space Physics)*, 96:1159–1172.

Heikkinen, A. (2009). Geant4 Hadronic Cascade Models and CMS Data Analysis - Computational Challenges in the LHC Era. In *Internal Report, Helsinki Institute of Physics, Finland*.

Heikkinen, A. and N. Stepanov (2003). Bertini intra-nuclear cascade implementation in Geant4. In *Computing in High Energy and Nuclear Physics, La Jolla, California*.

Heinrich, W., S. Roesler, and H. Schraube (1999). Physics of Cosmic Radiation Fields. *Radiation Protection Dosimetry*, 86(4):253–258.

Herbst, K., A. Kopp, B. Heber, F. Steinhilber, H. Fichtner, K. Scherer, and D. Matthiä (2010). On the importance of the local interstellar spectrum for the solar modulation parameter. *Journal of Geophysical Research (Space Physics)*, 115:120. doi:10.1029/2009JD012557.

Hess, V. (1912). Über Beobachtungen der durchdringenden Strahlung bei sieben Freiballonfahrten. *Physikalische Zeitschrift*, 13(21–22):1084–1091.

Hodgson, R. (1860). On a curious appearance seen in the Sun. *Monthly Notices of the Royal Astronomical Society*, 20:15.

Humble, J., M. Duldig, D. Smart, and M. Shea (1991). Detection of 0.5–15 GeV solar protons on September 29, 1989, at Australian stations. *Geophysical Research Letters*, 18:737–740.

Hundhausen, A., C. Sawyer, L. House, R. Illing, and W. Wagner (1984). Coronal Mass Ejections Observed During the Solar Maximum Mission: Latitude Distribution and Rate of Occurrence. *Journal of Geophysical Research (Space Physics)*, 89(A5):2639–2646. doi:10.1029/JA089iA05p02639.

Hundhausen, A., A. Stanger, and S. Serbicki (1994). Mass and energy contents of coronal mass ejections: SMM results from 1980 and 1984-1988. In Hunt, J. (editor), *Solar Dynamic Phenomena and Solar Wind Consequences, the Third SOHO Workshop*, volume 373 of *ESA Special Publication*, page 409.

ICRP (1990). *1990 Recommendations of the International Commission on Radiological Protection*. Annals of the ICRP, Publication 60. Pergamon Press, Oxford.

ICRP (1997). *Conversion Coefficients for Use in Radiological Protection against external Radiation*. Publication 74. Pergamon Press, Oxford.

ICRP (2007). *The 2007 Recommendations of the International Commission on Radiological Protection*. Annals of the ICRP, Publication 103. Elsevier.

ICRU (1980). *Radiation Quantities and Units*. ICRU Report 33. International Commission on Radiation Units and Measurements.

ICRU (1992). *Measurement of Dose Equivalents from External Photon and Electron Radiations*. ICRU Report 47. International Commission on Radiation Units and Measurements.

ICRU (1998). *Radiation Quantities and Units*. ICRU Report 60. International Commission on Radiation Units and Measurements.

ICRU (2001). *Determination of Operational Dose-Equivalent Quantities for Neutrons*. ICRU Report 60. International Commission on Radiation Units and Measurements.

ICRU (2010). ICRU Report 84. *Journal of the ICRU*, 10(2):1–33. doi:10.1093/jicru/ndq014.

ICRU (2011). Fundamental Quantities and Units for Ionizing Radiation (Revised). *Journal of the ICRU*, 11(1):1–32. doi:10.1093/jicru/ndr004.

Iwamoto, Y., M. Hagiwara, D. Satoh, H. Iwase, H. Yashima, T. Itoga, T. Sato, et al. (2010). Characterization of quasi-monoenergetic neutron energy spectra using the ^{7}Li(p,n) reactions at 246 and 389 MeV. In *Proceedings of the 10th Workshop on Shielding Aspects of Accelerators, Targets and Irradiation Facilities – SATIF-10, CERN, Geneva, Switzerland.*

Iwamoto, Y., M. Hagiwara, D. Satoh, H. Iwase, H. Yashima, T. Itoga, T. Sato, et al. (2011). Quasi-monoenergetic neutron energy spectra for 246 and 389 MeV ^{7}Li(p,n) reactions at angles from 0° to 30°. *Nuclear Instruments and Methods in Physics Research, Section A*, 629:43–49. doi:10.1016/j.nima.2010.12.022.

James, F. (1990). A review of pseudorandom number generators. *Computer Physics Communications*, 60(3):329–344.

Kadri, O., V. Ivanchenko, F. Gharbi, and A. Trabelsi (2007). Geant4 Simulation of Electron Energy Deposition in Extended Media. *Nuclear Instruments and Methods in Physics Research, Section B*, 258(2):381–387.

Kahler, S. (1992). Solar flares and coronal mass ejections. *Annual Review of Astronomy and Astrophysics*, 30:113–141. doi:10.1146/annurev.aa.30.090192.000553.

Kahler, S. (1994). Injection profiles of solar energetic particles as functions of coronal mass ejection heights. *The Astrophysical Journal*, 428(2):837–842. doi:10.1086/174292.

Kahler, S., E. Hildner, and M. Hollebeke (1978). Prompt solar proton events and coronal mass ejections. *Solar Physics*, 57(2):429–443. doi:10.1007/BF00160116.

Kahler, S., D. Reames, and N. Sheeley (2001). Coronal Mass Ejections Associated with Impulsive Solar Energetic Particle Events. *The Astrophysical Journal*, 562:558–565.

Kahler, S., N. Sheeley, R. Howard, M. Koomen, D. Michels, R. McGuire, T. Rosenvinge, et al. (1984). Associations Between Coronal Mass Ejections and Solar Energetic Proton Events. *Journal of Geophysical Research (Space Physics)*, 89(A11):9683–9693. doi:10.1029/JA089iA11p09683.

Kimball, D. (1960). A study of the aurora of 1859. *Technical Report UAG-R109*, University of Alaska.

Klecker, B., R. Mewaldt, J. Bieber, A. Cummings, L. Drury, J. Giacalone, J. Jokipii, et al. (1998). Anomalous Cosmic Rays. *Space Science Reviews*, 83:259–308. doi:10.1023/A:1005031108919.

Kocharian, N., G. Saakian, and Z. Kirakosian (1959). Energy Spectra and Interactions of Cosmic Ray Particles. *Soviet Physics Journal JETP*, 35:933–942.

Koi, T., M. Asai, D. Wright, K. Niita, Y. Nara, K. Amakao, and T. Sasaki (2003). Interfacing the JQMD and JAM nuclear reaction codes to GEANT4. *Technical Report SLAC-PUB 9978*, Stanford Linear Accelerator Center (SLAC).

Kremer, J., M. Boezio, M. Ambriola, G. Barbiellini, S. Bartalucci, R. Bellotti, D. Bergström, et al. (1999). Measurements of Ground-Level Muons at Two Geomagnetic Locations. *Physical Review Letters*, 83(21):4241–4244. doi:10.1103/PhysRevLett.83.4241.

Lange, I. and S. Forbush (1942). Note on the Effect on Cosmic-Ray Intensity of the Magnetic Storm of March 1, 1942. *Terrestrial Magnetism and Atmospheric Electricity*, 47(2):185–186. doi:10.1029/TE047i002p00185.

Lantos, P. and N. Fuller (2003). History of the solar flare radiation doses on-board aeroplanes using a semi-empirical model and Concorde measurements. *Radiation Protection Dosimetry*, 104(3):199–210.

Lara, V. and J. Wellisch (2001). Preequilibrium and equilibrium decays in GEANT4. In *Proceedings of the 9th International Conference on Calorimetry in High Energy Physics, Annecy, France*, volume XXI of *Frascati Physics Series*, pages 449–458.

Lechner, A., V. N. Ivanchenko, and J. Knobloch (2010). Validation of recent Geant4 physics models for application in carbon ion therapy. *Nuclear Instruments and Methods in Physics Research, Section B*, 268:2343–2354.

Lechner, A., M. Pia, and M. Sudhakar (2009). Validation of Geant4 Low Energy Electromagnetic Processes Against Precision Measurements of Electron Energy Deposition. *IEEE Transactions on Nuclear Science*, 56:398–416. doi:10.1109/TNS.2009.2013858.

Lederer, C., V. Shirley, E. Browne, J. Dairiki, R. Doebler, A. Shihab-Eldin, L. Jardine, et al. (1978). *Table of Isotopes*. John Wiley and Sons, 7 edition.

Leuthold, G., V. Mares, W. Eühm, E. Weitzenegger, and H. Paretzke (2007). Long-term measurements of cosmic ray neutrons by means of a Bonner spectrometer at mountain altitudes - first results. *Radiation Protection Dosimetry*, 126(1-4):506–511.

Levenberg, K. (1944). A Method for the Solution of Certain Problems in Least Squares. *Quarterly of Applied Mathematics*, 2:164–168.

Lewis, H. (1950). Multiple scattering in an infinite medium. *Physical Review*, 78:526.

Lovell, J., M. Duldig, and J. Humble (1998). An extended analysis of the September 1989 cosmic ray ground level enhancements. *Journal of Geophysical Research (Space Physics)*, 103(A10):23733–23742. doi:10.1029/98JA02100.

Lutgens, F., E. Tarbuck, and D. Tasa (2009). *The Atmosphere: an Introduction to Meteorology*. Prentice Hall, 11th edition.

MacFarlane, R. (1994a). Data Testing of ENDF/B-VI. In *International Conference on Nuclear Data for Science and Technology, Gatlinburg, Tennessee*. Los Alamos National Laboratory preprint LA-UR-94-1541.

MacFarlane, R. (1994b). New Thermal Neutron Scattering Files for ENDF/B-VI Release 2. In *U.S. National Nuclear Data Center*. Los Alamos National Laboratory preprint,LA–12639-MS.

Macmillan, S. and C. Finlay (2011). The International Geomagnetic Reference Field. In Mandea, M., M. Korte, and B. Hultqvist (editors), *Geomagnetic Observations and Models*, volume 5 of *IAGA Special Sopron Book Series*, pages 265–276. Springer Netherlands. doi: 10.1007/978-90-481-9858-0_10.

Mandzhavidze, N. and R. Ramaty (1993). Particle acceleration in solar flares. *Nuclear Physics B (Proceedings Supplements)*, 33:141–160. doi:10.1016/0920-5632(93)90087-M.

Mares, V., T. Maczka, G. Leuthold, and W. Rühm (2009). Air crew dosimetry with a new version of EPCARD. *Radiation Protection Dosimetry*, 136(4):262–266.

Mares, V., C. Pioch, W. Rühm, H. Iwase, Y. Iwamoto, T. Sato, M. Hagiwara, et al. (2012). Bonner sphere measurements in quasi-mono-energetic p-Li neutron fields of 244 and 387 MeV. *IEEE Transactions on Nuclear Science*, submitted.

Mares, V., A. Sannikov, and H. Schraube (1998). The response functions of a ^{3}He-Bonner spectrometer and their experimental verification in high energy neutron fields. In *Proceedings of third specialist meeting on shielding aspects of accelerators, targets and irradiation facilities (SATIF 3), Sendai, Japan, OECD Nuclear Energy Agency*, pages 237–248.

Mares, V., A. Sannikov, and H. Schraube (2002). Response functions of the Andersson-Braun and extended range rem counters for neutron energies from thermal to 10 GeV. *Nuclear Instruments and Methods in Physics Research, Section A*, 476:341–346.

Mares, V., G. Schraube, and H. Schraube (1991). Calculated neutron response of a Bonner sphere spectrometer with ^{3}He counter. *Nuclear Instruments and Methods in Physics Research, Section A*, 307:398–412.

Mares, V. and H. Schraube (1994). Evaluation of the response matrix of a Bonner sphere spectrometer with LiI detector from thermal energy to 100 MeV. *Nuclear Instruments and Methods in Physics Research, Section A*, 337(2–3):461–473.

Mares, V. and H. Schraube (1998). High energy neutron spectrometry with Bonner spheres. In *Proceedings of the IRPA-Symposium 1997, Prague*, pages 543–547.

Marquardt, D. (1963). An algorithm for least-squares estimation of nonlinear parameters. *Journal of the Society for Industrial and Applied Mathematics*, 11(2):431–441.

Marsaglia, G., A. Zaman, and W. Tsang (1990). Toward a universal random number generator. *Statistics Probability Letters*, 9:35–39.

Mason, G., G. Gloeckler, and D. Hovestadt (1984). Temporal variations of nucleonic abundances in solar flare energetic particle events II – Evidence for large-scale shock acceleration. *The Astrophysical Journal*, 280:902–916. doi:10.1086/162066.

Masuda, A., T. Matsumoto, H. Harano, J. Nishiyama, Y. Iwamoto, M. Hagiwara, D. Satoh, et al. (2010). Response measurement of a Bonner sphere spectrometer for high-energy neutrons. *IEEE Nuclear Science Symposium Conference Record (NSS/MIC)*, pages 986–990. doi:10.1109/NSSMIC.2010.5873911.

Masuda, A., T. Matsumoto, H. Harano, J. Nishiyama, Y. Iwamoto, M. Hagiwara, D. Satoh, et al. (2012). Response measurement of a Bonner sphere spectrometer for high-energy neutrons. *IEEE Transactions on Nuclear Science*, 59(1):161–166. doi:10.1109/TNS.2011.2175406.

Mattes, M. and J. Keinert (2005). Thermal Neutron Scattering Data for the Moderator Materials H_2O, D_2O and ZrHx in ENDF-6 Format and as ACE Library for MCNP(X) Codes. In *International Nuclear Data Committee, INDC(NDS)-0470*. International Atomic Energy Agency.

Matthiä, D. (2009). *The Radiation Environment in the Lower Atmosphere - a Numerical Approach*. Ph.D. thesis, Christian-Albrechts-Universität zu Kiel.

Matthiä, D., B. Heber, G. Reitz, M. Meier, L. Sihver, T. Berger, and K. Herbst (2009a). Temporal and spatial evolution of the solar energetic particle event on 20 January 2005 and resulting radiation doses in aviation. *Journal of Geophysical Research (Space Physics)*, 114:A08104.

Matthiä, D., B. Heber, G. Reitz, L. Sihver, T. Berger, and M. Meier (2009b). The ground level event 70 on December 13th, 2006 and related effective doses at aviation altitudes. *Radiation Protection Dosimetry*, 137(4):304–310. doi:10.1093/rpd/ncp141.

Matthiä, D., L. Sihver, and M. Meier (2008). Monte-Carlo Calculations of Particle Fluences and Dose Rates in the Atmosphere. *Radiation Protection Dosimetry*, 131(2):222–228. doi:10.1093/rpd/ncn130.

Matzke, M. (1988). Estimation of dose equivalent from reaction rates without using a priori fluence information. *Radiation Protection Dosimetry*, 23:297–300.

Matzke, M. (2002). Propagation of uncertainties in unfolding procedures. *Nuclear Instruments and Methods in Physics Research, Section A*, 476:230–241.

Matzke, M. (2003). Unfolding Procedures. *Radiation Protection Dosimetry*, 107:155–174.

McCracken, K., G. Dreschhoff, E. Zeller, D. Smart, and M. Shea (2001a). Solar cosmic ray events for the period 1561-1994; 1. Identification in polar ice, 1561-1950. *Journal of Geophysical Research (Space Physics)*, 106:21585–21598.

McCracken, K., G. Dreschhoff, E. Zeller, D. Smart, and M. Shea (2001b). Solar cosmic ray events for the period 1561-1994; 2. The Gleissberg periodicity. *Journal of Geophysical Research (Space Physics)*, 106:21599–21609.

McCracken, K., F. McDonald, J. Beer, G. Raisbeck, and F. Yiou (2004). A phenomenological study of long-term cosmic-ray modulation, 850-1958 AD. *Journal of Geophysical Research (Space Physics)*, 109:12103.

McCracken, K., U. Rao, B. Fowler, M. Shea, and D. Smart (1968). Cosmic Rays (Asymptotic Directions, etc.) Chapter 14. In Minnis, C. (editor), *Annals of the IQSY 1*, page 198. MIT press Cambridge.

McCracken, K., U. Rao, and M. Shea (1962). The trajectories of cosmic rays in a high degree simulation of the geomagnetic field. *Technical Report 77 (NYO-2670)*, Massachusetts Institute of Technology.

McCracken, K., D. Smart, M. Shea, and G. Dreschhoff (2001c). 400 years of large fluence solar proton events. In *Proceedings of the 27th International Cosmic Ray Conference, ICRC XXVII, Hamburg, Germany*.

McElroy, W., S. Berg, T. Crockett, and R. Hawkins (1967). Spectra Unfolding. *Technical Report AFWL-TR-67-41*, US Air Force Weapons Laboratory.

McLane, V. (1991). ENDF/B-VI Summary Documentation. *Technical Report BNL-NCS-17541 (ENDF-201)*, Upton NY, National Nuclear Data Center, Brookhaven National Laboratory.

Miura, I., T. Yamazaki, A. Shimizu, K. Hosono, T. Itahashi, T. Saito, A. Ando, et al. (1993). Commissioning of the RCNP Ring Cyclotron. In Dutto, G. and M. Craddock (editors), *Proceedings of the 13th International Conference on Cyclotrons and Their Applications, Vancouver, Canada*, pages 3–10. World Scientific Publications.

Morishita, I., K. Nagashima, and S. Sakakibara (1991). Space distribution and rigidity spectrum of solar particles of the GLE observed on 29 September 1989. In *Proceedings of the 22nd International Cosmic Ray Conference, ICRC XXII, Dublin*, volume 3, pages 121–124.

Mullan, D. and K. Schatten (1979). Motion of solar cosmic rays in the coronal magnetic field. *Solar Physics*, 62:153–177. doi:10.1007/BF00150142.

Müller-Mellin, R., H. Kunow, V. Fleißner, E. Pehlke, E. Rode, N. Röschmann, C. Scharmberg, et al. (1995). COSTEP – Comprehensive Suprathermal and Energetic Particle Analyser. *Solar Physics*, 162(1–2):483–504. doi:10.1007/BF00733437.

Nakagawa, T., K. Shibata, S. Chiba, T. Fukahori, Y. Nakajima, Y. Kikuchi, T. Kawano, et al. (1995). Japanese evaluated Nuclear Data File Version 3 Revision 2: JENDL-3.2. *Journal of Nuclear Science and Technology*, 32:1259.

Nakamura, K. and Particle Data Group (2010). Review of Particle Physics. *Journal of Physics G: Nuclear and Particle Physics*, 37(7A):075021. doi:10.1088/0954-3899/37/7A/075021.

Nevanlinna, H. (2006). A study of the great geomagnetic storm of 1859: Comparisons with other storms in the 19th century. *Advances in Space Research*, 38:180–187.

Ng, C. and D. Reames (2008). Shock acceleration of solar energetic protons: the first 10 minutes. *The Astrophysical Journal*, 686:L123–L126.

Niita, K., N. Matsuda, Y. Iwamoto, H. Iwase, T. Sato, H. Nakashima, Y. Sakamoto, et al. (2010). PHITS: Particle and Heavy Ion Transport code System, Version 2.23. *Technical Report JAEA-Data/Code 2010-022*, Japan Atomic Energy Agency (JAEA).

Ninomiya, S., I. Miura, T. Yamazaki, A. Shimizu, K. Hosono, T. Itahashi, T. Saito, et al. (2004). Ultra high stabilization of the magnetic field of the RCNP cyclotron. In *Proceedings of the 15th International Conference on Cyclotrons and Their Applications, Tokyo, Japan*, page 140.

Nolte, R., M. Allie, P. Binns, F. Brooks, A. Buffler, V. Dangendorf, J. Meulders, et al. (2002). High-energy neutron reference fields for the calibration of detectors used in neutron spectrometry. *Nuclear Instruments and Methods in Physics Research, Section A*, 476:369–373.

Nymmik, R., M. Panasyuk, T. Pervaya, and A. Suslov (1992). A model of galactic cosmic ray fluxes. *International Journal of Radiation Applications and Instrumentation, Part D, Nuclear Tracks and Radiation Measurements*, 20(3):427–429.

Nymmik, R., M. Panasyuk, T. Pervaya, and A. Suslov (1994). An analytical model describing dynamics of galactic cosmic ray heavy particles. *Advances in Space Research*, 14(10):759–763.

Nymmik, R., M. Panasyuk, and A. Suslov (1996). Galactic Cosmic Ray Flux Simulation and Prediction. *Advances in Space Research*, 17(2):219–230.

O'Brien, K. and G. de Burke (1973). Calculated Cosmic Ray Neutron Monitor Response to Solar Modulation of Galactic Cosmic Rays. *Journal of Geophysical Research (Space Physics)*, 78(16):3013–3019.

Ohyama, M. and K. Shibata (1998). X-Ray Plasma Ejection Associated with an Impulsive Flare on 1992 October 5: Physical Conditions of X-Ray Plasma Ejection. *The Astrophysical Journal*, 499:934–947.

O'Neill, P. (2006). Badhwar–O'Neill galactic cosmic ray model update based on advanced composition explorer (ACE) energy spectra from 1997 to present. *Advances in Space Research*, 37:1727–1733.

O'Neill, P. (2010). Badhwar–O'Neill 2010 Galactic Cosmic Ray Flux Model–Revised. *IEEE Transactions on Nuclear Science*, 57(6):3148–3153.

Parker, E. (1958). Dynamics of the Interplanetary Gas and Magnetic Fields. *The Astrophysical Journal*, 128:664. doi:10.1086/146579.

Parker, E. (1965). The passage of energetic charged particles through interplanetary space. *Planetary and Space Science*, 13(1):9–49.

Pelliccioni, M. (1998). Fluence to dose equivalent conversion data and radiation weighting factors for high energy radiation. *Radiation Protection Dosimetry*, 77(3):159–170.

Pelliccioni, M. (2000). Overview of Fluence-to-effective Dose and Fluence-to-ambient Dose Equivalent Conversion Coefficients for High Energy Radiation Calculated Using the FLUKA Code. *Radiation Protection Dosimetry*, 88(4):279–297.

Pelliccioni, M. (2004). The impact of ICRP publication 92 on the conversion coefficients in use for cosmic ray dosimetry. *Radiation Protection Dosimetry*, 109(4):303–309.

Pfotzer, G. (1936a). Dreifachkoinzidenzen der Ultrastrahlung aus vertikaler Richtung in der Stratosphäre I. Meßmethode und Ergebnisse. *Zeitschrift für Physik*, 102:23–40. doi:10.1007/BF01336829.

Pfotzer, G. (1936b). Dreifachkoinzidenzen der Ultrastrahlung aus vertikaler Richtung in der Stratosphäre II. Analyse der gemessenen Kurve. *Zeitschrift für Physik*, 102:41–58. doi:10.1007/BF01336830.

Picone, J., A. Hedin, D. Drob, and A. Aikin (2002). NRLMSISE-00 empirical model of the atmosphere: Statistical comparisons and scientific issues. *Journal of Geophysical Research (Space Physics)*, 107(A12):1468. doi:10.1029/2002JA009430.

Pioch, C. (2008). *Messung und Analyse von Sekundärneutronen-Spektren der kosmischen Strahlung*. Diploma thesis. Technische Universität München.

Pioch, C., V. Mares, and W. Rühm (2010). Influence of Bonner sphere response functions above 20 MeV on unfolded neutron spectra and doses. *Radiation Measurements*, 45(10):1263–1267. doi:10.1016/j.radmeas.2010.05.007.

Pioch, C., V. Mares, W. Rühm, H. Iwase, Y. Iwamoto, T. Sato, M. Hagiwara, et al. (2011a). Calibration of a Bonner sphere spectrometer in quasi-monoenergetic neutron fields of 244 and 387 MeV. *Journal of Instrumentation*, 6:P10015. doi:10.1088/1748-0221/6/10/P10015.

Pioch, C., V. Mares, W. Rühm, E. Vashenyuk, and Y. Balabin (2011b). Measurement of cosmic ray neutrons with Bonner sphere spectrometer and neutron monitor at $79°N$. *Nuclear Instruments and Methods in Physics Research, Section A*, 626–627:51–57. doi: 10.1016/j.nima.2010.10.030.

Plainaki, C., A. Belov, E. Eroshenko, H. Mavromichalaki, and V. Yanke (2007). Modeling ground level enhancements: Event of 20 January 2005. *Journal of Geophysical Research (Space Physics)*, 112:A04102. doi:10.1029/2006JA011926.

Prael, R. and H. Lichtenstein (1989). User Guide to LCS: the LAHET code system. *Technical Report LA-UR-89-3014*, Los Alamos National Laboratory.

Reames, D. (1990). Energetic particles from impulsive solar flares. *The Astrophysical Journal (Supplement Series)*, 73:235–251. doi:10.1086/191456.

Reames, D. (1998). Solar Energetic Particles: Sampling Coronal Abundances. *Space Science Reviews*, 85(1–2):327–340. doi:10.1023/A:1005123121972.

Reames, D. (1999). Particle acceleration at the Sun and in the heliosphere. *Space Science Reviews*, 90(3-4):413–491. doi:10.1023/A:1005105831781.

Reames, D. (2000). Particle acceleration by CME-driven shock waves. In *Proceedings of the 26th International Cosmic Ray Conference, ICRC XXVI*, volume 516 of *American Institute of Physics Conference Series*, pages 289–300. doi:10.1063/1.1291483.

Roesler, S., W. Heinrich, and H. Schraube (1998). Calculation of Radiation Fields in the Atmosphere and Comparison to Experimental Data. *Radiation Research*, 149:87–97.

Roesler, S., W. Heinrich, and H. Schraube (2002). Monte Carlo Calculations of the Radiation Fileld at Aircraft Altitudes. *Radiation Protection Dosimetry*, 98(4):367–388.

Rollet, S., S. Agosteo, G. Fehrenbacher, C. Hranitzky, T. Radon, and M. Wind (2009). Intercomparison of radiation protection devices in a high-energy stray neutron field, Part I: Monte Carlo simulations. *Radiation Measurements*, 44:649–659.

Rühm, W., V. Mares, C. Pioch, G. Simmer, and E. Weitzenegger (2009a). Continuous measurement of secondary neutrons from cosmic radiation at mountain altitudes and close to the north pole - a discussion in terms of H*(10). *Radiation Protection Dosimetry*, 136(4):256–261. doi:10.1093/rpd/ncp161.

Rühm, W., V. Mares, C. Pioch, E. Weitzenegger, and H. Paretzke (2008). Continuous measurements of secondary neutrons from cosmic radiation at low atmospheric and low geomagnetic shielding by means of Bonner Sphere Spectrometers. In *Proceedings of the 21st European Cosmic Ray Symposium, ECRS XXI, Košice, Slovakia.*

Rühm, W., V. Mares, C. Pioch, E. Weitzenegger, R. Vockenroth, and H. Paretzke (2009b). Measurements of secondary neutrons from cosmic radiation with a Bonner sphere spectrometer at 79°N. *Radiation and Environmental Biophysics*, 48:125–133.

Saito, T., I. Miura, T. Yamazaki, A. Shimizu, K. Hosono, T. Itahashi, T. Saito, et al. (1995). The flat-topping system for the RCNP ring cyclotron. In *Proceedings of the 14th International Conference on Cyclotrons and Their Applications, Cape Town, South Africa*, page 169.

Sannikov, A., V. Mares, and H. Schraube (1997). High energy response functions of Bonner spectrometers. *Radiation Protection Dosimetry*, 70:291–294.

Sanuki, T., M. Fujikawa, H. Matsunaga, K. Abe, K. Anraku, H. Fuke, S. Haino, et al. (2003). Measurement of cosmic-ray proton and antiproton spectra at mountain altitude. *Physics Letters B*, 577:10–17. doi:10.1016/j.physletb.2003.10.021.

Sanuki, T., M. Motoki, H. Matsumoto, E. Seo, J. Wang, K. Abe, K. Anraku, et al. (2000). Precise Measurement of Cosmic-Ray Proton and Helium Spectra with the BESS Spectrometer. *The Astrophysical Journal*, 545(2):1135–1142.

Sato, T., , and K. Niita (2006). Analytical Functions to Predict Cosmic-Ray Neutron Spectra in the Atmosphere. *Radiation Research*, 166(3):544–555.

Sato, T., A. Endo, M. Zankl, N. Petoussi-Henss, and K. Niita (2007). Fluence-to-dose conversion coefficients for neutrons and protons calculated using the PHITS code and ICRP/ICRU adult reference computational phantoms. *Physics in Medicine and Biology*, 54:1997–2014. doi:10.1088/0031-9155/54/7/009.

Sato, T., H. Yasuda, K. Niita, A. Endo, and L. Sihver (2008). Development of PARMA: PHITS based Analytical Radiation Model in the Atmosphere. *Radiation Research*, 170(2):244–259.

Satoh, D., T. Sato, A. Endo, Y. Yamaguchi, M. Takada, and K. Ishibashi (2006a). Measurement of response functions of liquid organic scintillator for neutrons up to 800 MeV. *Journal of Nuclear Science and Technology*, 43:714–719.

Satoh, D., T. Sato, N. Shigyo, and K. Ishibashi (2006b). SCINFUL-QMD: Monte Carlo based computer code to calculate response function and detection efficiency of a liquid organic scintillator for neutron energies up to 3 GeV. *Technical Report JAEA-Data/Code 2006-023*, Japan Atomic Energy Agency (JAEA).

Savitskaya, E. and A. Sannikov (1995). High Energy Neutron and Proton Kerma Factors for different Elements. *Radiation Protection Dosimetry*, 60(2):135–146.

Schraube, H., J. Jakes, A. Sannikov, E. Weitzenegger, S. Roesler, and W. Heinrich (1997). The Cosmic Ray Induced Neutron Spectrum at the Summit of the Zugspitze (2963 m). *Radiation Protection Dosimetry*, 70:405–408.

Schraube, H., G. Leuthold, W. Heinrich, S. Roesler, V. Mares, and G. Schraube (2002). EPCARD (European Program Package for the Calculation of Aviation Route Doses). *Technical Report GSF-Report 08/02*, Helmholtz Zentrum München.

Schraube, H., V. Mares, , S. Roesler, and W. Heinrich (1999). Experimental verification and calculation of aviation route doses. *Radiation Protection Dosimetry*, 86(4):309–315.

Serber, R. (1947). Nuclear Reactions at High Energies. *Physical Review*, 72(11):1114–1115.

Shea, M. and D. Smart (1982). Possible evidence for a rigiditiy-dependent release of relativistic protons from the solar corona. *Space Science Reviews*, 32:251–271.

Shea, M. and D. Smart (1990). A summary of major solar proton events. *Solar Physics*, 127:297–320.

Shea, M. and D. Smart (1993). Solar Proton Events: History, Statistics and Predictions. In *Solar-Terrestrial Predictions – IV, Volume 2*.

Shea, M., D. Smart, K. McCracken, G. A. Dreschhoff, and H. Spence (2006). Solar proton events for 450 years: The Carrington event in perspective. *Advances in Space Research*, 38:232–238. doi:10.1016/j.asr.2005.02.100.

Shrimpton, P., H. Miller, M. Lewis, and M.Dunn (2004). *Doses from Computed Tomography (CT) examinations in the UK - 2003 Review*. In *Report of the National Radiological Protection Board, NRPB-W67*.

Sihver, L., D. Matthiä, T. Koi, and D. Mancusi (2008). Dose calculations at high altitudes and in deep space with GEANT4 using BIC and JQMD models for nucleus-nucleus reactions. *New Journal of Physics*, 10:105019. doi:10.1088/1367-2630/10/10/105019.

Simpson, J. (1983). Elemental and Isotopic Composition of the Galactic Cosmic Rays. *Annual Review of Nuclear and Particle Science*, 33:323–382. doi:10.1146/annurev.ns.33.120183.001543.

Smart, D. and M. Shea (1997). World grid of cosmic ray vertical cutoff rigidities for epoch 1990. In *Proceedings of the 25th International Cosmic Ray Conference, ICRC XXV, Durban, South Africa*, page 401.

Smart, D. and M. Shea (2003a). The limitations of using vertical cutoff rigidities determined from the IGRF field models for computing aircraft radiation dose. *Advances in Space Research*, 32(1):95–102.

Smart, D. and M. Shea (2003b). The space developed dynamic vertical cutoff rigidity model and its application to aircraft radiation dose. *Advances in Space Research*, 32(1):103–108.

Smart, D., M. Shea, and E. Flückiger (2000). Magnetospheric Models and Trajectory Computations. *Space Science Reviews*, 93:305–333.

Smart, D., M. Shea, and K. McCracken (2006). The Carrington event: possible solar proton intensity-time profile. *Advances in Space Research*, 38:215–225.

Smart, D., M. Shea, and P. Tanskanen (1971). A determination of the spectra, spatial anisotropy, and propagation characteristics of the relativistic cosmic ray flux on November 18, 1968. In *Proceedings of the 12th International Cosmic Ray Conference, ICRC XII, Hobart*, volume 2, pages 483–488.

Smart, D., M. Shea, M. Wilson, and L. Gentile (1991). Solar Cosmic Rays on 29 September 1989: an Analysis using the world-wide Network of Cosmic Ray Stations. In *Proceedings of the 22nd International Cosmic Ray Conference, ICRC XXII, Dublin*, volume 3, pages 97–100.

Stephens, D., L. Townsend, and J. Hoff (2005). Interplanetary crew dose estimates for worst case solar particle events based on historical data for the Carrington flare 1859. *Acta Astronautica*, 56:969–974.

Stoker, P. (1994). Relativistic solar proton events. *Space Science Reviews*, 73:327–385.

Stone, E., C. Cohen, W. Cook, A. Cummings, B. Gauld, B. Kecman, R. Leske, et al. (1998). The Cosmic-Ray Isotope Spectrometer for the Advanced Composition Explorer. *Space Science Reviews*, 86(1–4):258–356.

Störmer, C. (1930). Periodische Elektronenbahnen im Felde eines Elementarmagneten und ihre Anwendung auf Brüches Modellversuche und auf Eschenhagens Elementarwellen des Erdmagnetismus. *Zeitschrift für Astrophysik*, 1:237–274.

Sutherland, K., S. Miyajima, and H. Date (2007). A simple parallelization of GEANT4 on a PC cluster with static scheduling for dose calculations. *Journal of Physics: Conference Series*, 74:8.

Swinson, D. and M. Shea (1990). The September 29, 1989 ground-level event observed at high rigidity. *Geophysical Research Letters*, 17:1073–1075. doi:10.1029/GL017i008p01073.

Taddeucci, T. N., W. P. Alford, M. Barlett, R. C. Byrd, T. A. Carey, D. E. Ciskowski, C. C. Foster, et al. (1990). Zero-degree cross sections for the ^{7}Li(p,n)^{7}Be (g.s.+0.43 MeV) reaction in the energy range 80-795 MeV. *Physical Review C*, 41(6):2548–2555.

Taniguchi, S., N. Nakao, T. Nakamura, H. Yashima, Y. Iwamoto, D. Satoh, Y. Nakane, et al. (2007). Development of a quasi-monoenergetic neutron field using the ^{7}Li(p,n)^{7}Be reaction in the energy range from 250 to 390 MeV at RCNP. *Radiation Protection Dosimetry*, 126:23–27.

Thomas, D. and A. Alevra (2002). Bonner sphere spectrometry - a critical review. *Nuclear Instruments and Methods in Physics Research, Section A*, 476:12–20.

Thomas, D., A. Alevra, J. Hunt, and H. Scharube (1994). Experimental determination of the response of four Bonner sphere sets to thermal neutrons. *Radiation Protection Dosimetry*, 54(1):25–31.

Townsend, L., J. Hoff, and D. Stephens (2004). Hypothetical Worst Case Solar Particle Event Doses in LEO. In *IEEE Aerospace Conference Proceedings*.

Townsend, L., D. Stephens, J. Hoff, E. Zapp, H. Moussa, T. Miller, C. Campbell, et al. (2006). The Carrington event: possible doses to crews in space from a comparable event. *Advances in Space Research*, 38:226–231.

Townsend, L., E. Zapp, D. Stephens, and J. Hoff (2003). Carrington Flare of 1859 as a Prototypical Worst-Case Solar Energetic Particle Event. *IEEE Transactions on Nuclear Science*, 50:2307–2309.

Trenberth, K. and L. Smith (2005). The Mass of the Atmosphere: A Constraint on Global Analyses. *Journal of Climate*, 18:864–875. doi:10.1175/JCLI-3299.1.

Tsyganenko, N. (1987). Global quantitative of the geomagnetic field in the cislunar magnetosphere for different disturbance levels. *Planetary and Space Science*, 35:1347–1358.

Tsyganenko, N. (1989). Modeling the Earths magnetospheric magnetic field with a warped tail current sheet. *Planetary and Space Science*, 37:5–20.

Tsyganenko, N. (1995). Modeling the Earth's magnetospheric magnetic field confined within a realistic magnetopause. *Journal of Geophysical Research (Space Physics)*, 100:5599–5612.

Tsyganenko, N. (2002a). A model of the near magnetosphere with dawn-dusk asymmetrie 1. Mathematical structure. *Journal of Geophysical Research (Space Physics)*, 107(A8):1179–1195.

Tsyganenko, N. (2002b). A model of the near magnetosphere with dawn-dusk asymmetrie 2. Parameterization and fitting to observations. *Journal of Geophysical Research (Space Physics)*, 107(A8):1–17.

Turner, J. (1995). *Atoms, Radiation, and Radiation Protection*. John Wiley & Sons, Inc., 2nd edition.

Tylka, A., J. Adams, P. Boberg, B. Brownstein, W. Dietrich, E. Flückiger, E. Petersen, et al. (1997). CREME96: A Revision of the Cosmic Ray Effects on Micro-Electronics Code. *IEEE Transactions on Nuclear Science*, 44(6):2150–2160.

Uchiyama, Y., F. Aharonian, T. Tanaka, T. Takahashi, and Y. Maeda (2007). Extremely fast acceleration of cosmic rays in a supernova remnant. *Nature*, 449:576–578. doi:10.1038/nature06210.

Usoskin, I., K. Alanko, K. Mursula, and G. Kovaltsov (2002). Heliospheric modulation strength during the neutron monitor era. *Solar Physics*, 207(2):389–399.

Usoskin, I., K. Alanko-Huotari, A. Gennady, G. Kovaltsov, and K. Mursula (2005). Heliospheric modulation of cosmic rays: Monthly reconstruction for 1951–2004. *Journal of Geophysical Research (Space Physics)*, 110:A12108. doi:10.1029/2005JA011250.

Usoskin, I., G. Bazilevskaya, A. Gennady, and G. Kovaltsov (2011). Solar modulation parameter for cosmic rays since 1936 reconstructed from ground-based neutron monitors and ionization chambers. *Journal of Geophysical Research (Space Physics)*, 116:A02104. doi:10.1029/2010JA016105.

Vashenyuk, E., Y. Balabin, and B. Gvozdevsky (2008). Relativistic solar cosmic ray dynamics in large ground level events. In *Proceedings of the 21st European Cosmic Ray Symposium, ECRS XXI, Košice, Slovakia.*

Vashenyuk, E., Y. Balabin, and B. Gvozdevsky (2009a). Characteristics of relativistic solar cosmic rays from GLE modeling studies. In *Proceedings of the 31st International Cosmic Ray Conference, ICRC XXXI, Łódź, Poland.*

Vashenyuk, E., Y. Balabin, B. Gvozdevsky, and A. V. Germanenko (2009b). Relativistic SCRs during the events of solar cycle 19. *Bulletin of the Russian Academy of Sciences: Physics*, 73(3):31–33. doi:10.3103/S1062873809030058.

Vashenyuk, E., Y. Balabin, B. Gvozdevsky, S. Karpov, V. Yanke, E. Eroshenko, A. Belov, et al. (2005). Relativistic solar cosmic rays in January 20, 2005 event on the ground based observations. In *Proceedings of the 29th International Cosmic Ray Conference, ICRC XXIX, Pune, India.*

Vashenyuk, E., Y. Balabin, and P. Stoker (2007). Responses to solar cosmic rays of neutron monitors of a various design. *Advances in Space Research*, 40:331–337. doi:10.1016/j.asr.2007.05.018.

Vashenyuk, E., L. Miroshnichenko, J. Perez-Peraza, H. Kananen, and P. Tanskanen (1997). Generation and propagation chracteristics of relativistic solar protons during GLE of September 1989. In *Proceedings of the 25th International Cosmic Ray Conference, ICRC XXV*, volume 1, pages 161–167.

Walters, L. (editor) (1999). *MCNPX User's Manual.* TPO-E83-G-UG-X-00001, Revision 0.

Wang, L., X. Yang, J. Rappaport, C. Goodman, C. Foster, Y. Wang, J. Piekarevicz, et al. (1994). (p,n) quasi-free excitations in p-shell nuclei at 186 MeV. *Physical Review C*, 50(5):2438–2448.

Waxman, E. (1995). Cosmological Gamma-Ray Bursts and the Highest Energy Cosmic Rays. *Physical Review Letters*, 75(3):386–389.

Webber, W., R. Golden, S. Stochaj, J. Ormes, and R. Strittmatter (1989). A measurement of the cosmic-ray H-2 and He-3 spectra and H-2/He-4 and He-3/He-4 ratios in 1989. *The Astrophysical Journal*, 380:230–234.

Wiedenbeck, M. E., N. E. Yanasak, A. C. Cummings, A. J. Davis, J. S. George, R. A. Leske, R. A. Mewaldt, et al. (2001). The Origin of Primary Cosmic Rays: Constraints from ACE Elemental and Isotopic Composition Observations. *Space Science Reviews*, 99:15–26. doi:10.1023/A:1013816209004.

Wiegel, B., S. Agosteo, R. Bedogni, M. Caresana, A. Esposito, G. Fehrenbacher, M. Ferrarini, et al. (2009). Intercomparison of radiation protection devices in a high-energy stray neutron field, Part II: Bonner sphere spectrometry. *Radiation Measurements*, 44:660–672.

Wiegel, B. and A. Alevra (1994). Calculations of the Response Functions of Bonner Spheres with a Spherical ^{3}He Proportional Counter Using a Realistic Detector Models. *Technical Report PTB-Bericht PTB-N-21*, Physikalisch-Technische Bundesanstalt.

Wiegel, B. and A. Alevra (2002). NEMUS - the PTB Neutron Multisphere Spectrometer: Bonner spheres and more. *Nuclear Instruments and Methods in Physics Research, Section A*, 476:36–41.

Wiegel, B., A. Alevra, M. Matzke, U. Schrewe, and J. Wittstock (2002). Spectrometry using the PTB neutron multisphere spectrometer (NEMUS) at flight altitudes and at ground level. *Nuclear Instruments and Methods in Physics Research, Section A*, 476(1-2):52–57.

Wissmann, F., M. Reginatto, and T. Moller (2010). Ambient dose equivalent at flight altitudes: A fit to a large set of data using a Bayesian approach. *Journal of Radiological Protection*, 30:513–524.

Xapsos, M., J. Barth, E. Stassinopoulos, S. Messenger, R. Walters, G. Summers, and E. Burke (2000). Chracterizing solar proton energy spectra for radiation effects application. *IEEE Transactions on Nuclear Science*, 47(6):2218–2223.

Yashiro, S., N. Gopalswamy, G. Michalek, O. St. Cyr, S. Plunkett, N. Rich, and R. Howard (2004). A catalog of white light coronal mass ejections observed by the SOHO spacecraft. *Journal of Geophysical Research (Space Physics)*, 109:A07105. doi:10.1029/2003JA010282.

Yoshimori, M. (2005). Production and behavior of beryllium 7 radionuclide in the upper atmosphere. *Advances in Space Research*, 36(5):922–926. doi:10.1016/j.asr.2005.04.093.

Yurchyshyn, V., S. Yashiro, V. Abramenko, H. Wang, and N. Gopalswamy (2005). Statistical distribution of speeds of coronal mass ejections. *The Astrophysical Journal*, 619:599–603.

Zeller, E., G. Dreschhoff, and C. Laird (1986). Nitrate flux on The Ross Ice Shelf, Antarctica and its relations to solar cosmic rays. *Geophysical Research Letters*, 13:1264–1267.

Zhizhin, M., E. Kihn, R. Redmon, D. Medvedev, and D. Mishin (2008). Space Physics Interactive Data Resource - SPIDR. *Earth Science Informatics*, 1(2):79–91.

Zimbardo, G., P. Pommois, A. Ippolito, and P. Veltri (2006). Angular size of Coronal Mass Ejections deduced from Energetic Particle Observations . *Memorie della Società Astronomica Italiana Supplement*, 9:75.

LIST OF FIGURES

LIST OF TABLES

APPENDIX

A

MISCELLANEOUS SUPPLEMENTARY INFORMATION

In this chapter miscellaneous supplementary information is provided including a glossary of definitions and explanations of physical quantities as well as the relations among them. Subsequently, the most important quantities in dosimetry and fluence-to-dose conversion coefficients used in the present work are discussed.

A.1 Definition of physical quantities

In the following, several physical quantities are defined and the corresponding terminology used throughout the present work is explained. Most important for the description of particle spectra and the physical characterization of radiation are the following (also see *ICRU*, 1998, 2011, Reports 60 and 85):

$$\Phi = \frac{dN}{dA} = \frac{\text{number of particles}}{\text{area}} = \text{fluence} \tag{A.1}$$

$$\dot{\Phi} = \frac{d\Phi}{dt} = \frac{d^2N}{dAdt} = \frac{\text{number of particles}}{\text{area} \cdot \text{time}} = \text{fluence rate} \tag{A.2}$$

$$\begin{aligned} J &= \frac{d^2\Phi}{dt d\Omega} = \frac{d^3N}{dAdt d\Omega} = \frac{\text{number of particles}}{\text{area} \cdot \text{time} \cdot \text{solid angle}} \\ &= \text{intensity or radiance} \end{aligned} \tag{A.3}$$

These quantities are also used as differentials with respect to the kinetic energy E_k:

$$\frac{d\Phi}{dE_k} = \frac{d^2N}{dAdE_k} = \frac{\text{fluence}}{\text{kinetic energy}} = \text{differential fluence} \tag{A.4}$$

$$\frac{d\dot{\Phi}}{dE_k} = \frac{d^3N}{dAdtdE_k} = \frac{\text{fluence rate}}{\text{kinetic energy}} = \text{differential fluence rate} \tag{A.5}$$

$$\begin{aligned} j &= \frac{dJ}{dE_k} = \frac{d^3\Phi}{dtd\Omega dE_k} = \frac{d^4N}{dAdtd\Omega dE_k} = \frac{\text{intensity}}{\text{kinetic energy}} \\ &= \text{differential intensity} \end{aligned} \tag{A.6}$$

All the definitions outlined above are related to and can be derived from each other. The fluence rate $\dot{\Phi}$ is most frequently used in the present work in order to describe secondary cosmic ray particles calculated in the atmosphere or measured on ground. The fluence rate can easily be derived from the corresponding spectral intensity via integration over certain intervals of kinetic energy and solid angle ΔE_k, $\Delta\Omega$:

$$\dot{\Phi} = \int_{\Delta E_k} \int_{\Delta\Omega} j(E_k, \Omega, t) dE_k d\Omega \ . \tag{A.7}$$

For an isotropic particle intensity, which is e.g. the case for galactic cosmic ray particles, the fluence rate is given as

$$\dot{\Phi} = 4\pi \int_{\Delta E_k} j(E_k, t) dE_k \ . \tag{A.8}$$

To avoid misunderstandings, please note that some of the prescribed quantities are frequently used in terms of spectral distributions, i.e. they are explicitly considered as a function of kinetic energy. Equivalent to this terminus, such distributions are simply called spectra (e.g. spectral fluence rate distribution = fluence rate spectrum or differential intensity distribution = differential energy spectrum). Furthermore it should be noted that for simplicity sometimes the terminus flux may applied to any of the quantities. Since “flux” is rather poorly defined as a physical quantity, the meaning should be clear from the context.

For the characterization of primary cosmic ray particles, the magnetic rigidity or simply rigidity R is a very useful quantity. In a given magnetic field of magnitude $|\vec{B}|$ it is defined as

$$R = \frac{pc}{|q|} = \frac{pc}{Ze} = r_L|\vec{B}|c, \tag{A.9}$$

where p denotes the particle’s momentum, c the speed of light, q the charge, Z the atomic number, e the elementary charge, and r_L the Larmor radius. Applying basic relativistic calculus, the rigidity is connected to the total energy E of a particle via

$$R = \frac{\sqrt{E^2 - m_0^2c^4}}{Ze} = \frac{\sqrt{E_k(E_k + 2E_0)}}{Ze}, \tag{A.10}$$

where m_0 is the rest mass and E_0 the rest energy.

Differential primary cosmic ray particle spectra are usually given as a function of rigidity

$$j = j(R) = \frac{dJ(R)}{dR}. \tag{A.11}$$

The corresponding differential spectra with respect to the kinetic energy are derived via

$$j(E_k) = \frac{dJ(E_k)}{dE_k} = \frac{dJ(R)}{dR} \cdot \frac{dR(E_k)}{dE_k}. \tag{A.12}$$

With Equation A.10 this becomes

$$j(E_k) = \frac{dJ(E_k)}{dE_k} = \frac{dJ(R)}{dR} \cdot \frac{E_k + E_0}{Ze\sqrt{E_k(E_k + 2E_0)}}. \tag{A.13}$$

For the calculation of secondary particle fluence rates in the atmosphere due to primary cosmic radiation it is essential to have a measure for the air mass overburden at the altitude of interest. This is described by the atmospheric depth d = mass/area. The atmospheric depth at an altitude h is related to the pressure $p(h)$ for a given gravitational acceleration $g(h)$ according to

$$d = \frac{m(h)}{A} = \frac{F_g(h)}{A \cdot g(h)} = \frac{p(h)}{g(h)} = \int_h^\infty \rho(h')dh', \tag{A.14}$$

where $m(h)$ is the mass of air above the point of interest, $\rho(h)$ is the air density, and F_g the gravitational force on area A. For considerations in the lower atmosphere, the gravitational acceleration is assumed to be constant with a value of $g = 9.81$ m/s^2.

Any kind of particle impinging on a volume of matter, such as cosmic rays in the atmosphere, undergoes interactions with the constituents of the material. The probability of an interaction to occur for N particles in a beam impinging on a target with area A is related to the total cross section σ_{tot}:

$$\sigma_{tot} = \sum_i \sigma_i = \frac{A \cdot N_{int}}{N \cdot N_T}, \tag{A.15}$$

where N_T denotes the number of target particles and N_{int} the number of interactions that have been encountered. The total cross section is the sum of all partial cross sections σ_i for all potential interactions (e.g. elastic scattering, nuclear break-up, or spallation). In general, cross sections are further divided into elastic σ_{el} and inelastic σ_{inel}. The elastic cross section is related to processes in which only kinematical exchanges occur, whereas the inelastic is related to processes in which new particles are generated. The total cross section, however, defines the mean free path λ a particle can travel in the material without interacting:

$$\lambda = \frac{1}{\sigma_{tot} \cdot n_T}, \tag{A.16}$$

where n_T is the atom density in the target. For cosmic rays it is straightforward to consider the mean free path in terms of atmospheric depth d_λ which may be approximated by multiplication with the mass density of the air at the altitude of interest

$$d_\lambda = \rho \cdot \lambda = \frac{\rho}{\sigma_{tot} \cdot n_T}. \tag{A.17}$$

A.2 Dosimetry

Any kind of ionizing radiation, such as e.g. photon, electron, or neutron radiation traversing a volume of matter interacts with atoms and molecules contained in the volume. In these interactions energy may either be transferred to secondary particles (e.g. ionization, excitation) which may also leave the volume or deposited locally via diverse mechanisms (e.g. scattering, nuclear reactions). The energy transfer depends of course on the characteristics of the radiation, i.e. its type, energy, and intensity as well as on the characteristics of the material, i.e. the composition and density.

Energy depositions in biological tissue may produce free radicals and potentially cause damage such as DNA single and double strand breaks. This may in turn lead to cell malfunctioning or cell death. In order to suitably quantify radiation including its potential biophysical impact, the **I**nternational **C**ommission on **R**adiation **U**nits and Measurements (ICRU) was founded. This commission gives recommendations regarding definitions of appropriate quantities and units for radiation as well as guidelines, procedures, and data for corresponding measurements and clinical applications. Furthermore, in order to recommend limits on radiation exposure and to provide radiological protection standards as well as a scientific basis for legislations, the **I**nternational **C**ommission on **R**adiological **P**rotection (ICRP) was founded. What follows, is a description and explanation of radio-biophysical quantities used in the present work. The definitions of all these most important quantities in dosimetry are based on *ICRU* (1980, Report 33), *ICRU* (1998, Report 60), *ICRU* (2011, Report 85) *ICRP* (1990, Publication 60), and *ICRP* (2007, Publication 103).

The basic physical quantity in dosimetry is the absorbed dose D in a volume element with mass dm

$$D = \frac{dE}{dm}, \tag{A.18}$$

where dE is the amount of energy deposited in the volume, which is given as

$$dE = T_{in} - T_{out} + Q_{\Delta m}. \tag{A.19}$$

T_{in} denotes the energy of all particles entering, T_{out} that of all particles leaving the volume, and $Q_{\Delta m}$ denotes the change in rest mass of all particles involved. The unit of absorbed dose is gray, where 1 Gy = 1 J/kg.

Another very important quantity describing the effectiveness of the energy transfer for ionizing particles along their path through matter is the linear energy transfer (LET) which is defined as the mean energy loss per unit path length dl due to collisions with electrons in the material:

$$L_{\Delta} = \frac{dE_{\Delta}}{dl}. \tag{A.20}$$

The index Δ denotes a cut-off level taking only individual energy losses smaller than this threshold into account. High LET particles are densely ionizing, whereas low LET particles are loosely ionizing. If no energy cut-off is considered, the unrestricted linear energy transfer L_{∞} is identical to the stopping power and may be denoted by L for simplicity reasons.

The absorbed dose defined in Equation A.18 is independent of the characteristics of radiation, i.e. its type, energy, and LET. In order to accurately estimate the radio-biological impact and the severeness of damage in tissue exposed to radiation, these characteristics have to be taken into account. For this reason, the ICRP introduced the equivalent dose H_T which is defined as the sum of absorbed doses D_T in the volume of a particular organ or given tissue T weighted by a factor w_R related to the characteristics of the radiation type R:

$$H_T = \sum_R w_R D_{T,R}. \tag{A.21}$$

The unit of the equivalent dose is sievert [Sv]. The radiation-specific factors w_R were introduced to account for the relative biological effectiveness (RBE) of radiation with certain type and energy compared to low LET photons that have a weighting factor of $w_R = 1$. In *ICRP* (1990, Publ. 60) which is referred to as ICRP-60 in the following, the first set of weighting factors was provided for all kinds of radiation. The factors for neutrons and protons were revised in *ICRP* (2007, Publ. 103; referred to as ICRP-103), with the most important change being the reduction of the w_R for protons from 5 to 2. The changes in the factors for neutrons and protons result in a significant reduction of equivalent doses due to cosmic radiation, in particular for aircrews where contributions of protons and neutrons are most important (see Chapter 6). All weighting factors recommended in ICRP-60 and ICRP-103, respectively, are listed in Table A.1.

In order to define an appropriate radiation protection quantity for humans and suitably quantify the impact of radiation on the whole human body, specific sensitivities of various organs and tissue types have to be taken into account in addition to the radiation weighting factors. For this purpose, the ICRP defined tissue weighting factors w_T for certain organs in ICRP-60 and updated them in ICRP-103 (details and numerical values are given in *ICRP*, 1990, 2007). Accounting for organ and tissue specific sensitivities as well as for radiation specific RBEs, the effective dose E is given as the tissue-weighted sum of the equivalent doses in all

TABLE A.1: Radiation weighting factors given by ICRP Publication 60 and 103 (*ICRP*, 1990, 2007) for all radiation types.

RADIATION TYPE	RADIATION WEIGHTING FACTOR w_R	
	ICRP-60	ICRP-103
Photons	1	1
Electrons, Muons	1	1
Protons, charged Pions	5	2
Alpha particles, heavy Ions	20	20
Neutrons (ICRP-60)	$w_R = \begin{cases} 5, & E_n < 1\ \text{keV} \\ 10, & 1\ \text{keV} \leq E_n \leq 100\ \text{keV} \\ 20, & 100\ \text{keV} < E_n \leq 2\ \text{MeV} \\ 10, & 2\ \text{MeV} < E_n \leq 20\ \text{MeV} \\ 5, & E_n > 20\ \text{MeV} \end{cases}$	
Neutrons (ICRP-103)		$w_R = \begin{cases} 2.5 + 18.2e^{-(ln(E_n))^2/6}, & E_n < 1\ \text{MeV} \\ 5.0 + 17.0e^{-(ln(2E_n))^2/6}, & 1\ \text{MeV} \leq E_n \leq 50\ \text{MeV} \\ 2.5 + 3.2e^{-(ln(0.04E_n))^2/6}, & E_n > 50\ \text{MeV} \end{cases}$

organs specified by the ICRP:

$$E = \sum_T w_T H_T = \sum_T w_T \cdot \sum_R w_R D_{T,R} \tag{A.22}$$

As for the equivalent dose, the unit of the effective dose is sievert [Sv].
Due to their definition with respect to the radio-biophysical impact on humans, both the equivalent dose and the effective dose are not directly accessible in measurements. Therefore, an operational quantity, the dose equivalent H [Sv], is defined as the product of the absorbed dose $D_L = dD(L)/dL$ with respect to the unrestricted LET $L_\infty = L$ and a quality factor Q. This factor accounts for different efficiencies of different types and energies of radiation to cause a certain biological effect and is defined as a function of L in water. Accordingly, the dose equivalent is finally given by:

$$H = Q \cdot D = \int_0^\infty Q(L) \frac{dD(L)}{dL} dL = \int_0^\infty Q(L) D_L dL \tag{A.23}$$

$$Q(L) = \begin{cases} 1, & L < 10 \text{ keV}/\mu\text{m} \\ 0.32 \cdot L - 2.2, & 10 \text{ keV}/\mu\text{m} \leq L \leq 100 \text{ keV}/\mu\text{m} \\ 300/\sqrt{L}, & L > 100 \text{ keV}/\mu\text{m} \end{cases} \tag{A.24}$$

Following the definition of the dose equivalent H, the ICRP recommends to use the ambient dose equivalent $H^*(d)$ [Sv] as operational quantity for measuring and monitoring radiation fields in terms of dose. According to the ICRP, $H^*(d)$ at a particular point in a given field is the dose equivalent that would result in the ICRU sphere at depth d (measured from the sphere surface in opposite direction to the radius vector) if the corresponding field were expanded and aligned. The ICRU sphere is defined as a soft-tissue-equivalent sphere with 30 cm diameter and a mass density of 1 g/cm^3 (for details refer to *ICRU*, 1980, Report 33). As it is required for radiation protection purposes, $H^*(d)$ is supposed to allow for a conservative estimation of the effective dose in any radiation field. In most cases the ambient dose equivalent is used at a depth of 10 mm, accordingly denoted as $H^*(10)$, and measurement devices such as e.g. REM or scintillation counters are usually calibrated to $H^*(10)$ in radiation fields with known spectral shape and intensity.
For the sake of completeness, it should be mentioned that in many cases radiation fields change with time. To account for any time dependence, all dose quantities defined above can be given as dose rates, i.e. the doses per unit time (denoted by $\dot{H}^*(10)$ or $\dot{E}$).
For a given spectral fluence rate distribution, so-called fluence-to-dose conversion coefficients can be used to calculate ambient dose equivalent and effective dose rates. In the frame of the present work spectral fluence rate distributions were determined both by means of Monte Carlo techniques and by means of Bonner sphere spectrometry. All these spectra were converted to effective dose rates according to ICRP-60 and ambient dose equivalent rates using conversion coefficients provided by *Ferrari et al.* (1996, 1997a,b,c,d, 1998), *Pelliccioni* (2000), and references therein. Effective dose rates following ICRP-103 were obtained using conversion factors based on *Sato et al.* (2007) for protons and neutrons. The final ICRP-103 values used, which will be included in the next ICRP recommendation, were kindly provided by *T. Sato* in private communication. All these conversion coefficients were computed by means of Monte Carlo codes (FLUKA and PHITS) and, in case of effective dose, for

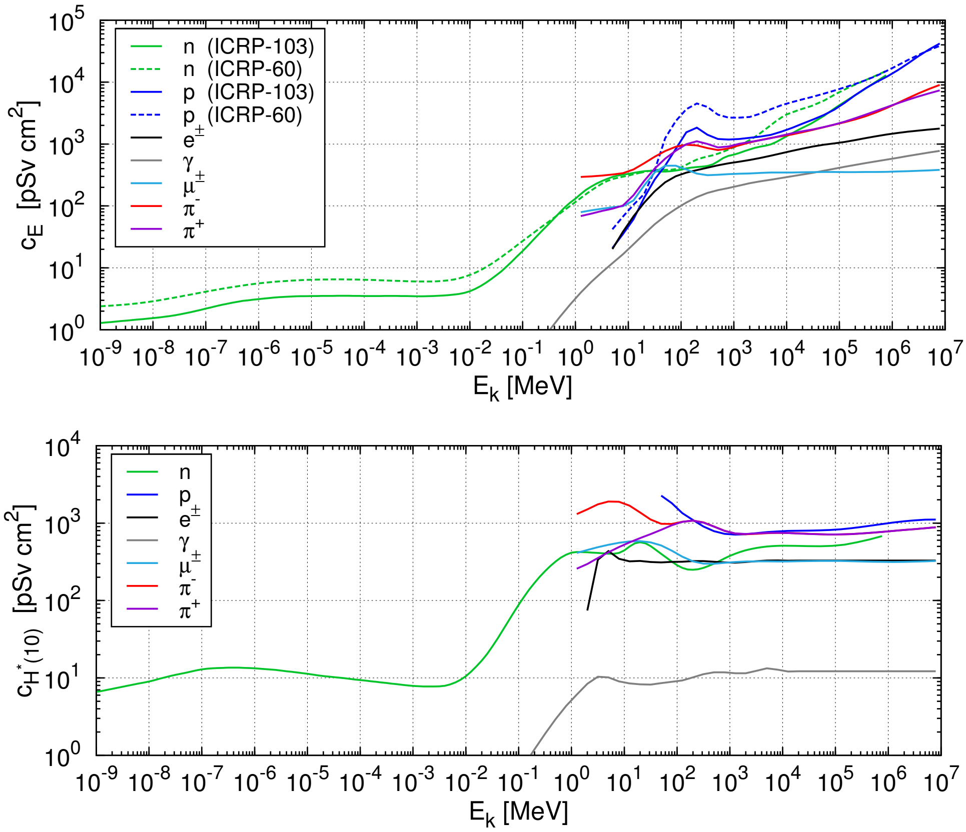

FIGURE A.1: Fluence-to-dose conversion coefficients for effective dose E in an isotropic irradiation field (top panel) and ambient dose equivalent $H^*(10)$ (bottom panel) for all relevant species of secondary cosmic radiation as a function of kinetic energy. Coefficients for effective dose according to ICRP-60 and those for ambient dose equivalent are from *Pelliccioni* (2000) and references therein. Fluence-to-effective dose factors following ICRP-103 for neutrons and protons are based on *Sato et al.* (2007).

several irradiation geometries using voxel phantoms representing the human body. In Figure A.2 the coefficients used in the present work are shown for all particles of secondary cosmic radiation which are important in terms of radiation protection.

Using the coefficients ($c_{E,i}$) for effective dose E_i, the corresponding dose rates related to a spectral fluence rate distribution $\dot{\Phi}_i(E_k)$ can be calculated for a particle type i via

$$\dot{E}_i = \int c_{E,i}(E_k) \frac{d\dot{\Phi}_i(E_k)}{dE_k} dE_k, \tag{A.25}$$

where E_k is the kinetic energy. The total effective dose rate is then obtained by summing over contributions of all particles:

$$\dot{E} = \sum_i \dot{E}_i \; . \tag{A.26}$$

The accumulated dose is easily calculated via integration with respect to the time interval Δt considered:

$$E = \int_{\Delta t} \dot{E} dt. \tag{A.27}$$

In the same way, the individual and total ambient dose equivalent (rates) are obtained using the corresponding conversion coefficients.

APPENDIX

B

SUPPLEMENTARY INFORMATION ON GEANT4 CALCULATIONS

In this chapter various supplementary information on the Monte Carlo (MC) calculations performed in the frame of the present work is provided. For all particle transport simulations the three-dimensional MC code GEANT4[1] (*Agostinelli et al.*, 2003; *Allison et al.*, 2006) was used. This code was developed at CERN and particularly designed to simulate high-energy processes with nearly any kind of particle. It is freely available[2] as source code written in C++. Applying this object oriented software technology provides a high degree in transparency, allowing the user to change and combine any parts of the code according to his demands. The philosophy behind the GEANT4 project is that the users are the ones being aware of the specific demands on a simulation problem and not the code developers. This in turn requires detailed knowledge at the user side, especially about the physics, and it is the user's responsibility to make sure the problem is properly modeled.

Therefore, in the first sections of this chapter necessary background knowledge on the MC method and a general overview of the GEANT4 simulation toolkit is given. Basic information on the handling of the code itself is not described here but may be found in the manual (*GEANT4 Collaboration*, 2009b). The very details of each transport calculation done in the present work are described in the corresponding chapters in the main part. Since all these calculations were mainly based on hadronic interactions over a wide range in energy, important features of the hadronic framework available in GEANT4 are outlined in every detail in the following.

---

[1] GEANT4 is an acronym for **GE**ometry **AN**d **T**racking

[2] http://geant4.cern.ch/

B.1 Fundamentals of the Monte Carlo method

As a Monte Carlo code, GEANT4 simulates particle tracks in matter by throwing random numbers in order to sample interaction probability distributions defining physical processes and final state characteristics. The interaction probabilities are given by cross sections which are either based on experimental data or theoretical models. The mean free path or interaction length for a certain reaction with cross section σ_i on isotope i of mass m_i is (see also A.16)

$$\lambda = \left(\rho \sum_i x_i \sigma_i(Z_i, A_i, E)/m_i \right)^{-1}, \tag{B.1}$$

where x_i is the mass fraction in the current material of density ρ.
The number of mean free paths n_λ a particle can travel before the next interaction occurs is

$$n_\lambda = \int_0^l \frac{dl}{\lambda(l)}. \tag{B.2}$$

The path length l and also λ are energy and material dependent, whereas n_λ is independent of both. Therefore, the probability of surviving a distance l without interacting is given as (*Carter and Cashwell*, 1975)

$$P(l) = 1 - \exp(-n_\lambda). \tag{B.3}$$

By throwing a random number η uniformly distributed in $[0, 1[$, the probability distribution function is sampled to give

$$n_\lambda = -\ln(\eta). \tag{B.4}$$

This allows to determine the distance $s = n_\lambda \cdot l$ to the point of interaction.
In GEANT4 each possible reaction at a given point proposes a step length according to the Monte Carlo approach outlined above. The process suggesting the shortest, i.e. the one with the highest partial reaction cross section, is invoked and finally determines the reaction and the next interaction point. A boundary condition for this method is that the cross section must not change considerably along each step. This is ensured in GEANT4 by not allowing the residual range of a particle to decrease by more than 20% per step. Further details may be found in *GEANT4 Collaboration* (2009a,b).

B.2 Geometry

GEANT4 provides a user friendly and powerful geometry environment. The user defined geometrical details can be modeled by constructive solid primitives (e.g. boxes, spheres) and boolean operations. In GEANT4 the geometry setup is done following the Russian doll (Matrjoshka) principal, i.e. various parts of the geometry are fully contained in bigger mother volumes. This defines a geometrical hierarchy and increases the tracking efficiency. All necessary information on the setup such as the exact positioning and orientation or the material characteristics can be implemented in straightforward manner and is well described in the manual (*GEANT4 Collaboration*, 2009b).

B.3 Physics

In GEANT4 certain physical processes (e.g. (in)elastic scattering) can be assigned to certain particle types, and several models can be assigned to certain processes. Therefore, it is clearly distinguished between processes and models. Processes describe a particular initial or final state and have a well-defined cross-section or mean lifetime in case of decay. On the other hand, models describe the production of secondary particles. During run time the models are used by certain processes in order to determine the secondaries generated in an event and to calculate their momenta. This approach gives the possibility of applying multiple models for the same process which was done in the frame of this work with high-energy hadronic interactions. A huge variety of physical processes is available in the GEANT4 simulation toolkit. Depending on its nature, this process can either take place at rest (e.g. decay), continuously along a step (e.g. Čerenkov radiation), or after a step such as e.g. evaporation of nucleons. Among others, the process categories embedded in GEANT4 can be divided into electromagnetic, hadronic, transportation, and decay. For the particle transport simulations performed in the frame of the present work, the electromagnetic processes including charged muons and pions and the hadronic interactions were most important. For this reason the following discussion is restricted to these processes with main focus on hadronic interactions.

B.3.1 Electromagnetic physics

The electromagnetic physics in GEANT4 comprise standard handling of basic processes for electrons, positrons, photons, and ions. This includes Compton scattering, photoelectric effect, pair production, muon-pair production for photons, ionization, δ-electron production, Bremsstrahlung, Čerenkov radiation, and annihilation. Further low-energy electromagnetic physics taking the atomic shell structure into account, such as Rayleigh scattering, are also available. Special process classes handle muon interactions like Bremsstrahlung, capture, and annihilation. Additionally, multiple scattering processes based on the theory of *Lewis* (1950) are provided in separate classes for muons, electrons/positrons, and other charged particles. The corresponding classes deliver corrections for path lengths and lateral displacements of multiply scattered charged particles. Also ionization processes for muons, electrons/positrons, and other charged particles are treated in their particular physics class since GEANT4 release 9.0.

Generally, electromagnetic interactions are well understood over a wide range in energy and the corresponding physics implemented in GEANT4 has been well validated below several MeV energy against experimental data (see e.g. *Amako et al.*, 2006; *Kadri et al.*, 2007; *Guatelli et al.*, 2007; *Lechner et al.*, 2009, 2010).

In order to increase the computational efficiency, a certain production cutoff in range has to be set for electrons, positrons, and photons according to the specific demands of the simulation. Especially when rather large geometries such as the Earth's atmosphere are simulated with particle energies covering a wide range in energy this has to be considered. In any material the cutoff value is translated to an energy below which the continuous slowing down approximation is used and no secondary particles are produced. The particle then looses its remaining kinetic energy continuously along the track. In geometries where the density of the same material strongly varies in different parts, which is e.g. the case in modeling the atmosphere, it is not feasible to set an overall cutoff for the geometry since the mean free path of a particle with given energy strongly varies within the geometry. By setting up additional regions in the geometry various cutoffs can be applied for various regions which in turn may contain several other volumes. This allows to increase the simulation performance significantly without loosing necessary information.

B.3.2 The GEANT4 hadronic framework

As already stated, GEANT4 offers the possibility to replace models assigned to certain interaction processes. This is particularly the case in the hadronic framework of GEANT4. All hadronic models can be categorized in data-driven, parametrization-driven, and theory-driven modeling approaches. The data-driven hadronic models mainly deal with the detailed transport of low-energy neutrons and isotope production. The low- and high-energy parametrized models include fission, capture, elastic, and inelastic scattering reactions. At high energies above several 10 - 100 MeV, the simulation of hadronic interactions relies on theoretical models since experimental cross section data are scarce. All these models can be arranged in complementary or alternative manner.

In all transport calculations in the present work neutrons and protons were of main importance. For both particle types the interactions considered and models used for the description of hadronic processes are summarized in Table B.1. The related physics and specific features are described in the following.

Low-energy neutron physics and thermal scattering

The low-energy neutron transport in GEANT4 is mainly treated in a data-driven approach. For this purpose various cross section datasets are available in the G4NDL bundle. If not stated otherwise, results from the present work were obtained using G4NDL v. 3.13 which is mainly based on the ENDF/B-VI cross section evaluation (*McLane*, 1991; *MacFarlane*, 1994a). This evaluation is complemented with others such as the Japanese evaluations JENDL3.2 (*Nakagawa et al.*, 1995) and JENDL-HE (*Fukahori et al.*, 2002) including extensions to 150 MeV for several isotopes.

The high-precision models (`G4NeutronHP*` in Table B.1) either use these data to sample the corresponding double differential reaction cross section or rely on theoretical approaches when no data are available. The high-precision modeling of neutrons contains elastic scattering based on the free gas approximation, inelastic scattering with tabulated final state information, capture, and fission.

At neutron energies below 4 eV scattering processes have to be treated differently and the free gas approximation used in the high-precision models does not give an accurate description. At thermal neutron energies the specific thermal motion of the scattering nucleus gains importance. In molecules of the scattering material translational motion as well as vibration and rotation of the chemically bound atoms may be excited. This in turn highly affects the neutron scattering cross section and the final state characteristics such as energy gain or loss and the scattering angle. For this reason, thermal scattering cross sections for neutron scattering on bound hydrogen nuclei in water and polyethylene (PE) are adapted in GEANT4

TABLE B.1: List of hadronic interactions considered and models used in GEANT4 proton and neutron transport calculations.

NEUTRONS		
Process	Energy	Model
Elastic	< 4 eV	G4NeutronHPThermalScattering
	< 20 MeV	G4NeutronHPElastic
	> 19.5 MeV	G4HadronElastic
Inelastic	< 20 MeV	G4NeutronHPInelastic
	19.9 MeV – 9.9 GeV	G4BinaryCascade
	19.9 MeV – 10 GeV	G4CascadeInterface
	9.5 MeV – 15 GeV	G4LENeutronInelastic
	>10 GeV	QGSP
Fission	< 20 MeV	G4NeutronHPFission
	> 20 MeV	G4LFission
Capture	< 20 MeV	G4NeutronHPCapture
	> 20 MeV	G4LCapture

PROTONS		
Process	Energy	Model
Elastic	> 0.0 MeV	G4HadronElastic
Inelastic	< 9.9 GeV	G4BinaryCascade
	< 10 GeV	G4CascadeInterface
	9.9 MeV – 15 GeV	G4LEProtonInelastic
	>10 GeV	QGSP

from the low-energy extension of ENDF/B-VI (*MacFarlane*, 1994b). In this evaluation neutron scattering is divided into inelastic, coherent elastic, and incoherent elastic, where the inelastic part is most important for neutron transport in PE and water. The corresponding cross section is given as

$$\sigma(E \to E', \Omega \to \Omega') = \frac{\sigma_b}{4\pi kT}\sqrt{\frac{E}{E'}}S(\alpha, \beta), \tag{B.5}$$

where E, E' denote the initial and final neutron energy, respectively, and Ω the scattering angle in the laboratory system. σ_b is the characteristic bound scattering cross section of the material with temperature kT in eV, and $S(\alpha, \beta)$ is the asymmetric form of the thermal scattering law which is basically the Fourier transform of a material-dependent scattering function. The scattering law only depends on two parameters the momentum transfer α and the energy transfer β. These parameters are provided in tabulated form in GEANT4 and have to be explicitly sampled for accurate neutron transport calculations at thermal energies. Further details on thermal scattering may be found in *Mattes and Keinert* (2005).

Modeling spallation reactions in intra-nuclear cascade (INC) models

At energies above approximately 20 MeV only very few experimental data are available, and the modeling of interactions fully relies on theory in GEANT4 as in any other MC code. Of large importance for the results of particle transport simulations is the energy range between a few hundreds of MeV to a few GeV where spallation reactions are induced. Spallation is a nuclear reaction in which a relativistic neutron or proton hits a heavy nucleus. The characteristics of the target nucleus during spallation are usually described in two steps. In the first step the target nucleus is heated and ejects several rather fast nucleons and heavier compounds (e.g. α particles, deuterons). With a typical duration of 10^{-23} - 10^{-22} s, this step results in a highly excited nucleus. In this so-called pre-equilibrium stage, the nucleus again ejects several nucleons and/or is split by fission reactions. Subsequently follows a slower (10^{-18} - 10^{-16} s) phase, the de-excitation step, which is characterized by evaporation of nucleons with average energies of 1 - 2 MeV. The residual nucleus then is still highly excited and emits γ-rays to further cool down (see e.g. *Walters*, 1999).

In MC codes the first step of spallation processes is modeled in the frame of intra-nuclear cascade (INC) models which aim to describe the initial collision with the target nucleus and all potential processes until the pre-equilibrium stage is reached. According to *Serber* (1947) this step can be regarded as individual particle-nucleon collisions if the De Broglie wavelength of the incoming particle is shorter than the mean intra-nucleon distance in the target nucleus. In this case the incoming particle is able to see the individual sub-atomic structure in the target, and particular collisions lead to the ejection of fast nucleons and heavier fragments. After the cascade the remaining nucleus is modeled in a sequence of several other models for the pre-equilibrium stage, fission, Fermi break-up, evaporation, and final nucleus de-excitation. The conditions for an INC are fulfilled at energies below 10 GeV (*Heikkinen*, 2009) and accordingly the models were not applied at higher energies.

In the frame of the present work, two different INC models were used. One is based on the Bertini model and included in the `G4CascadeInterface` framework. The other one is part of the `G4BinaryCascade`. As outlined above, spallation processes contain a variety of reactions and only a small part is treated in an INC model. Both INC frameworks in GEANT4 (`G4CascadeInterface, G4BinaryCascade`) come along with their own models to describe spallation processes after the initial cascade. For simplicity, however, it is only referred to the Bertini (BERT) and Binary (BIC) INC models, but one should keep in mind that this includes several other models. In the following, certain features and differences of the INC models applied in the present work are described.

Bertini INC

According to *Bertini* (1963, 1969) a heavy nucleus may be described by three concentric spherical shells approximating the continuously changing nuclear density and the corresponding potential. The ratio of neutron and proton density is considered to be identical in all regions (ρ_n/ρ_p = const.). The target nucleus is assumed to be a completely degenerate Fermi gas. As a consequence, the nucleons follow a Fermi gas momentum distribution $p_f \propto \rho(r)^{1/3}$ which is a function of the local nucleon density $\rho(r)$ in each nuclear shell at distance r from the center. The local Fermi energy is then given as

$$E_f = \frac{p_f^2}{2m_N}, \tag{B.6}$$

with m_N being the nucleon mass.
If the target nucleus is hydrogen, in `G4CascadeInterface` a regular particle-particle collision is performed without nuclear modeling. Nuclei with mass numbers below 4 are described by a single shell and only heavier nuclei have three shells. The Bertini-based approach in `G4CascadeInterface` can handle incident protons, neutrons, pions, kaons, and hyperons. A projectile particle entering the nucleus is tracked by solving the Boltzmann equation of motion on average. The reaction cross sections defining the locations of interactions inside the nucleus are calculated for free particles and modified with respect to the local Fermi momentum distribution, i.e. accounting for the Fermi potential. Following the Pauli principle, reactions in which the secondary particles have an energy below the local Fermi level are suppressed. After an initial collision, the INC finally terminates when the energy of all nucleons involved drops below the corresponding Fermi energy, and the nucleus is further treated with specific other models. The `G4CascadeInterface` framework has its own models for pre-equilibrium, fission, Fermi break-up, evaporation, and final nucleus de-excitation. A discussion of all these models is beyond the scope of this work but a detailed description may be found in *Heikkinen and Stepanov* (2003) and *Heikkinen* (2009) or in the Physics Reference Manual (*GEANT4 Collaboration*, 2009a).

Binary INC

The approach implemented in the `G4BinaryCascade` framework is very different from the prescribed Bertini INC model. It is basically a hybrid model of a classical cascade code and a quantum molecular dynamics (QMD) model (*Folger et al.*, 2004). Like in QMD, each participating nucleon is modeled as a Gaussian wave package. The nucleus consists of nucleons explicitly positioned in space in a manner that is consistent with the nuclear density distribution, the Pauli's exclusion principle, and the total nuclear mass. Therefore, each nucleon has its own Fermi momentum, and interactions take place as binary collisions between the projectile or scattered nucleons and an individual other nucleon in the target nucleus. Like in the Bertini INC, free hadron-hadron reaction cross sections are used to define collision locations in the nucleus and to calculate the corresponding momenta of all particles involved. The tracking inside the nucleus is done by numerical integration of the Boltzmann equation of motion. The Binary INC progresses after an initial collision until the average energy of all participants in the nucleus drops below a given nucleus-specific threshold (for details see *Folger et al.*, 2004). The remnant nucleus is then also further treated via pre-equilibrium, fission, Fermi break-up, evaporation, and final nucleus de-excitation models. These models differ somewhat from the ones used in the Bertini INC framework. Specific information on the models included in the Binary INC may be found in *Lara and Wellisch* (2001).

As outlined above, very different approaches for modeling the target nucleus and the actual collisions inside the nucleus are used in the INC frameworks `G4CascadeInterface` and `G4BinaryCascade`, respectively. Moreover, different criteria for the termination of an initial INC are implemented, and the remaining excited nuclei are further treated by different de-excitation models. As a consequence, differences in the simulation results are highly expected. Both cascade models have been validated against experimental data in terms of comparing double differential cross sections ($d\sigma/d\Omega dE$) for isotope production or nucleon yields. For both models satisfying and reasonable agreement with measurements may be found for various angles, energies, and target materials. Such validations as well as several successful applications of the models in sophisticated experiments can be found in e.g. *Heikkinen and Stepanov* (2003); *Folger et al.* (2004); *Heikkinen* (2009); *Apostolakis et al.* (2009) and references therein.

Quark Gluon String Precompound (QGSP) model

For the simulation of the radiation environment in the Earth's atmosphere the so-called Quark Gluon String Precompound (QGSP) model was used at very high energies. In this state-of-art code inelastic scattering of incident neutrons, protons, pions, and kaons is modeled in the energy range from 10 GeV to 100 TeV. This model is composed of several components which handle various parts of a high-energy interaction. The Quark-Gluon String (QGS) component models the formation of strings in an initial hadron-nucleon collision inside a nucleus. The subsequent fragmentation of strings into hadrons is handled by the Quark-Gluon String fragmentation model. The de-excitation of the remnant nucleus after the initial collision is finally handled by the precompound component. A complete description of this string-theory based model is beyond the scope of this work but details may be found in *GEANT4 Collaboration* (2009a).

B.4 Random number generation

The quality of any Monte Carlo simulation relies on the quality of the random numbers used to sample probability distribution functions (see B.1). There are several requirements to be fulfilled by an accurate pseudo random number generator. Most important of all is a good randomness in a preferably large period of numbers before the sequence is repeated. Another requirement is the ability to generate long disjoint subsequences allowing the user to combine independent simulation results or to parallelize the simulation.

All results from the present work were calculated with the `HepJamesRandom` algorithm from the `HEPRandom` module included in the CLHEP library of the GEANT4 toolkit (*GEANT4 Collaboration*, 2009b). This pseudo random number generator was first introduced by *Marsaglia et al.* (1990) and is a modified version of an algorithm by *James* (1990). It provides a well evaluated randomness in a very long period of about 2×10^{43}. Furthermore, 9×10^{8} different disjoint subsequences can be generated with an average length of 10^{30}. Therefore, all requirements for an appropriate pseudo random number generator are adequately fulfilled. In all calculations independence of the results was ensured by initializing the random number engine in each run with a unique time seed given by the current PC time.

B.5 Parallelization of calculations

In order to obtain simulation results with high statistical precision, usually the tracks of several millions of primary particles have to be simulated. Especially when modeling huge geometries such as the Earth's atmosphere this is very CPU time consuming. For this reason, it is straightforward to parallelize a transport calculation. This can be done by distributing the program to several CPUs and combining the results afterwards. A commonly used programming standard which can manage the communication between several CPUs is the Message Passing Interface (MPI)[3].

In the frame of the present work, OpenMPI[4] was used on Intel Core i7 machines with four physical CPUs and eight available threads each. The GEANT4 programs were modified in a way that the primary particles are distributed to all CPUs and calculated separately. After each CPU calculated all assigned particle tracks, the main CPU collects the results from all clients, further processes them, and finally gives an user defined output. The algorithm is based on a work of *Sutherland et al.* (2007) where the computing time was shown to linearly decrease with the number of CPUs involved. Furthermore, there is almost no limit for a potential acceleration of calculations with a finite number of CPUs since the traffic between the CPUs is extremely small during run time. However, it must be ensured that each CPU is initialized with a different random number in order to obtain independent results that can be combined. This was done in the present work by multiplying the time seed for each random number generator with the specific identification number of each CPU in the MPI interface.

---

[3] http://www-unix.mcs.anl.gov/mpi/

[4] www.open-mpi.org/

APPENDIX

C

SUPPLEMENTS ON BONNER SPHERE NEUTRON SPECTROMETRY

In the following some supplementary information on Bonner sphere neutron spectrometry is provided. In the first part the mathematical background of the unfolding procedure applied throughout the present work is explained. Subsequently, the complete sets of response matrices for neutrons and protons calculated in the frame of the present work with GEANT4 are discussed, before the correction of BSS measurements on the Zugspitze mountain and in Ny-Ålesund, Spitsbergen, (see Chapter 3) with respect to contributions from atmospheric protons is discussed. Finally, additional information on measurements performed in quasi-monoenergetic neutron fields at the RCNP in Osaka, Japan, is given in the last part of this chapter with main focus on results obtained at 30° emission angle.

C.1 Unfolding procedure in Bonner sphere spectrometry

What follows is a description of the mathematical background of the unfolding procedure applied in Bonner sphere spectrometry in the frame of the present work. The HMGU has been operating two Bonner sphere spectrometers consisting of 16 spheres each for continuous monitoring of secondary neutrons from cosmic radiation. The count rate ζ_i of each proportional counter in sphere i for a given spectral fluence rate distribution $\dot{\Phi}(E_k)$ can be calculated assuming 100% electronic efficiency of the system via

$$\zeta_i = \int_0^\infty R_i(E_k) \frac{d\dot{\Phi}(E_k)}{dE_k} dE_k \ , \quad i = 1, ..., 16, \tag{C.1}$$

where $R_i(E_k)$ is the response function at kinetic neutron energy E_k.
In any unfolding procedure the spectral fluence rate distribution from measured count rates has to be deduced by solving the inversion problem according to Equation C.1 for each sphere considered. Throughout the present work the unfolding code MSANDB developed by *Matzke* (1988, 2002, 2003) was used in order to accomplish this task. This deconvolution algorithm is a modified version of the SAND-II code developed by *McElroy et al.* (1967) that allows to take relative uncertainties of measurements into account.
Starting from a user-defined 'a priori' spectrum (start spectrum) $\dot{\Phi}^0$ MSANDB searches for the best fit to all measured count rates in an iterative manner. The basic underlying steps are the following:

1. In the first step the fluence rate $\dot{\Phi}^0$ and the corresponding response values in the energy bin j are used to calculate initial detector count rates ζ_i^0 for each sphere i:

$$\zeta_i^0 = \sum_{j=1}^{n} R_{ij} \dot{\Phi}_j^0 \tag{C.2}$$

2. Based on the calculated ζ_i^0 and measured count rates ζ_i^m as well as the corresponding uncertainties $\Delta\zeta_i$ an integral correction factor M is determined

$$\ln M = \frac{\sum_i \ln\left(\frac{\zeta_i^m}{\zeta_i^0}\right) \cdot (\Delta\zeta_i)^2}{\sum_i (\Delta\zeta_i)^2} \tag{C.3}$$

   With this factor the initial calculated count rates and the 'a priori' spectrum is scaled to the correct order of magnitude of the real fluence rate:

$$\dot{\Phi}_j^1 = M \cdot \dot{\Phi}_j^0 \quad , \quad \zeta_i^1 = M \cdot \zeta_i^0 \tag{C.4}$$

3. In the next step the actual iteration starts (iteration index k) by calculating relative contributions of the fluence rate $\dot{\Phi}_j$ in the energy bin j to the detector count rates of each sphere using the response functions:

$$W_{ij}^k = \frac{R_{ij} \dot{\Phi}_j^k}{\zeta_i^k} \tag{C.5}$$

4. With these weighting factors W_{ij}^k correction factors M_j^k are determined for each energy interval:

$$\ln M_j^k = \frac{\sum_i W_{ij}^k \ \ln\left(\frac{\zeta_i^m}{\zeta_i^0}\right) \cdot (\Delta\zeta_i)^2}{\sum_i W_{ij}^k \cdot (\Delta\zeta_i)^2} \tag{C.6}$$

5. Applying the correction factors M_j^k, updated fluence and count rates are calculated and the iteration loop starts again in step 3:

$$\dot{\Phi}_j^{k+1} = M_j^k \cdot \dot{\Phi}_j^k \quad , \quad \zeta_i^{k+1} = \sum_j R_{ij} \dot{\Phi}_j^k M_j^k \tag{C.7}$$

6. Two different criteria for the termination of the iteration process can be applied. Either a user-defined maximum number of iteration loops may be given or a user-defined minimum least square threshold ϵ for the relative changes of the total calculated count rates in subsequent iteration loops may be set:

$$\frac{\chi^{k+1}}{\chi^{k}} - 1 \leq \epsilon \quad \text{with} \quad \chi^{k} = \sum_{i} \left(\ln \frac{\zeta_i^m}{\zeta_i^k} \right)^2 \cdot (\Delta\zeta_i)^2 \tag{C.8}$$

For the unfolding of a spectral neutron fluence rate distribution using MSANDB the user has to provide appropriate data files including the response matrix, the measured count rates with related uncertainties (measurement vector), the start spectrum, the maximum iteration number, and/or the termination threshold ϵ. In order to make sure that the global minimum of deviations between measured and iteratively determined count rates is found, the ‘a priori’ spectrum may include all expected features (e.g. thermal, evaporation, cascade peak). In the low-energy region, however, it was shown in the frame of the present work that MSANDB is fully capable of deducing accurate spectral information even if a course inverse proportional to the energy is assumed, i.e. if almost no ‘a priori’ information is given (see Chapter 4). It should be noted, though, that due to the logarithmic weighting in step 2 and 4, MSANDB tends to produce resonances in the spectrum in case the maximum iteration number is too large. Therefore, the number of iteration loops should be below 900.

C.2 Bonner sphere response functions

In the following sections, the Bonner sphere response matrices for neutrons and protons calculated with GEANT4 are discussed, and a correction approach of BSS measurements with respect to cosmic ray protons is presented.

C.2.1 Responses to neutrons

The complete sets of neutron response functions calculated with GEANT4 are shown in Figure C.1. As described in Chapter 3 in detail, two different intra-nuclear cascade frameworks were applied above 20 MeV, the Bertini INC (`G4CascadeInterface`, solid lines) and the Binary INC (`G4BinaryCascade`, dashed lines).

With increasing sphere diameter the degree of moderation and the number of capture reactions in PE increase. Accordingly, in small spheres only low-energy neutrons have a high probability to reach the detector, whereas high-energy neutrons tend to escape. On the other hand, in larger spheres the low-energy neutrons are either reflected or absorbed in (n,γ) reactions, whereas higher energetic neutrons have a reasonable probability to be thermalized and detected in the proportional counter. For this reason, the sensitivity of each sphere peaks at a certain neutron energy. Small and medium-sized PE spheres have a broad maximum at lower energies, whereas large spheres have a sharp maximum at higher energies. Between about 20 MeV and several hundreds of MeV the sensitivity of all PE spheres drops since neutrons with these energies cannot be moderated efficiently within the corresponding PE volume. At higher energies secondary neutrons are produced in spallation processes in the moderator

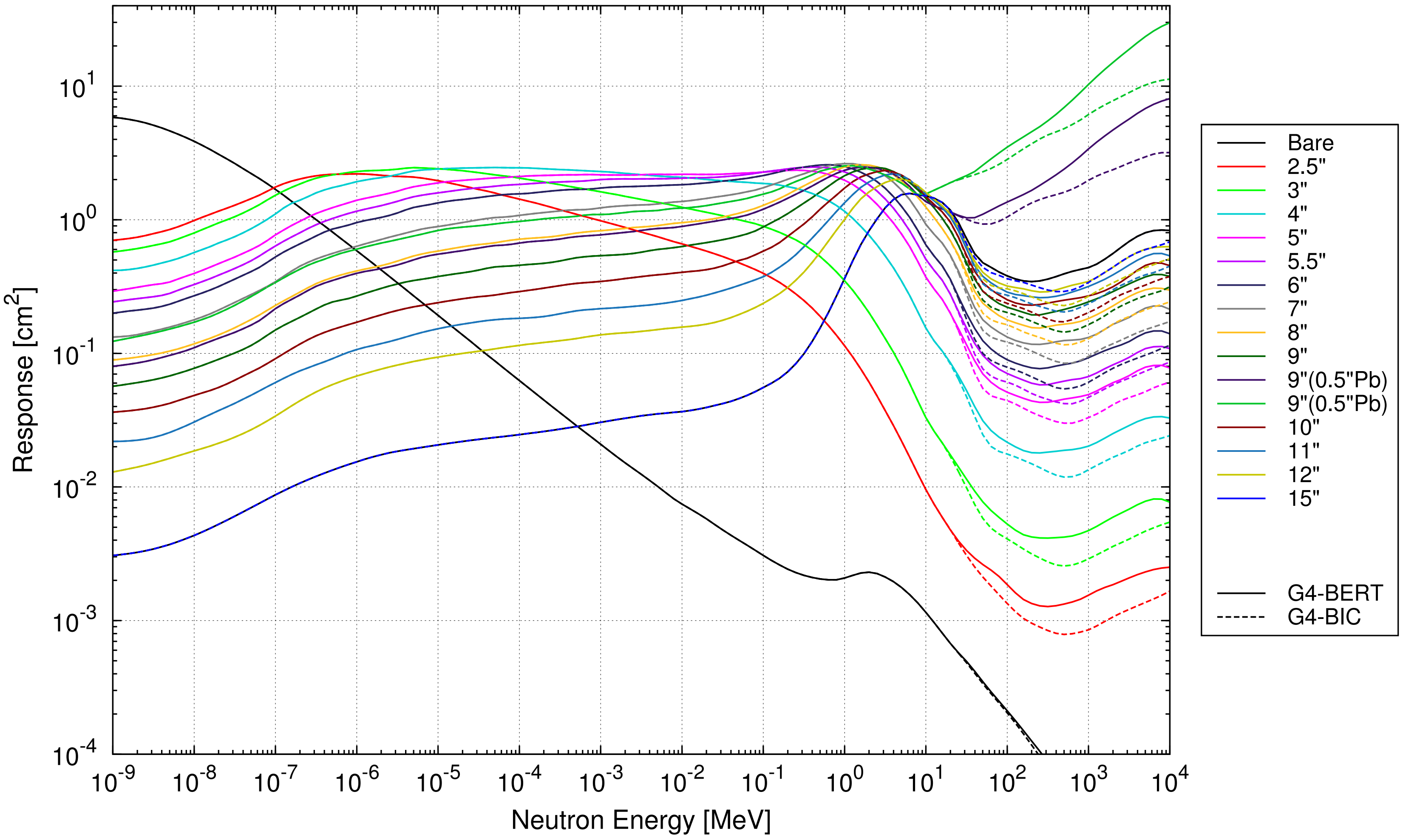

FIGURE C.1: Complete sets of BSS neutron response functions calculated with the GEANT4 Bertini (G4-BERT, solid lines) and the Binary (G4-BIC, dashed lines) intra-nuclear cascade models above 20 MeV. The response matrices contain 13 polyethylene spheres with 2.5, 3, 4, 5, 5.5, 6, 7, 8, 9, 10, 11, 12, 15 inches diameter, one bare ^{3}He proportional counter, and two 9 inch spheres with lead shells (0.5 and 1.0 inch thickness).

and the detector material which leads to an increasing response at very high energies. As obvious in Figure C.1, the course of all responses at these energies strongly depends on the INC model used for the high-energy neutron transport. Application of the Binary INC results in systematically lower responses compared with the Bertini INC.

The two spheres with 9 inch outer diameter and lead shells of 0.5 and 1.0 inch thickness, respectively, are special cases. The Pb nuclei provide a large target to incident high-energy neutrons and, accordingly, neutron multiplication due to spallation processes is much more efficient than in PE. Therefore, the responses of the two spheres including lead shells strongly increase above about 10 MeV.

Another special case is the bare detector which is not surrounded by any moderating material. Its response function basically resembles the course of the total ^{3}He cross section above a few meV energy. At lower energies all incoming neutrons are captured in ^{3}He(n,p) reactions, and the bare detector's response approaches its maximum value given by the cross sectional area of the proportional counter.

C.2.2 Responses to protons

The calculation of the proton response function was performed using the same physics as in the neutron transport calculations presented in Chapter 3. The spectrometers operated and maintained in the frame of the present work are applied for measurements of secondary cosmic radiation, where only protons with energies above several tens to hundreds of MeV exist. Protons at these energies generate secondary neutrons in the outer shells and the detector material which, in turn, may lead to pulses in the proportional counter. Besides, protons entering the counter would definitely also lead to ionizations in the counter gas. High-energy protons, however, deposit a much larger amount of energy in the counter gas than the 765 keV of the neutron-induced ^{3}He(n,p) reaction. Such pulses are, thus, discriminated anyway during operation of the spectrometers and were neglected. Low-energy protons below 10 MeV, on the other hand, cannot penetrate through the PE shells and, thus, do not lead to pulses in the detector. The proton response calculations were, therefore, completely restricted to pulses resulting from proton-induced spallation reactions where secondary neutrons are generated. Furthermore, the calculations were only performed using the Bertini hadronic framework in GEANT4. The results of the proton response calculations are shown in Figure C.2 for all spheres. Due to energy losses in the bulk material of all spheres, the proton responses are very low around 10 - 20 MeV. Furthermore, such low-energetic protons are barely capable of inducing spallation reactions since the binding energy per nucleon (several MeV) is too high with respect to the projectile's energy. With increasing proton energy losses per unit path length rapidly decrease and more protons are able to produce secondary neutrons in hadronic interactions with nuclei constituting a Bonner sphere. The proton responses, thus, rapidly increase with increasing energy and expectedly follow the neutron response functions above about 1 GeV.

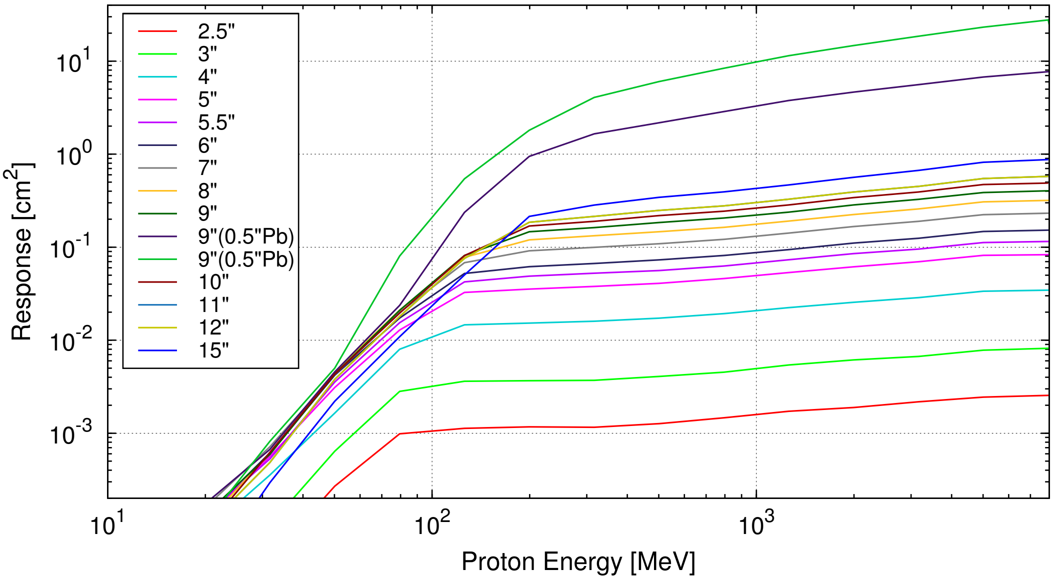

FIGURE C.2: Complete set of BSS proton response functions calculated with the GEANT4 Bertini intra-nuclear cascade model above 20 MeV. The response matrices contain 13 polyethylene spheres with 2.5, 3, 4, 5, 5.5, 6, 7, 8, 9, 10, 11, 12, 15 inches diameter and two 9 inch spheres with lead shells (0.5 and 1.0 inch thick).

C.3 Contributions of cosmic ray protons in BSS measurements

With the calculated responses of the Bonner spheres to protons, contributions of atmospheric protons to the BSS measurements of secondary cosmic ray neutrons performed at the Zugspitze mountain and in Ny-Ålesund, Spitsbergen (see Chapter 3) can be corrected.

C.3.1 Contributions in terms of detector readings

For this correction contributions to the detector readings were calculated with Equation C.1 using proton spectra simulated with GEANT4. In Chapter 5.4 it was shown that proton spectra calculated with the Bertini INC model agree much better with experimental data. Since the responses to protons were furthermore only calculated applying the Bertini INC, also Bertini-based spectra have to be taken in order to guarantee coherence in the correction approach. To estimate contributions at the locations of the two spectrometers, the corresponding proton spectra were used. In case of Ny-Ålesund this means sea-level conditions (1030 g/cm^2) and a vertical effective cutoff rigidity of 0 GV, whereas in case of the Zugspitze mountain this means 750 g/cm^2 and 4.4 GV cutoff. Using spectra calculated during solar minimum and maximum conditions, the corresponding proton contributions to the BSS measurements were estimated for a full solar cycle.

In Figure C.3 the absolute hourly contributions to the detector readings calculated with the prescribed spectra and the proton response functions are shown as a function of sphere diameter for solar minimum and maximum conditions. The top panel depicts the results for the

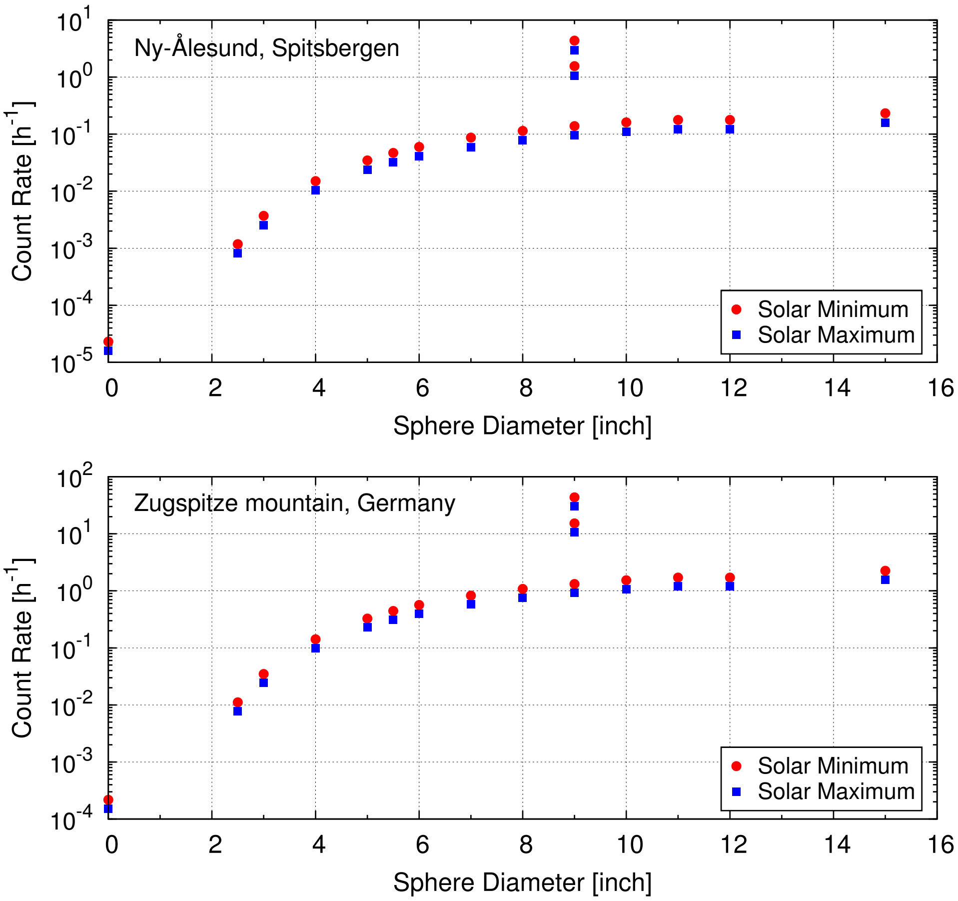

FIGURE C.3: Hourly contributions of cosmic ray protons to the detector readings of the two BSS systems operated by the HMGU in Ny-Ålesund, Spitsbergen (top panel), and the Zugspitze mountain (bottom panel) for solar minimum and maximum conditions.

BSS in Ny-Ålesund and the bottom panel those for the Zugspitze mountain. As expected, the bare detector and the small PE spheres detect only very few proton events, whereas medium-sized, larger spheres, and those including lead shells detect more protons due to the corresponding responses (see Fig. C.2). Differences in the count rates during solar minimum and maximum conditions are in the order of 30 - 35%. As a consequence of the higher proton flux at mountain altitudes, the contributions are about one order of magnitude higher at the Zugspitze mountain than in Ny-Ålesund.

C.3.2 Contributions in terms of unfolded fluence rates

The impact of the correction of Bonner sphere detector readings with respect to contributions from protons is demonstrated in the following for the sea-level BSS on Spitsbergen. Therefore, average count rates detected in January 2011 were corrected for protons and the spectra were unfolded with MSANDB (see C.1) using the GEANT4-BERT response matrix, 400 iteration loops, and a start spectrum including all spectral features expected for cosmic ray neutrons.

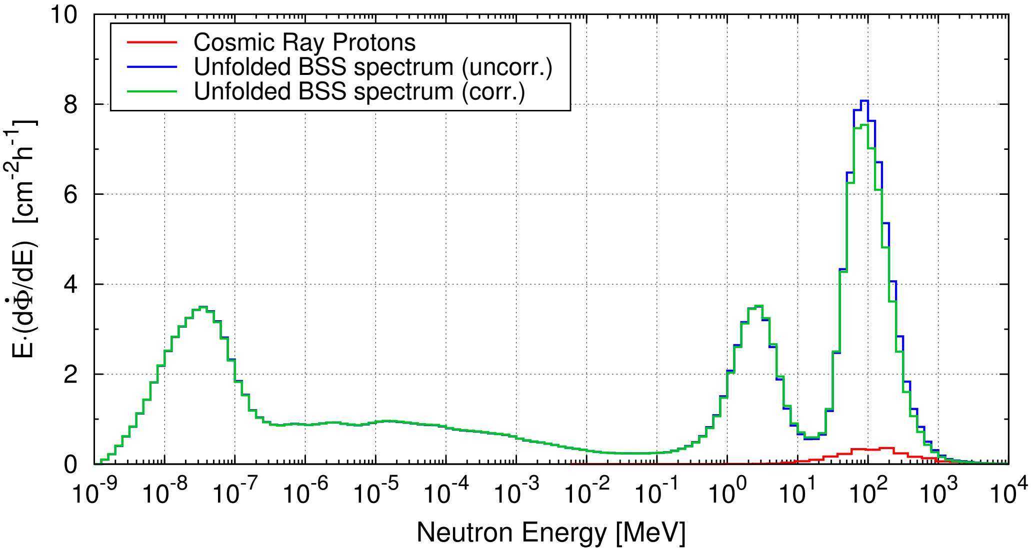

FIGURE C.4: Impact of the correction of proton contributions to the Bonner sphere detector readings recorded during January 2011 in Ny-Ålesund, Spitsbergen. The red spectrum shows the spectral fluence rate distribution of protons at sea-level, 0 GV cutoff, and solar minimum conditions as calculated with GEANT4 and the Bertini INC.

In Figure C.4 the corresponding unfolded corrected and uncorrected spectra are shown. Additionally, the spectral fluence rate distribution of protons at sea-level, 0 GV cutoff, and solar minimum conditions as calculated with GEANT4 and the Bertini INC is also depicted (red curve). Obviously, the impact of a correction of BSS data with respect to protons is rather small. Cosmic ray protons have a maximum around 100 - 200 MeV and, thus, protons only contribute to the cascade peak of the unfolded neutron spectrum. The correction of Bonner sphere count rates leads to a reduction in the energy-integrated fluence rate above 20 MeV of about 8%.

For the BSS on the Zugspitze mountain the same features are observed, but the overall contribution of protons to the integral fluence rates above 20 MeV is with a value of approximately 15% somewhat higher. This is due to the fact that at mountain altitudes the ratio of neutrons to protons in terms of particle numbers is somewhat lower than at sea-level.

C.4 Measurements in high-energy neutron fields at 30° emission angle

In Chapter 4 the unique BSS calibration measurements in quasi-monoenergetic neutron fields of 244 and 387 MeV at the RCNP in Osaka, Japan, were presented. These measurements were performed at 0° and 30° emission angles in order to get rid of low-energy contributions applying a subtraction method first proposed by *Nolte et al.* (2002). Unfortunately it turned out that the low-energy part of the spectra changed significantly, and subtraction of the 30° from the 0° measurements could not be applied. For the sake of completeness, however, the results obtained at 30° emission are presented in the following.

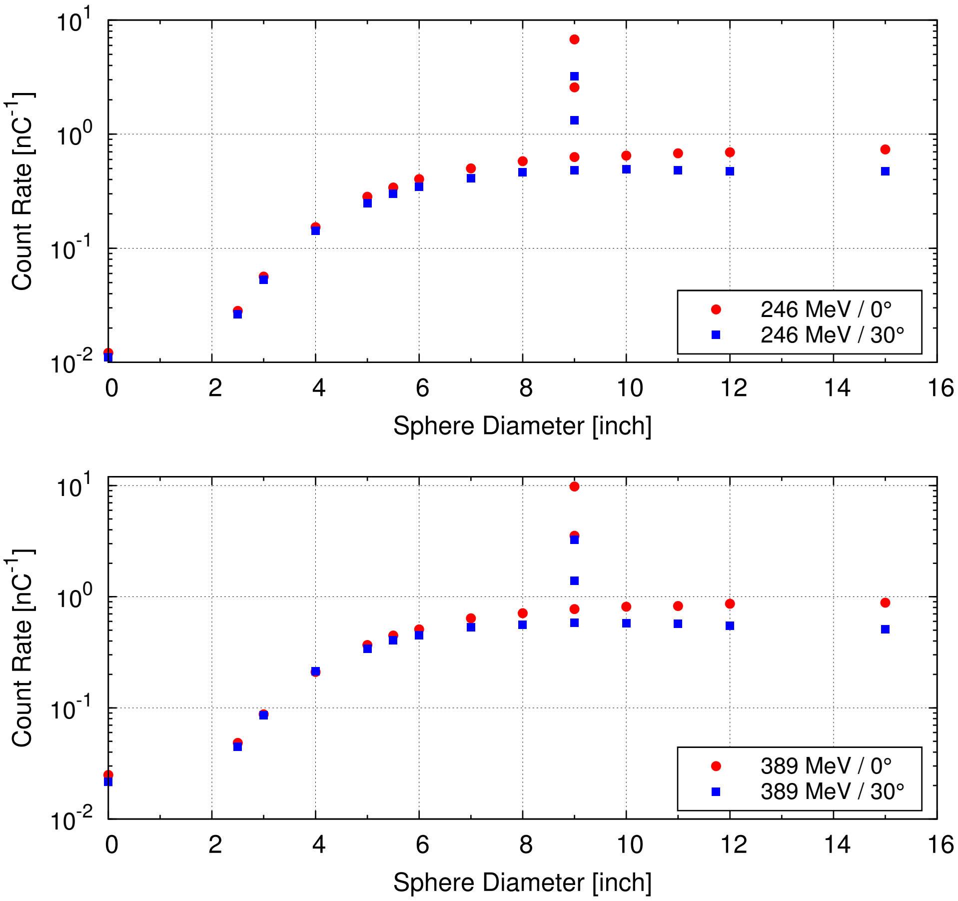

FIGURE C.5: Count rates measured with the BSS at a distance of 35 m from the target at 0° and 30° emission angles. In the top panel the measurement vectors are depicted for 246 MeV proton beam energy and in the bottom panel for 389 MeV. Statistical uncertainties are well below 1% for each sphere at both energies and angles.

The count rates measured at both emission angles are depicted in Figure C.5 as a function of sphere diameter. In the top panel of this figure the measurement vectors obtained at 246 MeV and in the bottom panel those at 389 MeV beam energy are shown. The statistical uncertainties were well below 1% for each sphere and all measurements. Comparison of the spheres' count rates at 0° and 30° already reflects the changes in the spectral neutron fluence rate distributions between both angles. Apparently, major changes occur in the high-energy region leading to major changes in the count rates of large PE spheres and in particular the two 9 inch spheres with lead shells. However, also the count rates of small and medium-sized PE spheres change significantly. Therefore, subtraction of 30° from 0° measurements could not be applied. This especially becomes obvious at 389 MeV beam energy where the 4 inch PE sphere even recorded about 1.5% higher count rates at 30° emission than at 0°. Since the statistical uncertainties of both measurements are below 0.4%, this difference is statistically significant.

To research the changes in the spectra at the two emission angles in more detail, the count rates shown in Figure C.5 were unfolded using the MSANDB unfolding code (*Matzke*, 1988, 2002, 2003). A detailed description of this unfolding code may be found in Appendix C.1. As start spectra for both angles and beam energies, the corresponding TOF measurements

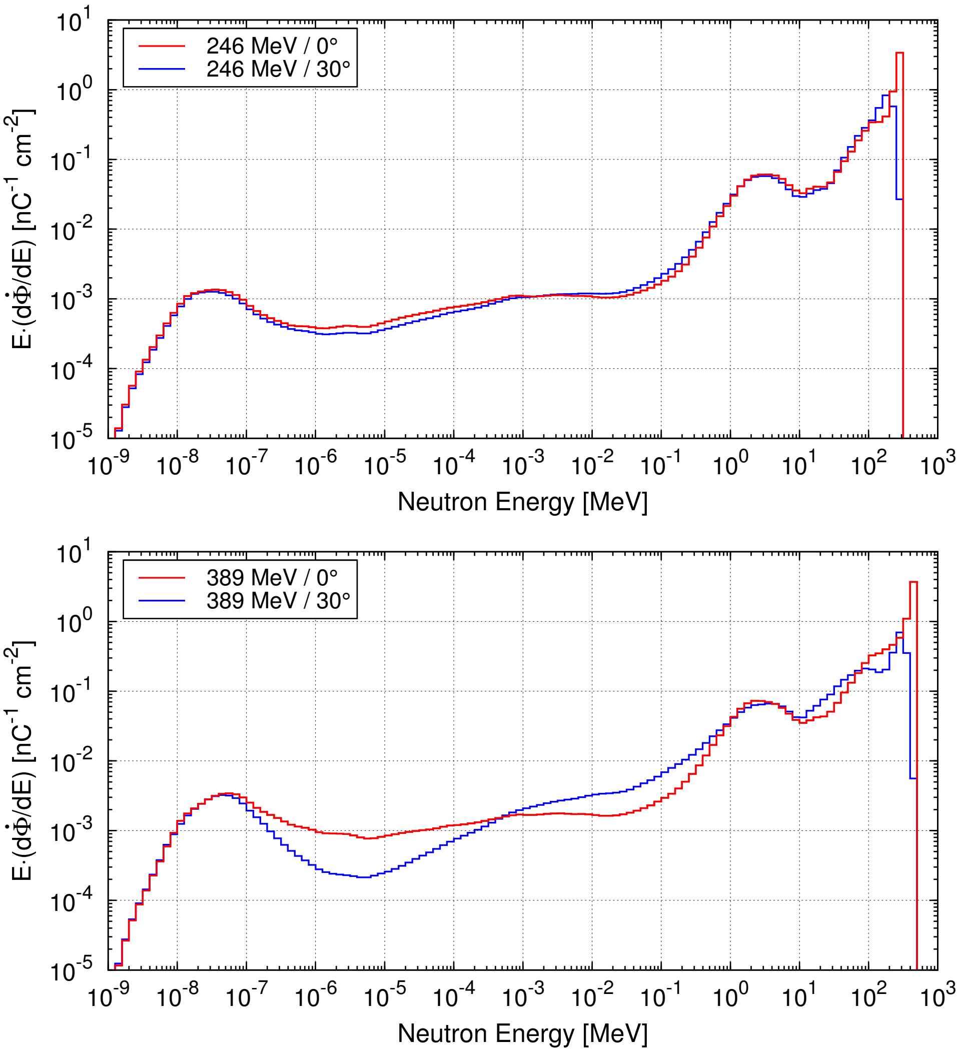

FIGURE C.6: Unfolded BSS spectra at 0° and 30° using the count rates from Figure C.5 and the GEANT4-BERT response matrix (Fig. C.1). In the top panel spectra are shown for 246 MeV and in the bottom panel for 389 MeV beam energy.

were used in an energy resolution of ten bins per decade above 10 MeV. These ‘a priori’ spectra were extended down to 1 meV with a course proportional to $1/E$, i.e. almost no ‘a priori’ information was assumed at low energies and a maximum iteration number of 500 was preset (see discussion in Chapter 4).

The resulting unfolded spectral fluence rate distributions are shown in Figure C.6 as differential neutron fluence rates $d\dot{\Phi}/d\ln(E)$ at 35 m distance from the target for both emission angles. The top panel summarizes the results for 246 MeV and the bottom panel those for 389 MeV beam energy. To give an example for the differences in the spectra observed at different angles, all spectra in Figure C.6 were unfolded using the response matrix calculated with GEANT4 and the Bertini INC model. In case of 246 MeV beam energy (top panel) the unfolded fluence rates at 0° and 30° emission angles agree very well for energies below about 100 MeV. At higher energies some discrepancies were observed between the two angles. These differences are in particular important for the two spheres including lead shells because they are very sensitive in this energy region. In case of 389 MeV beam energy, on the other hand, even in the epithermal energy region major differences between the measurements at different angles are observed, and differences in the high-energy region are much more pronounced than at 246 MeV. Extensive additional studies in the frame of the present work have shown that using different start spectra or changing the iteration number did not influence the resulting unfolded spectra at 30° much for all three sets of response functions. This clearly demonstrates that for the calibration of the BSS subtraction of 30° from 0° measurements should not necessarily be applied. It might be much more reasonable and feasible to calibrate the BSS by only using 0° measurements as presented in Chapter 4 in order to prevent the calibration results from being strongly biased due to a subtraction of the low-energy part of the spectra which might be influenced by an artifact.

ACKNOWLEDGMENTS
DANKSAGUNGEN

Allen voran möchte ich Herrn Prof. Dr. Herwig G. Paretzke danken, der mir dieses interessante Thema als Doktorarbeit ermöglicht und stets Vertrauen in meine Arbeit gesetzt hat. Großer Dank gebührt Herrn Prof. Dr. Werner Rühm für die Betreuung meiner Arbeit am Institut für Strahlenschutz des Helmholtz Zentrum München, der während der gesamten Promotionszeit dafür Sorge getragen hat, das Ziel nicht aus den Augen zu verlieren. Zu außerordentlichem Dank bin ich Herrn Vladimir Mares für zahlreiche fruchtbare Diskussionen, Gespräche und Anregungen verpflichtet. Stets hat er mich hilfsbereit und unermüdlich in allen Belangen meiner Arbeit und darüber hinaus unterstützt. Herzlichen Dank für die tolle Zusammenarbeit.
Frau Anita Herrling, der guten Seele unserer Arbeitsgruppe, möchte ich ebenfalls großen Dank für die unerläßliche Hilfe bei allen administrativen Angelegenheiten und die vielen auflockernden Gespräche aussprechen. Ebenso danke ich allen weiteren Kollegen der Arbeitsgruppe Personendosimetrie für den Erhalt einer angenehmen und produktiven Arbeitsatmosphäre.
Auch dem technischen Team der Umweltforschungsstation Schneefernerhaus auf der Zugspitze und dem der Koldewey-Station der French-German Arctic Research Base in Ny-Ålesund, Spitzbergen, gebührt besonderer Dank für die Unterstützung bei der Instandhaltung der kontinuierlichen Messungen mit Bonner-Vielkugelspektrometern.

Special thanks go to all Japanese colleagues for their kind support during the measurement campaigns at the Research Center for Nuclear Physics in Osaka, Japan. In particular I would like to thank Prof. Dr. Takashi Nakamura for initiating this fruitful collaboration. Extraordinary thanks go to Dr. Hiroshi Iwase and Dr. Yosuke Iwamoto for their enormous efforts in organizing the beam-times, providing all necessary information and data, and for taking care of any other issue during the experiments.

Furthermore, I would like to thank all institutes and researchers who contributed to my thesis in terms of providing data or scientific support, especially the Neutron Monitor stations South Pole, Terre Adelie, Oulu, Calgary, Climax, Goose Bay, Mawson, Apatity, Barentsburg, and Jungfraujoch.

Des Weiteren danke ich all meinen Freunden, die während der letzten Jahre für den nötigen Ausgleich auf privater Ebene gesorgt und mir auf viele Arten Freude bereitet haben.
Ganz besonderen Dank spreche ich zu guter Letzt meinen Eltern aus, ohne deren umfaßende Unterstützung in allen Lebensbereichen ich meine Doktorarbeit vermutlich weder begonnen noch fristgerecht abgeschlossen hätte.